

UNIVERSITÀ  
DEGLI STUDI  
DI PADOVA

SEDE AMMINISTRATIVA: UNIVERSITÀ DEGLI STUDI DI PADOVA  
DIPARTIMENTO DI SCIENZE CHIMICHE

---

CORSO DI DOTTORATO DI RICERCA IN SCIENZE MOLECOLARI  
CURRICOLO: SCIENZE CHIMICHE  
CICLO XXXI

# **The Photoexcited Triplet State as a Spin Probe for Distance Determination in Pulse EPR Dipolar Spectroscopy**

Coordinatore: Ch.mo Prof. Leonard Prins

Supervisore: Ch.ma Prof. Marilena Di Valentin

Dottoranda: Maria Giulia Dal Farra



*To Enrico*



## Abstract

The biological function of macromolecules such as protein, DNA, and RNA depends on their folding and on the relative movements of domains with dimensions of a few nanometers. This length scale can be accessed by distance measurements between paramagnetic spin centers employing Electron Paramagnetic Resonance (EPR) pulsed dipolar spectroscopy (PDS) techniques. In order to use this spectroscopic methods, the biomolecule has to contain either stable or transient paramagnetic centers, which can be metal ions or clusters, amino acid radicals, or organic cofactor radicals. If the biomolecule is diamagnetic, it can be spin-labeled with nitroxides or a diamagnetic metal may be substituted with a paramagnetic one. Nitroxides are the most employed spin probes in PDS, especially for structural studies in proteins where they can be attached to specific sites following a protocol of mutagenesis and site-directed spin labeling (SDSL) on cysteine residues. However, the introduction of a spin label can modify the structure around the labeling site and in some regions it may even interfere with the correct folding. For this reason, exploiting endogenous probes i.e. paramagnetic centers which are naturally present in the protein, represents an primary task in PDS. Indeed, PSD has been tentatively performed on various classes of proteins naturally containing metal base-prosthetic groups such as and low-spin ferric heme centers, iron-sulfur cluster, Mn clusters for which mainly the  $\Delta m_S = \pm 1/2$  transition can be selected. Utilizing endogenous probes for EPR detection only causes minimal functional perturbation to the macromolecules. Another advantage is that they are firmly anchored in the protein and, therefore, are not fraught with the problem of flexible linkers as the commonly used spin labels.

In recent years photoexcited triplet state of porphyrin has been introduced in the selection of spin labels for PDS applications. In their ground state, these chromophores are diamagnetic and thus EPR-silent, but, upon laser photoexcitation, their triplet state can be populated via inter-system crossing from the lowest excited singlet state, generating in this way the paramagnetic center. The inter-system crossing mechanism makes the population of the triplet sublevels different from the Boltzmann distribution, significantly enhancing the intensity of their EPR signals. Moreover porphyrin-derivative groups are suitable to be exploited as endogenous probes because are present in numerous systems such as heme-protein and photosynthetic proteins. The orthogonal labeling method, based on the use of spectroscopically nonidentical labels which can be addressed selectively in the EPR experiment, is attracting increasing interest in the spectroscopic community. Triplet states work very efficiently as orthogonal labels, adding to the spectroscopic selectivity the advantage of behaving as photoinduced spin probes. This feature allows to perform PDS in the presence of light excitation to measure intramolecular triplet-nitroxide

distances or in the absence of light excitation revealing intermolecular nitroxide-nitroxide interactions.

While the feasibility of the PDS experiment had already been demonstrated for a photoexcited porphyrin moiety interacting with a nitroxide radical [Di Valentin, M.; Albertini, M.; Zurlo, E.; Gobbo, M. and Carbonera, D. *J. Am. Chem. Soc.*, **2014**, *136*, 6582 -6585], the accuracy of the new labeling approach for distance determination, and the theoretical frame describing the behavior of polarized high-spin systems for application in dipolar techniques were still lacking. In this thesis work a complete spectroscopic and theoretical characterization of photoexcited triplet state probes has been carried out. The reliability and versatility of such spin labels has been tested employing different dipolar pulse schemes and exploiting diverse chromophores for the photogeneration of the paramagnetic center, both in peptide-based model systems and in protein belonging to different classes. The study has been completed with an exhaustive theoretical description.

The reliability and the accuracy of the new labeling approach has been demonstrated by measuring the dipolar traces of a spectroscopic ruler composed by  $\alpha$ -helix peptides of increasing length, labeled with a porphyrin chromophore, that upon photoexcitation gives the EPR-active species, and a nitroxide artificial amino acid. The good correlation between the distances obtained by experimental PDS data and calculation, is used to assess the accuracy of the new labeling approach. In PDS, there are different pulse sequences that exploits diverse mechanisms to induce the dipolar oscillations. Such pulse schemes have been tested on the triplet state in order to classify the performances of the various PDS techniques with the novel labeling approach. The availability of different light-induced PDS sequences increases the versatility of triplet state probes allowing to select case by case the pulse scheme that guarantees the best signal-to-noise ratio.

The new labeling approach has been extended to two paradigmatic proteins: the light-harvesting complex Peridinin-Chlorophyll *a*-Protein from *Amphidinium Cartarae* and the human Neuroglobin belonging to the globins family where the endogenous prosthetic groups have been exploited to photo-generated the triplet state. In the photosynthetic protein the dipolar trace arising from the interaction between the triplet state of one of the carotenoids in the photoactive site and a nitroxide, introduced via site-directed spin labeling, have been measured. This allowed to identify the pigment involved in the photoprotective mechanism and demonstrated that, not only porphyrin-derivatives, but also other chromophores can be used as spin probes. In human neuroglobin the Zn-substitution of the heme has allowed to populate the triplet state of the Zn protoporphyrin IX and successfully measure the dipolar trace proving the applicability of this labeling procedure on the class of heme proteins.

The full characterization of triplet state probes has been completed with a theoretical study based on the density matrix formalism. First, the analytic formula describing the modulation of the dipolar trace for a simplified radical-triplet state system has been obtained, highlighting a time an analogous dependence to the radical-radical case. Subsequently, a program for time-domain numerical calculation of radical-triplet state dipolar traces has been implemented and employed for a quantitative characterization of triplet state probes in PDS.

## Sommario

Il ruolo di molte macromolecole di interesse biologico come ad esempio proteine ed acidi nucleici, dipende dalla loro struttura tridimensionale e da movimenti di domini dell'ordine di pochi nanometri. La spettroscopia paramagnetica elettronica (EPR) ed in particolare le tecniche di spettroscopia impulsata dipolare (PDS) costituiscono lo strumento ideale per studiare sistemi di quest'ordine di grandezza. Tuttavia, per poter utilizzare tecniche PDS nella caratterizzazione di bio-macromolecole, queste devono contenere centri paramagnetici come ad esempio ioni o *cluster* metallici, oppure centri radicalici. Nel caso in cui il sistema sia diamagnetico è necessario quindi inserire delle sonde paramagnetiche o sostituire eventuali metalli diamagnetici con altri metalli EPR-attivi. I radicali nitrossidi sono le sonde di spin più comunemente impiegate nella spettroscopia dipolare, soprattutto per studi in proteina in cui, per introdurre di tali sonde, è possibile seguire un protocollo di mutagenesi sito-specifica seguita da *spin labeling* diretto alle cisteine. L'inserimento di sonde di spin tuttavia può causare forti modifiche strutturali alla macromolecola o addirittura interferire con il suo corretto *folding*. Per questo motivo, quando possibile si tenta di sfruttare centri paramagnetici che siano naturalmente presenti in proteina. Sono stati infatti effettuati diversi studi di spettroscopia dipolare in metallo-proteine sfruttando la transizione  $\Delta m_S = \pm 1/2$  del gruppo prostetico contenente il centro metallico. L'utilizzo di tali gruppi prostetici non causa alcuna alterazione strutturale alla molecola, inoltre, diversamente da molte sonde endogene, questi sono strettamente ancorati all'intorno proteico e forniscono quindi informazioni strutturali più accurate.

La porfirina in stato di tripletto fotoeccitato è stata di recente introdotta tra la collezione di sonde di spin utilizzabili nelle tecniche PDS. Nel loro stato fondamentale le porfirine sono diamagnetiche e pertanto EPR silenti, ma in seguito a fotoeccitazione laser possono popolare tramite *inter-system crossing* lo stato di tripletto eccitato a più bassa energia, diventando in tal modo EPR-attive. Il popolamento tramite *inter-system crossing* fa sì che la popolazione dei sottolivelli di tripletto devii dalla distribuzione di Boltzmann, aumentando enormemente l'intensità del segnale EPR di tale specie che vengono per questo motivo definite "polarizzate". Inoltre derivati porfirinici sono presenti in numerosi sistemi naturali, come ad esempio le emoproteine o le proteine coinvolte in processi fotosintetici, e ciò li rende particolarmente interessanti per l'utilizzo in spettroscopia dipolare in quanto possono essere sfruttati come sonde endogene. Il *labeling* ortogonale, basato sull'impiego di sonde di spin spettroscopicalmente distinte che possono essere eccitate selettivamente durante un esperimento EPR, rappresenta un approccio particolarmente vantaggioso nelle tecniche PDS. Gli stati di tripletto fotoeccitato hanno un valore aggiunto come sonde ortogonali perchè aggiungono alla selezione spettrale il fatto di essere sonde foto-indotte.

Questa caratteristica fa sì che sia possibile misurare distanze intramolecolari tripletto-nitrossido, applicando la fotoeccitazione laser, e distanze intermolecolari nitrossido-nitrossido spegnendo invece la fotoeccitazione.

Mentre la fattibilità di esperimenti di spettroscopia dipolare applicati a stati di tripletto fotoeccitati era già stata dimostrata precedentemente a questo lavoro di tesi [Di Valentin, M.; Albertini, M.; Zurlo, E.; Gobbo, M. and Carbonera, D. *J. Am. Chem. Soc.*, **2014**, *136*, 6582 -6585], mancavano completamente indagini in grado di stabilire l'affidabilità e l'accuratezza del nuovo sistema di *labeling* e un inquadramento teorico in grado di descrivere il comportamento di tali sistemi polarizzati ad alto spin durante l'esperimento PDS. Il lavoro alla base della presente tesi è consistito nella completa caratterizzazione spettroscopica e teorica di questi sistemi di spin. Per verificare l'affidabilità del nuovo approccio, le sonde di tripletto sono state testate con diverse tecniche PDS, e sono stati inoltre utilizzati vari cromofori per la foto-generazione del centro paramagnetico, effettuando l'analisi sia su sistemi modello che in proteina. Lo studio è stato completato con un esaustivo trattamento teorico dei sistemi tripletto-radicali in spettroscopia dipolare.

La precisione e l'accuratezza del metodo sono state verificate misurando le tracce dipolari di un righello spettroscopico costituito da una serie di peptidi in  $\alpha$ -elica di lunghezza crescente, ognuno marcato con un cromoforo porfirinico e un radicale nitrossido. L'ottima correlazione trovata tra le distanze ottenute analizzando le tracce sperimentali e i dati strutturali derivanti dai calcoli ha permesso di dimostrare l'affidabilità delle sonde di tripletto nelle tecniche PDS.

Attualmente sono disponibili diverse sequenze PDS che sfruttano diversi meccanismi per indurre l'oscillazione dipolare nelle tracce sperimentali. Molte di queste sequenze sono state quindi testate sulla sonda di tripletto in modo da verificarne le prestazioni con le diverse tecniche. La disponibilità di molteplici sequenze PDS e il loro buon funzionamento su sistemi fotoindotti permette di selezionare, a seconda dei casi, lo schema di impulsi che garantisce le migliori prestazioni in termini di rapporto segnale-rumore e ciò dimostra la versatilità delle sonde di tripletto.

La nuova metodologia è stata estesa anche a studi in proteina utilizzando come sistemi modello la *Peridinin-Chlorophyll a-Protein*, appartenente alla classe delle proteine fotosintetiche, e neuroglobina umana, facente parte della famiglia delle globine. In *Peridinin-Chlorophyll a-Protein* è stata misurata l'interazione dipolare tra uno dei carotenoidi presenti nel sito attivo e un nitrossido inserito tramite *spin labeling*, permettendo non solo l'individuazione del pigmento coinvolto nel meccanismo di fotoprotezione, ma espendendo anche l'applicabilità dell'esperimento a cromofori diversi dai derivati porfirinici. Nella neuroglobina umana invece la zinco-sostituzione dell'eme ha permesso di popolare lo stato di tripletto nel gruppo endogeno e dimostrando che la tecnica dipolare fotoindotta può essere utilizzata anche nello studio strutturale di proteine (macromolecole) appartenenti alla classe delle emoproteine.

Infine è stata effettuata anche un'esaustiva caratterizzazione teorica delle sonde di tripletto basata sul formalismo della matrice densità. È stata ricavata l'espressione che descrive la modulazione delle tracce dipolari in sistemi tripletto-radicali, che è risultata essere analoga a quella ottenuta per sistemi di due radicali interagenti. Successivamente è stato implementato un programma per il calcolo numerico di tracce dipolari che ha permesso una descrizione quantitativa di di-



versi sistemi tripletto-radicale.



# Thesis Outline

This thesis is organized in two parts: the first gives an overview on the theoretical background concerning the EPR spectroscopy and the physics triplet states; the second is devoted to the presentation of the experimental results.

The introduction is divided in three chapters regarding: (i) the fundamental concepts at the basis of the resonance phenomenon in EPR and the magnetic interactions investigated with this technique; (ii) the physics of the triplet state and the mechanisms that induce electron spin polarization; (iii) the EPR instrumentation and the spectroscopic experiments that have been employed in the studies presented this thesis.

The second part, where the results are presented, is divided in seven chapters edited with a scientific-paper layout. These works are the result of many different collaborations, both inside and outside the University of Padova. The EPR experiments have been performed partly in the EPR laboratory of the Dipartimento di Scienze Chimiche (Università degli studi di Padova) and partly at the Centre for Advanced Electron Spin Resonance (CAESR - University of Oxford), in collaboration with Prof. Christiane Timmel's group. The experimental data have been collected both on porphyrin-based model peptides, and on protein samples. The model peptides have been synthesized in Prof. Marina Gobbo's group at the Dipartimento di Scienze Chimiche (Università degli studi di Padova). The protein samples studied in this thesis are the Peridinin Chlorophyll *a*-Protein, that has provided by Professor Eckhard Hofmann at Department of Biology and Biotechnology (Ruhr-University, Bochum), and the Human Neuroglobin prepared by Caterina Martin in the group of Prof. Elisabetta Bergantino at the Dipartimento di Biologia (Università degli studi di Padova).

Besides the experimental spectroscopic work, a theoretical study, accomplished with the implementation routine for the numerical calculation of radical-triplet state dipolar traces, has been carried out, in collaboration with Dr. Claudia E. Tait and Prof. Stefan Stoll, at the University of Washington, Seattle. The calculations presented in this thesis have been partly performed on the Hyak supercomputer system (University of Washington) and partly on the C3P clusters (Dipartimento di Scienze Chimiche, Università di Padova).

DFT calculations on the model peptides series have been performed by Prof. Laura Orian at the Dipartimento di Scienze Chimiche (Università degli studi di Padova).



# Acknowledgments

I would like to thank Marilena Di Valentin for supervising me during the PhD. I am very grateful to her for being such a good mentor, for living me room for my ideas and pushing me beyond my limits, for being always present and supportive in the times of need.

I would like to thank Prof. Donatella Carbonera for accepting me in the EPR group, and all the members of the group for making a pleasant working atmosphere. In particular I would like to thanks Prof. Lorenzo Franco and Prof. Antonio Barbon for helping me with the EPR instrumentation.

I would like to express my gratitude to all the people that contributed to the projects that have been developed in this thesis, for sharing with me ideas and experiences. I would like to thank especially Prof. Stefan Stoll for giving me the possibility to spend a period in his group, and for guiding me through the theoretical part, for having been always available (even when I came back to Padova), and finding brilliant solutions to very complicated problems. Thanks to Claudia Tait for her precious help and suggestions on the spin dynamic theory and computer simulations. Thanks to all the people from the Stoll's group and to Meiling for making unique the experience in Seattle. I am very grateful also to the Ermenegildo Zegna Group for the financial support that made possible my stay at the University of Washington. I would like to thank Prof. Christiane Timmel, Sabine Richert and Alice Bowen for the fruitful collaboration and the long skype calls.

I can't thank enough my amazing friends in Padova for sharing with me the joys and the difficulties of these years. They are the reason why I loved the PhD experience. A special thanks goes to Maurizio Coden and Andrea Volpato for their invaluable help during the writing period. Thanks to Paola, for making the hard moments of the last months easier to face.

Last but not least, I want to thank my family and Jody for having been always present and for believing in me more than I did.



# Contents

<b>1 EPR spectroscopy and Magnetic Interaction</b>	<b>1</b>
1.1 The Resonance Phenomenon . . . . .	3
1.2 The spin Hamiltonian . . . . .	6
1.2.1 The Zeeman interaction . . . . .	6
1.2.2 The hyperfine interaction . . . . .	8
1.2.3 Nuclear quadrupole interaction . . . . .	9
1.2.4 Zero-field splitting interaction . . . . .	10
1.2.5 Weak coupling interaction between electron spins . . . . .	10
1.3 Relaxations . . . . .	11
1.3.1 Spin–lattice relaxation . . . . .	12
1.3.2 Spin–spin relaxation . . . . .	12
Bibliography . . . . .	14
<b>2 The Photoexcited Triplet State</b>	<b>15</b>
2.1 The Triplet State . . . . .	17
2.2 Spin Polarization . . . . .	20
2.2.1 Inter-system crossing . . . . .	20
2.2.2 Triplet-Triplet Energy Transfer . . . . .	23
2.2.3 Chemically Induced Dynamic Electron Polarization . . . . .	24
Bibliography . . . . .	27
<b>3 Experimental Setup and EPR Techniques</b>	<b>29</b>
3.1 Experimental setup . . . . .	31
3.1.1 CW-EPR . . . . .	31
3.1.2 TREPR . . . . .	32
3.1.3 Pulse EPR . . . . .	34
3.2 Pulse EPR techniques . . . . .	35
3.2.1 Pulse dipolar spectroscopy . . . . .	36
3.3 Light-induced dipolar techniques . . . . .	43
3.4 Spin labels in dipolar spectroscopy . . . . .	45
Bibliography . . . . .	47

## CONTENTS

<b>4</b>	<b>The Spectroscopic Ruler</b>	<b>51</b>
1	Introduction . . . . .	53
2	Experimental Section . . . . .	55
2.1	Synthesis . . . . .	55
2.2	EPR samples . . . . .	55
2.3	EPR and PELDOR spectroscopy . . . . .	55
2.4	Theory . . . . .	55
2.5	Quantum mechanical calculations . . . . .	56
2.6	PELDOR data analysis . . . . .	56
3	Results and Discussion . . . . .	56
3.1	Synthesis . . . . .	56
3.2	Triplet state versus Cu(II)-based-PELDOR . . . . .	57
3.3	Theoretical and computational results . . . . .	58
3.4	PELDOR spectroscopic ruler . . . . .	59
4	Conclusion . . . . .	61
5	References . . . . .	62
<b>5</b>	<b>Peridinin-Chlorophyll <i>a</i>-Protein</b>	<b>65</b>
1	Introduction . . . . .	67
2	Material and methods . . . . .	68
2.1	Mutegenesis protein expression and purification . . . . .	68
2.2	Labeling . . . . .	68
2.3	Pulse EPR and PELDOR measurements . . . . .	69
2.4	Spectral analysis . . . . .	69
3	Results . . . . .	69
4	Discussion . . . . .	70
5	Conclusions . . . . .	73
6	References . . . . .	73
<b>6</b>	<b>Pulse Dipolar Spectroscopy Techniques</b>	<b>75</b>
1	Introduction . . . . .	77
2	Experimental details . . . . .	79
2.1	Synthesis and EPR samples . . . . .	79
2.2	EPR measurements . . . . .	79
2.3	Data analysis and theory . . . . .	79
3	Result and discussion . . . . .	79
3.1	PELDOR on the porphyrin triplet-state spin label in a peptide-based spectroscopic ruler . . . . .	79
3.2	PELDOR on the carotenoid triplet-state spin label in the protein PCP . . . . .	81
3.3	LaserIMD on the porphyrin triplet-state spin label . . . . .	83
3.4	Comparison between photoexcited PELDOR and LaserIMD X-band experiments on the spectroscopic ruler . . . . .	84



3.5	Theory . . . . .	85
4	Conclusions . . . . .	88
5	References . . . . .	88
6	Appendix . . . . .	89
<b>7</b>	<b>Refocused-echo Laser Induced Modulation Dipole Spectroscopy</b>	<b>93</b>
1	Introduction . . . . .	95
2	Materials and Methods . . . . .	97
3	Results and Discussion . . . . .	98
4	Conclusions . . . . .	102
	Bibliography . . . . .	102
<b>8</b>	<b>Pulsed Dipole Spectroscopy in Human Neuroglobin</b>	<b>107</b>
	Bibliography . . . . .	113
<b>9</b>	<b>CIDEP in Human Neuroglobin</b>	<b>121</b>
1	Introduction . . . . .	123
2	Materials and Methods . . . . .	125
3	Experimental results . . . . .	125
4	Theoretical mechanism . . . . .	128
5	Discussion . . . . .	130
6	Conclusions . . . . .	132
	Bibliography . . . . .	134
<b>10</b>	<b>Theory</b>	<b>137</b>
1	Introduction . . . . .	139
2	Theory . . . . .	140
3	Method . . . . .	141
4	Results and Discussion . . . . .	143
5	Conclusions . . . . .	145
	Bibliography . . . . .	151



**CHAPTER** | **1**

**EPR spectroscopy and Magnetic Interaction**



## 1.1 The Resonance Phenomenon

EPR (Electron Paramagnetic Resonance) or ESR (Electron Spin Resonance) spectroscopy is a technique that allows to study the characteristics of paramagnetic centers. The magnetic moment associated to an electron is proportional to its angular momentum  $\hat{\mathbf{J}}$ :

$$\hat{\boldsymbol{\mu}} = -g \frac{e\hbar}{2m_e} \hat{\mathbf{J}} \quad (1.1)$$

where  $e$  and  $m_e$  are the charge and the mass of the electron and  $\hbar = h/2\pi$  is the reduced Planck constant.  $g$  is a pure number whose value depends on the relative contributions of the orbit and spin to the total angular momentum. If only the angular momentum  $\hat{\mathbf{l}}$  is present  $g$  is unity, apart from small corrections due to diamagnetic and relativistic effects that most of the times can be neglected [1]. If instead only the spin angular momentum  $\hat{\mathbf{s}}$  is present, a quantum electrodynamical correction has to be introduced and  $g = g_e$  and  $g_e$  is the  $g$ -value for the free electron corresponding to 2.00231930436082(52) [2]. When both orbital and spin momentum are present the value of  $g$  depends on the nature of the coupling between them.

In the presence of a static magnetic field  $\mathbf{B}_0$ , the magnetic moment experience a torque and the equation of motion is:

$$\hbar \frac{d\hat{\mathbf{S}}}{dt} = \hat{\boldsymbol{\mu}} \times \mathbf{B}_0 \quad (1.2)$$

The behavior of an ensemble of spins can be described in term of the total magnetization defined as the net magnetic moment per unit volume  $\hat{\mathbf{M}} = \frac{1}{V} \sum_i \hat{\boldsymbol{\mu}}_i$ . Equation 1.2 therefore becomes:

$$\hbar \frac{d\hat{\mathbf{M}}}{dt} = -\frac{g_e \mu_B}{\hbar} \hat{\mathbf{M}} \times \mathbf{B}_0 \quad (1.3)$$

where  $\mu_B = \frac{e\hbar}{2m_e}$  is the Bohr magneton. Only when the macroscopic magnetization is aligned along the magnetic field direction (i.e. the  $z$ -axis in the following description) it is invariant. When this is not the case, there is a torque, perpendicular to  $\hat{\mathbf{M}}$  that causes the magnetization to precess about the field direction at a characteristic frequency  $\omega_L$  called the *Larmor frequency*:

$$\omega_L = \frac{g\mu_B}{\hbar} B_0 \quad (1.4)$$

If a circularly polarized magnetic field, rotating at the microwave frequency  $\omega_{\text{mw}}$ , with components  $B_{1x} = B_1 \cos[\omega_{\text{mw}}t]$ ,  $B_{1y} = B_1 \sin[\omega_{\text{mw}}t]$  and  $B_{1z} = 0$ , is applied on the sample, the motion of the magnetization is described by the Bloch equations [3, 4, 5]:

$$\begin{aligned} \frac{d\hat{M}_x}{dt} &= \frac{g_e \mu_B}{\hbar} (B_0 \hat{M}_y - B_1 \sin[\omega_{\text{mw}}t] \hat{M}_z) \\ \frac{d\hat{M}_y}{dt} &= \frac{g_e \mu_B}{\hbar} (B_1 \cos[\omega_{\text{mw}}t] \hat{M}_z - B_0 \hat{M}_x) \\ \frac{d\hat{M}_z}{dt} &= \frac{g_e \mu_B}{\hbar} (B_1 \sin[\omega_{\text{mw}}t] \hat{M}_x - B_1 \cos[\omega_{\text{mw}}t] \hat{M}_y) \end{aligned} \quad (1.5)$$

Equations 1.5 can be simplified if the description is done in the so-called *rotating frame*, that rotates at the frequency of the microwave radiation and in which  $\mathbf{B}_1$  is time-independent:

$$\begin{aligned}\frac{d\hat{M}_x}{dt} &= -\Omega\hat{M}_y \\ \frac{d\hat{M}_y}{dt} &= \Omega\hat{M}_x - \omega_1\hat{M}_z \\ \frac{d\hat{M}_z}{dt} &= \omega_1\hat{M}_y\end{aligned}\tag{1.6}$$

where  $\Omega = (\omega_L - \omega_{mw})$  and  $\omega_1 = \frac{g_e\mu_B B_1}{\hbar}$ . The magnetization therefore precesses about an effective field which is tilted by an angle  $\theta = \arctan[\omega_1/\Omega]$  with respect to the static field direction. At resonance conditions  $\omega_L = \omega_{mw}$  and  $\Omega = 0$  thus, the magnetization, precesses only about the field  $B_1$ . The description above did not include relaxations but these are always present in any real spin system. Relaxations can be described as exponential decays that restore the equilibrium values of the magnetization components: zero for the  $x,y$ -plane and a quantity  $M_0$ , that depends on the Boltzmann population of the spin sublevels, for the  $z$ -direction. If relaxations are included in the description, the steady-state solution of the Bloch equations yield the Lorentzian function describing the EPR lineshape.

During an EPR experiment, a time-dependent linearly polarized magnetic field, is applied to the sample, either continuously or in the form of microwave pulses. This linearly polarized field can be considered as the superposition of a right-hand and a left-hand circularly polarized radiations. The left-hand component, after the transformation to the rotating frame, is  $2\omega_{mw}$  off-resonance and can therefore be neglected. In this situation the motion of the magnetization can still be described by Equations 1.5 and 1.6.

Bloch-equations are particularly useful not only in the explanation of the magnetic resonance phenomenon during a continuous microwave irradiation, but also in the description a pulse EPR experiment. At the resonance condition, the integration of Equations 1.6, for a  $B_1$  field, applied for a time  $t_p$ , gives:

$$\hat{M}_x = 0; \quad \hat{M}_y = -M_0 \sin[\omega_1 t_p] \quad \hat{M}_z = M_0 \cos[\omega_1 t_p]\tag{1.7}$$

The magnetization is therefore described by a vector whose components are determined by the angle  $\beta = \omega_1 t_p$ . By using the *vector model* description, the effect of a microwave pulse sequence is represented as a series of successive rotations of the magnetization vector. During the nutation periods, when the pulses are applied, the rotation is about the  $B_1$  direction, whereas in the free-precession periods between the pulses, the magnetization precesses about  $B_0$ . In the simplest pulse EPR experiment a single  $\pi/2$ -pulse, that tilts the magnetization in the  $x,y$ -plane, is applied and the return of the magnetization to its equilibrium position is recorded. In Figure 1.1, the effect of a  $\pi/2$ -pulse, and the subsequent return of the magnetization at the equilibrium position, is shown both in the rotating frame and in the laboratory frame. In the rotating frame, when all the spins are perfectly on resonance, the relaxation of the magnetization is simply a rotation in the  $y,z$ -plane. In the laboratory frame instead the magnetization precesses about the  $z$ -axis while

the  $x$  and  $y$  components exponentially decay.

The vector model is an easy and intuitive way for describing the motion of the magnetization, however it is strictly valid only for a two levels spin system or for experiments in which two levels of a larger spin system are involved. For the description of more sophisticated experiments the use of the density matrix formalism is required.

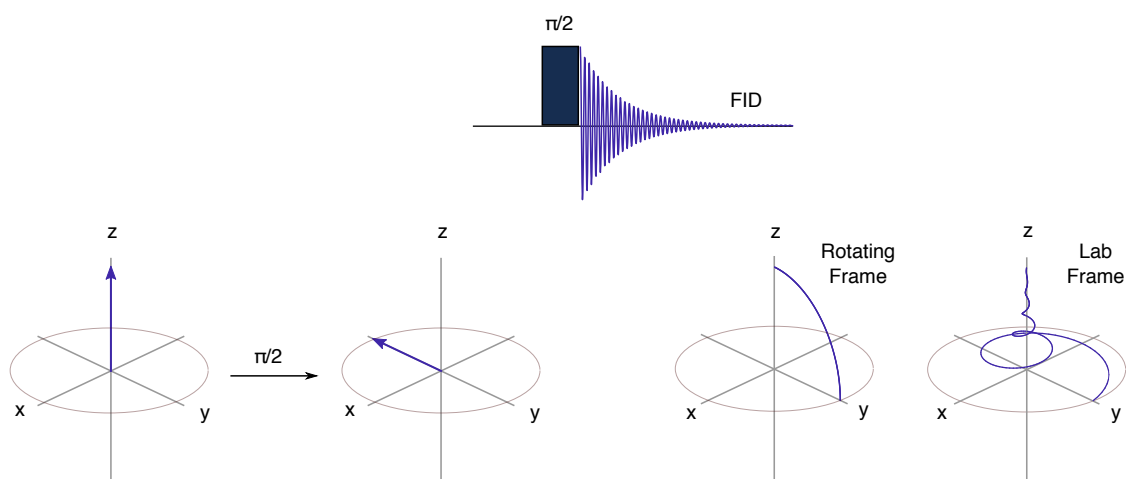


**Figure 1.1:** Representation of the free-induction decay experiment: at equilibrium the magnetization vector lies along the  $z$ -axis, after the application of a  $\pi/2$  pulse along the  $x$ -axis the magnetization is rotated along  $-y$ . The return to the equilibrium position observed from the rotating frame is simply a motion in the  $y,z$ -plane, whereas in the laboratory frame the precession toward equilibrium is a spiral motion.

## 1.2 The spin Hamiltonian

The fundamental tool for the interpretation of an EPR experiment is the spin Hamiltonian whose parameters represent a bridge between the physical observables and the molecular geometry and electronic structure [1]. The spin Hamiltonian is a sum of terms that describe the interactions among electronic and nuclear spins and between the spins and the applied magnetic. This should not be confused with the total Hamiltonian of the system governing the many-particles Schrödinger equation that allows to calculate the real energy levels of a molecule in the presence of a magnetic field [6]. The spin Hamiltonian is built with effective spin operators (fictitious angular momentum operators) that, nonetheless, allow a correct interpretation of the EPR spectrum. The advantage of using the spin Hamiltonian is that it simplifies the theoretical treatment allowing to work in a reduced Hilbert space of dimension:

$$n_H = \prod_{k=1}^n (2S_k + 1) \prod_{k=1}^m (2I_k + 1) \quad (1.8)$$

where  $n$  and  $m$  are the number of electron spin  $S$  and nuclear spin  $I$  [4].

The Spin Hamiltonian is in general written as a sum of different contributions:

$$\hat{H}_0 = \hat{H}_{EZ} + \hat{H}_{NZ} + \hat{H}_{ZFS} + \hat{H}_{HFI} + \hat{H}_{EE} + \hat{H}_{NQR} \quad (1.9)$$

respectively the electron Zeeman interaction, the nuclear Zeeman interaction, the zero-field splitting (ZFS), the hyperfine coupling between electron and nuclei, the electron–electron coupling and nuclear quadrupole interaction.

### 1.2.1 The Zeeman interaction

At the beginning of this Chapter, the expression describing the electronic magnetic moment of a free atom or ion has been introduced. In a more composite molecular system, due to the presence of other ions or bound atoms, we can no longer assume that the paramagnetic center is free. In such a situation the Zeeman interaction does not depend only on the angle between the external magnetic field and the spin vector, but also on the angle with certain symmetry axes of the magnetic complex [3]. Therefore, a convenient expression for the Zeeman interaction, which takes into account the anisotropy of the molecular system, is:

$$\hat{H}_{EZ} = \frac{\mu_B}{\hbar} \mathbf{B}_0 \cdot \mathbf{g} \cdot \hat{\mathbf{S}} \quad (1.10)$$

$\mathbf{g}$  is usually called  $\mathbf{g}$ -tensor. Strictly speaking  $\mathbf{g}$  is a matrix but most of the time, if the symmetry of the paramagnetic substance is not too low, it behaves like a tensor and even when this is not the case, the experimentally observed  $g$ -value for a given transition depends on the tensor  $\mathbf{g}\mathbf{g}^T$ :

$$\Delta\nu = \frac{\mu_B}{\hbar} B_0 \{ \mathbf{n} \cdot \mathbf{g} \cdot \mathbf{g}^T \cdot \mathbf{n} \}^{1/2} \quad (1.11)$$



where  $\mathbf{n}$  is the versor along the static magnetic field direction. The superscript "T" indicates the transpose operation, for simplicity this is neglected when referred to vectors.

In its principal axes system,  $\mathbf{g}$  is diagonal with principal values  $g_x$ ,  $g_y$  and  $g_z$ . If the three values are all different, the  $g$ -tensor is *rhombic* and the EPR spectrum of a powder sample has three turning points corresponding to molecular orientations in which the magnetic field is parallel to the principal axes. If instead there is at least a threefold symmetry rotation about a unique axis, two principal values coincide while the third is different. In this situation the  $g$ -tensor is *axial* and two turning points are present in the spectrum. For a cubic  $g$ -tensor no anisotropy of the Zeeman interaction is observed and the powder EPR spectrum is a single line. These three situations are depicted in Figure 1.2.

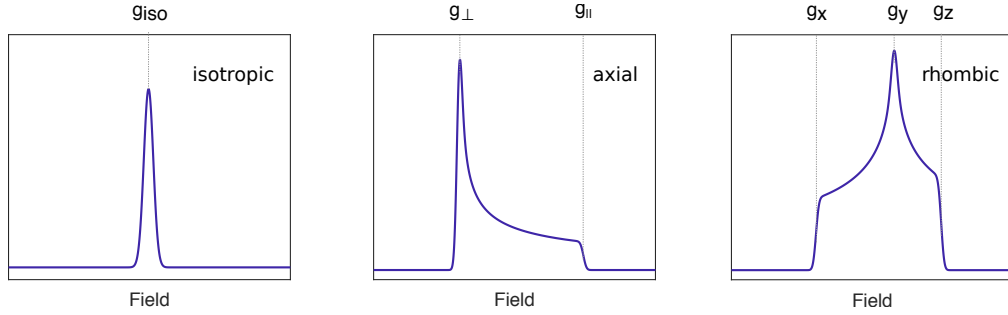


**Figure 1.2:** Calculated powder EPR spectra, with indicated the corresponding turning points, for three different  $g$ -tensors: isotropic (left), axial (center) and rhombic (right).

Provided that the numbers of protons and neutrons are not both even, nuclei also have spins angular momentum  $\hat{\mathbf{I}}$ . The magnetic moment associated to the nuclear spin is:

$$\hat{\boldsymbol{\mu}}_N = \mu_N g_N \hat{\mathbf{I}} \quad (1.12)$$

where  $\mu_N = e\hbar/2M$  is the nuclear magneton and  $M$  mass of the proton. Consequently, the nuclear Zeeman Hamiltonian is:

$$\hat{H}_{NZ} = -\frac{\mu_N}{\hbar} g_N \mathbf{B}_0 \cdot \hat{\mathbf{I}} \quad (1.13)$$

The Larmor frequency of a nuclear spin is  $\omega_L = -\frac{\mu_N}{\hbar} g_N B_0$ . Due to the much bigger mass of nuclei compared to that of electrons, the nuclear Larmor frequency is much smaller than that of the electron, even though strong differences exist among the various nuclei. As an example, with a field of about 0.34 T, the resonance frequency of the electron falls in the microwave region whereas that of a proton is in the radio frequency region.

The above spin Hamiltonians have been expressed in angular frequency units, this will be the unit of measurement of all the spin Hamiltonians in this thesis.

## 1.2.2 The hyperfine interaction

The hyperfine coupling is the interaction between the electron the nuclear spins and is described by the Hamiltonian:

$$\hat{H}_{\text{HFI}} = \hat{\mathbf{S}} \cdot \mathbf{A} \cdot \hat{\mathbf{I}} \quad (1.14)$$

where  $\mathbf{A}$  is the hyperfine tensor. The hyperfine interaction arises from the dipolar interaction between the nuclear and the electron magnetic moments [7]:

$$\hat{H}_{\text{T}} = \frac{\mu_0}{4\pi\hbar} g_e \mu_B g_N \mu_N \left[ \frac{3(\hat{\mathbf{S}} \cdot \mathbf{r})(\mathbf{r} \cdot \hat{\mathbf{I}})}{r^5} - \frac{\hat{\mathbf{S}} \cdot \hat{\mathbf{I}}}{r^3} \right] \quad (1.15)$$

where  $\mu_0$  is the vacuum permeability. The position of the electron is determined by the electronic wave function  $\psi_0$  thus, the terms of the Hamiltonian 1.15, are obtained integrating over the electron spatial coordinates. For spin only contribution to the magnetic moment, the integrals are:

$$T_{ij} = \frac{\mu_0}{4\pi} g_e \mu_B g_N \mu_N \left\langle \psi_0 \left| \frac{3r_i r_j}{r^5} - \frac{\delta_{ij}}{r^3} \right| \psi_0 \right\rangle \quad (1.16)$$

These are nonzero for all orbitals except for the  $s$ -orbital and hence there is no through-space dipolar coupling between an unpaired electron in a pure  $s$ -orbital and the nuclear spin of the same atom.

For an electron in the  $s$ -orbital, the integral of the dipolar field at the nucleus position is given by a delta function  $\frac{4\pi}{3}\delta(r)$ . This expression, that constitutes the isotropic contribution to the hyperfine coupling, was first derived by Fermi and is called *Fermi contact interaction*:

$$\hat{H}_{\text{F}} = a_{\text{iso}} \hat{\mathbf{S}} \cdot \hat{\mathbf{I}} \quad \text{with} \quad a_{\text{iso}} = \frac{2\mu_0}{3\hbar} g_e \mu_B g_N \mu_N |\psi_0(\mathbf{r}=0)|^2 \quad (1.17)$$

The hyperfine Hamiltonian is usually written as a sum of the two contributions:

$$\hat{H}_{\text{HFI}} = \hat{\mathbf{S}} \cdot (a_{\text{iso}} \mathbb{1} + \mathbf{T}) \cdot \hat{\mathbf{I}} \quad (1.18)$$

where  $\mathbb{1}$  is the identity matrix.

In the presence of a magnetic field, when no quadrupole interaction is present, the complete spin Hamiltonian  $\hat{H}_0$  is:

$$\hat{H}_0 = -\frac{\mu_B}{\hbar} \mathbf{B}_0 \cdot \mathbf{g} \cdot \hat{\mathbf{S}} + \sum_i \left( -\frac{\mu_N}{\hbar} g_N \mathbf{B} \cdot \hat{\mathbf{I}}_i + \hat{\mathbf{S}} \cdot \hat{\mathbf{A}}_i \cdot \hat{\mathbf{I}}_i \right) \quad (1.19)$$

where the sum runs over all the coupled nuclei. In solution, because of the rapid tumbling of the molecules, only the average value of  $\mathbf{A}$ - and  $\mathbf{g}$ -tensors are accessible. In this case the EPR spectrum of a  $S=1/2$  system occurs in its simplest form, with a number of peaks given by  $\sum_i [2n_i \cdot I_i + 1]$  where  $n_i$  is the number of nuclei, characterized by  $I_i$  spin, coupled to the electron. The EPR spectrum of a powder sample instead appears more structured since it holds information about the anisotropy of  $\mathbf{A}$ - and  $\mathbf{g}$ -tensors.

As an example, the calculated spectra of a nitroxide radical, both in liquid and in solid phase, are

depicted in Figure 4. The two spectra present a hyperfine structure due to the coupling between the unpaired electron and the  $^{14}\text{N}$  nucleus ( $I=1$ ). In liquid solution, the spectrum is dominated by the isotropic hyperfine interaction and shows three well resolved peaks (displayed in Figure 4 as the derivative of the absorption signals) corresponding to the different values of  $m_I$ . The powder spectrum instead includes the information if the anisotropy of the A- and g-tensors..

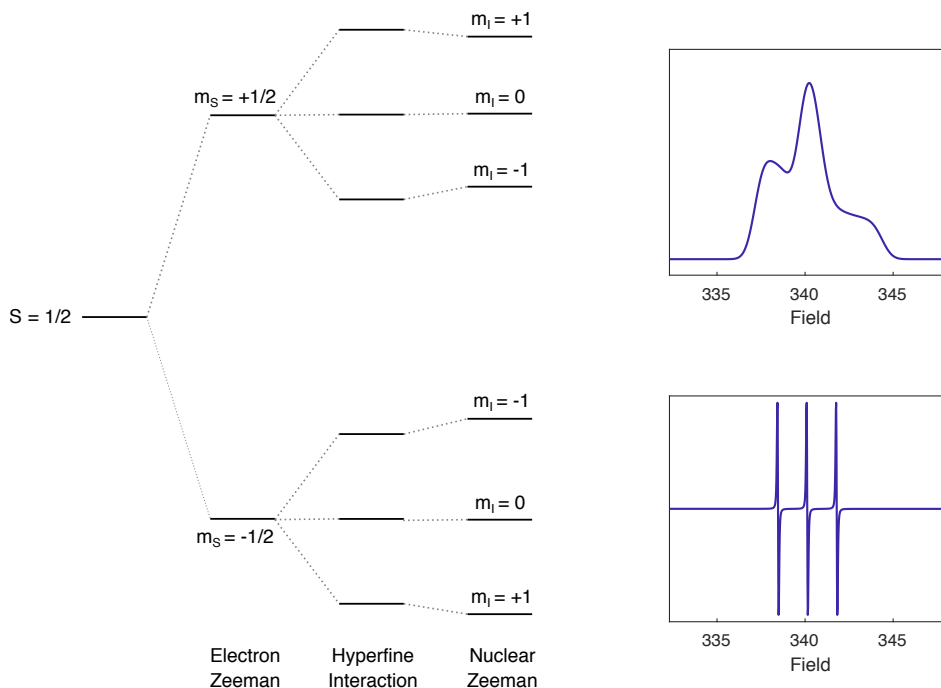


**Figure 1.3:** Left: Schematic representation of the splitting of the spin sublevels in a nitroxide radical. Right: calculated powder EPR spectrum (top) and EPR spectrum in the fast motion regime, displayed as the derivative of the absorption signal (bottom), of a nitroxide radical. The spectra have been calculated with EasySpin [8]. The parameters of the simulations are  $[g_x, g_y, g_z] = [2.01, 2.01, 2.008]$  and  $[A_x, A_y, A_z] = [12, 12, 100]$  MHz.

### 1.2.3 Nuclear quadrupole interaction

If the nuclear spin quantum number is bigger than 1/2, the electric quadrupole moment of the nucleus strongly interacts with the electric field gradients generated by the surrounding electrons and nuclei. The quadrupole Hamiltonian can be written as:

$$\hat{H}_{\text{NQ}} = \hat{I} \cdot \mathbf{Q} \cdot \hat{I} \quad (1.20)$$

where  $\mathbf{Q}$  is the quadrupole tensor.  $\mathbf{Q}$  is a symmetric and traceless tensor and thus it averages out to zero in liquid samples. When it is smaller than the nuclear Zeeman and the hyperfine coupling, the quadrupole interaction, in solid samples, only shifts the energy levels according to the nuclear states  $m_I$  [9].

### 1.2.4 Zero-field splitting interaction

When two or more unpaired electrons are present in a paramagnetic center and they are strongly interacting, the description of the system is conveniently carried out in the coupled representation by using the total spin angular momentum. In such a system the dipolar interaction between the electrons, or, in the presence of heavy metal centers, the spin-orbit coupling, cause the so-called zero-field splitting (ZFS). This interaction is responsible for the removal of the degeneration of the spin sublevels that take place also in the absence of an applied magnetic field. The ZFS Hamiltonian is [5]:

$$\hat{H}_{ZFS} = \hat{\mathbf{S}} \cdot \mathbf{D} \cdot \hat{\mathbf{S}} \quad (1.21)$$

where  $\mathbf{D}$  is the ZFS tensor. In its principal axes system, the ZFS tensor is diagonal and the Hamiltonian 1.21 can be written as a function of the three principal values  $X, Y, Z$ :

$$\hat{H}_{ZFS} = D_{XX}\hat{S}_x^2 + D_{YY}\hat{S}_y^2 + D_{ZZ}\hat{S}_z^2 \quad (1.22)$$

A more detailed description of the ZFS interaction is given in Chapter 2.

### 1.2.5 Weak coupling interaction between electron spins

Weakly coupled electron spins are usually described by their individual spins rather than by the total spin angular momentum. These spins interact via exchange and dipolar interaction. For the sake of simplicity, the description of such interactions in the next sections is limited to the case of two unpaired electrons.

#### Exchange interaction

The exchange interaction Coulomb interaction that originates from the overlap of the spatial wavefunctions of the coupled electrons. This is responsible of the energy splitting between the triplet and the singlet state and is described by the following Hamiltonian:

$$\hat{H}_{exc} = \hat{\mathbf{S}}_1 \cdot \mathbf{J} \cdot \hat{\mathbf{S}}_2 \quad (1.23)$$

where  $\mathbf{J}$  is a 3x3 matrix that takes into account the Coulomb interaction between the unpaired electrons indicated by the subscripts 1 and 2 [10]. The anisotropic contribution to the exchange coupling is mainly due to spin-orbit coupling but for organic radicals this is generally very small and can be neglected. The isotropic part of the exchange interaction is:

$$(\hat{H}_{exc})_{iso} = J_0 \hat{\mathbf{S}}_1 \cdot \hat{\mathbf{S}}_2 \quad (1.24)$$

where  $J_0$  is the exchange integral. Whether the singlet or the triplet state lies lower in energy depends on the sign of  $J_0$ : if  $J_0 > 0$  the singlet state lower in energy compared to the triplet while the opposite is true for  $J_0 < 0$ . The magnitude of  $J_0$  decrease exponentially with the distance between the two electrons and in solids 1.5 nm is usually accepted as the limit value beyond

which the exchange interaction can be neglected with respect to the other spin-spin interactions [11].

### Dipole–dipole interaction

The dipole–dipole coupling between two electron spins can be derived from the classical analogue of two interacting magnetic dipoles, substituting the in the expression the proper operators:

$$\hat{H}_{\text{dip}} = \frac{\mu_0 \mu_B^2 g_e^2}{4\pi \hbar r_{12}^3} (\hat{\mathbf{S}}_1 \cdot \hat{\mathbf{S}}_2 - 3(\hat{\mathbf{S}}_1 \cdot \mathbf{n}_{12})(\hat{\mathbf{S}}_2 \cdot \mathbf{n}_{12})) \quad (1.25)$$

where  $\mathbf{n}_{12}$  is the versor along the direction connecting the two electrons. The scalar products in Equation 1.25 can be expanded to give six terms [12]:

$$\hat{H}_{\text{dip}} = \frac{\mu_0 \mu_B^2 g_e^2}{4\pi \hbar r_{12}^3} [\hat{A} + \hat{B} + \hat{C} + \hat{D} + \hat{E} + \hat{F}] \quad (1.26)$$

The explicit form of the terms is:

$$\begin{aligned} \hat{A} &= \hat{S}_{1z} \hat{S}_{2z} (1 - 3 \cos^2 \theta) \\ \hat{B} &= -\frac{1}{4} [\hat{S}_{1+} \hat{S}_{2-} + \hat{S}_{1-} \hat{S}_{2+}] (1 - 3 \cos^2 \theta) \\ \hat{C} &= -\frac{3}{2} [\hat{S}_{1z} \hat{S}_{2+} + \hat{S}_{1+} \hat{S}_{2z}] \sin \theta \cos \theta e^{-i\phi} \\ \hat{D} &= -\frac{3}{2} [\hat{S}_{1z} \hat{S}_{2-} + \hat{S}_{1-} \hat{S}_{2z}] \sin \theta \cos \theta e^{i\phi} \\ \hat{E} &= -\frac{3}{4} \hat{S}_{1+} \hat{S}_{2+} \sin^2 \theta e^{-2i\phi} \\ \hat{F} &= -\frac{3}{4} \hat{S}_{1-} \hat{S}_{2-} \sin^2 \theta e^{2i\phi} \end{aligned} \quad (1.27)$$

where  $\hat{S}_{\pm}$  are the raising and the lowering operators of the two electrons and  $\theta$  is the angle between the inter-spin vector and the external field  $\mathbf{B}_0$ . In the high field approximation, i.e.  $\hat{H}_{ZE}^1, \hat{H}_{ZE}^2 \gg \hat{H}_{\text{dip}}$ , the non-secular terms, C-F, can be neglected. Moreover in the case of weak coupling, when the difference between the resonance frequencies of the two electrons is much greater than the dipolar frequency ( $\Delta\omega_{1-2} \gg \omega_{\text{dd}}$ ), also the pseudosecular term  $B$  drops and the dipolar Hamiltonian becomes:

$$\hat{H}_{\text{dip}} = \omega_{\text{dd}} (3 \cos^2 \theta - 1) \hat{S}_{1z} \hat{S}_{2z} \quad (1.28)$$

with:

$$\omega_{\text{dd}} = \frac{\mu_0 \mu_B^2 g_e^2}{4\pi \hbar r_{12}^3} \quad (1.29)$$

## 1.3 Relaxations

Relaxation is a fundamental phenomenon in EPR that causes the loss of polarization and coherence of the spin system. At Boltzmann equilibrium, at the fields that are commonly used in EPR,

the difference of population between the spin sublevels is very small (for example, in a field of 0.34 mT, for a  $S=1/2$  spin system, is about 0.1%), thus, the excitation of even a small fraction of the spins can approximately equalize the populations of the sublevels, with the results that no net EPR signal can be observed. Therefore in designing and interpreting EPR experiments, relaxations processes must be taken into account [13].

Relaxation in EPR is describe in term of two processes: spin-lattice relaxation, described by the time constant  $T_1$ , and spin-spin relaxation, characterized by the constant  $T_2$ .

### 1.3.1 Spin–lattice relaxation

During an EPR experiment the spin system is perturbed by the microwave radiation that moves the magnetization from its equilibrium position along the magnetic field direction. Spin–lattice relaxation, also called longitudinal relaxation, determines how quickly the magnetization realigns to the magnetic field. During this process the magnetic quantum number changes and the spin system exchanges energy with its surrounding. The energy transfer between the spins and the lattice is mediated by fluctuating magnetic fields at the Larmor frequency. In solids these are mainly caused by modulation of the spin-orbit coupling induced by lattice vibrations. In liquids the fluctuating fields are generated by molecular motion.

Longitudinal relaxation time is a crucial parameter in pulse EPR because it determines the repetition time and thus the duration of the experiment.  $T_1$  can be experimentally measured by an inversion-recovery experiment in which the magnetization is inverted by a  $\pi$ -pulse and its return to equilibrium is recorded typically by a primary echo detection sequence.

### 1.3.2 Spin–spin relaxation

Spin–spin relaxation, also called transverse relaxation, is the process that causes the loss of coherence of the spin system in the  $x,y$ -plane. The main mechanism that contributes to spin–spin relaxation is the flip-flop mechanism which, in a two levels system, it can be described as a change of the spin A from the  $\alpha$  to the  $\beta$  state accompanied by the flip of the spin B from  $\beta$  to  $\alpha$  without the transfer of energy to the surroundings. Also longitudinal relaxation contributes in destroying the phase coherence of the spin system, but this process is slower then the flip-flop mechanism. Transverse relaxation is determined by the coupling with both nuclear and electronic spins in the surrounding. In liquid solutions  $T_2$  depends on the spectral density of the thermal motion process at zero frequency.

In solids, where a virtually infinite network of coupled spins is present,  $T_2$  is not well defined. Instead, the description of the loss of in-plane coherence is usually described in term of an empirical parameter  $T_m$  called *phase-memory time*.  $T_m$  can be quantified as the decay of the primary echo when the inter-pulse delay is increased. This is usually an exponential or a stretched exponential decay.

There are many processes that in an EPR experiment contribute to decreasing the phase-memory time. One of this is for example the longitudinal or spin-spin relaxations of non resonant nuclear or electron spins which are coupled to the observed spins. These cause fluctuating fields

that enhance the loss of coherence of the magnetization. Such a process is particularly strong in systems with many protons and the phase-memory time can indeed be increased by deuterating the sample.

Another contribution derives from spectral diffusion in which the relaxation of an off-resonance spin B changes the local field at the A spin position moving its magnetization to portions of the spectrum that are not detected. At the same time, due to relaxation of A spins, the equilibrium magnetization of some B spins may be transferred to parts of the spectrum that are detected. Overall, this process appears like a relaxation of the spin A. Instantaneous diffusion instead occurs because samples cannot be considered as magnetically diluted and the spins interact via dipole–dipole interaction. Hence, the flip of one spin changes the local field experienced by all the coupled spins interfering with the refocusing. Even in the absence of additional pulses, dipolar coupling between two spins mixes their polarization and the effect is called spin diffusion [4].

## Bibliography

- [1] A. Abragam and B. Bleaney. *Electron Paramagnetic Resonance of Transition Ions*. Oxford University Press, 1970.
- [2] Robert S. Van Dyck, Paul B. Schwinberg, and Hans G. Dehmelt. Electron magnetic moment from geonium spectra: Early experiments and background concepts. *Phys. Rev. D*, 34:722–737, 1986.
- [3] N. M. Atherton. *Principles of electron spin resonance*. Ellis Horwood PTR Prentice Hall, 1993.
- [4] Arthur Schweiger and Gunnar Jeschke. *Principles of pulse electron paramagnetic resonance*. Oxford University Press, New York, 2001.
- [5] John A. Weil and James R. Bolton. *Electron Paramagnetic Resonance: Elementary Theory and Practical Applications*. Wiley, 2nd edition, 2007.
- [6] Frank Neese. *Quantum Chemistry and EPR Parameters*, pages 1–22. American Cancer Society, 2017.
- [7] Marina Bennati. EPR Interactions – Hyperfine Couplings. In *eMagRes*, pages 271–282. American Cancer Society, 2017.
- [8] Stefan Stoll and Arthur Schweiger. EasySpin, a comprehensive software package for spectral simulation and analysis in EPR. *J. Magn. Reson.*, 178(1):42–55, 2006.
- [9] Marina Brustolon and Elio Giamello. *Electron Paramagnetic Resonance: A Practitioner's Toolkit*. John Wiley & Sons, New Jersey, 2008.
- [10] G E Pake and Thomas L Estle. *The physical principles of electron paramagnetic resonance*. Reading, W.A. Benjamin, MA, USA, 2nd edition, 1973.
- [11] Bela E. Bode, Jörn Plackmeyer, Michael Bolte, Thomas F. Prisner, and Olav Schiemann. PELDOR on an exchange coupled nitroxide copper(II) spin pair. *J. Organomet. Chem.*, 694(7-8):1172–1179, 2009.
- [12] Alice M Bowen, Claudia E Tait, Christiane R. Timmel, and Jeffrey R Harmer. *Orientation-Selective DEER Using Rigid Spin Labels, Cofactors, Metals, and Clusters*, pages 283–327. Springer Berlin Heidelberg, Berlin, Heidelberg, 2013.
- [13] Sandra S Eaton and Gareth R Eaton. *Relaxation Mechanisms*, pages 1543–1556. American Cancer Society, 2016.



**CHAPTER** | **2**

**The Photoexcited Triplet State**



## 2.1 The Triplet State

Although the spin of the electron is invariably  $1/2$ , the total spin of paramagnetic species can reach plenty of integer values depending on the number of unpaired electrons and the coupling scheme. The magnitude of the spin–spin interaction determines whether the description of the system is better done in the coupled or the uncoupled representation. For a paramagnetic center with two unpaired electrons, if the exchange interaction is much bigger than the dipolar interaction, the coupled representation is much more appropriate and the system in a triplet state [1]. The electronic wavefunction can be described as the product of a spatial function  $\Phi$  acting only on the spatial coordinates and a spin function  $\Xi$  acting on the spin coordinates:

$$\Psi = \Phi * \Xi \quad (2.1)$$

According to the Pauli's principles the wavefunction must be antisymmetric with respect to the electronic exchange operation. Considering the first excited state obtained by promoting one electron from the HOMO to the LUMO, the system can be either in a singlet ( $2S + 1 = 1$ ) or in a triplet ( $2S + 1 = 3$ ) state. While the excited singlet state is described by an antisymmetric spin function and a symmetric spatial function:

$$\Psi_{1,S} = \frac{1}{\sqrt{2}} [\phi_A(1)\phi_B(2) + \phi_A(2)\phi_B(1)] [\alpha(1)\beta(2) - \alpha(2)\beta(1)] \quad (2.2)$$

the three triplet wavefunctions are the product of a symmetric spatial function and an antisymmetric spin function:

$$\begin{aligned} \Psi_{1,T_{-1}} &= [\phi_A(1)\phi_B(2) + \phi_A(2)\phi_B(1)] [\beta(1)\beta(2)] \\ \Psi_{1,T_0} &= \frac{1}{\sqrt{2}} [\phi_A(1)\phi_B(2) + \phi_A(2)\phi_B(1)] [\alpha(1)\beta(2) + \alpha(2)\beta(1)] \\ \Psi_{1,T_{+1}} &= [\phi_A(1)\phi_B(2) + \phi_A(2)\phi_B(1)] [\alpha(1)\alpha(2)] \end{aligned} \quad (2.3)$$

$\phi_{A/B}$  are the spatial wavefunctions acting on the spatial coordinates of the electrons 1 and 2, while  $\alpha/\beta$  are the spin wavefunctions acting on the spin coordinates. Whether the triplet or the singlet lies lower in energy is defined by the sign of the exchange interaction: if  $J_0 > 0$  the singlet state lower in energy compared to the triplet while the opposite is true for  $J_0 < 0$  [2].

For the interpretation of EPR properties of the triplet state it is useful to define the triplet functions in term of only the spin coordinates as:

$$\begin{aligned} |-1\rangle &= \beta(1)\beta(2) \\ |0\rangle &= \frac{1}{\sqrt{2}} (\alpha(1)\beta(2) + \alpha(2)\beta(1)) \\ |+1\rangle &= \alpha(1)\alpha(2) \end{aligned} \quad (2.4)$$

These are eigenfunctions of  $\hat{S}^2$  and  $\hat{S}_z$  operators and are indicated by the ket  $|M_S\rangle$ .

Unless the molecule has cubic or higher symmetry, the three triplet sublevels, even in the ab-

sence of an applied magnetic field, are split apart in energy due to the ZFS interaction. The ZFS interaction arises from two contributions: the spin-orbit coupling (SOC), which is the interaction between the spin angular momentum of the electron with its orbit angular momentum, and the dipole–dipole coupling. The general form of the ZFS Hamiltonian has already been introduced in Chapter 1, here a more detailed description of the ZFS tensor is given. In organic chromophores, such as those investigated in this thesis, the SOC is negligible and the main contribution to the ZFS Hamiltonian derives from the dipolar interaction:

$$\hat{H}_{\text{ZFS}} = \hat{\mathbf{S}} \cdot \mathbf{D} \cdot \hat{\mathbf{S}} \quad \text{with} \quad \mathbf{D} = \frac{\mu_0 \mu_B^2 g_c^2}{4\pi \hbar} \begin{bmatrix} \left\langle \frac{r^2 - 3x^2}{r^5} \right\rangle & \left\langle \frac{-3xy}{r^5} \right\rangle & \left\langle \frac{-3xz}{r^5} \right\rangle \\ \left\langle \frac{-3xy}{r^5} \right\rangle & \left\langle \frac{r^2 - 3y^2}{r^5} \right\rangle & \left\langle \frac{-3yz}{r^5} \right\rangle \\ \left\langle \frac{-3xz}{r^5} \right\rangle & \left\langle \frac{-3yz}{r^5} \right\rangle & \left\langle \frac{r^2 - 3z^2}{r^5} \right\rangle \end{bmatrix} \quad (2.5)$$

The element of the  $\mathbf{D}$  are averaged over the electronic wave function therefore the parameters of the ZFS tensor are representatives of the spin density distribution.

In term of the principal values  $D_{XX}, D_{YY}, D_{ZZ}$  of the dipolar tensor, the ZSF Hamiltonian is:

$$\hat{H}_{\text{ZFS}} = D_{XX} \hat{S}_x^2 + D_{YY} \hat{S}_y^2 + D_{ZZ} \hat{S}_z^2 \quad (2.6)$$

$\mathbf{D}$  is not necessarily traceless, but only the symmetric and traceless tensor is accessible by EPR experiments [3]. Subtracting a constant value  $\frac{2(D_{XX} + D_{ZZ} + D_{ZZ})}{3}$  to each diagonal term, three principal values  $X, Y$  and  $Z$  that sum to zero are obtained thus, the ZFS Hamiltonian, can be written as a function of just two independent parameters called  $D$  and  $E$ :

$$\hat{H}_{\text{ZFS}} = D \left( \hat{S}_z^2 - \frac{1}{3} S(S+1) \hat{1} \right) + E (\hat{S}_x^2 - \hat{S}_y^2) \quad (2.7)$$

where  $\hat{1}$  is the identity operator.

By convention the principal ZFS axes are chosen in order to have  $|D| \geq 3|E|$ . The relations between  $X, Y, Z$  and  $D, E$  therefore are:

$$\begin{aligned} X &= \frac{1}{3}(D - E) & Y &= \frac{1}{3}(D + E) & Z &= -\frac{2}{3}D \\ D &= -\frac{3}{2}Z & E &= \frac{1}{2}(X - Y) \end{aligned} \quad (2.8)$$

The sign of  $D$  depends on the shape of the spin density distribution: for a flat system such as a porphyrin the  $z$ -axis is perpendicular to the molecular plane and  $D$  is positive (oblate distribution); for an elongated molecule, such as a carotenoid, the  $z$ -axis lies along the molecular axis and  $D$  is negative (prolate distribution) [4]. The sign of  $E$  is related to the assignment of the  $X$  and  $Y$  axes of the ZFS tensor.

As an example, the ZFS-axes and the zero-field energy levels, for a carotenoid and a chlorophyll are depicted in Figure 2.1.

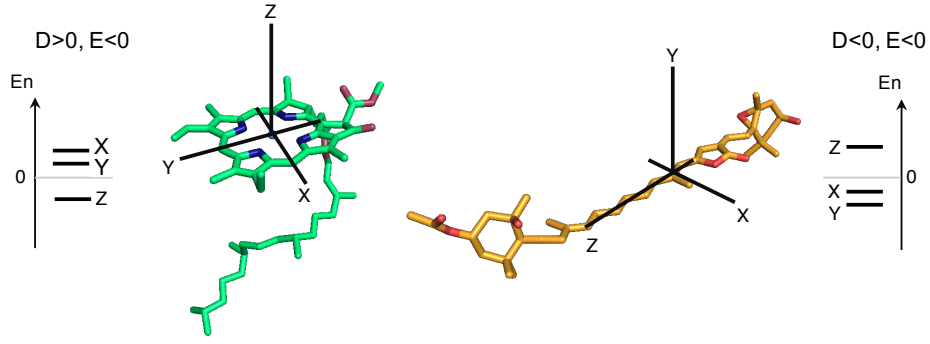


**Figure 2.1:** ZFS-axes orientation and triplet sublevels for a chlorophyll *a* (left) and a peridinin (right).

The eigenfunctions of the ZFS Hamiltonian can be expressed as a linear combinations of the triplet functions introduced in Equation 2.4:

$$\begin{aligned}
 |T_X\rangle &= \frac{1}{\sqrt{2}}(|-1\rangle - |+1\rangle) \\
 |T_Y\rangle &= \frac{1}{\sqrt{2}}(|-1\rangle + |+1\rangle) \\
 |T_Z\rangle &= |0\rangle
 \end{aligned} \tag{2.9}$$

In the presence of an external magnetic field, the spin Hamiltonian of a triplet state, neglecting any hyperfine contribution, is the sum of the Zeeman and the ZFS interaction:

$$\hat{H}_0 = \frac{\mu_B}{\hbar} \mathbf{B}_0 \cdot \mathbf{g} \cdot \hat{\mathbf{S}} + D \left( \hat{S}_z^2 - \frac{1}{3} S(S+1) \hat{1} \right) + E(\hat{S}_x^2 - \hat{S}_y^2) \tag{2.10}$$

Due to the presence of the Zeeman interaction,  $|T_X\rangle$ ,  $|T_Y\rangle$  and  $|T_Z\rangle$  are not eigenfunctions of the Hamiltonian 2.10. Its eigenfunctions and eigenvalues depend on the relative orientation of the  $\mathbf{g}$  and the ZFS principal frames and on the orientation of the whole system with respect to the static magnetic field  $\mathbf{B}_0$ . For this reasons they do not have a clean analytical form. Simple solutions however can be found, in the absence of a significant  $\mathbf{g}$ -anisotropy (as is usually the case for organic chromophores), for some particular directions of the external magnetic field with respect to the ZFS system. These correspond to orientations in which  $\mathbf{B}_0$  is parallel either to  $X$ , to  $Y$  or to  $Z$  axes of ZFS. As an example, we consider the case with  $\mathbf{B}_0$  parallel to the  $Z$ -axis. In this situation, the energy of  $|T_Z\rangle$  is independent on the field intensity and the function is the same also at high field. The  $|T_X\rangle$  and  $|T_Y\rangle$  levels instead are split apart in energy proportionally to the field intensity and the two zero-field eigenfunctions are mixed by the Zeeman interaction:

$$\begin{aligned}
 |T_{+1}\rangle &= \cos[\theta]|\alpha\alpha\rangle + \sin[\theta]|\beta\beta\rangle & E &= (1/3)D + (\mu_B g B_0 / \hbar) \sqrt{1 + \tan^2[2\theta]} \\
 |T_0\rangle &= |T_Z\rangle & E &= -(2/3)D \\
 |T_{-1}\rangle &= -\sin[\theta]|\alpha\alpha\rangle + \sin[\theta]|\beta\beta\rangle & E &= (1/3)D - (\mu_B g B_0 / \hbar) \sqrt{1 + \tan^2[2\theta]}
 \end{aligned} \tag{2.11}$$

where  $\theta = (1/2) \arctan[\hbar E / (\mu_B g B_0)]$ . As it is possible to notice in Equation 2.11, in the high field limit  $(\mu_B g B_0 / \hbar) \gg D, E$ , therefore the  $-1$ ,  $0$  and  $+1$  becomes good quantum numbers. In this

situation there are two possible EPR transitions that, according to the selection rule  $\Delta m_S = \pm 1$ , are:  $|T_{+1}\rangle \leftrightarrow |T_0\rangle$  and  $|T_{-1}\rangle \leftrightarrow |T_0\rangle$ . The intensity of such transitions depends on the difference of populations between the levels involved. At thermal equilibrium this is simply determined by the Boltzmann distribution. The same is true for any other orientation of the ZFS frame with respect to the external magnetic field: always two transitions are present:  $|T_{+1}\rangle \leftrightarrow |T_0\rangle$  and  $|T_{-1}\rangle \leftrightarrow |T_0\rangle$ . The schemes of the energy levels for the static magnetic field parallel to the ZFS canonical axes and the EPR spectrum of a triplet at thermal equilibrium are depicted in Figure 2.2

The magnitude of the ZFS interaction ranges from MHz to THz but, at least for the system studied in this thesis, it is usually smaller than Zeeman interaction.

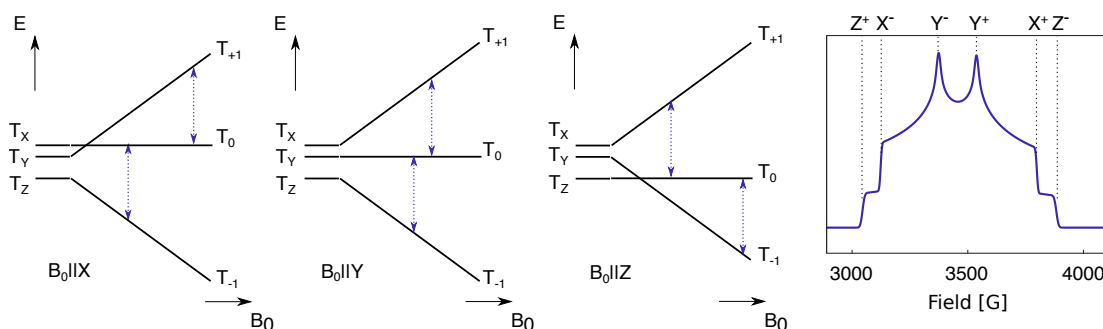


**Figure 2.2:** Schemes of the triplet energy levels for  $B_0$  parallel to the three ZFS canonical orientations and powder EPR spectrum of a triplet at thermal equilibrium. The “+” and “-” signs refer to the triplet transitions that take place between the levels  $|T_0\rangle - |T_{+1}\rangle$  and  $|T_0\rangle - |T_{-1}\rangle$ , respectively. The spectrum has been calculated with EasySpin [5] and the ZFS parameters used for the simulation are:  $[D E] = [1175 -239]$  MHz.

## 2.2 Spin Polarization

The equilibrium populations of the spin sublevels of a paramagnetic species in the presence of a static magnetic field is determined by the Boltzmann distribution. However, there are paramagnetic centers that, due to the mechanism of formation or to some specific reactions, have a population that deviates from the Boltzmann distribution. This phenomenon is called *spin polarization*. In this section some of the mechanisms that generate spin polarized states are presented.

### 2.2.1 Inter-system crossing

The photoexcitation of a chromophore induces a series of photophysical processes that are conveniently summarized in the Jablonski diagram (Figure 2.3). For a chromophore in the singlet ground state, photoexcitation at the proper wavelength, can populate one of the singlet excited states. There are many possible relaxation paths, whose probabilities depend on the relative kinetic constants of the different processes. Most of the times, if a  $S_n$  with  $n > 1$  is excited, the system relaxes to the  $S_1$  via consecutive vibrational relaxation and internal conversion steps. In some systems the lowest excited triplet state may be populated via inter-system crossing (ISC).

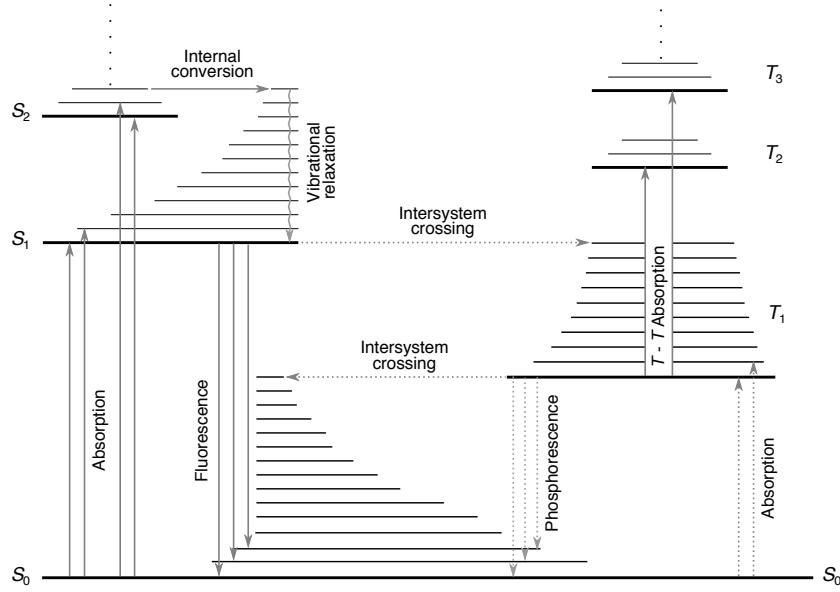


**Figure 2.3:** Schematic representation of the Jablonski diagram.

This is a spin-prohibited process that becomes partially allowed due to the SOC that causes a mixing of the singlet and the triplet wavefunctions [2]. Triplet states that are populated in this way are in a polarized state because SOC is different for the three sublevels:

$$\langle \Psi_{1,S} | \hat{H}_{so} | \Psi_{1,T_X} \rangle \neq \langle \Psi_{1,S} | \hat{H}_{so} | \Psi_{1,T_Y} \rangle \neq \langle \Psi_{1,S} | \hat{H}_{so} | \Psi_{1,T_Z} \rangle \quad (2.12)$$

In Equation 2.12  $\Psi_{1,T_X}$ ,  $\Psi_{1,T_Y}$  and  $\Psi_{1,T_Z}$  are the triplet wave functions and  $\hat{H}_{so}$  is the spin-orbit Hamiltonian. The triplet sublevels' populations are proportional to the square of the matrix elements:

$$u_j \propto |\langle \Psi_{1,S} | \hat{H}_{so} | \Psi_{1,T_j} \rangle|^2 \quad (2.13)$$

with  $j = X, Y, Z$  principal directions of the ZFS tensor.

Analogously, the rate of the depopulation of the triplet sublevels  $w_j$  is proportional to the square of the matrix elements  $|\langle \Psi_{1,T_j} | \hat{H}_{so} | \Psi_{0,S} \rangle|^2$ , where  $\Psi_{0,S}$  is the ground state wavefunction.

Without taking into account any relaxation process, the population of the triplet state in the presence of an applied magnetic field, can be obtained as linear combination of the zero-field populations ( $p_x, p_y, p_z$ ):

$$p_l = \sum_j |c_{lj}|^2 p_j \quad (2.14)$$

$c_{lj}$  indicates the extent of the  $j$ -th zero-field eigenfunction in the  $l$ -th eigenfunction of the Hamiltonian containing also the Zeeman interaction (see Equation 2.10).

In the high field limit ( $\mu_B g B_0 / \hbar$ )  $\gg D, E$ , for  $\mathbf{B}_0$  parallel to a generic ZFS-axis, the populations are:

$$p_0 = p_j \quad p_{\pm 1} = \frac{1}{2}(p_j + p_{j'}) \quad (2.15)$$

The intensities of the EPR transitions are proportional to the difference of population between the levels involved, scaled by the probability of the transition:

$$I_W = \left[ p_j - \frac{1}{2}(p_j + p_{j'}) \right] |(\hat{S}_x)_{jW}|^2 \quad (2.16)$$

For each direction of the magnetic field there are two transitions, one in enhanced absorption and one in emission and the powder EPR spectrum of a photoexcited triplet state has indeed absorptive and emissive transitions (Figure 2.4).

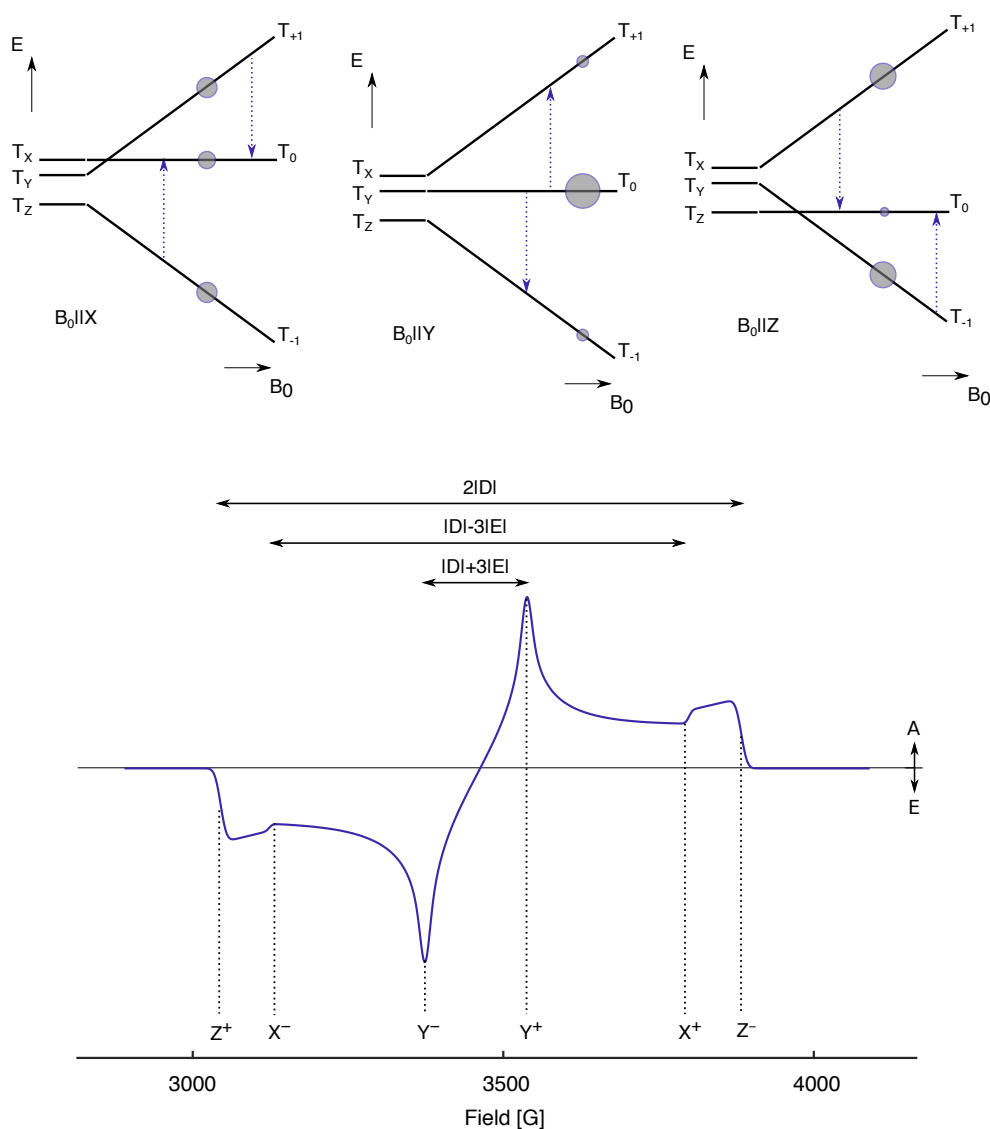


**Figure 2.4:** Schemes of the triplet energy levels for  $B_0$  parallel to the three ZFS canonical orientations and powder EPR spectrum of a polarized triplet state. The “+” and “-” signs refer to the triplet transitions that take place between the levels  $|T_0\rangle - |T_{+1}\rangle$  and  $|T_0\rangle - |T_{-1}\rangle$ , respectively. The spectrum has been calculated with EasySpin [5] and the ZFS parameters used for the simulation are:  $[D \ E] = [1175 \ -239]$  MHz,  $[p_x \ p_y \ p_z] = [0.31 \ 0.58 \ 0.11]$ .

Although the SOC is the principal interaction that causes ISC from the excited singlet state  $S_1$  to the triplet state  $T_1$ , another mechanism has been reported for those triplets that form in prox-



imity to a paramagnetic center such as a radical. In such systems, the exchange interaction between the excited singlet state of the chromophore and the unpaired electron of the radical can promote ISC. This mechanism, called J-ISC, is more likely to take place if the triplet precursor and the radical are close enough to interact when excited singlet state is formed [6, 7].

### 2.2.2 Triplet-Triplet Energy Transfer

Beyond ISC, several other population paths are possible for triplet states. Among these, the *Triplet-Triplet Energy Transfer* (TTET) is of particular interest, especially when dealing with photosynthetic systems where this process is at the basis of the photoprotective mechanism from singlet oxygen formation, in numerous light harvesting complexes. TTET implies the simultaneous exchange of two electrons between a donor (D) and an acceptor (A) and takes place with conservation of the total spin angular momentum. This process is based on the Dexter mechanism depicted in Figure 2.5.

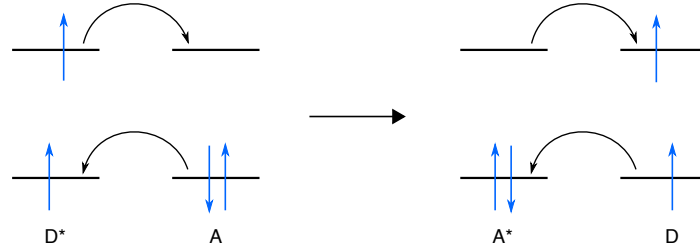


**Figure 2.5:** Dexter exchange mechanism describing the triplet-triplet energy transfer.

The probability of energy transfer between a triplet state sublevel of the donor and a triplet state sublevel of the acceptor can be expressed as a two-centers two-electron exchange integral [8]:

$$\begin{aligned}
 P_t^j &\propto \left| \sum_{1,2} \left\langle \sum_k \phi^A S_0^A \phi^{D*} T_j^{D*} \left| \frac{1}{r_{12}} \right| \phi^D S_0^D \phi^{A*} T_k^{A*} \right\rangle \right|^2 \\
 &= |\langle S_0^A | S_0^D \rangle|^2 \left| \left\langle \sum_k T_j^{D*} \left| T_k^{A*} \right\rangle \right|^2 \times \left| \sum_{1,2} \left\langle \phi^A \phi^{D*} \left| \frac{1}{r_{12}} \right| \phi^D \phi^{A*} \right\rangle \right|^2 \\
 &= C \left| \sum_k \left\langle T_j^{D*} T_k^{A*} \cos(\theta_{jk}) \right\rangle \right|^2
 \end{aligned} \tag{2.17}$$

where  $C$  is constant for donor-acceptor configuration,  $\phi$  and  $\phi^*$  are the spatial wavefunctions of the singlet ground state and the triplet excited state respectively,  $S_0$  are the singlet ground state spin functions,  $T$  are the excited triplet state spin functions at zero field.

Equation 2.17 shows that the spin angular momentum, along the generic  $j$  direction of the donor triplet state, is conserved in the TTET process. This conservation results from the fact that: (1) the spin and orbit motions are assumed independent from one another both in the donor and the acceptor; and (2) the transfer results from an electrostatic exchange mechanism and not from a magnetic-type interaction. In systems where either of these assumptions becomes invalid, e.g. molecules with heavy nuclei, is possible that the conservation of the spin direction in the TTET

process would fail.

The direct consequence of Equations 2.17 is that the populations of the acceptor ( $p_k^A$ ) are inherited from the donor ( $p_j^D$ ) and depend on the relative orientation of the ZFS frames of the two moieties:

$$p_k^A = \sum_j \cos[\theta_{jk}]^2 p_j^D \quad (2.18)$$

where  $\theta_{jk}$  is the angle between the  $j$ -ZFS axis of the donor and the  $k$ -ZFS axis of the acceptor.

In the presence of an applied magnetic field, the populations of the triplet sublevels can be expressed in term of the zero-field populations and Equation 2.18 can be rewritten as:

$$p_i^A = \sum_j \sum_l |c_{lj}|^2 \cos[\theta_{il}]^2 p_j^D \quad (2.19)$$

where  $i$  indicates the  $T_{-1}$ ,  $T_0$ ,  $T_{+1}$  eigenfunctions of the the acceptor, and  $j$  those of the donor.

The dependence of the acceptor's sublevels population on the direction cosines holds the structural information on the donor-acceptor ZFS axes orientation and can be exploited for structural studies in systems where these processes take place such as in antenna complexes.

### 2.2.3 Chemically Induced Dynamic Electron Polarization

Chemically Induced Dynamic Electron Polarization (CIDEP) has been widely studied by TREPR, leading to the evolution of the CIDEP generation mechanisms. CIDEP identifies a series of phenomena that lead to the observation of anomalous intensities of EPR transitions due to photochemical processes. Analyses of CIDEP provide valuable information about the structures, kinetics, and spin relaxations of reaction precursory excited states, intermediate radical pairs, and radicals [9].

The earliest observations of these phenomena involved polarizations of pair of radicals and they was mainly interpreted by two mechanisms: the triplet mechanism (TM) [10] and the radical pair mechanism (RPM) [11]. TM was introduced to explain the electron spin polarization produced in radicals generated from a triplet precursor. Photoexcited triplets are usually generated in a spin polarized state because of the selectivity of the ISC from the excited singlet state to the three triplet sublevels, therefore, if the chemical reaction that creates the two radicals is faster than the triplet relaxation, the spin polarization is transferred to the radical pair.

RPM instead accounts for the polarization observed in pairs of radicals originated by homolytic scission, by reaction of an excited molecule (such as the extraction of H $\cdot$ ) or by random encounter of the two partners. At short inter-radical distances, when there is a strong exchange interaction, the radicals are either in a singlet or in a triplet state depending on the sign of the exchange constant. At longer distances the singlet functions are mixed with the  $|T_0\rangle$  and, to a minor extent, with the  $|T_{-1}\rangle$  triplet functions. Such mixing generates the polarization of the spin sublevels.

Many cases of CIDEP concerning systems with more than two unpaired electrons have been reported in literature [12, 13, 14]. Most of them involves the formation of a triplet state close to a radical. The spin polarized EPR signals observed in such systems are generally explained in the

context of two theories: Radical-Triplet Pair Mechanism (RTPM)[15] and Electron-Spin Polarization Transfer (ESPT)[16, 17].

RTPM has been introduced to explain the polarization observed in radicals when they are close to photoexcited triplet molecules either because they are diffusing in solution between each other or because they are bound together. Strongly interacting triplet and radical states can generate, according to the Clebsch-Gordan series, a quartet state with eigenfunctions  $|Q_{+3/2}\rangle$ ,  $|Q_{+1/2}\rangle$ ,  $|Q_{-1/2}\rangle$ ,  $|Q_{-3/2}\rangle$ , or a doublet state with eigenfunctions  $|D_{-1/2}\rangle$ ,  $|D_{+1/2}\rangle$ . Provided that the g-anisotropy is negligible, these states are eigenfunctions of the Zeeman and the exchange Hamiltonian and are separated in energy by the exchange interaction. The sign of the exchange constant determines whether the quartet or the doublet lies lower in energy (e.g. if the coupling constant  $J_0$  is negative, the doublet state is lower in energy).

If the states were pure quartet and doublet, the decay from  $|Q_{\pm 3/2, \pm 1/2}\rangle$  to the ground state would be spin-forbidden and could not take place. On the other hand the decay from  $|D_{\pm 1/2}\rangle$  would not induce any polarization of the ground state radical. However,  $|Q_{\pm 3/2, \pm 1/2}\rangle$  and  $|D_{\pm 1/2}\rangle$  are not eigenfunctions of the ZFS Hamiltonian and the dipolar interaction causes a mixing of these states. The new eigenfunctions, resulting from the mixing, will be indicated as:  $|Q_{\pm 3/2}\rangle'$ ,  $|Q_{\pm 1/2}\rangle'$ ,  $|D_{\pm 1/2}\rangle'$ . The decay rate from the  $|D_{\pm 1/2}\rangle'$  states is the same for the two spin sublevels and generates polarization only if  $|D_{-1/2}\rangle'$  and  $|D_{+1/2}\rangle'$  are differently populated. The decay from the  $|Q_{\pm 1/2}\rangle'$  does not produce polarization of the ground state because they decay at the same rate and are equally populated. The  $|Q_{\pm 3/2}\rangle'$  instead, decay with different rates and, depending on the sign of the  $J_0$ , they can produce positive or negative polarization on the ground state radical (Figure 2.6).

Although ZFS is the largest interaction that causes the mixing of the quartet and the doublet functions, there are other terms, such as the hyperfine coupling, that could in principle contribute to this process. This is less common because the hyperfine coupling is usually two orders of magnitude smaller than the ZFS, however it can lead to the observation of radical signals with hyperfine-dependent intensities (*multiplet effect*) [18].

Another mechanism, reported to explain the polarization of radicals mediated by exchange interaction with photoexcited triplet states, is ESPT. In the ESPT mechanism, the polarization is transferred from the triplet to the radical by spin exchange, resulting in quenching of the triplet state to the ground singlet state. The polarization generated on the stable radical is the same as that of the excited triplet state, in particular this is absorptive if the  $T_{-1}$  level in the triplet manifolds has more populations than the  $T_{+1}$  end emissive when  $T_{+1}$  is more populated than  $T_{-1}$ . ESPT has not been completely contextualized in a comprehensive theory, nonetheless there are many examples of studies that successfully interpret experimental results on the basis of the kinetic equations of such a mechanism [16, 9].

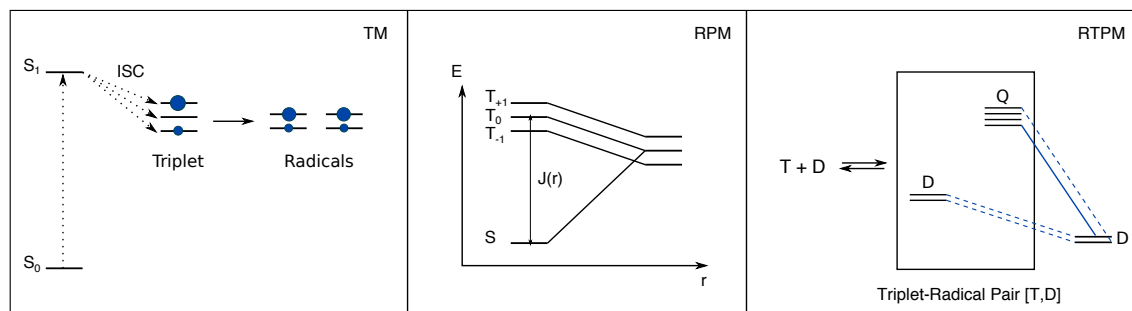


**Figure 2.6:** Schematic representation of the main CIDEP mechanism: TM (left), RPM (center), RTPM (right).

## Bibliography

- [1] John A. Weil and James R. Bolton. *Electron Paramagnetic Resonance: Elementary Theory and Practical Applications*. Wiley, 2nd edition, 2007.
- [2] S. P. McGlynn, T. Azumi, and M. Kinoshita. *Molecular Spectroscopy of the Triplet State*. Prentice-Hall, 1969.
- [3] Joshua Telser. *EPR Interactions – Zero-Field Splittings*, pages 207–234. American Cancer Society, 2017.
- [4] Sabine Richert, Claudia E. Tait, and Christiane R. Timmel. Delocalisation of photoexcited triplet states probed by transient EPR and hyperfine spectroscopy. *J. Magn. Reson.*, 280:103–116, 2017.
- [5] Stefan Stoll and Arthur Schweiger. EasySpin, a comprehensive software package for spectral simulation and analysis in EPR. *J. Magn. Reson.*, 178(1):42–55, 2006.
- [6] A.R. Watkins. Quenching of electronically excited states by the free radical tetramethylpiperidine nitroxide. *Chem. Phys. Lett.*, 29(4):526–528, dec 1974.
- [7] James A Green, Lawrence A Singer, and Joel H Parks. Fluorescence quenching by the stable free radical di-t-butyl nitroxide. *J. Chem. Phys.*, 58(7):2690–2695, 1973.
- [8] M. A. El-Sayed, D. S. Tinti, and E. M. Yee. Conservation of spin direction and production of spin alignment in triplet-triplet energy transfer. *J. Chem. Phys.*, 51(12):5721–5723, 1969.
- [9] Jun-Ichi Fujisawa, Yasunori Ohba, and Seigo Yamauchi. Electron-spin polarizations generated from interactions between excited triplet porphyrins and stable radicals studied by time-resolved electron paramagnetic resonance. *J. Phys. Chem. A*, 101(4):434–439, 1997.
- [10] S. K. Wong, D. A. Hutchinson, and J. K. S. Wan. Chemically induced dynamic electron polarization. II. A general theory for radicals produced by photochemical reactions of excited triplet carbonyl compounds. *J. Chem. Phys.*, 58(3):985–989, 1973.
- [11] Frank J. Adrian. Theory of anomalous electron spin resonance spectra of free radicals in solution. Role of diffusion-controlled separation and reencounter of radical pairs. *J. Chem. Phys.*, 54(9):3918–3923, 1971.
- [12] Yasuhiro Kobori, Akio Kawai, and Kinichi Obi. Direct Observation of CIDEP Generated through Enhanced Intersystem Crossing. *J. Phys. Chem.*, 98:6425–6429, 1994.
- [13] Akio Kawai and Kinichi Obi. First Observation of a Radical-Triplet Pair Mechanism (RTPM) with Doublet Precursor. *J. Phys. Chem.*, 96(1):52–56, 1992.
- [14] Carlo Corvaja, Elena Sartori, Antonio Toffoletti, Fernando Formaggio, Marco Crisma, Claudio Toniolo, Jean Paul Mazaleyrat, and Michel Wakselman. CIDEP effects of intramolecular quenching of singlet and triplet excited states by nitroxide radicals in oligopeptides: A

- potentially useful new method for investigating peptide secondary structures in solution. *Chem. - A Eur. J.*, 6(15):2775–2782, 2000.
- [15] C. Blättler, F. Jent, and H. Paul. A novel radical-triplet pair mechanism for chemically induced electron polarization (CIDEP) of free radicals in solution. *Chem. Phys. Lett.*, 166(4):375–380, 1990.
- [16] Jun-ichi Fujisawa, Kazuyuki Ishii, Yasunori Ohba, Masamoto Iwaizumi, and Seigo Yamauchi. Electron Spin Polarization Transfer from Excited Triplet Porphyrins to a Nitroxide Radical via a Spin Exchange Mechanism. *J. Phys. Chem.*, 99(47):17082–17084, 1995.
- [17] Takashi Imamura, Osamu Onitsuka, and Kinichi Obi. Memory of spin polarization in triplet-doublet systems. *J. Phys. Chem.*, 90(26):6741–6744, 1986.
- [18] Akio Kawai, Tetsuo Okutsu, and Kinichi Obi. Spin Polarization Generated in the Triplet-Doublet Interaction: Hyperfine-Dependent Chemically Induced Dynamic Electron Polarization. *J. Phys. Chem.*, 95:9130–9134, 1991.

**CHAPTER** | **3**

**Experimental Setup and EPR Techniques**





## 3.1 Experimental setup

EPR is an extremely heterogeneous spectroscopy which allows to perform a great number of diverse experiments. The different EPR techniques can be divided into three main categories: continuous wave (CW) EPR, pulse EPR and Time-Resolved EPR (TREPR). In the first part of this chapter, a general description of the basic EPR instrumentation is given while, in the second part, the theoretical background of some pulse techniques is introduced.

### 3.1.1 CW-EPR

Due to the Zeeman interaction, the spin sublevels of a paramagnetic sample, in the presence of a static magnetic field, are split apart in energy. The resonance phenomenon at the basis of EPR, takes place when a quantum  $h\nu$  matches the energy separation between the spin sublevels. The standard EPR instruments are X-band spectrometers that work at about 9.5 GHz and in which the resonance condition for a species with  $g = 2$  is fulfilled at  $\sim 340$  mT. More powerful but commercially available instruments are: Q-band ( $\sim 33$  GHz) and W-band ( $\sim 95$  GHz) spectrometers. The firsts are now widespread because represent a good compromise between sensitivity and costs, while the second ones are less common due to the maintenance work related to the superconducting magnet [1].

In a classical CW experiment, the magnetic field that causes the split of the spin sublevels is varied while a constant microwave radiation is applied on the sample. The typical outlay of an EPR spectrometer is shown in Figure 3.1.

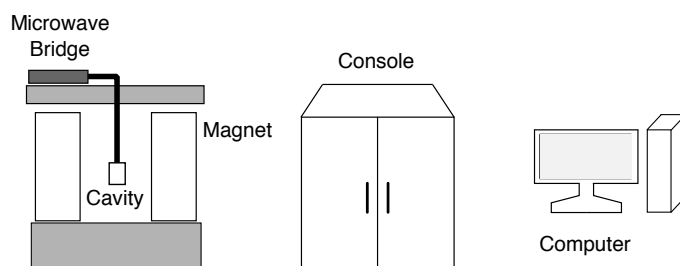


**Figure 3.1:** Schematic representation of an EPR spectrometer.

The heart of the instrument is the microwave bridge that houses both the microwave source and the detector. The microwave source of modern spectrometers is a Gunn diode electronic oscillator, that supplies a relatively low power constant radiation. The power of the microwave is tuned, immediately after the source, by an attenuator. EPR spectrometers normally work in reflection mode rather than in transmission, measuring the change in the amount of radiation reflected back from the microwave cavity containing the sample. The microwaves travel from the source along a hollow metal waveguide and reach the sample located into the resonator. The same path is then followed by the radiation reflected back from the resonator to the detector. The path of the microwaves is regulated by a circulator, a device that directs the microwaves from one port into the next one in a one-way rotation. The detector is a Schottky barrier diode which converts the microwaves reflected back from the cavity into an electrical current. To ensure the detec-

tor enough power to work in the linear region, where the diode current is proportional to the square root of the microwave power, the radiation reflected from the cavity is mixed with the microwaves coming from the reference arm which is supplied directly by the Gunn diode.

The magnetic field is supplied by an electromagnet which can sweep from 0 to ca. 1.7 T. The stability of the magnetic field is regulated by the field controller, which adjusts the amount of current flowing from the magnet power supply, combining the information of the Hall probe and the reference voltage.

The EPR cavity which is the metal box where the sample is stored. Cavities are specifically designed to accommodate electromagnetic radiation from the waveguide and store a considerable amount of energy as a standing wave at the fundamental resonance frequency. Their shape is also optimized to maximize the magnetic field in the position of the sample and consequently minimize the electric field which causes dissipative phenomena. The efficiency of the cavity in storing the microwave energy is quantified by its quality factor  $Q$  defined as:

$$Q = \frac{\nu_{\text{res}}}{\Delta\nu} \quad (3.1)$$

where  $\nu_{\text{res}}$  is the resonance frequency of the cavity and  $\Delta\nu$  is the width at half height of the resonance. The matching between the impedance of the cavity and the waveguides is regulated through a hole called *iris* whose opening determines how much microwaves enters the cavity. When the impedances are perfectly matched the resonator is said to be "critically coupled".

In order to obtain an enhancement of the signal-to-noise *phase-sensitive detection* is used. Briefly, the magnetic field intensity is modulated at a frequency (usually 100 kHz) therefore the amplitude of the EPR signal also is modulated at the same frequency. The modulated signal is compared with a reference that have the same frequency and any signal which is not modulated at the same frequency is cut out. Being the amplitude of the modulated signal proportional to the slope of the absorption spectrum, the EPR spectrum in phase-sensitive detection is shown in derivative [2].

### 3.1.2 TREPR

TREPR is the main technique for studying the time-evolution of paramagnetic species generated or modified by a perturbation. In a TREPR experiment, the time evolution of the EPR signal perturbed by a specific trigger, is studied at a fixed magnetic field and under constant microwave irradiation (Figure 3.2). A sweep of the magnetic field allows the reconstruction of the 2D time-dependent EPR spectrum. The perturbation is typically a laser pulse that generate or modifies the paramagnetic species and induces a series of dynamic processes that are recorded in the spectrum.

Since lock-in detection eliminates all the frequencies that do not match the frequency of the field modulation, it cannot be used in TREPR and the spectra, for this reason, are in absorption and not in derivative. Two different detection modes are typically possible on a standard Bruker spectrometer: direct detection or transient mode detection. In direct detection the signal is col-

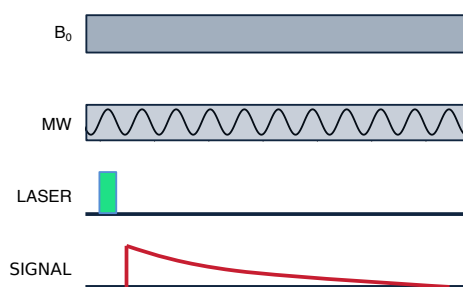


**Figure 3.2:** Schematic representation of a TREPR experiment.

lected from the preamplifier immediately after the microwave diode detector. In transient mode instead, quadrature phase detection is used: the signal from the resonator is downconverted, amplified by the video amplifier (bandwidth of 200 MHz) and digitized [3, 4]. In this mode, the microwave frequency must be locked using the DC-AFC instead of the AC-AFC. Direct detection is generally more sensitive than quadrature phase detection, but its time resolution may be limited by the bandwidth of the preamplifier.

Time-resolution is a crucial parameter in TREPR and it is determined by the bandwidths of the various components of the instrument. One of the main factors that influences the responses of the instrument, is the resonator bandwidth. This is determined by the ratio between the resonance frequency of the resonator ( $\nu_{\text{res}}$ ) and its quality factor  $Q$ . In TREPR therefore, cavities with low  $Q$  values should be used in order to avoid an excessive loss in time resolution. The TREPR spectra shown in this thesis have been collected on an X-band dielectric cavity with a nominal  $Q$ -value of 4000. At a frequency of  $\sim 10$  GHz the cavity bandwidth is 2.5 MHz and, as a consequence, the maximum time resolution achievable is about  $Q/(\nu_{\text{res}}) \simeq 400$  ns. The bandwidth of the preamplifier instead is 6.5 MHz, meaning that the limiting factor in our setup is the cavity bandwidth.

Light photoexcitation is usually performed with a pulsed laser that is synchronized with detection system. For the measurements presented in this thesis a Nd:YAG pulsed lasers (Quantel Brilliant) with  $\lambda = 532$  nm equipped with second and third harmonic modules and an optical parametric oscillators (OPOTECH) for tunable irradiation in the visible, has been used. The laser works at a maximum repetition rate of 10 Hz and typical pulse lengths are 5 ns.

TREPR data are processed by subtracting the background contribution that is usually superimposed on the desired signal owing to dielectric heating of the microwave resonator or the sample from optical excitation. For this purpose, a time profile recorded at an off-resonance magnetic field position is collected and subtracted from all transients of the two-dimensional data set. The field-domain TREPR spectrum is obtained by extracting the signal amplitude at a certain time after the laser pulse or by integrating it over a time window.

### 3.1.3 Pulse EPR

Even if the general outlay of a pulse EPR spectrometer is, for some aspects, similar to that shown in Figure 3.1 and modern spectrometers can work both in continuous wave and in pulse mode, many differences exist between the two setups. Typically, in a pulse EPR experiment, a discontinuous microwave irradiation is employed in the form of short and intense pulses (length of the order usually of nanoseconds and power of about kilowatts). Similarly to CW EPR, pulse EPR employs resonators to amplify the microwave fields at the sample, but the resonators have different bandwidths: for CW EPR narrow-band resonators are used, whereas for pulse EPR resonators with wider bandwidths are required [5].

The schematic representation of a pulse EPR instrument is shown in Figure 3.3. Low power microwaves (in the order of mW) are generated by a continuous source, such as a Gunn diode. The pulses are then generated in the microwave pulse-former unit which consist of several channels each equipped with individual attenuators and phase shifters to adjust the relative amplitudes, phases and lengths of the pulses. In addition to the main source, many spectrometers have a second independent microwave source for double resonance experiments usually called ELDOR source. The pulses are then amplified in the traveling wave tube (TWT) amplifier. Powers of about 1kW are used in X-band spectrometers while 100-150 W are used at Q-band. After the TWT amplifier, the microwaves encounter the high power pulse attenuator that allows to regulate the  $B_1$  applied to the sample.

In a pulse EPR experiment, the emission from the sample, which is of the order of nanowatts or microwatts, is measured. This very low signal before reaching the detector passes through a preamplifier which is protected from possible reflected power of the pulses by a defense diode. The amplified signal then goes to the quadrature detector where is mixed with the reference microwaves from the source and split in two arms with a 90° shift with respect to each other and provide the real and the imaginary component of the signal [6].

Most of the systems investigated in this thesis are species that in their ground state are EPR-silent and the paramagnetic species is generated by the laser excitation. Therefore, the measurement of their pulse EPR signal requires coupling the standard instrument with a pulsed laser. In our setup the pulse generator (PatternJet) of the spectrometer is synchronized with the laser via an out trigger coming from the laser. The delay between the laser pulse and the microwave pulse sequence is generally referred to as delay after flash (DAF) and is typically adjusted to maximize the EPR signal. The shot repetition time of pulse EPR experiments with laser excitation is typically determined by the repetition rate of the laser.

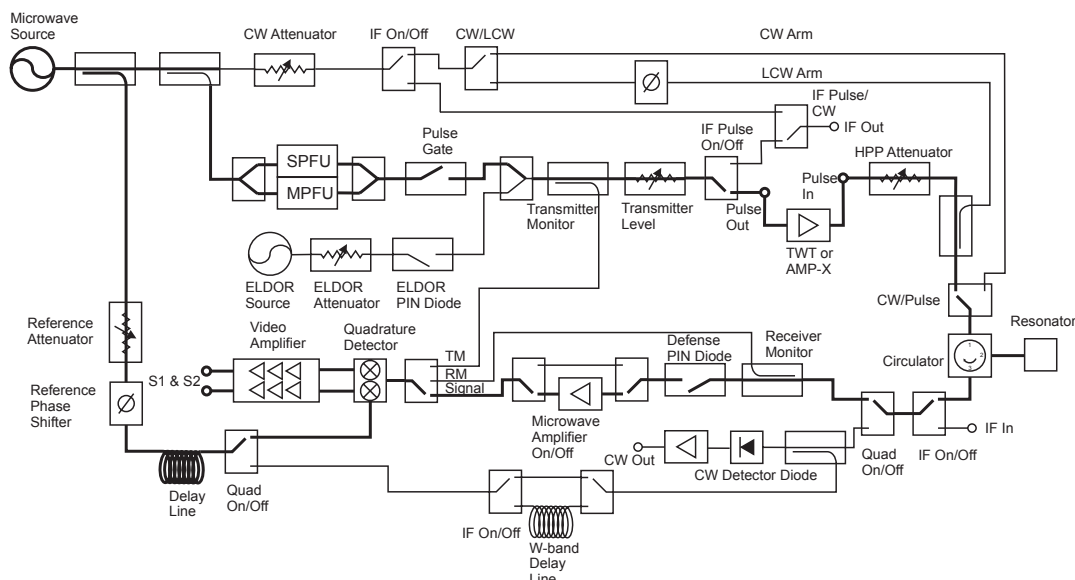


**Figure 3.3:** Block representation of the microwave bridge with indicated the signal path in a pulse EPR experiment (this image has been taken from *Elexsys E580 - Pulse EPR Spectrometer User's Manual*).

### 3.2 Pulse EPR techniques

Many pulse EPR experiments can be designed to separate or correlate interactions in the spin Hamiltonian. Most of them are based on the detection of a spin echo rather than an FID (free-induction decay) because the latter is usually inaccessible due to fast relaxations and long instrumental dead-times. The two fundamental pulse schemes for obtaining an electron spin echo are the 2-pulse sequence, that generate a *primary echo*, also called Hahn echo, and the 3-pulse sequence that give rise to a *stimulated echo* (Figure 3.4).

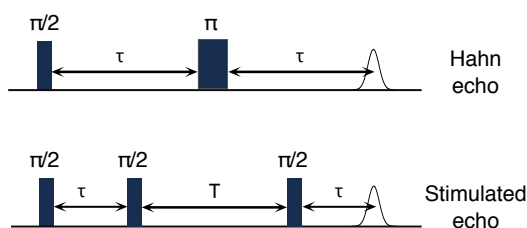


**Figure 3.4:** Schematic representation of a TREPR experiment.

In the primary echo sequence, the  $\pi/2_{(x)}$ -pulse rotates the magnetization along  $-y$ -axis and the various spin packets start to precess at different frequencies. The defocusing of the magnetization lasts for all the duration  $\tau$  of the free-precession period. The  $\pi_{(x)}$ -pulse, rotate the magnetization vectors of all the spin packets by  $180^\circ$ , leaving their precession frequencies unchanged. After a period  $\tau$  from the second pulse the spin packets refocus along the  $+y$ -axis forming in this way an electron spin echo. This sequence allows to recover the loss of magnetization related to local field inhomogeneity, but does not permit to recover the irreversible loss of magnetization caused by transverse relaxation processes.

### 3.2.1 Pulse dipolar spectroscopy

Pulsed dipolar EPR spectroscopy is a well-established technique to determine precise distance distributions between paramagnetic centers. In combination to site-directed spin labeling, it is ideally suited for structural characterizations of macromolecules and complexes and has emerged as valuable tool in structural biology [7]. The structural information is enclosed in the dipolar interaction between two or more paramagnetic centers. For the sake of simplicity, in this section, the description is limited to the case of doubly labeled objects.

The expression describing the dipolar interaction between two paramagnetic centers has been introduced in Chapter 1 (Equation 1.25). In the high field approximation, when the two spin magnetic moments are quantized along the static magnetic field direction, assuming that the difference between the resonance frequencies of the two electrons is much bigger than the dipolar frequency, the coupling is  $2\pi\nu_{\text{dd}}(3\cos^2\theta - 1)$  where  $\nu_{\text{dd}} = \omega_{\text{dd}}/2\pi$ .

Typically in a pulse dipolar experiment the signal of one spin called the *detection spin* is observed while a change of the *pump spin* modifies the dipolar coupling between the two species. This change can be either the inversion by a  $\pi$ -pulse such as in DEER (Double Electron-Electron Resonance) [8], longitudinal relaxation such as in RIDME (Relaxation-Induced Dipolar Modulation Enhancement)[9] or even the instantaneous generation of the pump spin such as in LaserIMD (Laser-Induced Modulation Dipolar Spectroscopy)[10]. Whatever the nature of the change is, the key event is that a variation of the precession frequency of the detection spin is generated and this causes a modification of its echo intensity. A dipolar time trace can therefore be obtained by varying the time of the pump spin alteration with respect to the initial time of the sequence.

Pulse dipolar experiments are usually performed on powder samples, in which the molecules are randomly oriented and the dipolar frequencies contributing to the time trace are determined by the statistical distribution of the inter-spin vectors with respect to the external magnetic field. If  $\theta$  is the angle between the inter-spin vector and the field direction, the probability associated to the corresponding dipolar frequency, in the absence of orientation selection effects, is proportional to  $\sin\theta$ . Hence, the plot of the probability associated to each dipolar frequency contributing to the trace yield a pake pattern (Figure 3.5). The pake pattern has turning points at the frequencies  $\nu_{\parallel} = 2\nu_{\text{dd}}$  corresponding to  $\theta = 0^\circ$  and  $\nu_{\perp} = \nu_{\text{dd}}$  corresponding to  $\theta = 90^\circ$  and its shape is determined by the statistical distribution of the molecules with respect to the external magnetic field. The mean distance between the two interacting spins can be calculated from  $\nu_{\perp}$  as:

$$r = \sqrt[3]{\frac{g_e^2 \mu_B^2 \mu_0}{4\pi h \nu_{\perp}}} \quad (3.2)$$

When the point dipole approximation cannot be assumed for the two paramagnetic centers, because the unpaired electrons are delocalized over many atoms, the expression for the dipolar Hamiltonian has to be corrected to take into account the spin population  $\rho$  over each atom:

$$\hat{H}_{\text{dip}} = \frac{\mu_0 \mu_e^2 g_e^2}{4\pi \hbar} \left\{ \sum_j \sum_k \rho_{1j} \rho_{2k} \frac{(3\cos^2\theta_{1j,2k} - 1)}{r_{1j,2k}^3} \right\} \hat{S}_{1z} \hat{S}_{2z} \quad (3.3)$$

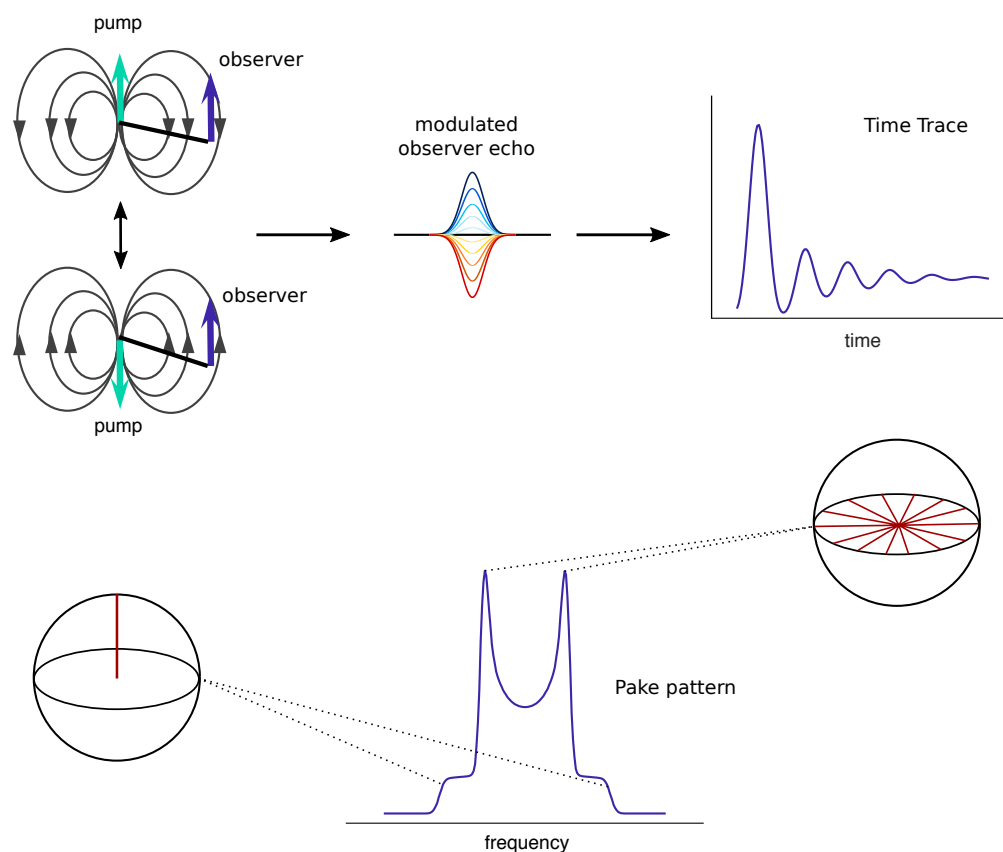


**Figure 3.5:** Schematic representation of a dipolar experiment: the modification of the dipolar field, induced by the pump spin, at the observer position makes the observer echo to be modulated at the coupling frequency and an oscillating time trace can be obtained integrating the echo. In a powder sample the frequencies corresponding to all the possible orientations of the molecular system with respect to the static magnetic field direction contribute to the time trace and hence the Fourier transform of the time trace yields a Pake pattern with singularities at  $\nu_{\parallel}$  and  $\nu_{\perp}$ .

## DEER

The most commonly employed dipolar spectroscopy is DEER. In this double resonance technique the echo of the detection spin is monitored while the pump spin is selectively inverted by a  $\pi$ -pulse [8]. Although many variations of the DEER sequence have been reported in literature, the two primary pulse schemes are the 3-pulse and the 4-pulse DEER (3P-DEER and 4P-DEER) [8, 11, 12]. A schematic representation of the 3P-DEER and the 4P-DEER sequences is presented in Figure 3.6.

The three-pulse DEER consists of a shorter pulse sequence and is therefore suitable for fast relaxing systems for which a longer sequence duration would implicate a considerable loss of signal. Moreover, since each microwave pulse enhances relaxation processes in the system, the use of three instead of four pulses constitutes another advantage in this sense. On the other hand the direct overlap of the first detection pulse and the pump pulse at zero-time prevents the complete reconstruction of the first modulation making much harder the data analysis and the extraction of a correct distance distribution between the two probes. The four pulse sequence instead is not affected by this problem because the pump pulse scans through the refocused echo

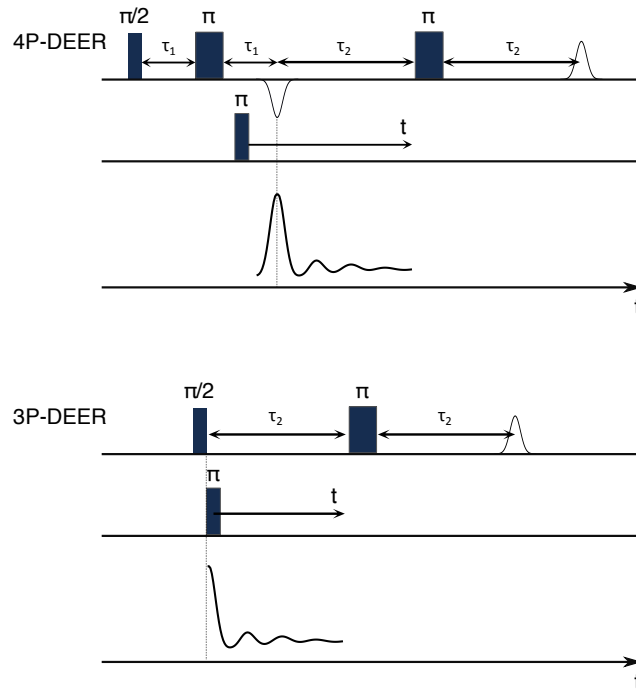


**Figure 3.6:** 4P-DEER and 3PDEER sequences and corresponding dipolar traces.

of the detection spin, allowing the measurement of dead-time free traces [13]. The DEER data presented in this thesis have been collected by using the 4-pulse sequence, therefore hereafter the discussion will be focused on this variant that will be simply called DEER.

The time trace recorded in a DEER experiment includes the contributions of all the intermolecular and intramolecular dipolar interactions between paramagnetic centers which are close enough to feel each other. Assuming that the sample is sufficiently dilute so that typical distances between spins in different molecules are much longer than distances within the same molecules, the expression of for the modulation of the DEER trace can be written as the product of a background factor  $B(t)$  due to intermolecular interactions and a form factor  $F(t)$  due to intramolecular interactions:

$$D(t) = B(t)F(t) \quad (3.4)$$

The structural information is enclosed in the form factor. Considering a sample in which (i) the molecules are doubly labeled, (ii) one spin is the detection and the other is the pump and (iii) they are selectively addressed by the corresponding pulses, the form factor is:

$$F(t) = V_0 (1 - \lambda(1 - \cos[\omega_{dd}T])) \quad (3.5)$$

where  $V_0$  is the intensity of the detection spin echo,  $\lambda$  is the modulation depth and  $T = t - \tau_1$ .  $\lambda$  represents the inversion efficiency of the pump spin and its value depends on the pulse parameters, on the orientation of the object with respect to the external magnetic field and on the relative orientation of the magnetic tensors of the pump and the detection. Also the intensity of the detection echo  $V_0$  is affected by the same parameters and this orientational dependence can potentially complicate the data analysis. The question of orientation selection in DEER requires



a separate discussion because an *ad hoc* data analysis procedures have to be introduced, therefore, for the moment, we assume that the orientational dependence of both  $\lambda$  and  $V_0$  can be neglected. The form factor then is obtained simply integrating Equation 3.5 over all the possible orientations of the inter-spin vector with respect to the magnetic field direction:

$$\langle F(t) \rangle = V_0 \left( 1 - \lambda + \lambda \int_0^1 \cos[(3x^2 - 1)\omega_{\text{dd}}T] dx \right) \quad (3.6)$$

where  $x = \cos(\theta)$ .

In order to isolate the form factor, that holds the structural information, the background contribution has to be removed from the experimental DEER trace. The background function is often approximated by a stretched exponential function:

$$B(t) = \exp[-kt^{d/3}] \quad (3.7)$$

where  $k$  is a coefficient proportional to the concentration of the paramagnetic species and  $d$  is the dimensionality of the background. For homogeneously distributed molecules, with a size much smaller than their typical distance,  $d = 3$ , whereas for peptides or membrane proteins  $d$  should be about 2 [14]. Actually, since short distances are underrepresented by this model,  $d$  may be slightly larger than the expected values. [15]

There are several routines implemented for carrying out the data processing, one of the most widespread is DeerAnalysis [16]. The analysis of experimental DEER data is usually made of four steps: (i) fitting of the background, (ii) extraction of the form factor  $F(t) = D(t)/B(t)$ , (iii) calculation of the reduced form factor  $f(t) = (\langle F(t) \rangle - \lambda)/(1 - \lambda)$ , (iv) fitting of the reduced form factor to extract a distance distribution between the two spin probes.

The extraction of the distance distribution requires solving the following equation:

$$f(t) = K(t, r)P(r) \quad (3.8)$$

where  $K$  is the kernel function:

$$K(t, r) = \int_0^1 \cos[(3x^2 - 1)\omega_{\text{dd}}(r)t] dx \quad (3.9)$$

Due to the fact that the kernel function  $K(t, r)$  has a condition number significantly smaller than 1, the computation of the distance distribution is an ill-posed problem and a least-square fitting cannot be used to this scope. The least biased method for stabilizing the solution of the ill-posed problem is Tikhonov regularization[15]. This approach imposes a smoothness condition on  $P(r)$  so that the best distance distribution is found minimizing the error function  $G_\alpha$  for a given value of the regularization parameter  $\alpha$ :

$$G_\alpha = \|f(t) - KP(r)\|^2 + \alpha \left\| \frac{d^2 P(r)}{dr^2} \right\|^2 = \rho + \alpha\eta \quad (3.10)$$

Small values of the regularization parameter over-estimate the term  $\eta$ , giving an under-smoothed distance distribution and introducing artifacts due to fitting of the noise. On the contrary, for large values of  $\alpha$  less noise artifacts are introduced, but the peaks in the distance distribution are artificially broadened. The optimum value of  $\alpha$  is not known beforehand, but the *L-curve* criterion may be helpful in this sense. The L-curve is a plot of  $\log \eta$  against  $\log \rho$  for different values of  $\alpha$ . For data with relative low noise levels and narrow peaks in the distance distribution, this log-log plot should have an "L" shape. The best value of  $\alpha$  is the one that gives the optimum compromise between goodness of the fitting and smoothness of the distance distribution. Deer-Analysis provides several tools for helping in the identification of the best value of the regularization parameter. The "L-curve corner" selects  $\alpha$  at the corner of the L-curve, but this tends to over-broaden the distance distributions. Alternatively two other procedures are available these are the Akaike (AIC) and the generalized-cross validation (GCV) method [17]. AIC treats the solutions determined with different values for  $\alpha$  as different models and determines the value that corresponds to the most parsimonious model. GCV drops one point from the dataset at a time and determines the  $\alpha$  value that generates a fit from the remaining points that best recovers this dropped point. This procedure is repeated for every point in the DEER time trace. These automatic methods can fail in determining the best  $\alpha$  and their use should be decided on the basis of the quality of the experimental data.

The distance distribution obtained in this way is of course affected by errors. However, the relation between error in the dipolar evolution function and error in the distance distribution is nonlinear. Hence, no analytical theory exists for predicting uncertainty of features in the distance distribution. An approach to numerically estimate the error consists in systematically varying the parameters that may be source of uncertainties, such as the background fit, the background dimensionality and the noise level, and repeating the Tikhonov regularization for all these parameters evaluating which peaks of the distance distribution are modified or deleted by this trials. This procedure is called "validation".

The ill-posed problem can be circumvented if some preliminary information on the structure of the investigated molecule are available and a distance distribution that conform to a simple model with only few parameters can be used. In this case a least-square fitting is carried out and the plausibility of the parameters obtained can be used as a criterion for judging the goodness of the fitting.

An important parameter that must be taken into account to assess the reliability of the distance distribution is the length of the time domain data. The distances accessible with good accuracy are strongly related to the length of the time trace. The longest reliable mean distance obtainable from a time trace of length  $t_{\max}$  is  $r_{\max} = 5\sqrt[3]{t_{\max}/2(\mu\text{s})}$  while the width of the distance distribution, which depends on the decay rate of the dipolar oscillations, is limited to  $r_{\max} \sigma = 4\sqrt[3]{t_{\max}/2(\mu\text{s})}$  [7].

#### *Orientation selection*

There are cases in which the orientational dependence of  $V_0$  and  $\lambda$  cannot be neglected [18]. This happens for example when the pump (detection) pulse excites only part of the pump (de-

tection) spectrum selecting only molecules in a certain orientation with respect to the static magnetic field. Orientation selection can be particularly effective for those systems that have strongly anisotropic EPR spectra due to large Zeeman, hyperfine or ZFS interactions [19, 20]. However, strongly anisotropic interaction are not necessary because orientation selection is present also when conventional nitroxide probes are used at Q- or W-band [21, 22]. The effect is enhanced if the pump and the detection spins are in a limited number of relative orientations, such as when the molecule is particularly rigid or for example in proteins where only few conformations of the spin probes are possible due to steric hindrance. In such situations some of the dipolar tensor orientations do not contribute to the DEER trace. This can be seen in the time-domain data where some feature that look like extra modulations appear in the trace, but is even more evident in the frequency-domain spectrum where the biased sampling of inter-spin vectors orientation erodes portions of the Pake pattern (see Figure 3.7).

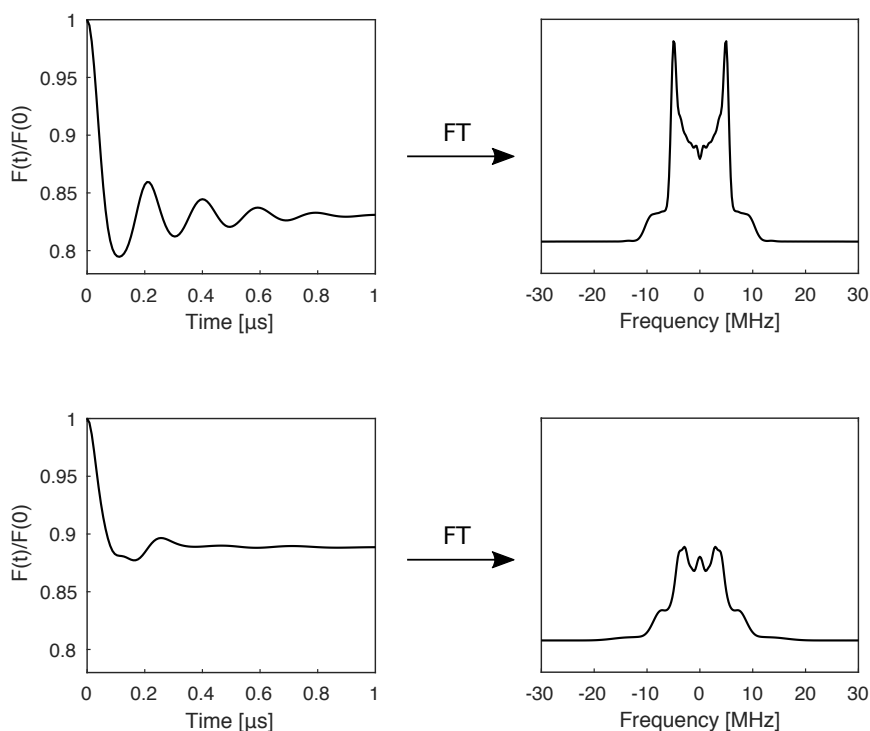


**Figure 3.7:** Effect of the orientation selection on a model dipolar trace. Top row: form factor and the corresponding Fourier transform in the absence of orientational effects. Bottom row: form factor and corresponding Fourier transform, on the same compound, collected reducing the excitation bandwidth of the detection pulse.

When orientation selection is present, the DEER trace holds information not only concerning the distance between the two spin probes, but also on the relative orientation of the magnetic tensors that have produced the orientational selectivity. This information is potentially very valuable for a 3D structure determination but at the same time make the processing of the experimental data more complicated and requires the use of *ad hoc* algorithms for the analysis. The standard procedure for extracting the distance distribution with DeerAnalysis may give spurious peaks due to the fitting of these extra features and should therefore be avoided. The theoretical description of the orientation selection in the DEER experiment has been extensively treated in

literature, and several algorithms for the analysis of the data are reported. Many of them start from a geometrical model of the system obtained for example from DFT calculations or molecular dynamics and vary the geometrical parameters until the simulated DEER traces matches the experimental one [19, 23]. Other, model the molecular geometry using as a constrain the fitting of the experimental data [24]. Alternatively several model-free approaches have been proposed [25]. Their fitting algorithm reconstructs an experimental data-set by searching for an optimal combination of pre-simulated DEER time traces of all relative orientations and inter-spin distances in the experimentally accessible range.

## RIDME

The building block of the RIDME sequence is the stimulated echo sequence and indeed the first version of the experiment was simply a 3 pulse sequence  $\pi/2 - t - \pi/2 - T \pi/2 - t - \text{echo}$  in which the interpulse delay  $t$  was progressively increased (Figure 3.8) [9].

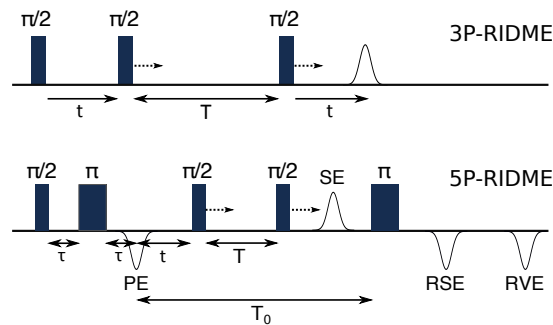


**Figure 3.8:** 3P-RIDME (top) and 4P-RIDME (bottom) pulse sequences.

In RIDME the event that causes the modulation of the detection echo is the longitudinal relaxation of the coupled spin. In a biradical sample in which the observed spin A is excited by the microwave pulses while the coupled spin B is not, if during the time interval  $T$ , the B spin flips under the effect of the  $T_1$  relaxation, the local dipolar field experienced by the A spin varies. Therefore, the stimulated echo, for increasing interpulse delay  $t$  will be modulated at the dipolar frequency. For this to happen, an odd number of flips of the B spin must take place in the  $T$  interval and this is described by the relation:

$$f_{\text{odd}} = \frac{1}{2}(1 - \exp - T/T_1) \quad (3.11)$$

The 3-pulse RIDME sequence suffers from the dead-time problem, mainly due to two reasons: (i) the overlap of the first and the second pulses for short  $\tau$  values causes distortions of the RIDME trace analogously to what happen with 3P-DEER; (ii) the resonator ringing prevents the echo detection immediately after the third pulse. In order to remove the dead-time problem in RIDME, a 5-pulse version (5P-RIDME) has been introduced (Figure 3.8) [26]. In 5P-RIDME, the positions of the third and the fourth pulse are simultaneously incremented, keeping the time  $T$  between

them constant. The detection can be performed both on the refocused stimulated echo (RSE) or on the refocused virtual echo (RVE) because are both modulated at the dipolar frequency. However, the RVE is usually employed because the detection of RSE, for  $t$  close to zero, has still dead-time problem related to the resonator ringing. In order to avoid the overlap between the last two pulses, the condition  $T_0 \geq T + t_{\text{dip}} + t_d$ , where  $t_{\text{dip}}$  is the length of the dipolar trace and  $t_d$  is the minimum interpulse delay, must be fulfilled [26].

Thanks to the fact that no pump pulse is employed and that relaxation could ideally flip all spins, the maximum inversion efficiency in RIDME is 0.5. Metal centers that usually have largely anisotropic spectra and short relaxations times are particularly suited to be used as pump spins in RIDME [27, 28, 29]. When using high spin systems as the pump in RIDME, relaxations involving transitions with  $\Delta m_S > 1$  introduce higher harmonics of the dipolar frequency in the time trace that, if not properly treated, are fitted as shorter distances in the analysis. A specific procedure to treat the problem of overtones in RIDME is described in [30] and a free-available software, for the distance analysis, called OvertonesAnalysis, is available.

### 3.3 Light-induced dipolar techniques

Nitroxide and metal-based paramagnetic centers such as Cu(II), Gd(III) and Fe(III) are have been widely studied in dipolar spectroscopy. Recently he photoexcited triplet state of porphyrin, coupled to a conventional nitroxide label, has been proposed as a spin probe in for dipolar spectroscopy application [31]. Porphyrin chromophores in their ground state are EPR silent, but upon photoexcitation can undergo to ISC from the lowest excited singlet state  $S_1$  to the lowest excited triplet state  $T_1$ , creating in this way the paramagnetic center.

#### Light-induced DEER

The first dipolar experiment exploiting a photoexcited triplet probe was the light-induced 4P-DEER (LiDEER) experiment proposed by Di Valentin *et al.* [31]. In LiDEER the laser photoexcitation is introduced before the classic 4-pulse sequence to generate the triplet state (Figure 3.9).

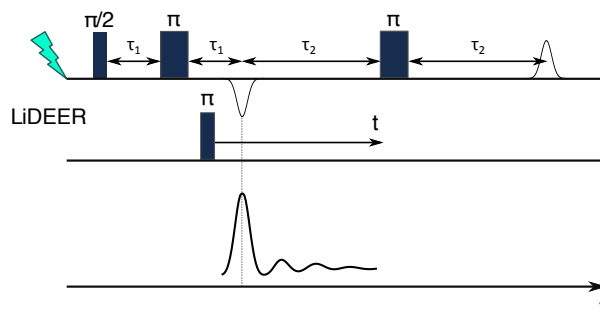


Figure 3.9: LiDEER pulse sequence.

The triplet state is instantaneously generated and, since its  $T_1$  and the decay to the ground state

are long compared to the duration of the sequence, it can be exploited as the detection spin. The porphyrin triplet is re-generated at each accumulation of the sequence and the shot-repetition time of the experiment is determined by the repetition rate of the laser.

In a proof-of-concept experiment, the measurement the dipolar trace was performed on a model  $\alpha$ -helix peptide, made of alternating alanine and  $\alpha$ -aminoisobutyric acid residues, labeled at one end with a porphyrin residue and at a specific position of the helix with a nitroxide probe (4-amino-1-oxyl-2,2,6,6-tetramethylpiperidine-4-carboxylic acid). The obtained LiDEER trace was characterized by a good modulation depth ( $\approx 40\%$ ) and well defined oscillations.

The full spectroscopic and theoretical characterization of triplet state probes has been the object of investigation of this thesis work and the results can be found in Part II.

### LaserIMD

The interesting peculiarities of the triplet states spin labels such as being switchable by light, or the occurrence of their chromophore precursors in numerous classes of proteins, where the triplet state could be potentially exploited as endogenous probes, have attracted the interest of many research groups. Recently a new technique, called laser-induced magnetic dipole spectroscopy (LaserIMD), based on optical switching of the dipole–dipole coupling between a triplet state and a radical, has been introduced by M. Drescher *et al.* [10]. The pulse scheme is presented in Figure 3.10.

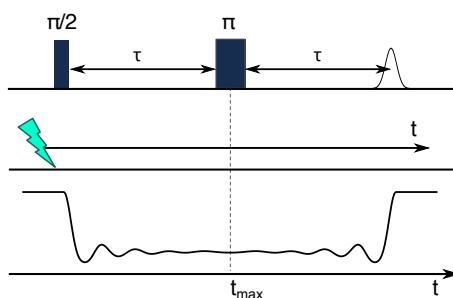


**Figure 3.10:** LaserIMD pulse sequence.

In LaserIMD, the change in the precession frequency of the radical observer spin is induced introducing the dipole–dipole coupling by instantaneous photo-generation the triplet probe. The experiment is performed by applying a 2-pulse sequence to the radical, to record its primary echo, while the position of the whole sequence relative to the (constant) position of the laser flash, is incremented. When the laser flash occurs at a time  $t$  before the refocusing of the echo of the radical, the dipolar interaction between the two spins creates a phase offset  $m_s \omega_{dd} t$ , (where  $m_s$  is the magnetic quantum number of the triplet) at the time of echo formation. This induces the echo of the radical to be modulated as a cosine function of the dipolar frequency.

### 3.4 Spin labels in dipolar spectroscopy

Nitroxides are the most common spin probes in dipolar spectroscopy, especially for structural studies in proteins where they can be attached to specific sites, through site-directed spin labeling (SDSL), on cysteine residues. SDSL has enormously increased the scope of dipolar spectroscopy studies of proteins [32] and now several different nitroxide labels such as MTS-4-oxy, 3-Carboxy-PROXYL and MTSSL (methanethiosulfonate spin label) are available and can be used in many diverse conditions. MTSSL is the most commonly used spin label in SDSL, due to its sulfhydryl specificity and its small molecular volume, similar to that of a tryptophan side chain [33]. This spin label reacts selectively with the thiol group of cysteines forming a disulfide bridge and the resulting spin label side chain is commonly abbreviated as R1 (Figure 3.11).

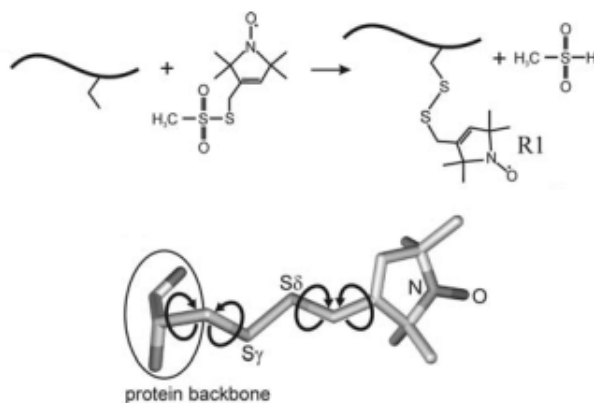


**Figure 3.11:** Reaction of MTSSL with the sulfhydryl group of a cysteine side chain, generating the spin label side chain R1. Flexible bonds within the R1 side chain are indicated. This image has been taken from [32].

The multiple tether bond, that links the nitroxide in R1 to the protein backbone, makes the spin labels particularly flexible, minimizing the perturbation of the native fold. The drawback is that the radical can sample substantial space around the point of attachment, broadening the distance distribution that is obtained with the dipolar measurement. Moreover, the large conformational space accessible to R1, does not allow to directly relate the spectroscopic data to the properties of the native side chain replaced by R1. [32]

A useful tool for examining the possible conformations of spin labels, once they have been attached in protein, is the free-available software called Multiscale Modeling of Macromolecules (MMM) [34]. Starting from the crystallographic structure of the protein, MMM allows to predict the distance distribution between nitroxides and the corresponding dipolar trace, and it is particularly helpful for making predictions and evaluating the best residues to label. The esteem of the possible conformations of the two nitroxide labels is based on a pre-computed library of rotamers of the free spin label obtained by long molecular dynamic trajectories. The probability of each rotamer, is evaluated on the basis of its internal energy, and of its interaction with the protein backbone evaluated as a sum of pairwise Lennard-Jones interactions between atoms be-

low a cutoff distance.

SDLS usually requires that the target protein possesses only cysteine residues at the desired sites and that, additional cysteines present in the protein, can be replaced by serines or alanines via site-directed mutagenesis. The disadvantages of using this approach is that each spin–spin distance to be determined requires a new protein mutant to be generated and the introduction of a spin label.

An alternative approach, that is used more in the study of small peptides, is the spin labeling synthesis either on a solid support or in solution. The paramagnetic  $\alpha$ -amino acid TOAC (4-amino-1-oxyl-2,2,6,6-tetramethyl-piperidine-4-carboxylic acid) is the most popular probe that can be chemically inserted. It is characterized by only one degree of freedom, the conformation of the six-membered ring, because the nitroxide is rigidly coupled to the peptide backbone, thereby providing the possibility to obtain direct information about the orientation of secondary structure elements. Although the synthesis of polypeptides has become possible through improvements in peptide chemistry, the incorporation of spin-labeled amino acids is still challenging due to the delicate nature of the nitroxide moiety. As, for instance, the nitroxide can be readily protonated under acidic conditions, synthesis conditions have to be identified which are chemically compatible in terms of retaining the oxidation state of the nitroxide group. [32]

Despite the numerous advantages of the different spin labeling procedures, the introduction of a spin probe causes some modifications around the labeling site, and in some regions it may even interfere with the correct folding of the protein. For this reason, the possibility of exploiting endogenous probes, i.e. paramagnetic centers which are naturally present in the protein, represents an highly attractive option for this kind of applications. Indeed, DEER has been tentatively performed on various classes of metalloproteins and proteins with metal-based spin tags at specific sites. These are  $S = 1/2$  systems or high-spin systems for which mainly the  $\Delta m_S = \pm 1/2$  transition can be selected, i.e., Cu(II), iron-sulfur centers, Gd(III), Mn(II), Mn clusters and low-spin ferric heme centers. [35, 36, 20, 37, 38] Moreover, the orthogonal labeling method, based on the use of spectroscopically nonidentical labels, which can be addressed selectively in the EPR experiment, is attracting increasing interest in the spectroscopic community and numerous efforts are devoted to the development of new spin labels to be coupled to conventional nitroxide probes [39, 40]. For this purpose, the photoexcited triplet state of organic chromophores has been introduced in the selection of spin labels for dipolar spectroscopy applications. [31] Chromophores that can efficiently populate the triplet state such as porphyrins, carotenoids and flavins are present as prosthetic groups in a number of natural systems namely photosynthetic proteins, heme-proteins and flavoproteins, [41, 42, 43] and are therefore suitable probes for application in pulse dipolar spectroscopy.



## Bibliography

- [1] Art Est. *Continuous-Wave EPR*, pages 1411–1422. American Cancer Society, 2016.
- [2] Gareth R. Eaton, Sandra S. Eaton, David P. Barr, and Ralph T. Weber. *Quantitative EPR: A practitioners guide*. SpringerWien, New York, 2010.
- [3] Sabine Richert, Claudia E. Tait, and Christiane R. Timmel. Delocalisation of photoexcited triplet states probed by transient EPR and hyperfine spectroscopy. *J. Magn. Reson.*, 280:103–116, 2017.
- [4] Stefan Weber. *Transient EPR*, pages 255–270. American Cancer Society, 2017.
- [5] Stefan Stoll. *Pulse EPR*, pages 23–38. American Cancer Society, 2017.
- [6] Arthur Schweiger and Gunnar Jeschke. *Principles of pulse electron paramagnetic resonance*. Oxford University Press, New York, 2001.
- [7] Gunnar Jeschke. DEER Distance Measurements on Proteins. *Annu. Rev. Phys. Chem.*, 63(1):419–446, 2012.
- [8] A.D. Milov, A.B. Ponomarev, and Yu.D. Tsvetkov. Electron-electron double resonance in electron spin echo: Model biradical systems and the sensitized photolysis of decalin. *Chem. Phys. Lett.*, 110(1):67–72, sep 1984.
- [9] L.V. Kulik, S.A. Dzuba, I.A. Grigoryev, and Yu.D. Tsvetkov. Electron dipole–dipole interaction in ESEEM of nitroxide biradicals. *Chem. Phys. Lett.*, 343(3-4):315–324, aug 2001.
- [10] Christian Hintze, Dennis Bückner, Silvia Domingo Köhler, Gunnar Jeschke, and Malte Drescher. Laser-Induced Magnetic Dipole Spectroscopy. *J. Phys. Chem. Lett.*, 7(12):2204–2209, 2016.
- [11] Rainer E. Martin, Matthias Pannier, François Diederich, Volker Gramlich, Michael Hubrich, and Hans W. Spiess. Determination of End-to-End Distances in a Series of TEMPO Diradicals of up to 2.8 nm Length with a New Four-Pulse Double Electron Electron Resonance Experiment. *Angew. Chemie Int. Ed.*, 37(20):2833–2837, 1998.
- [12] Peter P. Borbat, Elka R Georgieva, and Jack H. Freed. Improved Sensitivity for Long-Distance Measurements in Biomolecules: Five-Pulse Double Electron - Electron Resonance. *J. Phys. Chem. Lett.*, (4):170–175, 2012.
- [13] M Pannier, S Veit, A Godt, Gunnar Jeschke, and H.W Spiess. Dead-Time Free Measurement of Dipole–Dipole Interactions between Electron Spins. *J. Magn. Reson.*, 142(2):331–340, feb 2000.
- [14] A. D. Milov and Yuri D. Tsvetkov. Double electron-electron resonance in electron spin echo: Conformations of spin-labeled poly-4-vinylpyridine in glassy solutions. *Appl. Magn. Reson.*, 12(4):495–504, 1997.

- [15] Gunnar Jeschke. *Interpretation of Dipolar EPR Data in Terms of Protein Structure*, pages 83–120. Springer Berlin Heidelberg, Berlin, Heidelberg, 2011.
- [16] Gunnar Jeschke, V. Chechik, P. Ionita, A. Godt, H. Zimmermann, J. Banham, Christiane R. Timmel, D. Hilger, and H. Jung. DeerAnalysis2006—a comprehensive software package for analyzing pulsed ELDOR data. *Appl. Magn. Reson.*, 30(3-4):473–498, jun 2006.
- [17] Thomas H. Edwards and Stefan Stoll. Optimal Tikhonov regularization for DEER spectroscopy. *J. Magn. Reson.*, 288:58–68, 2018.
- [18] Russell G Larsen and David J Singel. Double electron-electron measurement of electron disordered solids resonance spin-echo spin pair separations modulation : Spectroscopic in orientationally disordered solids. *J. Chem. Phys.*, 98(1993):5134–5146, 1993.
- [19] Bela E. Bode, Jörn Plackmeyer, Thomas F. Prisner, and Olav Schiemann. PELDOR measurements on a nitroxide-labeled Cu(II) porphyrin: Orientation selection, spin-density distribution, and conformational flexibility. *J. Phys. Chem. A*, 112(23):5064–5073, 2008.
- [20] Alice M. Bowen, Echan O. D. Johnson, Francesco Mercuri, Nicola J. Hoskins, Ruihong Qiao, James S. O. McCullagh, Janet E. Lovett, Stephen G. Bell, Weihong Zhou, Christiane R. Timmel, Luet Lok Wong, and Jeffrey R. Harmer. A Structural Model of a P450-Ferredoxin Complex from Orientation-Selective Double Electron–Electron Resonance Spectroscopy. *J. Am. Chem. Soc.*, 140(7):2514–2527, feb 2018.
- [21] E. L. Fasanella, W. Gordy, J. Stubbe, and M. Bennati. ELECTRON SPIN RESONANCE OF AN IRRADIATED SINGLE CRYSTAL OF L-TYROSINE-HCL. *PNAS*, 62(2):299–304, sep 2006.
- [22] Yevhen Polyhach, A. Godt, C. Bauer, and Gunnar Jeschke. Spin pair geometry revealed by high-field DEER in the presence of conformational distributions. *J. Magn. Reson.*, 185(1):118–129, mar 2007.
- [23] J.E. Lovett, Alice M. Bowen, C. R. Timmel, M. W. Jones, J. R. Dilworth, D. Caprotti, S. G. Bell, L. L. Wong, and J. Harmer. Modern EPR spectroscopy: Beyond the EPR spectrum. *Phys. Chem. Chem. Phys.*, 11(31):6553–6554, 2009.
- [24] Dinar Abdullin, Gregor Hagelueken, Robert I. Hunter, Graham M. Smith, and Olav Schiemann. Geometric model-based fitting algorithm for orientation-selective PELDOR data. *Mol. Phys.*, 113(6):544–560, 2015.
- [25] Andriy Marko and Thomas F. Prisner. An algorithm to analyze PELDOR data of rigid spin label pairs. *Phys. Chem. Chem. Phys.*, 15(2):619–27, 2013.
- [26] Sergey Milikisyants, Francesco Scarpelli, Michelina G. Finiguerra, Marcellus Ubbink, and Martina Huber. A pulsed EPR method to determine distances between paramagnetic centers with strong spectral anisotropy and radicals: The dead-time free RIDME sequence. *J. Magn. Reson.*, 201(1):48–56, nov 2009.

- [27] Dinar Abdullin, Fraser Duthie, Andreas Meyer, Elisa S. Müller, Gregor Hagelueken, and Olav Schiemann. Comparison of PELDOR and RIDME for Distance Measurements between Nitroxides and Low-Spin Fe(III) Ions. *J. Phys. Chem. B*, 119(43):13539–13542, 2015.
- [28] A. Collauto, V. Frydman, M. D. Lee, E. H. Abdelkader, A. Feintuch, J. D. Swarbrick, B. Graham, G. Otting, and D. Goldfarb. RIDME distance measurements using Gd(III) tags with a narrow central transition. *Phys. Chem. Chem. Phys.*, 18(28):19037–19049, 2016.
- [29] Sahand Razzaghi, Mian Qi, Anna I. Nalepa, Adelheid Godt, Gunnar Jeschke, Anton Savitsky, and Maxim Yulikov. RIDME spectroscopy with Gd(III) centers. *J. Phys. Chem. Lett.*, 5(22):3970–3975, 2014.
- [30] Katharina Keller, Valerie Mertens, Mian Qi, Anna I. Nalepa, Adelheid Godt, Anton Savitsky, Gunnar Jeschke, and Maxim Yulikov. Computing distance distributions from dipolar evolution data with overtones: RIDME spectroscopy with Gd(III)-based spin labels. *Phys. Chem. Chem. Phys.*, 19(27):17856–17876, 2017.
- [31] Marilena Di Valentin, Marco Albertini, Enrico Zurlo, Marina Gobbo, and Donatella Carbonera. Porphyrin triplet state as a potential Spin label for nanometer distance measurements by peldor spectroscopy. *J. Am. Chem. Soc.*, 136(18):6582–6585, 2014.
- [32] Johann P. Klare and Heinz-Jürgen Steinhoff. Spin labeling EPR. *Photosynth. Res.*, 102(2-3):377–390, dec 2009.
- [33] Lawrence J. Berliner, Jacob Grunwald, H. Olga Hankovszky, and Kalman Hideg. A novel reversible thiol-specific spin label: Papain active site labeling and inhibition. *Anal. Biochem.*, 119(2):450–455, jan 1982.
- [34] Yevhen Polyhach, Enrica Bordignon, and Gunnar Jeschke. Rotamer libraries of spin labelled cysteines for protein studies. *Phys. Chem. Chem. Phys.*, 13(6):2356–2366, 2011.
- [35] Irene M C van Amsterdam, Marcellus Ubbink, Gerard W Canters, and Martina Huber. Measurement of a Cu-Cu Distance of 26Å by a Pulsed EPR Method. *Angew. Chemie Int. Ed.*, 42(1):62–64, jan 2003.
- [36] M. Ezhevskaya, Enrica Bordignon, Yevhen Polyhach, L. Moens, Sylvia Dewilde, Gunnar Jeschke, and S. Van Doorslaer. Distance determination between low-spin ferric haem and nitroxide spin label using DEER: the neuroglobin case. *Mol. Phys.*, 111(18-19):2855–2864, 2013.
- [37] Maxie M Roessler, Martin S King, Alan J Robinson, Fraser A Armstrong, Jeffrey Harmer, and Judy Hirst. Direct assignment of EPR spectra to structurally defined iron-sulfur clusters in complex I by double electron-electron resonance. *Proc. Natl. Acad. Sci. U. S. A.*, 107(5):1930–5, feb 2010.
- [38] Mizue Asada and Hiroyuki Mino. Location of the High-Affinity Mn 2+ Site in Photosystem II Detected by PELDOR. *J. Phys. Chem. B*, 119(32):10139–10144, aug 2015.

- [39] Ilia Kaminker, Hiromasa Yagi, Thomas Huber, Akiva Feintuch, Gottfried Otting, and Daniella Goldfarb. Spectroscopic selection of distance measurements in a protein dimer with mixed nitroxide and Gd<sup>3+</sup> spin labels. *Phys. Chem. Chem. Phys.*, 14(13):4355–4358, 2012.
- [40] Petra Lueders, Heidrun Jäger, Marcus A. Hemminga, Gunnar Jeschke, and Maxim Yulikov. Distance Measurements on Orthogonally Spin-Labeled Membrane Spanning WALP23 Polypeptides. *J. Phys. Chem. B*, 117(7):2061–2068, feb 2013.
- [41] H. Levanon and A. Wolberg. Electron spin polarization in the photoexcited triplet state of porphyrins. *Chem. Phys. Lett.*, 24(1):96–98, jan 1974.
- [42] Enrico Salvadori, Marilena Di Valentin, Christopher W M Kay, Alfonso Pedone, Vincenzo Barone, and Donatella Carbonera. The electronic structure of the lutein triplet state in plant light-harvesting complex II. *Phys. Chem. Chem. Phys.*, 14(35):12238, 2012.
- [43] J. M. Lhoste, A. Haug, and P. Hemmerich. Electron Paramagnetic Resonance Studies of the Triplet State of Flavin and Pteridine Derivatives. *Biochemistry*, 5(10):3290–3300, 1966.

**CHAPTER**

**4**

**Porphyrin-Based Spectroscopic Ruler for  
Nanometer Distance Measurements**



**Biophysics** | *Very Important Paper* |

**VIP** Light-Induced Porphyrin-Based Spectroscopic Ruler for Nanometer Distance Measurements

 Marilena Di Valentin,<sup>\*,[a]</sup> Marco Albertini<sup>+, [a]</sup>, Maria Giulia Dal Farra<sup>+, [a]</sup>, Enrico Zurlo,<sup>[a, b]</sup> Laura Orian,<sup>[a]</sup> Antonino Polimeno,<sup>[a]</sup> Marina Gobbo,<sup>[a]</sup> and Donatella Carbonera<sup>[a]</sup>

**Abstract:** We present a novel pulsed electron paramagnetic resonance (EPR) spectroscopic ruler to test the performance of a recently developed spin-labeling method based on the photoexcited triplet state ( $S=1$ ). Four-pulse electron double resonance (PELDOR) experiments are carried out on a series of helical peptides, labeled at the N-terminal end with the porphyrin moiety, which can be excited to the triplet state, and with the nitroxide at various sequence positions, spanning distances in the range 1.8–8 nm. The PELDOR traces provide accurate distance measurements for all the ruler series, showing deep envelope modulations at frequencies

varying in a progressive way according to the increasing distance between the spin labels. The upper limit is evaluated and found to be around 8 nm. The PELDOR-derived distances are in excellent agreement with theoretical predictions. We demonstrate that high sensitivity is acquired using the triplet state as a spin label by comparison with Cu(II)-porphyrin analogues. The new labeling approach has a high potential for measuring nanometer distances in more complex biological systems due to the properties of the porphyrin triplet state.

**Introduction**

Pulsed electron-electron double resonance (PELDOR)/double electron-electron resonance (DEER) spectroscopy is a pulsed EPR (electron paramagnetic resonance) method that measures, through the dipolar electron–electron coupling between two paramagnetic species, distances in the range of 1.5–8 nm.<sup>[1–6]</sup> This technique is characterized by high precision and reliability, although accessing distances above 7 nm is a significant challenge. Beyond mere mean distances, PELDOR yields relevant distance distributions, which provide access to conformational distributions and dynamics.

Conventionally, PELDOR measurements are performed between two nitroxide spin labels that have been attached to biological molecules either by site-directed spin labeling or by

chemical modification. For proteins, the most commonly used spin label is MTSSL [(1-oxyl-2,2,5,5-tetramethylpyrroline-3-methyl)methanethiosulfonate], which specifically reacts with the thiol group of cysteine residues, forming a disulfide bridge. By introducing cysteine residues to sites of interest by mutagenesis and subsequently allowing them to react with MTSSL, the nitroxide spin label can be positioned with high specificity and ease.<sup>[7]</sup>


Alternatively, researchers have tried to exploit endogenously bound paramagnetic metal ions in order to determine structural information in metalloproteins.<sup>[8]</sup> Utilizing these endogenously bound paramagnetic metal ions as spin probes for EPR detection causes only minimal functional perturbation to biomolecules. A limited number of examples have been reported to date, restricted to  $S=1/2$  metal centers or high-spin systems for which the  $m_s = \pm 1/2$  transition can be selected, mainly copper, iron-sulfur, and manganese centers.<sup>[9–16]</sup> For the majority of metal ions, fractional excitation of the spectrum and/or short relaxation times either severely limit the sensitivity or makes the application of the method impossible.

High sensitivity and accuracy are main issues regarding PELDOR spectroscopy, which is emerging as a powerful pulsed EPR technique, complementary to the methods of X-ray crystallography, NMR, and FRET for structural determination of biomolecules. They become a task of primary importance particularly in the field of large membrane proteins that pose a considerable challenge for crystallography and NMR spectroscopy. The use of perdeuterated proteins, application of shaped pulses, and increasing the spectrometer frequency to the Q-band, for which the conventional nitroxide labels still perform well, are the strategies adopted to broaden the applicability of

[a] Prof. M. Di Valentin, Dr. M. Albertini,<sup>+</sup> M. G. Dal Farra,<sup>+</sup> E. Zurlo, Prof. L. Orian, Prof. A. Polimeno, Prof. M. Gobbo, Prof. D. Carbonera  
Dipartimento di Scienze Chimiche, Università di Padova  
via Marzolo 1, 35131 Padova (Italy)  
E-mail: marilena.divalentin@unipd.it

[b] E. Zurlo  
Present affiliation: Leiden Institute of Physics  
Leiden University, Niels Bohrweg 2, 2333 CA Leiden (The Netherlands)

[†] These authors contributed equally to this work.

 Supporting information for this article can be found under <http://dx.doi.org/10.1002/chem.201603666>. It contains sample preparation details; optimized structures of the molecular ruler series, conformer analysis, and details on computed Mulliken atomic spin densities; raw experimental time traces of the molecular ruler series; a PELDOR trace of peptide 4 in TFE; distance analysis based on two-Gaussian and wormlike model fits and density matrix computations.

this methodology.<sup>[17,18]</sup> Alternatively, many efforts are devoted to the development of new labeling approaches to circumvent the problems emerged in the use of the nitroxide labels.<sup>[6]</sup> Gd(III) ( $S=7/2$ ) spin labels have been suggested as a valid alternative to nitroxide for Q- and W-band PELDOR distance measurements. Several characteristics of Gd(III) make it a candidate for PELDOR at high field delivering enhanced sensitivity, as has been demonstrated on model systems, proteins, peptides, and DNA.<sup>[19]</sup> In parallel, the orthogonal labeling approach, based on the use of spectroscopically nonidentical labels, which can be addressed selectively, has proved to be very promising for the Gd(III)–nitroxide pair on the same biomolecules.<sup>[20–22]</sup> In spite of this, the drawbacks of the X-band experiment must be solved in a different way as the Gd(III) tag is a high-performance label the benefits of which are effective specifically at higher microwave bands.

Recently, we have demonstrated the feasibility of applying PELDOR to determine the interspin distance between a photoexcited porphyrin triplet state ( $S=1$ ) and a nitroxide spin label chemically incorporated into a small helical peptide.<sup>[23]</sup> This new labeling approach provides high sensitivity due to the characteristics of the triplet state. Triplet states have a distinctive property compared to other spin labels: they are characterized by spin polarization enhancement of the EPR signal, resulting from a non-Boltzmann population of the triplet-state sublevels by intersystem crossing from the corresponding excited singlet state.<sup>[24]</sup> They work very efficiently as orthogonal labels, adding to the spectroscopic selectivity the advantage of behaving as photoinduced spin probes. This feature allows the intermolecular interactions and oligomerization states to be revealed in the same sample by performing PELDOR in the ab-

sence of light excitation to measure intermolecular nitroxide–nitroxide distances.

Among organic chromophores, we have selected porphyrins as they have been widely studied by EPR spectroscopy, based on their high triplet yields, strong spin polarization, and non-extreme relaxation times.<sup>[25,26]</sup> The well-characterized optical properties of the porphyrin chromophore can be also exploited to combine PELDOR to the complementary FRET spectroscopic method using a label that is fluorescent and paramagnetic at the same time. Moreover, porphyrin derivatives are frequently present as endogenous probes in several classes of proteins, that is, photosynthetic and heme proteins.<sup>[27–29]</sup> In the present work, we have developed a porphyrin-based molecular ruler to further improve the methodology for distance measurements based on the novel photoexcited triplet state spin-labeling scheme. A series of peptides, consisting of alternating L-alanine (Ala) and  $\alpha$ -aminoisobutyric acid (Aib) residues, were synthesized and covalently linked at the N-terminus with 5-(4-carboxyphenyl)-10,15,20-triphenylporphyrin (TPP). The nitroxide label was inserted at various sequence positions, spanning distances in the range of 1.8–8.0 nm (for details see Figure 1), replacing the original Aib amino acid with the structurally comparable 4-amino-1-oxyl-2,2,6,6-tetramethyl-piperidine-4-carboxylic acid (TOAC) residue, in which the nitroxyl radical is fixed on a rigid heterocyclic structure. Aib residues are strong promoters of helical conformations<sup>[30]</sup> and consequently ensure a well-defined geometry in terms of distance, relative orientation, and restricted conformational flexibility, as already demonstrated for the parent compound.<sup>[23]</sup>

The spectroscopic ruler, designed to cover the complete range of applicability of PELDOR spectroscopy, provides the re-

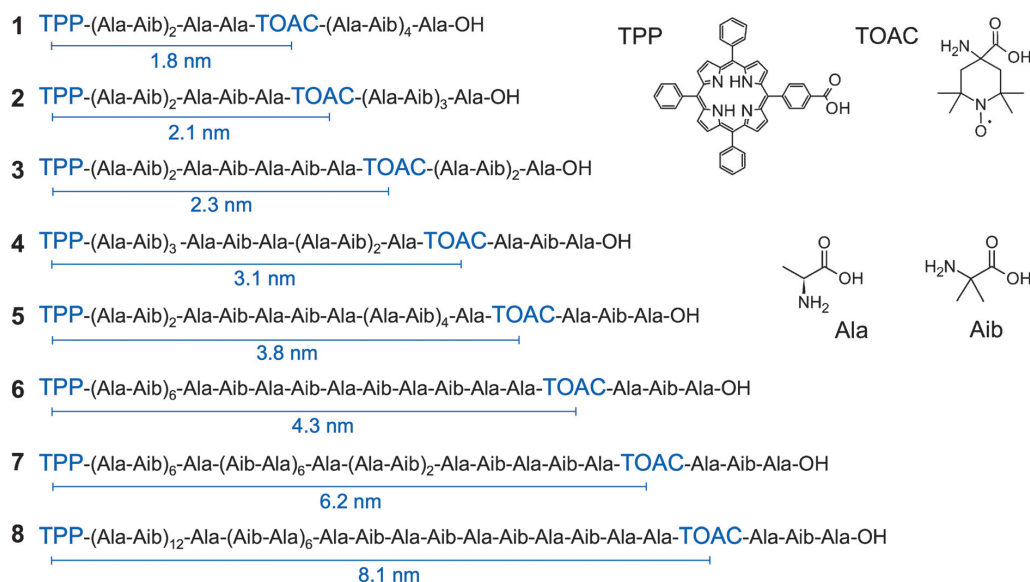


**Figure 1.** Amino acid sequences and structures of the components of the distance ruler series (1–8). The center-to-center distances between the spin labels are shown, as computed at PBE1PBE/6-31G(d) (1–3) or PBE1PBE/6-31G(d): PM3 (4–8) level of theory.



quired constraints to test the accuracy of the interspin distance determination and the range of applicability of the novel orthogonal spin-label approach. The accuracy will be assessed by comparison with modeled distance distributions based on hybrid computational (QM/QM) methods. In this systematic approach, the effects arising from the higher multiplicity of this spin system will also be analyzed using the density matrix formalism.

## Experimental Section

### Synthesis

Full experimental details for the synthesis and characterization of all the members from the “distance-ruler” series of porphyrin-based peptides are provided in the Supporting Information. The synthesis of **3** has been reported previously.<sup>[23]</sup>

### EPR samples

The overall series of bis-labeled model peptides were dissolved in a mixture of 98% deuterated methanol MeOD (Sigma Aldrich) and 2% D<sub>2</sub>O (Cambridge Isotopes) to reach a final concentration of ca. 200 μM. Peptide **4** was also dissolved in perdeuterated 2,2,2-trifluoroethanol ([D<sub>3</sub>]TFE) (Sigma Aldrich) to give ca. the same final concentration. The quartz EPR tubes, partially filled with the solutions, were sealed after several freeze–thaw cycles. Removal of oxygen, although not required, assures long-term stability of the porphyrin label.

### EPR and PELDOR spectroscopy

Pulsed EPR was performed on a Bruker Elexsys E580 pulse EPR spectrometer equipped with a Bruker split-ring resonator ER4118X-MS3 (microwave frequency = 9.55 GHz) and an Oxford CF935 cryostat. The measurements were performed at a temperature of 20 K. The sample was photoexcited with the second harmonic of a pulsed Nd:YAG laser (532 nm) with an average power of 5 mW and a repetition rate of 10 Hz.

For the electron spin-echo experiments a standard Hahn echo sequence (laser flash-DAF- $\pi/2$ - $\tau$ - $\pi$ - $\tau$ -echo) was employed with a nominal length of 16 ns for the  $\pi/2$  pulse, a delay after the laser flash (DAF) value of 50 ns and a  $\tau$  value of 180 ns. Data were collected with a single scan and 20 shots per point. For the Cu(II) analogue of **3**, data were collected without laser excitation, with a repetition rate of 330 Hz, a single scan and 100 shots per points.

For the PELDOR experiments a standard four-pulse sequence (laser flash-DAF- $\pi/2$ - $\tau_1$ - $\pi$ - $\tau_2$ - $\pi$ - $\tau_{\text{pump}}$ - $(\tau_1 + \tau_2 - t)$ - $\pi$ - $\tau_2$ -echo) was applied at a delay after the laser flash (DAF) of 50 ns; the microwave power was adjusted to obtain an observer sequence of 16/32/32 ns and a pump pulse of 12 ns. The difference between the pump (nitroxide) and observer (porphyrin triplet state) frequency was set to 240 MHz, whereas for the copper analogue the difference between the pump (nitroxide) and observer (Cu(II)–porphyrin) frequency was set to 210 MHz. A two-step phase cycle was applied to remove receiver offsets while deuterium nuclear modulations were suppressed using an 8 step  $\tau_1$  cycle from a 180 ns starting value with 56 ns increment steps. Data were collected with 5–10 scan and 50 shots per point. Typical acquisition time varied in the range from ~4 up to ~24 h at a repetition frequency of 10 Hz. For the copper analogue data were collected without laser excitation, with a repetition rate of 330 Hz, 20 scans, and 300 shots per points.

### Theory

The analytical expression describing the echo modulation for a 4-pulse PELDOR experiment for a system composed by a photoexcited triplet state interacting with a radical was derived in Mathematics, based on the density matrix formalism, first introduced for the analysis of ESEEM by Rowan, Hahn, and Mims<sup>[31]</sup> and later generalized and described in detail by Mims.<sup>[32]</sup>

The spin Hamiltonian for the weakly coupled triplet–radical pair in angular frequency units is:

$$\hat{H}_S = \omega_T \hat{S}_{T,z} + \omega_R \hat{S}_{R,z} + D \left( \hat{S}_{T,z}^2 - \frac{1}{3} \hat{S}_T^2 \right) + \omega_{dd} \hat{S}_{T,z} \hat{S}_{R,z} \quad (1)$$

in which the different terms stand for the electron Zeeman interaction ( $\omega_T$  and  $\omega_R$  are the Larmor frequency in the rotating frame of the triplet state and the radical), the zero-field splitting (ZFS) interaction within the triplet state, for  $B_0$  parallel to the Z-ZFS principal axis ( $D$  is the ZFS parameter), and the dipole–dipole interaction of the spins in the pair.

In the point-dipole approximation, the dipolar coupling frequency  $\omega_{dd}$  is:

$$\omega_{dd} = \frac{\mu_0 \mu_e^2}{4\pi \hbar} g_T g_R \frac{1 - 3 \cos^2 \theta_{TR}}{r_{TR}^3} \quad (2)$$

in which  $r_{TR}$  is the interspin distance and  $\theta_{TR}$  is the angle between the interspin vector and the direction of the external magnetic field  $B_0$ .

Alternatively, considering the spin density delocalization on the porphyrin ring, the dipolar frequency becomes:

$$\omega_{dd} = \frac{\mu_0 \mu_e^2}{4\pi \hbar} g_T g_R \sum_j \rho_j^i \frac{(1 - 3 \cos^2 \theta_{TR}^i)}{(r_{TR}^i)^3} \quad (3)$$

in which the  $j$  index runs on all the spin-bearing atoms on the porphyrin triplet state and  $\rho_j^i$  is their respective spin density. The interspin distance  $r_{TR}^i$  and the angle  $\theta_{TR}^i$  between the interspin vector and the direction of the external magnetic field  $B_0$  refer to each spin-bearing atom. From the radical point of view, the unpaired electron is localized in the midpoint of the N–O bond of the nitroxide moiety since DFT calculations show that 45% of the spin density is localized at the nitrogen and 50% at the oxygen atom (see the Results and Discussion Section).

A series of simplifying assumptions was necessary to derive the analytical expression for the echo modulation of a dipolarly coupled triplet–radical pair spin system. First of all, the derivation was based on an isotropic Zeeman interaction, no resolved hyperfine couplings were considered and the calculation was carried out in the high-field approximation, that is, ignoring the nonsecular terms of the ZFS. Only the secular term of the dipolar Hamiltonian was considered in the condition, which is usually fulfilled, that the difference of the Larmor frequencies of the two interacting spin systems is much larger than the weak dipolar coupling. The Heisenberg exchange coupling between the radical and the triplet state was neglected as our ruler, in line with most systems suitable for PELDOR studies, involve spins separated by  $r > 1.5$  nm.

All pulses were assumed to be ideal, that is, they excite only the pump or the observer without any spectral overlap and they rotate the magnetization by exactly the nominal angle  $\pi$  or  $\pi/2$ . Furthermore, since the spacing of the triplet state sublevels due to ZFS is generally such that the microwave frequency cannot simul-

aneously excite transitions that share a common sublevel, transition selective microwave pulses were considered.

Examining the four-pulse PELDOR sequence, laser flash-DAF- $\pi$ - $\tau_1$ - $\pi$ - $t$ - $\tau_{\text{pump}}$ - $(\tau_1 + \tau_2 - t)$ - $\pi$ - $\tau_2$ -echo, and denoting the pulse propagators for the  $\pi/2$  or  $\pi$  pulses by  $\hat{R}_{\pi/2}$  and  $\hat{R}_{\pi}$ , and the time evolution operators by  $\hat{R}_t$ ,  $\hat{R}_{\tau_1}$ , and  $\hat{R}_{\tau_2}$ , the echo amplitude is given by:

$$\text{Echo}(t, \tau_1, \tau_2) = \langle \hat{S}_x \rangle = \text{Tr} \left\{ \hat{R}_{\tau_2} \cdot \hat{R}_{\pi} \cdot \hat{R}_{\tau_1 + \tau_2 - t} \cdot \hat{R}_{\tau_{\text{pump}}} \cdot \hat{R}_t \cdot \hat{R}_{\pi} \cdot \hat{R}_{\tau_1} \cdot \hat{R}_{\pi/2} \cdot \hat{\rho}_0 \cdot \hat{R}_{\pi/2} \cdot \hat{R}_{\tau_1} \cdot \hat{R}_{\pi} \cdot \hat{R}_t \cdot \hat{R}_{\tau_2} \cdot \hat{S}_x \right\} \quad (4)$$

in which  $\hat{\rho}_0$  is the initial density operator and  $\hat{S}_x$  is the detection operator. Considering quadrature detection both  $\langle \hat{S}_x \rangle$  and  $\langle \hat{S}_y \rangle$  were evaluated.

The initial state of the system after the laser flash is described by the diagonal elements (populations) of the density matrix in the eigenbasis of the spin Hamiltonian, no coherences evolve during the DAF interval.<sup>[33]</sup> The pump spins are in the  $S=1/2$  state while the detection spins are in the  $S=1$  state, according to the setting of PELDOR experiment on the series of bis-labeled peptides.

The analytical result of the echo, normalized to the intensity at  $t = \tau_1$ , for the weakly coupled triplet-radical pair spin system applying the four-pulse PELDOR sequence is:

$$\text{Echo}(t) = \cos[\omega_{\text{dd}}(t - \tau_1)] \quad (5)$$

in which  $t$  indicates the variable time position of the pump pulse in between the second and fourth pulses. No out-of-phase echo is present for this sequence.

### Quantum mechanical calculations

All calculations were performed using Gaussian 09.<sup>[34]</sup> The initial geometries were built using a tetraphenylporphyrin and the motif Ala-Aib, extracted from the Cambridge Structural Database<sup>[35]</sup> and repeated many times as required to build the helix of adequate length; then the TOAC was attached in the chosen position. Two different optimization procedures were followed, suitably tailored to the length of the peptide. In all cases, the spin multiplicity was set to 2. For the shorter peptides (from 1 to 3) a purely DFT approach was used: PBE1PBE functional was used together with 6-31G(d) basis set for all atoms (level of theory: PBE1PBE/6-31G(d)).<sup>[36–38]</sup> In contrast, a quantum mechanics/quantum mechanics (QM/QM) protocol was set up for full geometry optimization of the longer components (from 4 to 8). The ONIOM (Our own N-layered Integrated molecular Orbital and molecular Mechanics) scheme was adopted.<sup>[39]</sup> The inner layer was described at the PBE1PBE/6-31G(d) level of theory, while the PM3 Hamiltonian<sup>[40–43]</sup> was used for the outer layer (PBE1PBE/6-31G(d):PM3). The former layer includes the two spin probes, that is, the TTP and the TOAC, whereas the latter one contains the rest of the peptide. All geometry optimizations were carried out in vacuo. Subsequently, for all the optimized geometries, the spin density of the interacting triplet-state-radical system (quartet state) was computed at the PBE1PBE/6-311G(d,p) level of theory. For all the systems, the calculations were carried out with the pyrrolic protons of the porphyrin ring in the two different positions.

The geometry of the Cu(II)TTP-peptide analogue of **3** was fully optimized in vacuo using the same functional (PBE1PBE) and basis set 6-31G(d) for C,O,N,H; Stuttgart RSC 1997 ECP was used for Cu;

the spin density was computed at PBE1PBE/6-311G(d,p),RSC1997 ECP.

The alpha-helix conformation of the peptides is rather rigid, but the two single bonds of the *para*-substituted benzoyl group with respect to the  $C^1_{\text{phenyl}}-\text{CO}$  and the  $C^4_{\text{phenyl}}$ -tetrapyrrole ring can introduce rotational degrees of freedom between the porphyrin and the nitroxide. In order to explore all the possible orientations and to measure the associated distances between the spin probes, a relaxed scan over  $360^\circ$  in  $10^\circ$  steps was performed for each of the two angles using a simplified model compound (to save computational time) consisting of the TTP and the first five amino acids of the helix. The two monodimensional scans were used to determine the accessible angles, that is, those with energy below  $k_B T$  calculated at the freezing temperature of the solvent (for methanol the freezing-point temperature is  $T = 175.6$  K; thus  $k_B T$  is 0.349 kcal mol<sup>-1</sup>). A set of rotamers, for each peptide of the ruler, was calculated by rotating about these single bonds. These sets of conformers have been subsequently used for the spectral simulations, as described in the next section.

### PELDOR data analysis

PELDOR time traces as obtained from the spectrometer were treated using the DeerAnalysis2013 routine.<sup>[44]</sup> Primary data from experiments were background corrected by fitting an exponential or a stretched exponential decay function. The dipolar spectra were obtained by Fourier transformation of the time domain data, apodized and zero filled. The form factors were processed by Tikhonov regularization, using the L curve as the criterion for determining the optimum regularization parameter. Alternatively distance distributions were obtained by a two-Gaussian or warm-like model fit. For the calculation of the PELDOR time traces and dipolar spectra, a program which evaluates the dipolar interaction between the triplet state and the radical spin system was implemented in MATLAB, based on the analytical expression describing the echo modulation for a 4-pulse PELDOR experiment [Eq. (5)]. The routine accounts for the effects of spin delocalization on the porphyrin moiety, calculating the dipolar frequency according to Equation (3). The PELDOR powder pattern was calculated by a uniform sampling of the  $B_0$  orientations in the unit sphere. The set of angles  $\theta$  and  $\phi$  for this average was taken from a spherical grid computed by the EasySpin function sphgrid.<sup>[45]</sup>

The full set of molecular conformers generated by quantum mechanical calculations was considered in the calculation, summing the PELDOR frequencies over the conformation distribution and considering also the presence of the NH tautomers.

The calculation of the four-pulse PELDOR traces in the time domain was followed by Fourier transformation to give the corresponding dipolar spectrum.

## Results and Discussion

### Synthesis

To test the accuracy of the interspin distance determination and the range of applicability of the nitroxide-porphyrin triplet-state orthogonal spin-label approach, we have designed and developed a distance ruler, consisting of a series of bis-labeled model peptides with well-defined, predictable separations between the paramagnetic sites. The peptides are labeled at the N-terminal end with the TPP moiety and with the unnatural amino acid TOAC at selected sequence positions,

spanning distances from 1.8 to 8 nm. The peptide sequences and the calculated distances between the two labels are reported in Figure 1.

Peptides **1–6** were assembled by standard solid-phase synthesis, following a protocol previously optimized for TOAC-containing peptides.<sup>[46]</sup> TPP was covalently linked to the N-terminus of the TOAC-containing peptide, still attached to the solid support, in the presence of *N,N'*-diisopropylcarbodiimide/1-hydroxybenzotriazole in CH<sub>2</sub>Cl<sub>2</sub>/DMF. Peptides **7** and **8** were synthesized by fragment condensation of the TOAC-containing C-terminal segment, still attached to the solid support, with the remaining TPP-*N*-terminal segment, in the presence of diisopropylcarbodiimide/1-hydroxy-7-azabenzotriazole as coupling reagents. For the cleavage of the porphyrin-peptide conjugate from the resin, a very mild acidic treatment was performed, to prevent the loss of the free radical character of the TOAC residue by protonation. A metallated analogue of **3** was also prepared, in which Cu(II) was inserted in the free-base porphyrin by the acetate method,<sup>[47]</sup> in order to estimate the performance of the novel triplet-state spin label compared to a conventional  $S=1/2$  label introduced in the same peptide.

### Triplet state versus Cu(II)-based-PELDOR

In Figure 2, top panel on the left, the photoexcited field-swept electron-spin echo spectrum of the TPP-conjugated peptide **3** is depicted, which shows the narrow central absorption signal due to the nitroxide spin label and the broad contribution, extending between 300 and 380 mT, due to the TPP triplet state (<sup>3</sup>TPP). In the same panel on the right, the field-swept electron-spin echo spectrum of the Cu(II)TPP-peptide analogue of **3** is reported, with the Cu(II) and nitroxide Boltzmann signal contributions. The triplet-state spectrum displays turning points corresponding to the canonical orientations of the anisotropic ZFS tensor and a specific spin-polarization pattern composed by enhanced absorptive (A) and emissive lines (E), as a result of a non-Boltzmann population of the triplet-state sublevels. The Cu(II) spectrum is characterized by an approximately axially symmetric *g*-tensor and hyperfine coupling to the copper and with the pyrrole nitrogen atoms.

Figure 2, bottom panel on the left, depicts the four-pulse PELDOR time trace, obtained by applying the pump pulse at the maximum of the nitroxide spectrum, in order to optimize

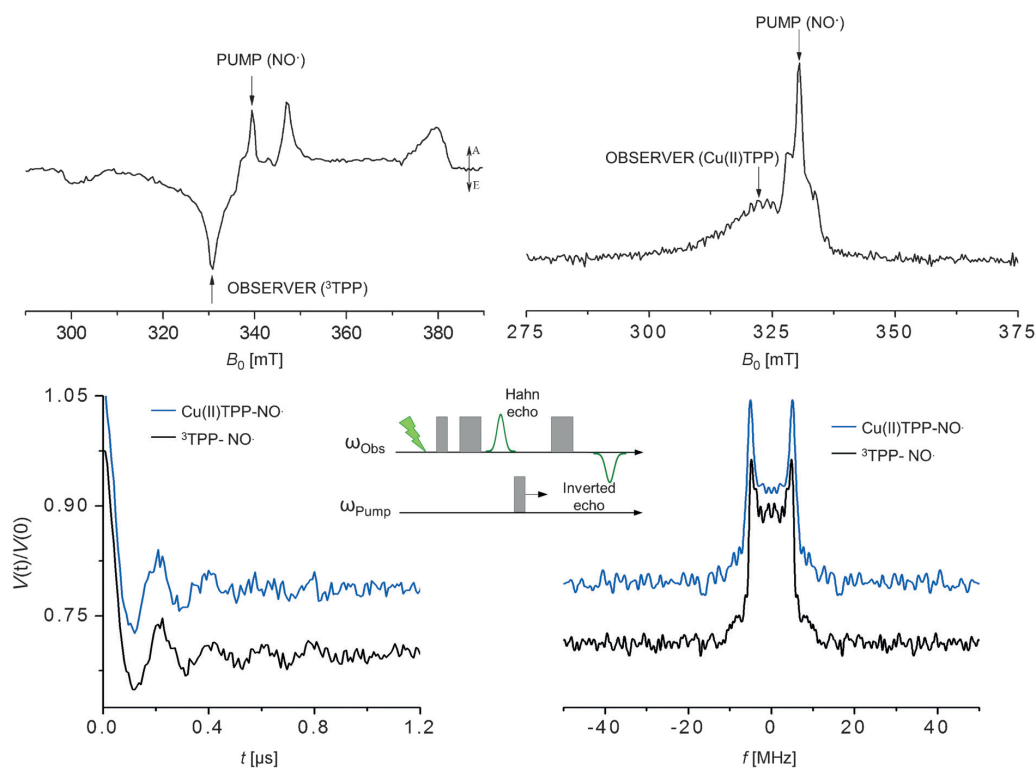


**Figure 2.** Top panel: X-band field-swept electron-spin echo spectrum recorded under photoexcitation for the TPP-conjugated model peptide **3** (left) and without photoexcitation for the Cu(II)TPP-peptide analogue of **3** (right) at 20 K. The arrows indicate the positions of the pump (nitroxide) and the detection spin (<sup>3</sup>TPP triplet state for **3** and Cu(II)TPP for the Cu(II) analogue of **3**) in the PELDOR experiments shown in the bottom panel. Bottom panel: X-band four-pulse PELDOR traces after background correction (left) and corresponding Fourier transform (right) recorded at 20 K under photoexcitation for peptide **3** (black trace) and without photoexcitation for the Cu(II) analogue of **3** (blue trace). The experimental conditions are indicated in the Experimental Section. The inset depicts the four-pulse PELDOR sequence in the presence of laser photoexcitation. A = enhanced absorption, E = enhanced emission

the pump efficiency, and the observer sequence in correspondence to the most intense emissive ZFS canonical transition of the polarized TPP triplet-state spectrum, generated by pulsed laser excitation. The PELDOR trace reveals a well-resolved and pronounced dipolar modulation and a weak damping, up to at least five complete periods. The modulation stems from dipolar coupling of spin pairs with a single dominating distance. The PELDOR trace obtained for the Cu(II) analogue, setting the pump pulse again on the maximum of the nitroxide spectrum and the observer pulses at the  $g_{\perp}$  region of the Cu(II) signal, shows three clear modulation periods corresponding to the same dipolar frequency. This behavior is characteristic of restricted conformational flexibility and distance distribution of the spin probes in both model compounds. Optimization of the time trace in terms of signal-to-noise ratio was achieved by reducing by a hundred times the number of scans for the triplet state-nitroxide PELDOR experiments. The significantly increased sensitivity is due to the intrinsic spin polarization of the triplet state, which is only partially lost in the broad features of the corresponding spectrum. Moreover, under the conditions commonly adopted for PELDOR measurements, the phase memory time of the triplet state at cryogenic temperature is comparable to that of nitroxide spin labels, whereas for Cu(II) the signal is significantly shorter.

After removal of the background decay from the envelope modulation, Fourier transformation of the signals provides the frequency spectra reported in Figure 2 (bottom panel on the right), in which the maximum intensity is observed at the dipolar frequency  $\omega_{dd} = 4.8$  MHz. Although a significant extent of orientation selection is expected in both the relatively broad porphyrin triplet and Cu(II) spectra, the effect is not visible in the PELDOR spectra, which are described by complete Pake patterns.

The orientation selectivity is washed out because at the observer position almost all the possible molecular orientations with the tetrapyrrole plane parallel to the magnetic field are detected for both the triplet-state and the Cu(II) spin system<sup>[48–50]</sup> and to a lesser extent by the small degree of rotational freedom of the *para*-substituted benzoyl group with respect to the  $C^1_{\text{phenyl}}\text{-CO}$  and the  $C^4_{\text{phenyl}}\text{-tetrapyrrole}$  ring bonds. In the case of the triplet state, the orientation selection is further compromised by the lack of collinearity between the ZFS principal axes and the spin–spin distance vector and by the presence of the NH tautomers of the free-base porphyrin. In PELDOR studies on Cu(II)–nitroxide and Cu(II)–Cu(II) model systems, excitation in the  $g_{\perp}$  region of the copper spectrum led to negligible orientation selection due to effects of the nitrogen hyperfine coupling in the *g*-region, which causes orientation smearing,<sup>[9,11,12]</sup> in these cases a reasonable analysis of the distance distribution is allowed.

The close correspondence between the dipolar spectra of the two analogues is by itself clear evidence that the orientational effects are suppressed since some difference should be expected in the selection of the molecular orientations. They can, therefore, be neglected in the spectral analysis described in the following sections.

The correspondence between the dipolar spectra of peptide **3** and the Cu(II) analogue can be also used to demonstrate that the point-dipole model is still valid despite the considerable delocalization of spin density in the porphyrin ring. A different spin-density distribution, as calculated for the two porphyrin moieties (reported in the next section), would cause differences in the dipolar frequency.

### Theoretical and computational results

The explicit analytical expression for the echo modulation due to the dipole–dipole interaction of a  $S = 1$  paramagnetic center with a  $S = 1/2$  center has been derived by following Mims' density matrix formalism. The echo is modulated with the dipolar frequency  $\omega_{dd}$  as described in Equation (5). This relation allows the characteristic features of the triplet-state experiment to be determined. The PELDOR formula takes a fairly simple form analogous to that for the conventional  $S = 1/2$ – $S = 1/2$  case with a sinusoidal dependence on the dipolar frequency. This result has, therefore, opened the possibility of implementing a computational approach for the simulation of the PELDOR dipolar spectra for the triplet–radical pair spin system.

A program has been written, as described in detail in the Experimental Section, which calculates the PELDOR trace and the corresponding dipolar spectrum, related to the time-domain echo modulation signal through Fourier transformation. The influence of conformational flexibility and spin-density distribution has also been analyzed. Simulations were guided by quantum mechanical calculations of the optimized structure of the bis-labeled peptide and the structures of the accessible conformers obtained by rotation of the *para*-substituted benzoyl group with respect to the  $C^1_{\text{phenyl}}\text{-CO}$  and the  $C^4_{\text{phenyl}}\text{-tetrapyrrole}$  ring bonds (for details see Figure S1 in the Supporting Information). The computational results are shown for the model peptide **3** compared with those for the Cu(II) analogue in Figure 3; they have been reported in Figure 4 for all the members of the distance ruler series.

A rodlike behavior of the  $\alpha$ -helical peptides can be assessed for the first four members of the series while the longer peptides, starting from **5**, show a slight chain bending, which is gradually becoming more marked to the end of the series. Mulliken atomic-spin densities have also been computed on the optimized structures for the triplet–radical pair and for the Cu(II)–radical spin system and they are shown in Figure 3. These values are in very good agreement with results previously reported in the literature.<sup>[14,48,51]</sup> The overall series of free-base peptides conserves the spin-density distribution found for compound **3** (comparison in Figure S3, Supporting Information, with representative members of the series).

The form factor was calculated for the ensemble of conformers belonging to each bis-labelled peptide, as generated by computation. A powder average distribution of the selected conformers has been considered although taking orientation selection into account produces similar results, in agreement with the considerations reported in the previous section. In case of extensive spin-density delocalization, the point-dipole approximation might break down and for this reason the dipole

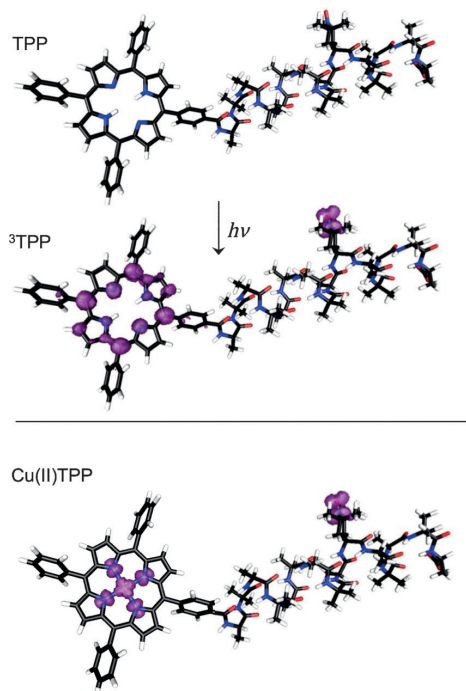


**Figure 3.** Top panel: Ground-state optimized structure of the TPP-conjugated peptide **3** (PBE1PBE/6-31G(d)) and relative spin density after excitation to the triplet state (PBE1PBE/6-311G(d,p)). Bottom panel: Ground-state optimized structure of the Cu(II)TPP-peptide analogue of **3** (PBE1PBE/6-31G(d), RSC1997 ECP) and relative spin density (PBE1PBE/6-311G(d,p), RSC1997 ECP).

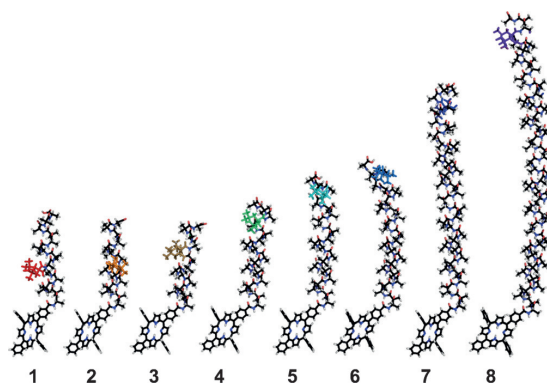


**Figure 4.** Ground-state optimized geometries (1–3: PBE1PBE/6-31G(d); 4–8: PBE1PBE/6-31G(d):PM3) of all the members of the distance ruler series.

lar coupling has been calculated treating all spin-bearing atoms explicitly, according to Equation (3). Figure 5 shows the frequency spectra for both the free-base porphyrin peptide **3** and the Cu(II) analogue and demonstrates that the rather large spin-density distribution on the porphyrin spin label has only

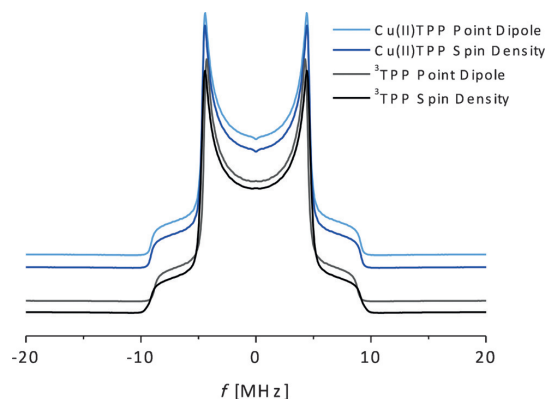


**Figure 5.** Fourier transformed PELDOR spectrum calculated for the TPP-conjugated model peptide **3** and for the Cu(II)TPP-peptide analogue of **3**: accounting for the spin-density delocalization (black and blue, respectively) and in the point dipole approximation (gray and light-blue lines, respectively).

a marginal effect on the simulated PELDOR spectra. This is also in agreement with the correspondence between the modulation frequency of the free-base and that of the Cu(II)–porphyrin system, despite the difference in the spin-density distribution on the two macrocycles, as pointed out in the previous section. The reason for this behavior derives from the concentric distribution of the spin density in the porphyrin macrocycle resulting only in a small orthorhombic contribution to the dipolar tensor.<sup>[52]</sup> For both model compounds, the maximum intensity is observed at the same dipolar frequency  $\omega_{dd} = 4.8$  MHz, demonstrating that the triplet state is equivalent to the Cu(II) center, when used in the orthogonal spin-label strategy, but it has the significant advantage of featuring higher sensitivity due to the intrinsic spin polarization compared to the  $S = 1/2$  metal centers. The computed dipolar frequencies are in agreement with those extracted from the experimental PELDOR spectra, reported in Figure 2, within the approximation of the adopted computational approach.

#### PELDOR spectroscopic ruler

The appearance of the echo and its modulation in the triplet-radical system is readily explained by the theory presented in this study. We have demonstrated that the time-dependence is the same as for two dipolar coupled  $S = 1/2$  species. Orientation selectivity and spin-density distribution effects can also be neglected and for this reason the PELDOR data can be analyzed with the standard software developed for the  $S = 1/2$  interacting systems.

An overview of the experimental background-corrected and simulated time domain signals and of the distance distributions obtained by Tikhonov regularization are shown in Figure 6 for the complete series of porphyrin-based peptides (1–8). Details of the background correction procedure and data analysis are available in the Supporting Information. The dipolar spectra, obtained after removal of the background

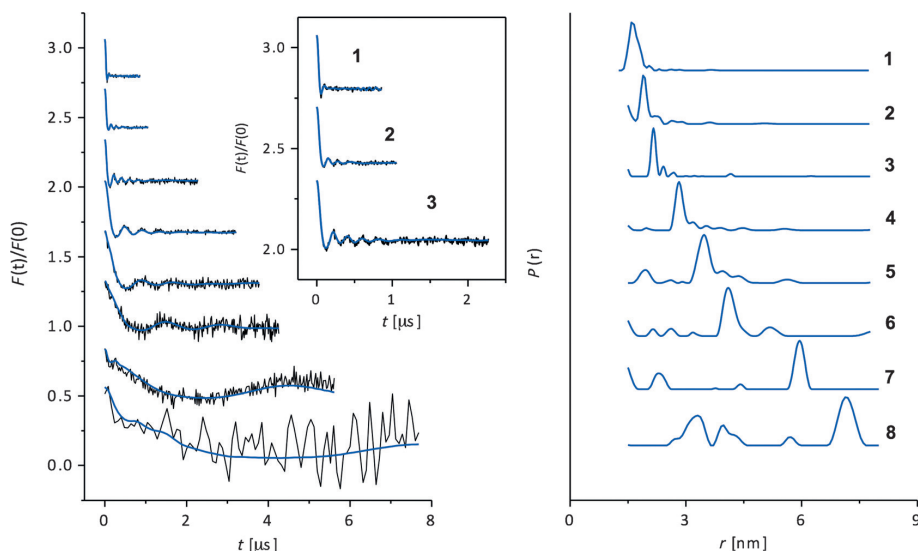


**Figure 6.** Left: time domain four-pulse PELDOR data after background correction (black) and relative DeerAnalysis fittings of the form factors (blue) for the distance ruler series (1–8). Right: experimental label-to-label distance obtained from the PELDOR data by Tikhonov regularization. Inset: enlargement of the PELDOR time traces and relative fittings for model peptides 1, 2, and 3. The experimental conditions are indicated in the Experimental Section.

decay from the envelope modulation and Fourier transformation of the signals, are also shown in the Supporting Information for some representative members of the ruler series and are characterized by a Pake pattern shape (see Figure S5).

It can be clearly seen that the time traces of all the bis-labeled peptides show oscillations and that the period of the oscillations increases with increasing distance between the spin-labels. Dipolar evolution functions with a good signal-to-noise ratio and modulation depth was observed for all the series. Visible dipolar oscillations allow well-defined distances to be defined by Tikhonov regularization in the overall range of distances explored by the spectroscopic ruler. To inspect the capability of the novel label to work on a wide range of distances, design criteria have included the bis-labeled peptide **1** at the lower limit of the distance range and more importantly peptide **8**, which represents the upper limit expected to be around 8 nm.

As shown in Figure 6, the properties of the triplet-state probe have permitted us to measure interspin distances up to 8 nm with a conventional X-band setup. However, extraction of distance and distributions is not faithful in this case because of possible errors in background removal. Furthermore, a high-frequency component is also present due to nuclear modulation, which is responsible for distance artifacts. It can be foreseen that a higher sensitivity of the experimental setup when combined with the properties of the porphyrin label would permit interspin distances of 8 nm to be accurately measured.

In the overall range explored, the model-free analysis of the traces gives a clear main peak but the main distance component is broken into a collection of individual small peaks. To assess the accuracy of the distance measurement afforded by

the novel PELDOR experiment, we modeled the distance distribution for all the members from the distance ruler series alternatively with two-Gaussian functions. Fitting with two-Gaussian functions yielded a peak maximum very close to that obtained by Tikhonov regularization, illustrating the robustness of the distance reported by the main peak (Figure S6).<sup>[53]</sup>

Applying the design criteria of the distance ruler presupposes the introduction of the spin-label functionalities in highly defined and rigid structures. The width of the distribution can be used to characterize the degree of flexibility of the peptide. Although the widths of the obtained distance distributions increase progressively with increasing separation between the spin labels, overall they remain quite narrow in the examined range up to 8 nm. This is a clear indication of the stiffness of the peptide bridge, further supported by the absence of the characteristic asymmetric shape of shape-persistent oligomers, with a steeper decay towards shorter rather than longer distances, as predicted by the wormlike chain model.<sup>[54]</sup> Indeed, the dipolar evolution data cannot be fit satisfactorily using the wormlike chain model fit, implemented in DeerAnalysis (Figure S6).

To investigate this further, PELDOR experiments have been performed on peptide **4** dissolved in TFE, exploiting the stabilizing effect of TFE on helicity (Figure S7). No difference has been detected in the time domain signals and distance distributions. This corroborates the evidence that the bis-labeled peptides have a high degree of rigidity not only in TFE but also in methanol and are, therefore, appropriate molecular rulers for the purpose of testing the accuracy and practical limits of the new labeling strategy. To illustrate the overall performance and consistency of the combined experimental/theo-

retical approach, Figure 7 shows a comparison of the mean distance obtained by DeerAnalysis and DFT calculations, respectively. Table 1 summarizes PELDOR and calculated distance parameters for the overall set of peptides: main and average distances, together with the widths of the distributions (details on these parameters are reported in the Experimental Section).

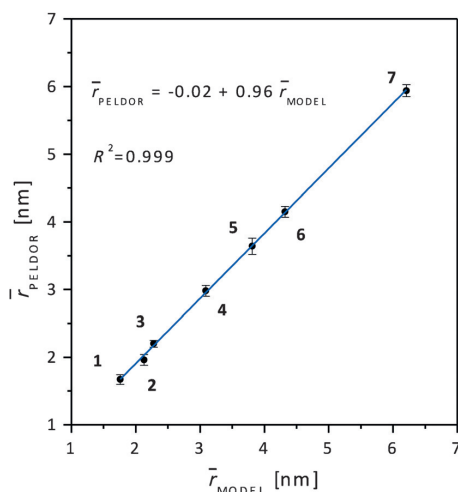


**Figure 7.** Correlation of the mean label-to-label distances obtained by PELDOR experiments and computations for the distance ruler series (1–7). The vertical bars indicate standard deviations of the principal peak in the PELDOR distance distribution. The solid line represents the linear fit.

**Table 1.** Distance parameters for the spectroscopic ruler are given by Tikhonov regularization and compared to computational results.

	PELDOR		MODEL			
	$\alpha^{[a]}$	$\bar{r}^{[b]}$ [nm]	$\sigma_r^{[c]}$ [nm]	$r_{mp}^{[d]}$ [nm]	f.w.h.m. <sup>[e]</sup> [nm]	$\bar{r}^{[f]}$ [nm]
1	0.1	1.71	0.14	1.59	0.30	1.76
2	0.1	2.05	0.16	1.89	0.19	2.13
3	1	2.31	0.10	2.16	0.14	2.28
4	10	3.11	0.16	2.83	0.23	3.09
5	10	3.53	0.24	3.47	0.36	3.81
6	10	4.20	0.16	4.10	0.33	4.32
7	10	5.94	0.18	5.95	0.58	6.21

a) Regularization parameter of Tikhonov regularization. [b] Mean distance. [c] Standard deviation of the main peak in the distance analysis. [d] Most probable distance. [e] Full width half maximum. [f] The variation is below 0.02 nm for each compound.

The results on peptide **8**, corresponding to the limit of the distance ruler, have not been plotted since the distance analysis, as already pointed out, is not as accurate as for the other members of the series. The linear fit to the data, corresponding to the measured average distances as a function of the calculated mean distances, has a slope of almost unity, an offset that is negligible compared to the distances measured and the correlation coefficient is 0.999 ( $\bar{r}_{\text{PELDOR}} = -0.02 + 0.96\bar{r}_{\text{MODEL}}$ ).

This analysis shows that the correlation between the data sets is very good and confirms the high degree of rigidity of the bis-labeled peptides, which maintain the  $\alpha$ -helical structure along the series with only a slight bending for the longer members, as demonstrated by computations. In the plot the standard deviation of the distribution function is reported together with the average distance as derived by DeerAnalysis. The flexibility of the molecular rods can be characterized by this parameter.<sup>[55]</sup> The standard deviation is in the range of 0.1–0.24 nm, further proving the stiffness of the  $\alpha$ -helical poly-peptides. For the purpose of our study, peptides with well-defined features, that is, a definite conformational preference and sufficient stiffness, are required. These properties are collectively possessed by the selected series of peptides as demonstrated by the computational results. A very precise PELDOR-based nanometer distance ruler is established and it is used to test the performance of the novel spin-labeling strategy based on the porphyrin triplet state. The excellent agreement between PELDOR-derived distances and computational results validates the approach used for the distance analysis for the radical-triplet state system, based on the DeerAnalysis software using the standard expressions of two  $S = 1/2$  spins and neglecting orientation and spin delocalization effects, owing to the specific properties of the porphyrin triplet-state label.

## Conclusion

This work demonstrates the potentiality of the PELDOR technique to determine the interspin distance when combined to the orthogonal spin-labeling strategy based on the porphyrin triplet-state nitroxide pair. It also provides the appropriate theoretical background to the simulation approach to adopt for this system.

We have explored the practical limits of the distance determination based on the four-pulse PELDOR experiment combined to the novel orthogonal spin-labeling method: we have constructed a porphyrin-based molecular ruler for which the nitroxide spin label is attached to different positions along the peptide sequence in the range of 1.8 to 8 nm. The time traces provide accurate distance measurements for all the ruler series, showing deep-envelope modulations at frequencies varying in a progressive way according to the increasing distance between the spin labels. The distance analysis highlights the stiffness of the peptide bridge, connecting the porphyrin and nitroxide spin labels, which is an important requisite for a molecular ruler designed to test the accuracy and practical limits of the triplet-state labeling strategy. The accuracy is assessed by comparing the PELDOR spin-spin distances with theoretical predictions. There is excellent agreement in the overall range of distances, up to the limit of 8 nm. The close correspondence between the computed and the experimentally measured distances reinforces the potentiality of the novel spin label as a reliable tool for establishing the structure and conformation of biological macromolecular assemblies. A corresponding Cu(II)-porphyrin-based system has also been investigated in order to estimate the performance of the triplet-state spin label compared to conventional  $S = 1/2$  systems. We have demonstrated

that accuracy is accompanied by high sensitivity due the spin polarization of the photoexcited triplet state.

The influence of the anisotropy of the triplet state ZFS tensor on the dipolar spectra and the effect of the spin distribution on the porphyrin system, bearing an extended  $\pi$ -conjugation, have been analyzed proving that orientation selection is not effective and the point-dipole model is still valid for the porphyrin triplet state. The effects arising from the higher dimensionality of the spin system have also been considered. The analytical expression for the echo modulation due to the dipole-dipole interaction of a  $S=1$  paramagnetic center with a  $S=1/2$  center in the four-pulse PELDOR experiment shows a cosine dependence on the dipolar frequency, analogous to that for the conventional  $S=1/2-S=1/2$  case.<sup>[56]</sup> These properties all together allow a straightforward data analysis and make the porphyrin in the triplet state an attractive spin label for high sensitivity distance measurements in biomolecules. Combined with the possibility of an accurate prediction of the distances by modeling, this new approach presents an outstanding tool for establishing the structure and conformation of biological macromolecular assemblies.

Porphyrin centers occur in different classes of proteins: photosynthetic proteins, with the chlorophyll chromophores and heme proteins, in which the heme group can be Zn-substituted in order to populate the Zn(II) protoporphyrin IX triplet state. The methodology will be extended from the peptide model system to paradigmatic proteins, for which the porphyrin derivative probe is endogenously bound, to prove that this labeling approach has a high potential for measuring nanometer distances in more complex biological systems.

### Acknowledgements

The authors thank A.M. Bowen, C.E. Tait, and C.R. Timmel for helpful discussions on orientationally selective PELDOR. We are also grateful to B. Biondi and F. Biscaglia for mass analysis and to R. Schiesari for IR spectra. Financial support from the University of Padova (PRAT 2014-CPDA145097/14) and Cariparo Foundation (M3PC project) is gratefully acknowledged. The calculations were carried out on Eurora (CINECA: Casalecchio di Reno, Italy) thanks to the ISCR Grant IDEAS 2 (PI: Laura Orian) and on the C3P clusters (Dipartimento di Scienze Chimiche, Università di Padova).

**Keywords:** DEER/PELDOR · distance ruler · EPR · ONIOM calculations · peptides · porphyrins

- [1] O. Schiemann, T. F. Prisner, *Q. Rev. Biophys.* **2007**, *40*, 1–53.
- [2] G. Jeschke, Y. Polyhach, *Phys. Chem. Chem. Phys.* **2007**, *9*, 1895–1910.
- [3] Y. D. Tsvetkov, A. D. Milov, A. G. Maryasov, *Russ. Chem. Rev.* **2008**, *77*, 487–520.
- [4] S. K. Misra, J. H. Freed, in *Multifrequency Electron Paramagnetic Resonance: Theory and Applications* (Ed.: S. K. Misra), Wiley-VCH, Weinheim, **2011**, 545–588.
- [5] G. Jeschke, *Annu. Rev. Phys. Chem.* **2012**, *63*, 419–446.
- [6] A. J. Fielding, M. G. Concilio, G. Heaven, M. A. Hollas, *Molecules* **2014**, *19*, 16998–17025.
- [7] J. P. Klare, H. J. Steinhoff, *Photosynth. Res.* **2009**, *102*, 377–390.
- [8] M. Ji, S. Ruthstein, S. Saxena, *Acc. Chem. Res.* **2014**, *47*, 688–695.
- [9] E. Narr, A. Godt, G. Jeschke, *Angew. Chem. Int. Ed.* **2002**, *41*, 3907–3910; *Angew. Chem.* **2002**, *114*, 4063–4066.
- [10] I. M. C. van Amsterdam, M. Ubbink, G. W. Canters, M. Huber, *Angew. Chem. Int. Ed.* **2003**, *42*, 62–64; *Angew. Chem.* **2003**, *115*, 64–67.
- [11] C. W. M. Kay, H. E. Mkami, R. Cammack, R. W. Evans, *J. Am. Chem. Soc.* **2007**, *129*, 4868–4869.
- [12] B. E. Bode, J. Plackmeyer, T. F. Prisner, O. J. Schiemann, *Phys. Chem. A* **2008**, *112*, 5064–5073.
- [13] J. E. Lovett, A. M. Bowen, C. R. Timmel, M. W. Jones, J. R. Dilworth, D. Caprotti, S. G. Bell, L. L. Wong, J. Harmer, *Phys. Chem. Chem. Phys.* **2009**, *11*, 6840–6848.
- [14] A. M. Bowen, M. W. Jones, J. E. Lovett, T. G. Gaule, M. J. McPherson, J. R. Dilworth, C. R. Timmel, J. R. Harmer, *Phys. Chem. Chem. Phys.* **2016**, *18*, 5981–5994.
- [15] C. Elsässer, M. Brecht, R. Bittl, *J. Am. Chem. Soc.* **2002**, *124*, 12606–12611.
- [16] M. Asada, H. Nagashima, F. H. M. Koua, J. R. Shen, A. Kawamori, H. Mino, *Biochim. Biophys. Acta Bioenerg.* **2013**, *1827*, 438–445.
- [17] R. Ward, A. Bowman, E. Sozudogru, H. El-Mkami, T. Owen-Hughes, D. G. Norman, *J. Magn. Reson.* **2010**, *207*, 164–167.
- [18] P. E. Spindler, S. J. Glaser, T. E. Skinner, T. F. Prisner, *Angew. Chem. Int. Ed.* **2013**, *52*, 3425–3429; *Angew. Chem.* **2013**, *125*, 3509–3513.
- [19] D. Goldfarb, *Phys. Chem. Chem. Phys.* **2014**, *16*, 9685–9699.
- [20] L. Garbuio, E. Bordignon, E. K. Brooks, W. L. Hubbell, G. Jeschke, M. Yulikov, *J. Phys. Chem. B* **2013**, *117*, 3145–3153.
- [21] P. Lueders, H. Ja, M. A. Hemminga, G. Jeschke, M. Yulikov, *J. Phys. Chem. B* **2013**, *117*, 2061–2068.
- [22] I. Kaminker, I. Tkach, N. Manukovsky, T. Huber, H. Yagi, G. Otting, M. Beninati, D. Goldfarb, *J. Magn. Reson.* **2013**, *227*, 66–71.
- [23] M. Di Valentin, M. Albertini, E. Zurlo, M. Gobbo, D. Carbonera, *J. Am. Chem. Soc.* **2014**, *136*, 6582–6585.
- [24] W. Lubitz, F. Lendzian, R. Bittl, *Acc. Chem. Res.* **2002**, *35*, 313–320.
- [25] C. W. M. Kay, M. Di Valentin, K. Möbius, *Sol. Energy Mater. Sol. Cells* **1995**, *38*, 111–118.
- [26] J. H. van der Waals, W. G. van Dorp, T. J. Schaafsma, *Electron Spin Resonance of Porphyrin Excited States, Vol. IV*, Academic Press, New York, **1979**, pp. 257–312.
- [27] M. Di Valentin, F. Biasibetti, S. Ceola, D. Carbonera, *J. Phys. Chem. B* **2009**, *113*, 13071–13078.
- [28] M. Di Valentin, E. Salvadori, G. Agostini, F. Biasibetti, S. Ceola, R. Hiller, G. M. Giacometti, D. Carbonera, *Biochim. Biophys. Acta Bioenerg.* **2010**, *1797*, 1759–1767.
- [29] D. Ferrari, M. Di Valentin, D. Carbonera, A. Merli, Z. W. Chen, F. S. Mathews, V. L. Davidson, G. L. Rossi, *J. Biol. Inorg. Chem.* **2004**, *9*, 231–237.
- [30] C. Toniolo, M. Crisma, F. Formaggio, C. Peggion, *Biopolymers* **2001**, *60*, 396–419.
- [31] L. G. Rowan, E. L. Hahn, W. B. Mims, *Phys. Rev. A* **1965**, *137*, A61–A71.
- [32] W. B. Mims, *Phys. Rev. B* **1972**, *5*, 2409–2419.
- [33] Y. E. Kandashkin, A. van der Est, *Appl. Magn. Reson.* **2014**, *45*, 217–237.
- [34] Gaussian 09, Revision B.01, M. J. Frisch, G. W. Trucks, H. B. Schlegel, G. E. Scuseria, M. A. Robb, J. R. Cheeseman, G. Scalmani, V. Barone, B. Mennucci, G. A. Petersson, H. Nakatsuji, M. Caricato, X. Li, H. P. Hratchian, A. F. Izmaylov, J. Bloino, G. Zheng, J. L. Sonnenberg, M. Hada, M. Ehara, K. Toyota, R. Fukuda, J. Hasegawa, M. Ishida, T. Nakajima, Y. Honda, O. Kitao, H. Nakai, T. Vreven, J. A. Montgomery Jr., J. E. Peralta, F. Ogliaro, M. J. Bearpark, J. Heyd, E. N. Brothers, K. N. Kudin, V. N. Staroverov, R. Kobayashi, J. Normand, K. Raghavachari, A. P. Rendell, J. C. Burant, S. S. Iyengar, J. Tomasi, M. Cossi, N. Rega, N. J. Millam, M. Klene, J. E. Knox, J. B. Cross, V. Bakken, C. Adamo, J. Jaramillo, R. Gomperts, R. E. Stratmann, O. Yazyev, A. J. Austin, R. Cammi, C. Pomelli, J. W. Ochterski, R. L. Martin, K. Morokuma, V. G. Zakrzewski, G. A. Voth, P. Salvador, J. J. Dannenberg, S. Dapprich, A. D. Daniels, Ö. Farkas, J. B. Foresman, J. V. Ortiz, J. Cioslowski, D. J. Fox, Wallingford, CT, USA, **2010**.
- [35] F. H. Allen, *Acta Crystallogr. Sect. B* **2002**, *58*, 380–388.
- [36] J. P. Perdew, K. Burke, Y. Wang, *Phys. Rev. B* **1996**, *54*, 16533–19539.
- [37] J. P. Perdew, K. Burke, M. Ernzerhof, *Phys. Rev. Lett.* **1997**, *78*, 1396–1396.
- [38] C. Adamo, V. Barone, *J. Chem. Phys.* **1999**, *110*, 6158–6170.



- [39] L. W. Chung, W. M. C. Sameera, R. Ramozzi, A. J. Page, M. Hatanaka, G. P. Petrova, T. V. Harris, X. Li, Z. F. Ke, F. Y. Liu, H. B. Li, L. N. Ding, K. Morokuma, *Chem. Rev.* **2015**, *115*, 5678–5796.
- [40] J. J. P. Stewart, *J. Comput. Chem.* **1989**, *10*, 209–220.
- [41] J. J. P. Stewart, *J. Comput. Chem.* **1989**, *10*, 221–264.
- [42] J. J. P. Stewart, *J. Comput. Chem.* **1991**, *12*, 320–341.
- [43] J. J. P. Stewart, *J. Mol. Model.* **2004**, *10*, 155–164.
- [44] G. Jeschke, V. Chechik, P. Ionita, A. Godt, H. Zimmermann, J. Banham, C. R. Timmel, D. Hilger, H. Jung, *Appl. Magn. Reson.* **2006**, *30*, 473–498.
- [45] S. Stoll, A. Schweiger, *J. Magn. Reson.* **2006**, *178*, 42–55.
- [46] M. Gobbo, E. Merli, B. Biondi, S. Oancea, A. Toffoletti, F. Formaggio, C. Toniolo, *J. Pept. Sci.* **2012**, *18*, 37–44.
- [47] J. W. Buchler, in *The Porphyrins, Vol. 1* (Ed.: D. Dolphin), Academic Press, New York, **1978–1979**, pp. 1–588.
- [48] V. Hamacher, J. Wrachtrup, B. von Maltzan, M. Plato, K. Möbius, *Appl. Magn. Reson.* **1993**, *4*, 297–319.
- [49] T. G. Brown, B. M. Hoffman, *Mol. Phys.* **1980**, *39*, 1073–1109.
- [50] M. Ubbink, J. A. R. Worrall, G. W. Canters, E. J. J. Groenen, M. Huber, *Annu. Rev. Bioph. Biom.* **2002**, *31*, 393–422.
- [51] C. E. Tait, P. Neuhaus, H. L. Anderson, C. R. Timmel, *J. Am. Chem. Soc.* **2015**, *137*, 6670–6679.
- [52] B. E. Bode, J. Plackmeyer, M. Bolte, T. F. Prisner, O. Schiemann, *J. Organomet. Chem.* **2009**, *694*, 1172–1179.
- [53] G. Jeschke, G. Panek, A. Godt, A. Bender, H. Paulsen, *Appl. Magn. Reson.* **2004**, *26*, 223–244.
- [54] J. Wilhelm, E. Frey, *Phys. Rev. Lett.* **1996**, *77*, 2581–2584.
- [55] S. Pornsuwan, G. Bird, C. E. Schafmeister, S. Saxena, *J. Am. Chem. Soc.* **2006**, *128*, 3876–3877.
- [56] A. Schweiger, G. Jeschke, *Principles of Pulse Electron Paramagnetic Resonance*, Oxford University Press, Oxford, **2001**, pp. 406–425.

Received: August 1, 2016



CHAPTER | **5**

**Light-Induced DEER Spectroscopy in  
Peridinin-Chlorophyll *a*-Protein**





Contents lists available at ScienceDirect

Biochimica et Biophysica Acta

journal homepage: [www.elsevier.com/locate/bbambio](http://www.elsevier.com/locate/bbambio)

## Distance measurements in peridinin-chlorophyll *a*-protein by light-induced PELDOR spectroscopy. Analysis of triplet state localization



Marilena Di Valentin<sup>a</sup>, Maria Giulia Dal Farra<sup>a</sup>, Laura Galazzo<sup>a</sup>, Marco Albertini<sup>a</sup>, Tim Schulte<sup>b,1</sup>, Eckhard Hofmann<sup>b</sup>, Donatella Carbonera<sup>a,\*</sup>

<sup>a</sup> Dipartimento di Scienze Chimiche, Università di Padova, via Marzolo 1, 35131 Padova, Italy

<sup>b</sup> Biophysics, Department of Biology and Biotechnology, Ruhr-University Bochum, D-44780 Bochum, Germany

### ARTICLE INFO

#### Article history:

Received 18 July 2016

Received in revised form 14 September 2016

Accepted 17 September 2016

Available online 20 September 2016

#### Keywords:

PCP

Peridinin

Carotenoid

Triplet state

Pulse EPR

PELDOR

### ABSTRACT

Triplet-triplet energy transfer from chlorophylls to carotenoids is the mechanism underlying the photoprotective role played by carotenoids in many light harvesting complexes, during photosynthesis. The peridinin-chlorophyll-*a* protein (PCP) is a water-soluble light harvesting protein of the dinoflagellate *Amphidinium carterae*, employing peridinin as the main carotenoid to fulfil this function.

The dipolar coupling of the triplet state of peridinin, populated under light excitation in isolated PCP, to the MTSSL nitroxide, introduced in the protein by site-directed mutagenesis followed by spin labeling, has been measured by Pulse Electron-electron Double Resonance (PELDOR) spectroscopy. The triplet-nitroxide distance derived by this kind of experiments, performed for the first time in a protein system, allowed the assignment of the triplet state to a specific peridinin molecule belonging to the pigment cluster. The analysis strongly suggests that this peridinin is the one in close contact with the water ligand to the chlorophyll *a*, thus supporting previous evidences based on ENDOR and time resolved-EPR.

© 2016 Published by Elsevier B.V.

### 1. Introduction

Carotenoids (Car) are found in light-harvesting complexes and reaction centers of natural photosystems where they act as both light-harvesting pigments and photoprotective agents. Their role as antenna pigments is fulfilled by absorbing light in the blue-green region, where chlorophylls (Chl) and bacteriochlorophylls (BChl) absorb weakly, and by delivering excitation energy to (B)Chl pigments. Moreover, Car play an important photoprotective role under high light conditions, by quenching (B)Chl triplet states via triplet-triplet energy transfer [1], thus preventing the formation of singlet oxygen, a potentially harmful oxidizing species.

Antenna complexes exhibit large structural and spectral variability, depending on the photosynthetic organisms. Marine algae possess an efficient light-harvesting system optimized for light-harvesting capacity especially in the blue-green spectral region because water functions as a filter of light in the red. Peridinin-chlorophyll-*a* proteins (PCP) are

water-soluble light harvesting proteins of dinoflagellates, which belong to the group of marine eukaryotic algae and usually employ peridinin as main pigment to perform the light-harvesting function. Most PCP forms contain only peridinin and Chl *a* in a stoichiometric ratio of 4:1. The crystal structure of the main form of PCP (MFPCP) from *A. carterae* has been determined to a resolution of 2.0 Å, revealing a ship-like structure with an outer shell composed of  $\alpha$ -helices that shields the internally coordinated pigments from the outer solvent [2]. This ship-like structure is formed by two pseudo-identical subdomains, which have 58% identical residues on the primary sequence level. Each of the two subdomains harbours four peridinin molecules that are arranged around a central Chl *a* (Fig. 1). The distances between peridinins within a single domain range from 4 to 11 Å, and their conjugated regions are in van der Waals contact (3.3–3.8 Å) with the tetrapyrrole ring of Chl *a*.

A reconstitution system has been established in which the isolated pigments are refolded with the polypeptide of the amino-terminal MFPCP domain (N-MFPCP) that is heterologously produced in *E. coli* [3]. The crystal structure of refolded PCP (RFPCP) has been determined to a resolution of 1.4 Å, and revealed that two identical N-MFPCP domains assemble into a homo-dimer, that is virtually identical to the structure of native MFPCP [4].

While most of the effort has been devoted to study singlet excitation and migration within the protein, there are still open questions concerning triplet-triplet energy transfer in PCP. The subject is highly relevant since it is related to the photoprotective role played by Car in

**Abbreviations:** PCP, peridinin-chlorophyll *a* binding protein; Car, carotenoid(s); Chl, chlorophyll; ZFS, zero field splitting; EPR, electron paramagnetic resonance; TTET, triplet-triplet energy transfer; PELDOR, pulse electron double resonance.

\* Corresponding author.

E-mail address: [donatella.carbonera@unipd.it](mailto:donatella.carbonera@unipd.it) (D. Carbonera).

<sup>1</sup> Current address: Science for Life Laboratory, Department of Medicine Solna, Karolinska Institutet, and Department of Infectious Diseases, Karolinska University Hospital, Solna, SE-17176 Stockholm, Sweden.

<http://dx.doi.org/10.1016/j.bbambio.2016.09.008>  
0005-2728/© 2016 Published by Elsevier B.V.

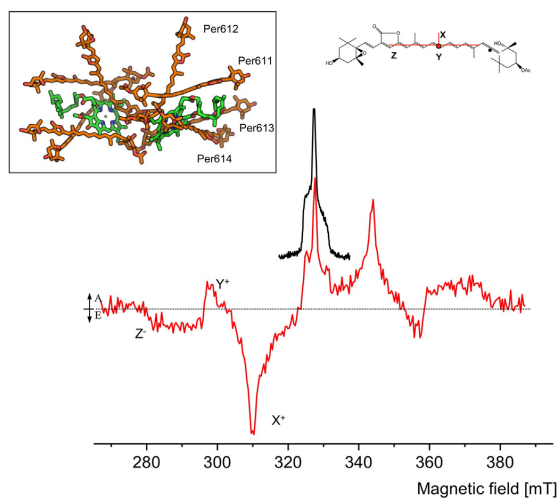


**Fig. 1.** Top: The pigment cluster structure of MFPCP from *A. carterae* (PDB: 1ppr) and scheme of the molecular structure of peridinin showing the X,Y,Z directions of ZFS axes, corresponding to the canonical field positions in the Field-swept ESE spectrum of the triplet state. Bottom: Field-swept ESE spectra of spin labeled RFPCP AOC mutant in frozen solution, detected in the dark (black) and 50 ns after laser flash (red). A = absorption, E = emission. For experimental conditions see Material and Methods.

different light-harvesting systems. When MFPCP gets photo-excited, the Chls *a* cannot transfer the excitation energy to other antenna complexes and de-excitation mainly proceeds through either fluorescence or intersystem crossing with triplet formation. Triplet states are also formed *in vivo* under excess light conditions. However, photo-protective carotenoids prevent the formation of harmful singlet oxygen by quenching these  $^1\text{Chl}$  triplet states. In the past, we have employed time-resolved and pulse electron paramagnetic resonance (EPR) techniques to study the peridinin triplet state ( $^1\text{Per}$ ) through its magnetic properties such as zero-field splitting (ZFS) parameters, electron spin polarization (ESP) and time-evolution of the ESP [5]. The ESP, shown by  $^1\text{Per}$  in the time resolved EPR spectrum detected immediately after the laser flash, is inherited from the Chl triplet ( $^1\text{Chl}$ ) according to spin angular momentum conservation taking place during triplet-triplet energy transfer [6–9], depending on the relative geometrical arrangement of the donor-acceptor couple. The concept of spin angular momentum conservation was exploited in the past to investigate the pathway of triplet transfer in isolated MFPCP [5]. During the  $^1\text{Chl}$  *a* lifetime in isolated PCP, a triplet state is formed on one of the circumferential peridinins and decays through radiationless intersystem crossing with a lifetime of about 10  $\mu\text{s}$  [10]. Starting from the relative populations of  $^1\text{Chl}$  sublevels and taking into account the relative positions among Chls and peridinins, as determined by the X-ray structure of PCP [2], the expected triplet state polarization of each of the peridinins in the complex was calculated. Comparison with the experimental data allowed suggesting that the chlorophyll-peridinin pair directly involved in the triplet-triplet energy transfer process, coincides with the one having the shortest center-to-center distance (Chl601/602 and Per614/624 according to the nomenclature used in [2] and adopted in Fig. 1 [5]).

Further information were obtained by pulse EPR and electron nuclear double resonance (ENDOR) spectroscopies combined with theoretical calculations, which provided details concerning the electronic structure of the excited triplet state in PCP, strongly supporting the localization of the triplet state on one specific peridinin [11]. In the backbone of  $^1\text{Per614}$ , a high spin density was found at the carbon atom position which is in close contact with the water ligand to Chl *a*. This result suggested that the water ligand may work as a super-exchange bridge in the triplet-triplet energy transfer [11–13].

Other groups applied time-resolved step-scan FTIR difference spectroscopy to investigate triplet formation in MFPCP from *A. carterae* [14–16]. The spectral analysis of the 298 K FTIR spectra obtained from MFPCP revealed two components with different decay kinetics, leading to the conclusion that two different  $^1\text{Per}$  are produced [14]. Moreover, beside signals arising from  $^1\text{Per}$ , also putative bands reflecting the presence of  $^1\text{Chl}$  *a* were identified implying that in PCP there is a significant involvement of Chl *a* in triplet delocalization [14]. The fact that the time-resolved FTIR difference spectra depend on the excitation wavelength of the triggering laser flash suggested the hypothesis that  $^1\text{Per}$  formation can proceed via different pathways [14,16]. On the other hand step-scan FTIR spectra recorded at 100 K indicated that, at low temperature, just one Per conformer is involved in triplet formation [15]. Thus, while the IR results, suggest a shared triplet state between Chl and Per, the above mentioned data obtained by advanced EPR techniques point towards a localization of the triplet state in Per614(624). These discrepancies are still under discussion, although, Mezzetti and Spezia suggested that some spectral features in the step-scan FTIR spectra from MFPCP from *A. carterae* may be due to a photo-thermal effect caused by too high laser power conditions [12,14,15].

In order to work towards clarification of the problem of triplet assignment and (de)localization in PCP, we have applied a new approach, that is based on Pulse Electron-Electron Double Resonance (PELDOR) measurements. PELDOR is a well-established technique for measuring nanometer distances in spin-labeled systems [17–21]. Conventionally, PELDOR is performed on proteins, measuring distances between couple of nitroxide spin labels, introduced in the system by site directed spin labeling. In a recent work, on a model system, we have shown that PELDOR can be used also to measure distances between a photoexcited triplet state and a nitroxide radical [22]. Due to the sensitivity acquired from the spin polarization of the photoexcited triplet state spectrum the method can be applied also in complex biological systems. Thus, in this work we applied the technique for the first time in a protein system, to measure the distance between the triplet populated under photoexcitation in isolated PCP and a nitroxide suitably introduced in the protein by site directed spin labeling.

## 2. Materials and methods

### 2.1. Mutagenesis, protein expression, and purification

RFPCP has an additional Alanine residue at the amino-terminus (Ala-0) compared to native N-MFPCP. This additional Alanine residue was mutated to Cysteine using QuikChange site-directed mutagenesis kit (Stratagene). The proteins were expressed heterologously in *Escherichia coli* JM109, purified and reconstituted with pigments, as previously described [4]. However, the final size exclusion step was skipped, since the purity of the reconstituted protein obtained from the anion exchange step is sufficient for spectral analysis. For all experiments, RFPCP was dissolved in 5 mM Tricine, 2 mM MgCl, pH 7.6. Prior labeling, the functional availability of the thiol group was assessed using thiol-biotinylation (Biotin-HPDP (Thermo Scientific)) of AOC-RFPCP and subsequent binding to Streptavidin agarose beads (Novagen).

### 2.2. Labeling

Labeling of AOC-RFPCP, used for EPR experiments, was obtained by adding a fivefold molar excess of MTSSL (SIGMA, dissolved in DMSO) to the purified protein at a homodimer concentration of 50  $\mu\text{M}$  and incubating the protein overnight in the dark at 4  $^{\circ}\text{C}$ . The sample was then concentrated and exchanged five times with deuterated buffer by centrifugal filters; this procedure was also useful to remove the excess of non-ligated spin label. The introduction of the nitroxide led to an estimated yield >90% of doubly labeled dimers at the zero position of each monomer. Oxygen was removed from the samples by flushing argon in the EPR tube before freezing. Deuterated glycerol (60% v/v)

was added before freezing. The final concentration of labeled protein was 150  $\mu\text{M}$ .

### 2.3. Pulse EPR and PELDOR measurements

Pulse EPR and PELDOR were performed on a Bruker Elexsys E580 pulse EPR spectrometer equipped with a Bruker ER4118X-MS3 splitting PELDOR resonator. Laser excitation at 532 nm (10 mJ per pulse and repetition rate of 10 Hz) was provided by the second harmonic of a Nd:YAG laser (Quantel Brilliant) in the optically transparent resonator.

Field-swept electron spin echo (ESE) spectra of the triplet state were recorded using a 2-pulse (flash-DAF- $\pi/2$ - $\tau$ - $\pi$ - $\tau$ -echo) ESE sequence with a DAF of 50 ns, between the laser flash and the first microwave (MW) pulse. The  $\pi/2$ -pulse was of 16 ns and the delay  $\tau$  was set at 200 ns.

Conventional PELDOR experiments to measure intra-dimer nitroxide-nitroxide dipolar interaction (NO-NO PELDOR) were done at a temperature of 50 K. A standard four-pulse sequence was applied; the microwave power was adjusted to obtain an observer sequence of 16/32/32 ns and a pump pulse of 16 ns. The difference between the pump and observer frequency was set to 70 MHz. Pump frequency, 9.21 GHz; observer frequency, 9.28 GHz; center of the resonator (with the sample), 9.21 GHz. A two-step phase cycle was applied for baseline correction while deuterium nuclear modulations were suppressed varying the tau value in an eight-step cycle starting from a value of 180 ns and using a 56 ns step.

The PELDOR experiments under laser excitation to measure the dipolar interaction between the nitroxide and photoexcited triplet state (triplet-NO PELDOR), were performed at 20 K. The pulse sequence, mentioned above, was preceded, in this case, by a laser pulse, with a delay after the flash (DAF) of 50 ns. The difference between the pump (nitroxide) and observer (peridinin triplet state) frequency was set to 500 MHz. Pump frequency, 9.21 GHz; observer frequency, 9.71 GHz; center of the resonator (with the sample), 9.21 GHz. Data were collected for 24 h.

### 2.4. Spectral analysis

The crystallographic structure used for all the simulations is the homodimer of the RFP (PDB: 3IIS) that, compared to the native protein, has an extra alanine residue at the N-ter of the sequence (0 position). The structure of the spin labeled protein was created by using the program MMM2013 (Multiscale Modelling of Macromolecular Systems) [23] which allows also to calculate the set of possible rotamers of the spin label, with the relative populations, within the protein. MMM2013 has also been employed for the prediction of the nitroxide-nitroxide distance distribution.

The simulations of the light-induced time domain triplet-NO PELDOR traces were carried out by considering the dipolar interaction between  $^1\text{Per}$  on one monomer (single excitations only, i.e. one triplet state excited in a protein dimer) and each of the two symmetry related nitroxides of the dimer, in a way that the final trace results as the sum of the two dipolar interactions (neglecting multiple spins effect). All the nitroxide rotamers, computed by MMM2013 were taken into account with their proper weight. Simulations were performed with a home-written routine, implemented in MATLAB, based on the analytical form of the Echo modulation in the four-pulse PELDOR experiment, for a weakly coupled triplet-radical pair spin system, as derived by Di Valentin et al. and described in detail elsewhere [24]. The simulation routine calculates the dipolar frequency between the triplet state and the radical spin system (and the corresponding time trace), taking into account the effects of spin delocalization on the carotenoid moiety. The spin distribution of the carotenoid triplet state used in the calculations was that derived before by DFT and validated on the basis of the good agreement of the calculated hyperfine couplings with the ones measured by ENDOR in PCP [11]. The frequency of the dipolar interaction, depending on the interspin distance and the angle between the interspin vector and the

direction of the external magnetic field  $B_0$ , refers to each spin-bearing atom of the molecule(s) carrying the triplet state. Concerning the nitroxide radical, the unpaired electron is localized in the midpoint of the N—O bond of the nitroxide moiety.

Only the secular term of the dipole Hamiltonian was considered in the condition that the difference of the Larmor frequencies of the two spins is much larger than the weak dipolar coupling. The Heisenberg exchange coupling was neglected as our system involves localized spins separated by  $r > 15 \text{ \AA}$ .

The input parameters needed for the calculations are:

- (i) The structure of the spin labeled protein;
- (ii) The spin density of the peridinin in its triplet state [25].

The PELDOR powder pattern is calculated by a uniform sampling of the magnetic field orientations in the unit sphere. The set of angles  $\theta$  and  $\varphi$  for this average is taken from a spherical grid computed by the *EasySpin* function *sphgrid* [26]. The full set of nitroxide rotamers, generated by MMM2013, has been considered in the simulation, summing the simulated traces over the conformation distribution. The frequency spectra were obtained by Fourier Transform of the calculated time domain traces, after apodization.

## 3. Results

The field-swept ESE spectra of the spin labeled A0C-RFPCP mutant detected in the dark corresponds to a typical field-swept ESE nitroxide spectrum, as expected because of the presence of the MTSSL spin probe (Fig. 1).

The spectrum recorded immediately after the light pulse is composed of two contributions: a) a component due to the  $^1\text{Per}$ , characterized by a *eaeaea* spin polarization pattern and ZFS parameters  $|D| = 449.7 \times 10^{-4} \text{ cm}^{-1}$ ,  $|E| = 43.9 \times 10^{-4} \text{ cm}^{-1}$ , in agreement with previously reported triplet-state EPR data on PCP proteins [5]; b) the nitroxide component detected also in the dark spectrum (Fig. 1). The  $^1\text{Per}$  spin polarization pattern is inherited from  $^1\text{Chl } a$  donor during triplet-triplet energy transfer, as extensively discussed in Ref. [5]. The Z axis of the ZFS tensor corresponds to the long molecular direction of peridinin, the X axis is along the C—H bonds in the conjugated chain and the Y axis is perpendicular to the conjugated XZ molecular plane (scheme in Fig. 1) [11]. The magnetic field positions corresponding to the canonical directions are indicated in the spectrum.

The time domain NO-NO PELDOR trace detected in the dark (after background correction) and the corresponding dipolar frequency spectrum are shown in Fig. 2. Tikhonov-derived distance distribution, obtained by DeerAnalysis2013 [27] provides a maximum peak at a distance of about 42  $\text{\AA}$  (Fig. 2B), which is in good agreement with the estimated intra-dimer nitroxide-nitroxide distance, based on the crystal structure of RFP (Fig. 2). Moreover, the distance distribution reflects the large number of conformations predicted by the MMM simulation [24], since the spin probe is characterized by a certain conformational freedom due to the ligation at the N-ter of the protein. The distance distribution predicted by MMM (see Supplementary information) is in good general agreement with the experimental one reported in Fig. 2B, although the latter results to be broader.

The triplet-NO PELDOR results obtained under photoexcitation are shown in Fig. 3. In this kind of experiment the laser pulse populates the  $^1\text{Per}$  and the dipolar triplet-doublet interaction is then measured, as modulation of the echo intensity generated by the observer pulse sequence.

The four-pulse sequence is performed by applying the pump pulse at the maximum of the nitroxide spectrum in order to optimize the pump efficiency, while applying the observer sequence in correspondence to the most intense emissive X canonical transition of the polarized  $^1\text{Per}$  spectrum. After removal of the background decay from the envelope

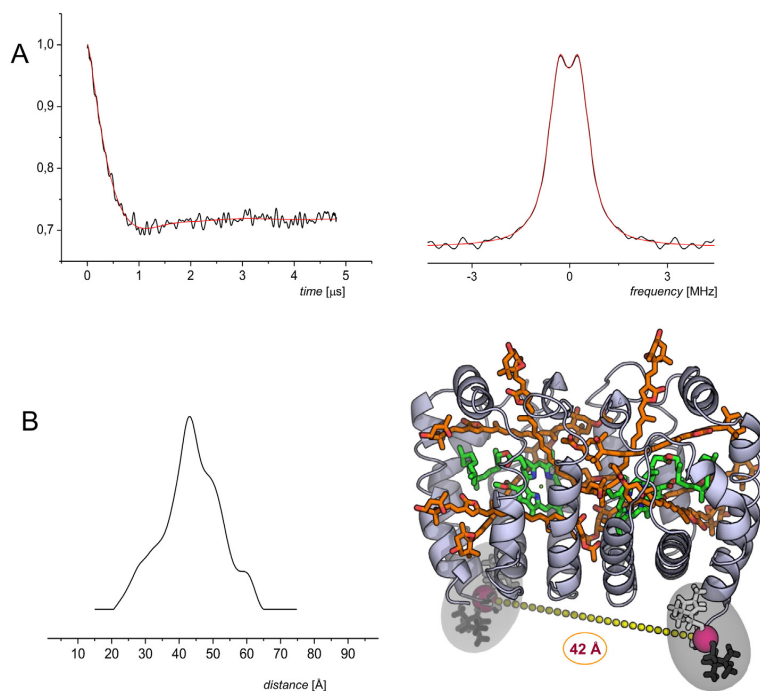


**Fig. 2.** A) Background-subtracted NO-NO PELDOR trace of spin labeled RFPCP AOC mutant detected in the dark at 50 K (left, black), and dipolar spectrum after Fourier transformation (right, black), with a corresponding model-free Tikhonov fitting obtained by DeerAnalysis2013, with the regularization parameter  $\alpha = 100$  (red). For experimental conditions see Material and Methods. B) Distance distribution obtained by DeerAnalysis2013 and graphical representation of some representative MTSSL conformers MMM-generated using the crystal structure of the protein.

modulation, the triplet-NO PELDOR time trace reveals clear dipolar modulations. The background was subtracted using an exponential (3d) background correction in DeerAnalysis2016 (the PELDOR traces before and after different background corrections are reported in Fig. S2 of Supplementary Data). In Fig. 3 the PELDOR trace reported is that resulting from a background correction fitted in the more extended time interval starting from 248 ns.

Fourier transformation of the signal provides the frequency spectrum. Although some orientation selection due to the broad triplet spectrum was expected, the frequency spectrum, seems to have a Pake pattern shape. This likely derives from the fact that the measurements were performed at the X canonical position of the triplet state, for which the orientation selection is expected to be relatively small.

The DeerAnalysis software was developed for doublet-doublet interacting spin systems assuming point dipole interactions. However, the triplet-doublet interaction in the spin-labeled AOC-RFPCP system comprises a delocalized spin density in the carotenoid triplet state. Therefore, we have developed a novel program for the spectral analysis, which is described in detail in Materials and methods. The theoretical time traces and frequency spectra were calculated for each single peridinin of the pigment cluster and compared to the experimental ones. Although the signal to noise ratio of the experimental traces is low, a satisfactory agreement is unambiguously found only for Per614 (Fig. 4).

#### 4. Discussion

It is well known that in isolated PCP proteins,  $^1\text{Chl}$ s populated by photoexcitation via ISC, are quenched by peridinins with an efficiency of  $\sim 100\%$  [4]. Recently Z. Kvíčalová et al. [28] showed that  $^1\text{Per}$  is formed with the same intrinsic  $\sim 5$  ns lifetime of  $^1\text{Chl}$ . A kinetic model indicated

that triplet-triplet transfer time is expected to be 0.1 ns or even faster in this system, preventing any accumulation of  $^1\text{Chl}$ . This is in agreement with the results reported in Fig. 1, showing the absence of features due to  $^1\text{Chl}$  in the pulse EPR spectrum detected 50 ns after the laser flash. As already mentioned, a different model according which the photoexcited triplet state is partially delocalized over the Chl *a* molecule leading, to the mixing of  $^1\text{Chl}$  character in  $^1\text{Per}$ , was proposed by Alexandre et al. to interpret step-scan Fourier transform infrared spectroscopy data on PCP from *A. carterae* [14]. The effect was quantified in terms of 25% and 40% contribution of Chl in triplet sharing, in MFPCP and in the high salt form PCP (HSPCP) respectively [29]. HSPCP is a minor component isolated from *A. carterae*, which is eluted from an anion exchange column at high-salt concentration. This form presents 31% identity in amino acid sequence with MFPCP. It contains only six peridinins and two Chl *a* molecules. It was found that HSPCP and MFPCP share most of the properties relatively to the triplet formation pathway and to the triplet localization in specific peridinins [30]. The comparison of triplet ENDOR spectra of MFPCP and HSPCP did not support the conclusion on a 25%/40% contribution of Chl in triplet sharing in the two different proteins, since a decrease of all the measured  $^1\text{Per}$  hyperfine constants in HSPCP, as expected for a higher level of triplet sharing, was not observed [30]. Moreover, DFT calculations of the electronic structure of the triplet states in PCP, ruled out the possibility of a Per-Chl *a* delocalization because of the large difference in the triplet state energy of the two pigments [11].

Since it was suggested that the delocalization of the triplet on the Chl molecule may have a physiological important role in dragging the energy of the shared triplet below that of singlet oxygen, with a resultant decrease in the probability of production of singlet oxygen, we used PELDOR spectroscopy to gain additional information. The experiments allow measuring the distance between the photo-excited triplet state



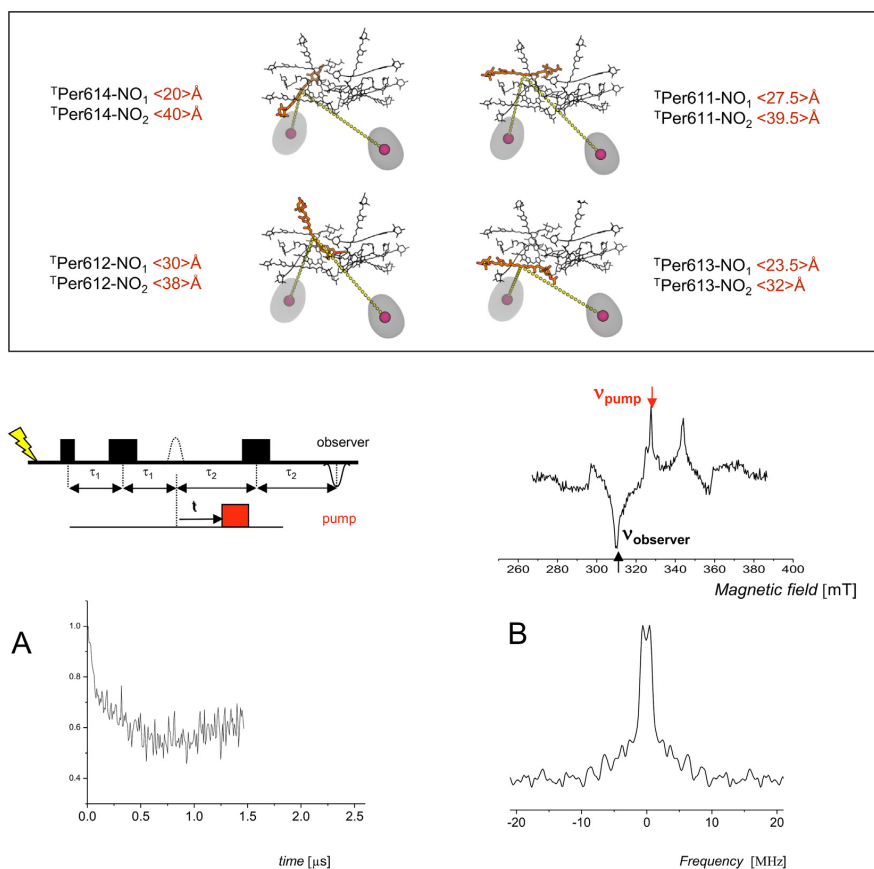


**Fig. 3. Top:** Center-to-center mean distances between each peridinin and the nitroxide labels in the dimer of the RFPCP AOC mutant, as calculated from the crystal structure remodelled with the MMM-generated MTSSL conformers (represented by the grey clouds). **Bottom:** Pulse sequence for the 4-pulse triplet-NO PELDOR experiment recorded under photoexcitation, and corresponding field-swept ESE spectrum showing the pump (nitroxide) and observer (triplet state) field positions. For experimental details see [Material and methods](#). (A) PELDOR trace after background removal and (B) Fourier transform of the time domain trace after background removal.

and a spin probe (nitroxide). This, together with crystallographic information and data analysis may help to get insight into the nature of the triplet state in PCP.

The position of the MTSSL spin label in the protein was chosen such that distances between the nitroxide and each of the peridinin molecules inside a protein monomer were sufficiently different from each other to be discriminated in the experiment, and also fell in a distance range (20–40 Å) that assures high sensitivity for PELDOR experiments. Spin labeling of a Cysteine at the amino-terminus of AOC-RFPCP resulted in theoretical nitroxide-Per center-to-center mean distances of 20 Å, 23.4 Å, 27.5 Å and 30 Å for Per-614, Per-613, Per-611 and Per-612, respectively.

Our NO-NO PELDOR experiments conducted in the dark show that the refolded protein, adopts a dimeric structure in solution, in line with the available crystal structural data of RFPCP. The direct comparison of the resolved X-ray structure of RFPCP and MFPCP showed that they are identical in terms of pigment arrangement [4]. Thus, inter-monomer distances were also expected to contribute to the triplet-NO PELDOR traces. These interspin distances are expected to contribute to the lower frequencies of the PELDOR spectrum and they resulted more difficult to be estimated with high precision since the low signal to noise ratio of the inverted echo limited the reliable detection window

to 1.5  $\mu\text{s}$ , a duration not sufficient to resolve distances in the order of 40 Å. However these signals affect the time traces and have to be included in the calculations to reach a good agreement with the experimental data.

The comparison of the experimental and calculated PELDOR traces (Fig. 4) clearly indicates that only Per614(624) may be responsible for the observed sharp initial drop of the PELDOR time trace, due to its shortest intra-monomer distance (20 Å) to the nitroxide in the cluster. It is interesting to note that the PELDOR results rule out a possible involvement of Per612 in the triplet-triplet energy transfer pathway of PCP. Per612 gives an expected polarization pattern of the time-resolved EPR spectrum, which is very similar to that of Per614 [5]. Its role in Chl triplet quenching was considered to be negligible before only for analogy with HSPCP, where Per612 is missing [30].

The PELDOR results show a dominant localization of the triplet state in Per614, since adding even small contribution from other peridinin to the calculated time traces reduces the agreement between theoretical and experimental traces.

It is worth mentioning, that the PELDOR spectra derived from the triplet-nitroxide interactions were calculated under the following assumptions 1) single triplet excitation for protein dimer, 2) negligible effects deriving from multi spin interactions, 3) random distribution of

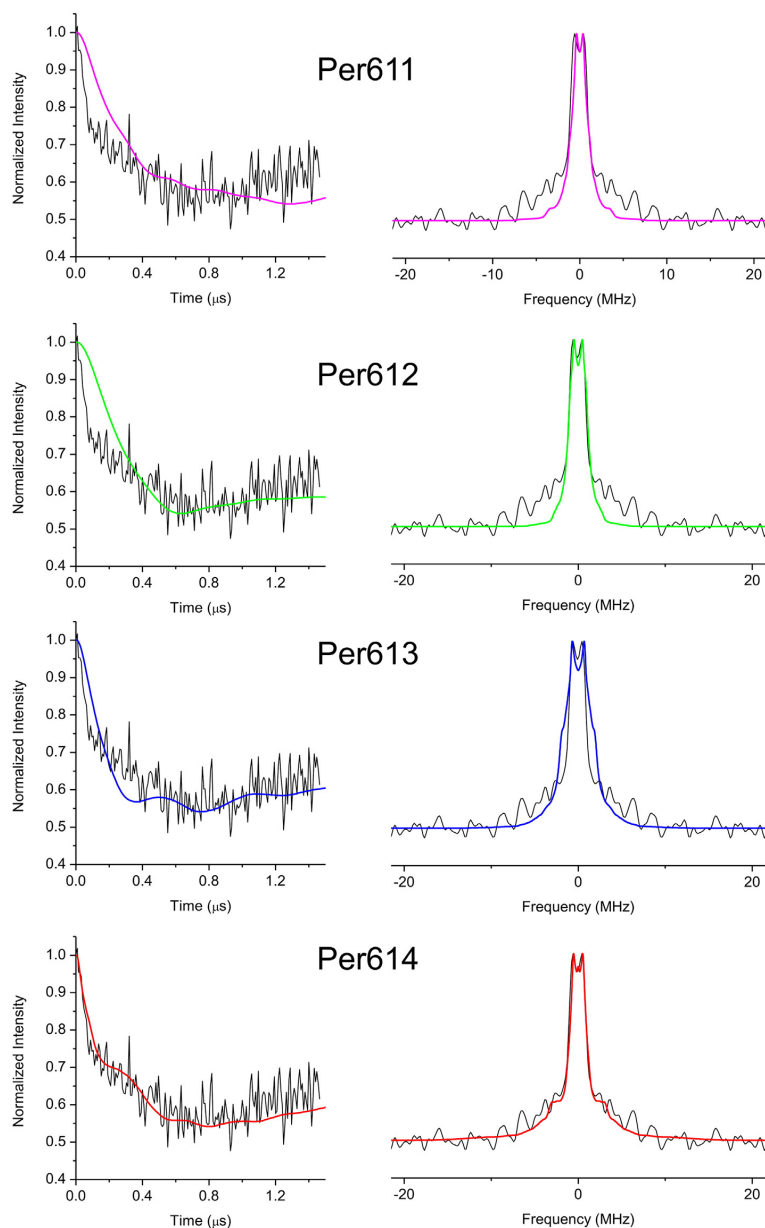


**Fig. 4.** Comparison of background-corrected experimental (black) and calculated (coloured) PELDOR time traces, and their corresponding Fourier transformed frequency spectra, for the triplet state localized on Per611 (magenta), Per612 (green), Per613 (blue) and Per614 (red) respectively. The calculations were performed as described in [Materials and methods](#).

peridinin-nitroxides distances for all conformers with respect to the magnetic field direction. However these assumptions seem appropriate, when applied to the system, for the following reasons. (1) The laser excitation power is maintained lower than the saturation level of the signal, (2) the small number of triplet-doublet dipolar interactions (two) within the dimeric protein is expected to limit the presence of possible artefacts present in multi-spin systems, and (3) the nitroxides may assume a large number of conformations, as shown by the number of MMM predicted

rotamers. In this respect, it is worth noting that, taking into account the orientation selection in the calculated spectra, the agreement with experimental data did not improve for any of the four peridinins (not shown).

Due to the extended molecular structure, the spin density distribution of the triplet state along the conjugated chain of the peridinin was taken into account. Neglecting this factor in the calculations gave a worse fitting of the experimental data. This is the reason why a home-written program was used for the calculation of the PELDOR

traces, instead of the commonly used DeerAnalysis software [27]. Actually, we observed that, the effect of introducing the spin distribution in the dipolar interaction calculation introduces some different combination of the oscillations at the different frequencies in the PELDOR traces.

Compared to the calculated ones, the experimental traces show less defined modulations. This is likely due not only to the low signal to noise ratio, but also to the restricted range of nitroxide conformations used for the calculations, as revealed by the comparison between the NO-NO PELDOR and the MMM calculated distance distribution (see Fig. S1 in Supplementary Data).

Calculations were performed also by considering a 25%–40% Chl triplet sharing. An influence in the calculated PELDOR traces appeared especially when assuming a high Chl contribution, (see Supplementary data, Fig. S3). The largest influence is found for Per611/612/613 while for Per614, due to the similar center to center distance of Per and Chl to the nitroxide, the PELDOR time trace is less affected, at least in the time interval spanned by our experiments. However, it appears that including in the calculations a 25–40% of Chl participation to the triplet delocalization decreases the agreement with the experimental time traces, in particular in the time region of the shoulder around 2.6  $\mu$ s. It is worth noting that subtraction of different backgrounds to the detected PELDOR traces while does not influence the assignment to Per614, leads on the other hand to even worse agreements of the experimental traces with those calculated by considering the Car/Chl sharing of the triplet (results are reported in Figs. S3 and S4 of Supplementary Data). In summary, although the low signal to noise ratio and the restricted time window of the detected traces of the present triplet-NO PELDOR experiments do not allow to rule out the presence of small contributions of Chl to triplet sharing in PCP, it has been demonstrated that the method is suitable to address this kind of questions.

## 5. Conclusions

In this work we exploited, for the first time in a protein system, the potentiality of PELDOR spectroscopy for measuring distances between a photoexcited triplet state and a nitroxide spin label inserted into the protein. The results corroborate our previous assessment based on time resolved EPR, pulse ENDOR and ESEEM experiments, of the central role of Per614(624) in the mechanism of chlorophyll triplet quenching in PCP proteins. As pointed out before, Per 614(624) possesses unique features among all the peridinin bound to the protein, namely the shortest center to center distance to the Chl molecule and an interfacial water molecule acting as a bridge in triplet-triplet energy transfer. Thus, Per614 has to be considered the most active carotenoid in the photoprotection process taking place in the Peridinin Chlorophyll Protein complex of *A. carterae*.

As a final remark, it is worth noting that the PELDOR method successfully applied here to measure the distance between the peridinin triplet state and a nitroxide inserted into the protein at suitable position, will open the unique possibility to identify the specific Car and/or Chl pigments involved in the triplet state formation and quenching in other light harvesting complexes of known atomic structure. This is an important starting point to find out the structural and electronic strategies adopted by the different light harvesting complexes for reaching an efficient mechanism of  $^1$ Chl deactivation.

## Transparency document

The Transparency document associated with this article can be found, in the online version.

## Acknowledgements

This work was supported by the Italian Ministry for University and Research (PRIN2010 prot.2010FM38P\_004).

## Appendix A. Supplementary data

Supplementary data to this article can be found online at <http://dx.doi.org/10.1016/j.bbabi.2016.09.008>.

## References

- [1] H.A. Frank, R.J. Cogdell, Carotenoids in photosynthesis, *Photochem. Photobiol.* 63 (1996) 257–264.
- [2] E. Hofmann, P.M. Wrench, F.P. Sharples, R.G. Hiller, W. Welte, K. Diederichs, Structural basis of light harvesting by carotenoids: peridinin-chlorophyll-protein from *Amphidinium carterae*, *Science* 272 (1996) 1788–1791.
- [3] D.J. Miller, J. Catmull, R. Puskeiler, H. Tweedale, F.P. Sharples, R.G. Hiller, Reconstitution of the peridinin-chlorophyll *a*-protein (PCP): evidence for functional flexibility in chlorophyll binding, *Photosynth. Res.* 86 (2005) 229–240.
- [4] T. Schulte, D.M. Niedzwiedzki, R.R. Birge, R.G. Hiller, T. Polivka, E. Hofmann, Identification of a single peridinin sensing Chl-*a* excitation in reconstituted PCP by crystallography and spectroscopy, *Proc. Natl. Acad. Sci. U. S. A.* 106 (2009) 20764–20769.
- [5] M. Di Valentin, S. Ceola, E. Salvadori, G. Agostini, D. Carbonera, Identification by time-resolved EPR of the peridinin directly involved in chlorophyll triplet quenching in the peridinin-chlorophyll *a*-protein from *Amphidinium carterae*, *Biochim. Biophys. Acta Bioenerg.* 777 (2008) 186–195.
- [6] D. Carbonera, M. Di Valentin, G. Agostini, G. Giacometti, P.A. Liddell, D. Gust, A.L. Moore, T.A. Moore, Energy transfer and spin polarization of the carotenoid triplet state in synthetic carotenoporphyrin dyads and in natural antenna complexes, *Appl. Magn. Reson.* 13 (1997) 487–504.
- [7] D. Carbonera, M. Di Valentin, C. Corvaja, G. Giacometti, G. Agostini, P.A. Liddell, A.L. Moore, T.A. Moore, D. Gust, Carotenoid triplet detection by time-resolved EPR spectroscopy in carotenopyropheophorbide dyads, *J. Photochem. Photobiol. A Chem.* 105 (1997) 329–335.
- [8] M.A. El-Sayed, D.E. Tinti, E.M. Yee, Conservation of spin direction and production of spin alignment in triplet-triplet energy transfer, *J. Chem. Phys.* 51 (1969) 5721–5723.
- [9] K. Akiyama, S. Terokubota, T. Ikoma, Y. Ikegami, Spin polarization conservation during intramolecular triplet-triplet energy-transfer studied by time-resolved EPR spectroscopy, *J. Am. Chem. Soc.* 116 (1994) 5324–5327.
- [10] J.A. Bautista, R.G. Hiller, F.P. Sharples, D. Gosztola, M. Wasielewski, H.A. Frank, Singlet and triplet energy transfer in the peridinin - chlorophyll *a* - protein from *Amphidinium carterae*, *J. Phys. Chem. A* 103 (1999) 2267–2273.
- [11] M. Di Valentin, S. Ceola, G. Agostini, G.M. Giacometti, A. Angerhofer, O. Crescenzi, V. Barone, D. Carbonera, Pulse ENDOR and density functional theory on the peridinin triplet state involved in the photo-protective mechanism in the peridinin-chlorophyll *a*-protein from *Amphidinium carterae*, *Biochim. Biophys. Acta Bioenerg.* 1777 (2008) 295–307.
- [12] D. Carbonera, M. Di Valentin, R. Spezia, A. Mezzetti, The unique photophysical properties of the peridinin-chlorophyll-*a*-protein, *Curr. Protein Pept. Sci.* 15 (2014) 332–350.
- [13] M. Di Valentin, E. Salvadori, V. Barone, D. Carbonera, Unravelling electronic and structural requisites of triplet-triplet energy transfer by advanced electron paramagnetic resonance and density functional theory, *Mol. Phys.* 111 (2013) 2914–293.
- [14] M.T.A. Alexandre, D.C. Luhrs, I.H.M. van Stokkum, R. Hiller, M.L. Groot, J.T.M. Kennis, R. van Grondelle, Triplet state dynamics in peridinin-chlorophyll-*a*-protein: a new pathway of photoprotection in LHCs? *Biophys. J.* 93 (2007) 2118–2128.
- [15] A. Mezzetti, R. Spezia, Time-resolved step scan FTIR spectroscopy and DFT investigation on triplet formation in peridinin-chlorophyll-*a*-protein from *Amphidinium carterae* at low temperature, *Spectrosc. Int. J.* 22 (2008) 235–250.
- [16] M. Alexandre, R. van Grondelle, Time-Resolved FTIR Difference Spectroscopy Reveals the Structure and Dynamics of Carotenoid and Chlorophyll Triplets in Photosynthetic Light-Harvesting Complexes, *Infrared Spectroscopy - Life and Biomedical Sciences* Edited by Prof. Theophanides T, InTech pen 2012, pp. 231–256.
- [17] G. Jeschke, M. Pannier, H.W. Spiess, L.J. Berliner, S.S. Eaton, G.R. Eaton (Eds.), *Distance Measurements in Biological Systems* by EPR, 19, Kluwer Academic, New York 2000, pp. 493–512.
- [18] O. Schiemann, T.F. Prisner, Long-range distance determination in biomacromolecules by EPR spectroscopy, *Q. Rev. Biophys.* 40 (2007) 1–53.
- [19] Y.D. Tsvetkov, A.D. Milov, A.G. Maryasov, Pulsed electron-electron double resonance (PELDOR) as EPR spectroscopy in nanometer range *Russ. Chem. Rev.* 77 (2008) 487–520.
- [20] G.W. Reginsson, O. Schiemann, Pulsed electron-electron double resonance: beyond nanometre distance measurements on biomacromolecules, *Biochem. J.* 434 (2011) 353–363.
- [21] G. Jeschke, DEER distance measurements on proteins, *Annu. Rev. Phys. Chem.* 63 (2012) 419–446.
- [22] M. Di Valentin, M. Albertini, E. Zurlo, M. Gobbo, D. Carbonera, Porphyrin triplet state as a potential spin label for nanometer distance measurements by PELDOR spectroscopy, *J. Am. Chem. Soc.* 136 (2014) 6582–6585.
- [23] Y. Polyhach, E. Bordignon, G. Jeschke, Rotamer libraries of spin labelled cysteines for protein studies, *Phys. Chem. Chem. Phys.* 13 (2011) 2356–2366.
- [24] M. Di Valentin, M. Albertini, M.G. Dal Farra, E. Zurlo, L. Orian, A. Polimeno, M. Gobbo, D. Carbonera, 2016 Light-induced porphyrin-based spectroscopic ruler for nanometer distance measurements, Unpublished results – submitted for publication.
- [25] M. Di Valentin, C.E. Tait, E. Salvador, L. Orian, A. Polimeno, D. Carbonera, Evidence for water-mediated triplet-triplet energy transfer in the photoprotective site of the peridinin-chlorophyll *a*-protein, *Biochim. Biophys. Acta* 1837 (2014) 85–97.
- [26] S. Stoll, A. Schweiger EasySpin, A comprehensive software package for spectral simulation and analysis in EPR, *J. Magn. Reson.* 178 (2006) 42–55.

- [27] G. Jeschke, V. Chechik, P. Ionita, A. Godt, H. Zimmermann, J. Banham, C.R. Timmel, D. Hilger, H. Jung, DeerAnalysis2006 – a comprehensive software package for analyzing pulsed ELDOR data, *Appl. Magn. Reson.* 30 (2006) 473–498.
- [28] Z. Kvíčalová, J. Alster, E. Hofmann, P. Khoroshyy, R. Litvín, D. Bina, T. Polívka, J. Pšenčík, Triplet–triplet energy transfer from chlorophylls to carotenoids in two antenna complexes from dinoflagellate *Amphidinium carterae*, *Biochim. Biophys. Acta Bioenerg.* 1857 (2016) 341–349.
- [29] A. Gall, R. Berera, M.T.A. Alexandre, A.A. Pascal, L. Bordes, M.M. Mendes-Pinto, S. Andrianambintsoa, K.V. Stoitchkova, A. Marin, L. Valkunas, P. Horton, J.T.M. Kennis, R. van Grondelle, A. Ruban, B. Robert, Molecular adaptation of photoprotection: triplet states in light-harvesting proteins, *Biophys. J.* 101 (2011) 934–942.
- [30] M. Di Valentin, S. Ceola, E. Salvadori, G. Agostini, G.M. Giacometti, D. Carbonera, Spectroscopic properties of the peridinin involved in chlorophyll triplet quenching in high-salt peridinin-chlorophyll *a*-protein from *Amphidinium carterae* as revealed by optically detected magnetic resonance, pulse EPR and pulse ENDOR spectroscopies, *Biochim. Biophys. Acta Bioenerg.* 1777 (2008) 1355–1363.

**CHAPTER** | **6**

**Triplet-State Spin Labels for Highly Sensitive  
Pulsed Dipolar Spectroscopy**



## Triplet-state spin labels for highly sensitive pulsed dipolar spectroscopy

M. G. Dal Farra, S. Ciuti, M. Gobbo, D. Carbonera and M. Di Valentin

Dipartimento di Scienze Chimiche, Università degli studi di Padova, Padova, Italy

### ABSTRACT

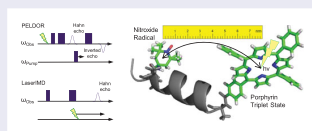
Pulsed dipolar spectroscopic methods allow nanometer distance measurements between pairs of spin labels. We have proposed a new spin labelling approach, based on the population of a chromophore triplet under light excitation, testing it on a peptide-based spectroscopic ruler and a photosynthetic protein. We have applied a modified Pulsed Electron DOuble Resonance (PELDOR) sequence where the photogeneration of the triplet spin precedes the conventional 4-pulse PELDOR sequence. In this experiment, the triplet-state serves as detection spin while the stable nitroxide is the pump spin. Alternatively, a new method, Laser-Induced Magnetic Dipole spectroscopy (LaserIMD), has been proposed: the nitroxide signal is detected while a time varying laser pulse acts as a pump to generate the triplet state [C. Hintze, D. Bucker, S. Domingo Köhler, G. Jeschke and M. Drescher, *J. Phys. Chem. Lett.* 7 (12), 2204 (2016)]. For the first time, in this work, we compare the two dipolar techniques performing X-band experiments in the same experimental conditions and deriving analytical expressions for the echo modulation by the density matrix formalism.

### ARTICLE HISTORY

Received 30 April 2018  
Accepted 13 July 2018

### KEYWORDS

PELDOR; DEER; LaserIMD; triplet state; spin label



## 1. Introduction

Pulsed Electron DOuble Resonance (PELDOR)/Double Electron–Electron Resonance (DEER) spectroscopy is a pulsed EPR (electron paramagnetic resonance) method that measures, via the dipolar electron–electron coupling between two paramagnetic species, distances in the range 1.5–8 nm [1–4]. This technique is characterised by high precision and reliability, although accessing distances above 8 nm is significantly challenging. It was shown that the limit can be overcome (ca. 12 nm) only using fully deuterated samples [5,6]. Beyond mere mean distances, PELDOR yields relevant distance distributions, which provide access to conformational distributions and dynamics.

Other EPR techniques for measuring electron–electron couplings include the Double-Quantum Coherence (DQC) [7] and relaxation-induced dipolar modulation enhancement (RIDME) [8]. Under suitable conditions and for distances less than ca. 2 nm for  $S = 1/2$

spin systems, the dipolar interaction can be estimated by continuous wave EPR [9].

Conventionally, PELDOR measurements are performed between two nitroxide spin labels which have been attached to biological molecules either by site-directed spin labelling or by chemical modification. For proteins, the most commonly used spin label is MTSSL [(1-oxy-2,2,5,5-tetramethylpyrroline-3-methyl)-methanethiosulfonate], which specifically reacts with the thiol group of cysteine residues, forming a disulphide bridge. By introducing cysteine residues to sites of interest via mutagenesis and subsequently allowing them to react with MTSSL, the nitroxide spin label can be positioned with high specificity and ease [10,11].

High sensitivity and accuracy are main issues in dipolar spectroscopy, which is emerging as a powerful pulsed EPR technique, complementary to the methods of X-ray crystallography, NMR and FRET for structural determination of biomolecules. These issues become a task

of primary importance particularly in the field of large membrane proteins which pose a considerable challenge for crystallography and NMR spectroscopy. The use of perdeuterated proteins, application of shaped pulses, and increasing the spectrometer frequency to Q-band, where the conventional nitroxide labels still perform well, are the strategies adopted to broaden the applicability of this methodology. Numerous efforts have been devoted also in the direction of developing alternative spin labels, featuring more attractive properties than conventional nitroxide radicals, despite their widespread employment for distance measurements.

Gd(III) ( $S = 7/2$ ) spin labels have been suggested as a valid alternative to nitroxide for Q-band and W-band PELDOR distance measurements [12]. Several characteristics of Gd(III) make it a candidate for PELDOR specifically at high-field delivering enhanced sensitivity, as it has been demonstrated for different systems [13]. In parallel, combining the nitroxide and the Gd(III) probes in an orthogonal labelling approach has proven to be very effective since the probes can be selectively excited in the pulsed dipolar EPR experiment [13,14].

As a contribution to the development of alternative spin labels, we have demonstrated the feasibility of applying PELDOR to determine the interspin distance between a photoexcited porphyrin triplet state ( $S = 1$ ) and a nitroxide spin label chemically incorporated into a peptide-based molecular ruler, designed to cover the complete range of applicability of PELDOR spectroscopy [15]. This new labelling approach provides high sensitivity because it fully exploits important characteristics of the triplet state [16].

Triplet states have a distinctive property compared to other spin labels: they are characterised by a spin polarisation enhancement of the EPR signal, resulting from a non-Boltzmann population of the triplet-state sublevels by intersystem crossing from the corresponding excited singlet state [17]. They work very efficiently as orthogonal labels, adding to the spectroscopic selectivity the advantage of behaving as photoinduced spin probes. This feature allows to reveal intermolecular interactions and oligomerization states in the same sample by performing PELDOR in the absence of light excitation measuring intermolecular nitroxide–nitroxide distances.

Among organic chromophores, we have selected porphyrins as they have been widely studied by EPR spectroscopy, because of their high triplet yields, strong spin polarisation and non-extreme relaxation times [18–20]. The well-characterised optical properties of the porphyrin chromophore can be also exploited to combine PELDOR to the complementary FRET spectroscopic method using a label which is both fluorescent and paramagnetic. Porphyrin derivatives can be used

as endogenous probes because of their presence in several classes of proteins, i.e. photosynthetic and heme proteins.

Researchers in the field of spin labelling EPR have used paramagnetic prosthetic groups as spin probes to determine structural constraints in proteins [21]. Employing endogenous probes for EPR detection only causes minimal functional perturbation to the biomolecules. Another advantage of such centres is that they are firmly anchored in the protein and, therefore, are not fraught with the problem of flexible linkers as the commonly used spin labels. For all these reasons, the methodology is becoming increasingly attractive but at the same time PELDOR experiments involving prosthetic group are very limited and restricted to  $S = 1/2$  or high-spin metal centres for which the  $m_S = \pm 1/2$  transition can be selected, mainly copper, iron-sulphur and manganese centres [22–25].

Recently, we have been able to measure the triplet–nitroxide distance using for the first time an endogenous probe in a protein system: the peridinin-chlorophyll *a* protein (PCP), a water soluble light-harvesting protein of the dinoflagellate *Amphidinium carterae* [26]. MTSSL was introduced in the protein by site-directed mutagenesis followed by spin labelling, while the triplet state is an endogenous carotenoid probe, populated under light excitation in isolated PCP by triplet–triplet energy transfer from the chlorophyll triplet state. This proves that not only porphyrin-derivatives but also other chromophores can be used as spin labels in the pulsed dipolar experiment.

In the meantime, the new technique of laser-induced magnetic dipole (LaserIMD) spectroscopy, based on optical switching of the dipole–dipole coupling, has been proposed [27]. In a proof of concept experiment, LaserIMD was applied to one of the model peptides belonging to the spectroscopic ruler series, and the same distance between the porphyrin and nitroxide probes was evaluated with the new methodology. Tentatively, the heme protein cytochrome C, spin labelled with MTSSL at the free cysteine position, was also investigated in order to demonstrate that LaserIMD could provide distance measurements between an endogenous prosthetic group and a nitroxide label. However, no triplet state was observed by EPR spectroscopy, as it should have been expected for a low-spin ferric heme. Zn-substitution of the heme is necessary in order to populate the Zn(II) protoporphyrin IX triplet state and perform the triplet–nitroxide dipolar spectroscopy on this class of proteins.

In this paper, we review the pulsed dipolar spectroscopy experiments exploiting photogenerated triplet state for distance measurements, outlining the main advantages of the novel spin label. We compare the two



different methods experimentally in order to quantify the signal-to-noise ratio (S/N) in the same measurement conditions and from a theoretical point of view in order to obtain analytical expressions in the frame of the density matrix formalism. Future perspectives are also presented.

## 2. Experimental details

### 2.1. Synthesis and EPR samples

The synthesis of the peptide was performed by standard solid-phase synthesis, following a protocol previously optimised for spin label-containing peptides [28]. 5-(4-Carboxyphenyl)-10,15,20-triphenylporphyrin (TPP) was covalently linked to the *N*-terminus of the 4-amino-1-oxyl-2,2,6,6-tetramethyl-piperidine-4-carboxylic acid (TOAC) containing peptide, still attached to the solid support, in the presence of *N,N'*-diisopropylcarbodiimide /1-hydroxybenzotriazole in  $\text{CH}_2\text{Cl}_2/\text{DMF}$ . Cleavage of the porphyrin-peptide conjugate from the resin was achieved by a mild acidic treatment that prevents the loss of the spin label by protonation. Further details on the synthesis can be found in [16]. The peptide was dissolved in 98% deuterated methanol MeOD (Sigma Aldrich) to reach a final concentration of ca. 200  $\mu\text{M}$ . The quartz EPR tubes, partially filled with the solutions, were sealed after several freeze-thaw cycles.

### 2.2. EPR measurements

Pulsed EPR was performed on a Bruker Eleksys E580 pulse EPR spectrometer equipped with a Bruker splitting resonator ER4118X- MS3 (microwave frequency = 9.55 GHz) and an Oxford CF935 cryostat. The measurements were performed at 20 K. The sample was photoexcited with the second harmonic of a pulsed Nd:YAG laser (532 nm) with an average power of 5 mW and a repetition rate of 10 Hz.

For the PELDOR experiments a standard 4-pulse sequence (laser-DAF- $\tau_1$ - $\pi$ - $t$ - $\pi_{\text{pump}}$ -( $\tau_1 + \tau_2 - t$ )- $\pi$ - $\tau_2$ -echo) was applied at a delay after the laser flash (DAF) of 50 ns; the microwave power was adjusted to obtain an observer sequence of 16/32/32 ns and a pump pulse of 8 ns. The difference between the pump (nitroxide) and observer (porphyrin triplet state) frequency was set to 250 MHz. A two-step phase cycle was applied to remove receiver offsets while deuterium nuclear modulations were suppressed using an 8-step  $\tau_1$  cycle from a 180 ns starting value with 56 ns increment steps. Data were collected with 2 scans and 100 shots-per-point.

The LaserIMD trace was acquired with a Hahn echo pulse sequence in which the laser pulse was inserted at variable position during the second evolution period:  $\pi/2 - \tau - \pi - t - \text{laser} - (\tau - t) - \text{echo}$ . The laser pulse was moved also after the standing echo in order to acquire a sufficient baseline. The synchronisation of the laser and the instrument was obtained triggering the EPR instrument with the flash-lamp of the laser. The number of shots-per-point and scans was regulated in order to be comparable with the PELDOR experiment: 100 shots-per-point with a 2-step phase cycle and 16 scans were used.

### 2.3. Data analysis and theory

The experimental time traces for the comparative study between PELDOR and LaserIMD were analysed using the DeerAnalysis2016 routine [29]. Primary data were background corrected by a polynomial decay function. The form factors were processed by Tikhonov regularisation.

The analytical calculations were performed in Mathematica.

The triplet sublevel populations were calculated in Matlab computing the static Hamiltonian of the porphyrin triplet state for a grid of molecular orientations with respect to the external magnetic field and expressing the population matrix, derived from the simulation of the triplet EPR spectrum, in the corresponding eigensystem. The integral over the whole set of orientations was then calculated for each of the three triplet sublevel populations.

## 3. Result and discussion

### 3.1. PELDOR on the porphyrin triplet-state spin label in a peptide-based spectroscopic ruler

To test the accuracy of the interspin distance determination and the range of applicability of the orthogonal spin labelling approach based on the nitroxide-porphyrin triplet-state pair, we designed and developed a distance ruler, consisting of a series of bis-labelled model peptides with well defined, predictable separations between the paramagnetic sites [15]. The peptides are labelled at the *N*-terminal end with the TPP moiety and with the unnatural amino acid TOAC at selected sequence positions, spanning distances from 1.8 to 8 nm. To inspect the capability of the novel label to work on a wide range of distances, design criteria have included the bis-labelled peptide **1** at the lower limit of the distance range and more importantly peptide **8** which represents the upper limit, which is expected to be around 8 nm. The peptide

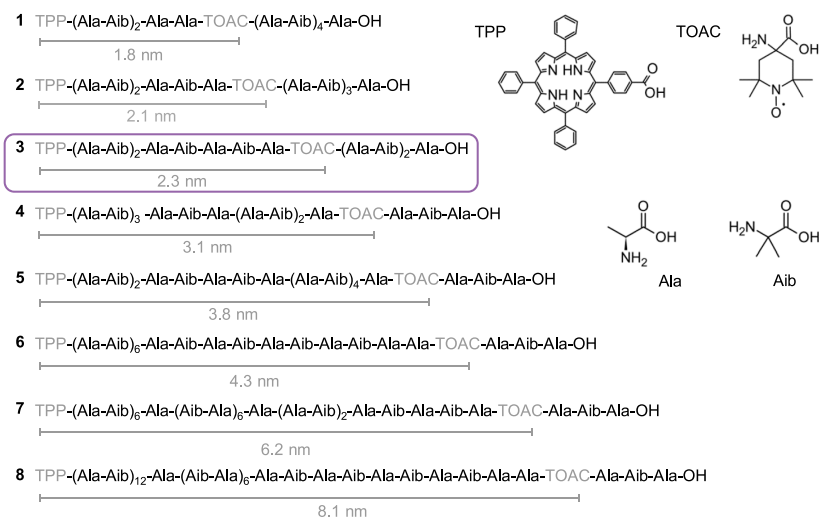


**Figure 1.** Amino acid sequences and structures of the components of the distance ruler series (1–8). The centre to centre distances between the spin labels are shown, as derived in [15].

sequences and the calculated distances between the two labels are reported in Figure 1.

An overview of the experimental background-corrected and simulated time domain signals and of the distance distributions obtained by Tikhonov regularisation

are shown in Figure 2 for the complete series of porphyrin-based peptides (1–8). In the same Figure 2 also the pulse sequence is reported, based on a 4-pulse scheme where the first observer pulse is preceded by the laser flash at the minimum delay compatible with

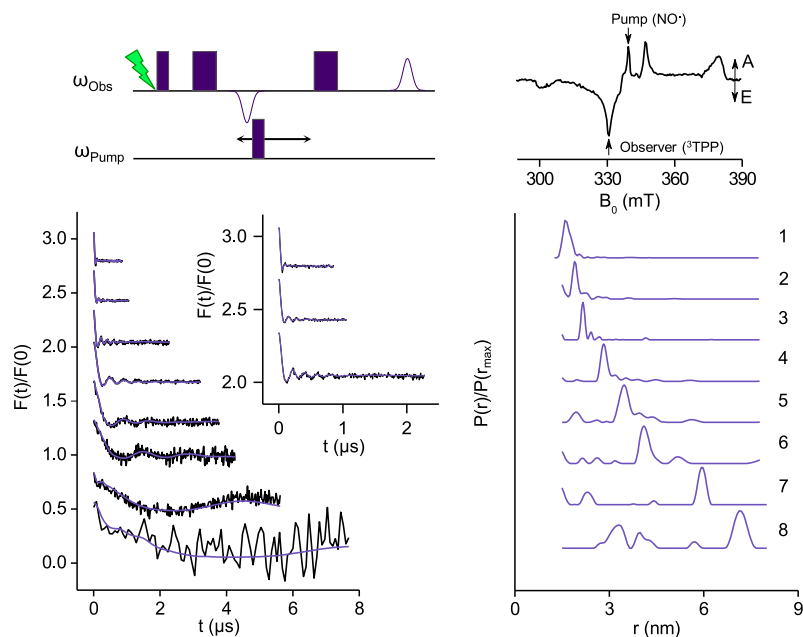


**Figure 2.** Left: X-band 4-pulse PELDOR traces after background correction and relative DeerAnalysis fittings of the form factors for the distance ruler series (1–8). Right: experimental label-to-label distance distributions obtained from the PELDOR data by Tikhonov regularisation. Inset: 4-pulse PELDOR sequence in presence of laser photoexcitation (left) and X-band field-swept electron-spin echo spectrum recorded under photoexcitation for the TPP-conjugated model peptide 3 (right). The arrows indicate the positions of the pump (nitroxide) and the detection spin (porphyrin triplet state). The figure is based on data from [15], experimental conditions are reported therein.

the set-up. The PELDOR time traces were obtained by applying the pump pulse at the maximum of the nitroxide spectrum, in order to optimise the pump efficiency, and the observer sequence in correspondence to the most intense emissive zero-field splitting (ZFS) canonical transition of the polarised TPP triplet-state spectrum, generated via pulsed laser excitation (see the top panel of Figure 2). The time traces of all the bis-labelled peptides show deep envelope modulations at frequencies varying in a progressive way according to the increasing distance between the spin labels. Well-defined distances have been derived by Tikhonov regularisation in the overall range of distances explored by the spectroscopic ruler. Details of the background correction procedure and data analysis are available in Di Valentin *et al* [15].

The work has proven the feasibility of the PELDOR experiment combined with the orthogonal spin labelling strategy based on the porphyrin triplet-nitroxide pair. We have then explored the practical limits of the distance determination based on the 4-pulse PELDOR experiment: the triplet state properties allow to measure inter-spin distances up to 8 nm with a conventional X-band set-up. The accuracy has been assessed by comparing the PELDOR spin-spin distances with theoretical predictions: there is an excellent agreement in the overall range of distances. A corresponding Cu(II) porphyrin-based system has also been investigated in order to estimate the performance of the triplet-state spin label compared to conventional  $S = 1/2$  systems [15,16]. Figure 3 depicts the 4-pulse PELDOR time trace of peptide **3** and the Cu(II) analogue obtained by applying the pump pulse at the maximum of the nitroxide spectrum in both cases and in the presence or absence of the laser pulse in

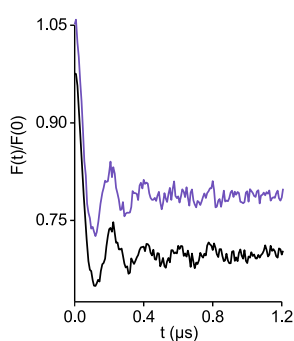


**Figure 3.** X-band 4-pulse PELDOR traces after background correction, recorded at 20 K under photoexcitation for peptide **3** (bottom trace) and without photoexcitation for the Cu(II) analogue of **3** (top trace). The figure is based on data from [15], experimental conditions are reported therein. The number of scans was reduced by a hundred times for the triplet-state nitroxide PELDOR experiments.

order to excite the triplet state or the Cu(II) spin label, at the corresponding appropriate field positions. We have demonstrated that accuracy is accompanied by high sensitivity: optimisation of the time trace in terms of signal-to-noise ratio was achieved by reducing a hundred times the number of scans for the triplet-state nitroxide PELDOR experiments. The significantly increased sensitivity is due to the intrinsic spin polarisation of the triplet state, which is only partially lost in the broad features of the corresponding spectrum. Moreover, in the conditions commonly adopted for PELDOR measurements, the phase memory time of the triplet state is comparable to that of nitroxide spin labels whereas for Cu(II) signal is significantly shorter.

The close correspondence between the dipolar traces of the two species, which are characterised by different principal tensor orientations, spin distribution on the macrocycle and different spin multiplicity, is a clear evidence that orientation selection is not effective, that the point-dipole model is still valid for the porphyrin triplet state, despite the extended  $\pi$ -conjugation on the porphyrin ring, and that the effects arising from the higher dimensionality of the spin system can be neglected. These properties all together allow a straightforward data analysis and make the porphyrin in the triplet state an attractive and reliable spin label for high sensitivity distance measurements in biomolecules.

### 3.2. PELDOR on the carotenoid triplet-state spin label in the protein PCP

As a further step, the technique was applied for the first time to a protein system, PCP from *Amphidinium carterae*, to measure the distance between the chromophore, whose triplet is populated under photoexcitation, and a nitroxide suitably introduced in the protein by site directed spin labelling [26,30].

PCP is the peripheral, water soluble light-harvesting complex of dinoflagellate algae, containing only chlorophyll *a* and the carotenoid named peridinin in a ratio of 1:4. The N- and C-terminal domains of the monomers are related by a pseudo-twofold symmetry and each of them contains a cluster of pigments with the central chlorophyll *a* surrounded by four peridinin molecules [30]. The protein arrangement is reported in Figure 4.

A reconstitution system has been established in which the isolated pigments are refolded with the polypeptide of the amino-terminal of the main fold PCP [31]. The crystal structure of refolded PCP (RFPCP) reveals that two identical domains assemble into a homo-dimer, that is virtually identical to the structure of the native PCP [32]. The RFPCP has an additional alanine residue at

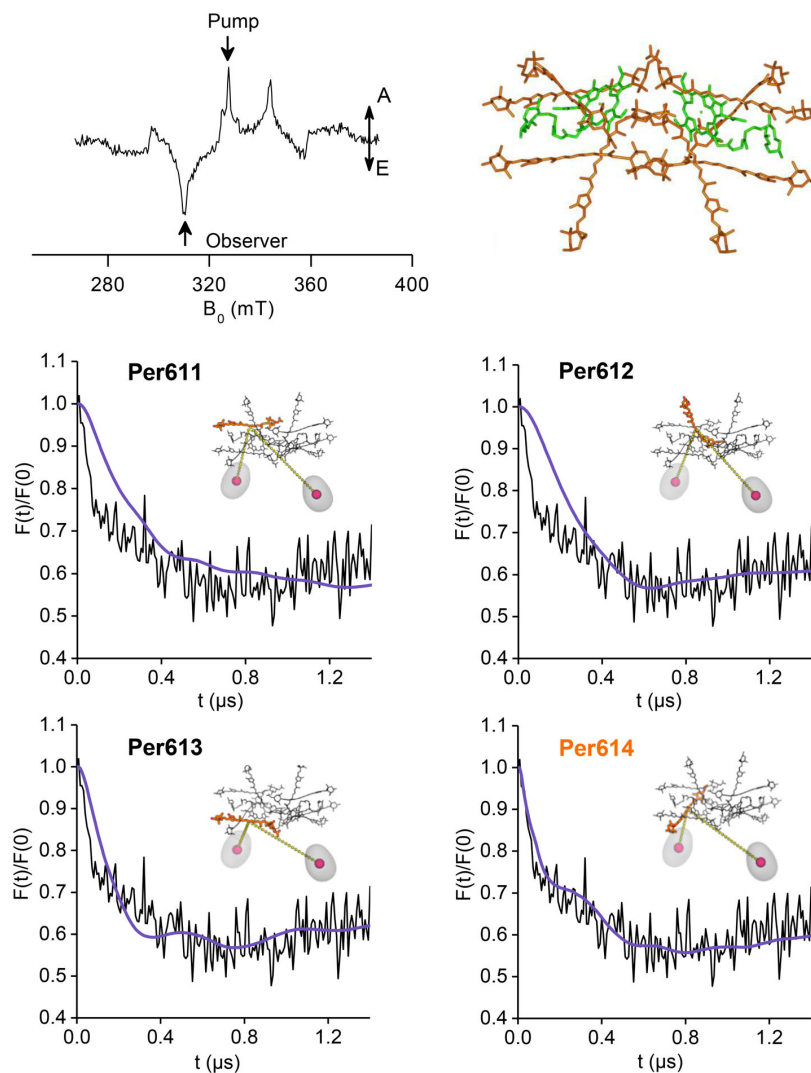


**Figure 4.** Top panel left: X-band field-swept electron-spin echo spectrum recorded under photoexcitation for spin labelled refolded PCP. The arrows indicate the positions of the pump (nitroxide) and the detection spin (peridinin triplet state). Top panel right: structure of the pigments associated with the monomeric basic unit of the PCP complex from *Amphidinium Cartarae* (pdb 1ppr). Bottom panel: Comparison of background-corrected experimental and calculated 4-pulse PELDOR time traces for the triplet state localised on each of the four Peridinin. Nomenclature for the peridinins is reported in [26] and Per614 is highlighted. Mean distances between each peridinin and the nitroxide labels in the dimer of the refolded PCP A0C mutant, are indicated. The figure is based on data from [26], experimental conditions and computational details are reported therein.

the N-terminal (Ala-0) compared to the main form of PCP. The alanine residue was mutated to a cysteine and then labelled with a MTSSL in A0C-RFPCP (for details see [30]). This specific labelling position was selected in a way that the distances between the nitroxide and each of the carotenoids present in the protein can be discriminated in the experiment.

The field-swept electron-spin echo spectrum of the spin labelled A0C-RFPCP mutant recorded immediately

after the light pulse is composed of two contributions: a component due to the peridinin triplet state and the nitroxide signal, as shown in Figure 4. The peridinin triplet spin polarisation is inherited from the chlorophyll *a* triplet donor during triplet-triplet energy transfer, as extensively discussed in [33]. The 4-pulse sequence was performed by applying the pump pulse at the maximum of the nitroxide spectrum and the observer sequence in correspondence to the most polarised transition of the

triplet spectrum. After removal of the background decay, the PELDOR time trace reveals clear dipolar modulations (see Figure 4). In order to identify the peridinin involved in triplet–triplet energy transfer, calculations of the PELDOR traces were carried out by considering the dipolar interaction between the triplet state on one monomer and both symmetry-related nitroxides of the dimer. The comparison between the experimental and calculated PELDOR traces shows that only one specific peridinin, in this carotenoid-rich protein, can satisfactorily reproduce the PELDOR time trace, confirming previous spectroscopic results [33,34].

In this work, we have demonstrated that PELDOR can be used also to measure distances between a photoexcited triplet state and a nitroxide radical in a protein system and that the chromophore, in which the triplet state is populated, can also be different from a porphyrin derivative. This type of orthogonal approach can be extended to chromophores whose triplet state is highly polarised and, due to the sensitivity acquired from the spin polarisation of the photoexcited triplet state, the method can be applied to complex biological systems. Triplet states characterised by smaller ZFS parameters are more suitable for this application due to the limited bandwidth of the EPR resonator.

We have also identified which are the specific pigments involved in the triplet–triplet energy transfer showing that the spectroscopic methodology for distance determination, complemented by the X-ray structural information, can provide valuable details on the structure–function relationship.

### 3.3. LaserIMD on the porphyrin triplet-state spin label

The porphyrin triplet-state spin label pair has proven to be advantageous compared to the orthogonal approach based on  $S = 1/2$  spin labels. Furthermore, application to proteins, where the photoexcited probe is endogenously bound, was an important step further in the spread of the novel methodology. Once the novel spin label was established, a new pulsed dipolar EPR technique, exploiting the same triplet-state probe, was proposed by the group of M. Drescher [27]. This new technique is based on the switching of the dipole-dipole coupling by optical excitation of the chromophore into its triplet state, instead of pumping the spin species by addressing it with a second microwave frequency; for this reason, it is called LaserIMD. The corresponding pulse sequence is shown in Figure 5 and compared to the 4-pulse PELDOR sequence. In the PELDOR experiment photoexcitation comes at the very beginning of the pulse sequence and after the photoexcited triplet-state species is excited,

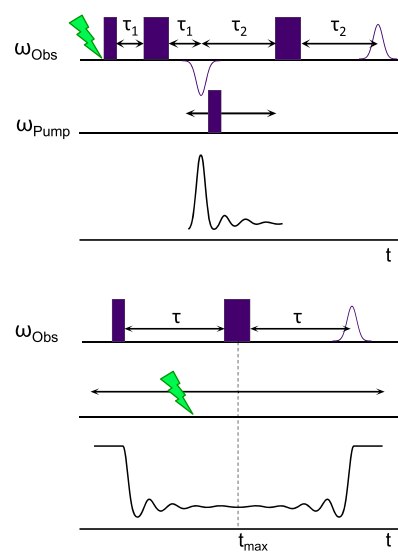


**Figure 5.** 4-pulse PELDOR sequence (top) and LaserIMD pulse sequence (bottom) with a representation of the corresponding dipolar modulation traces.

both the radical and triplet state are addressed by two microwave frequencies (pulse and observer). For LaserIMD, a radical spin label is used as the observed species, whereas the photogenerated triplet state, produced by a laser flash moving across the complete microwave sequence, replaces the pumped spin label species. A simple two-pulse Hahn echo sequence is sufficient to obtain dead-time free data. The modulated time trace corresponding to the LaserIMD sequence is symmetric around  $t_{\max}$  where the refocusing microwave pulse occurs. This symmetry can be used to determine the correct zero time.

When the LaserIMD sequence was proposed, in a proof of concept experiment, the synthesis of a member of the spectroscopic ruler series, peptide 3, was reproduced in order to perform the LaserIMD experiment [27]. While in the PELDOR experiment, the porphyrin was excited in the spectral region corresponding to the Q optical bands using the second harmonic of the YAG laser (532 nm), the LaserIMD sequence was applied in correspondence to the Soret band (351 nm). In Figure 6, the time domain signal obtained with LaserIMD in Q-band is shown as raw data and after processing. After background subtraction, a modulation depth  $\lambda \simeq 6\%$ , has been estimated. The Fourier transforms of the form factors lead to the dipolar coupling spectra in frequency domain and fitting via Tikhonov regularisation yields the distance distribution with a mean interspin distance which is perfectly in agreement with previous results obtained by 4-pulse PELDOR spectroscopy. The only drawback of the experiment is the low modulation depth,

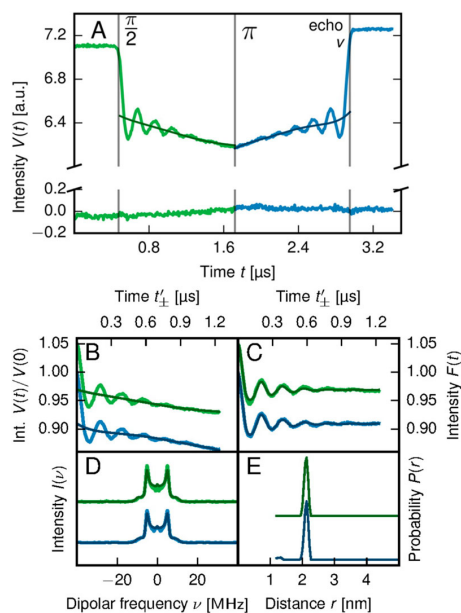


**Figure 6.** LaserIMD experiment on peptide **3**: (A) Raw data of the time domain signal, the top and bottom traces correspond to the real and imaginary parts of the quadrature signal, respectively. (B) Comparison of both branches of the LaserIMD raw data. (C) Corresponding form factor after experimental background correction obtained by Tikhonov regularisation. (D) Fourier-transformed dipolar coupling spectra with fit. (E) Corresponding distance distribution. Reprinted with permission from [27]. Copyright 2016 American Chemical Society.

which has been ascribed to the intrinsic triplet quantum yield of the porphyrin chromophore corresponding to the specific excitation of the Soret band in the LaserIMD experiment. A different excitation, according to the authors, might lead to an increase in the triplet quantum yield.

In order to prove the effectiveness of the triplet spin labelling method combined to the new dipolar sequence the porphyrin triplet–nitroxide LaserIMD experiment, performed on peptide **3**, has been compared to the nitroxide–nitroxide PELDOR, performed on a nitroxide variant of peptide **3**. The signal-to-noise ratio  $S/N$  was similar under the same conditions.

The feasibility of the LaserIMD experiment under photoexcitation of an endogenous prosthetic group in protein, the low-spin ferric heme moiety, was also investigated. The Cytochrome C from *Saccharomyces cerevisiae* labelled with MTSSL on the free cysteine 102 was used as a paradigmatic protein. In this case, the modulation of the LaserIMD trace, which corresponds to the distance between the nitroxide spin label and the heme group, cannot be ascribed to the dipolar interaction between the radical and the triplet state produced by photoexcitation

since no triplet-state signal was detected. The presence of the Fe(III) coordinated to the heme moiety complicates the photoexcitation pathways in the protein. Zn-substitution of the heme is necessary in order to populate the Zn(II) protoporphyrin IX triplet state and unambiguously prove the feasibility the triplet–nitroxide LaserIMD experiment using endogenous spin probes like heme.

### 3.4. Comparison between photoexcited PELDOR and LaserIMD X-band experiments on the spectroscopic ruler

As pointed out in the previous section, the distance distribution obtained applying LaserIMD on the same porphyrin–nitroxide spin labelled peptide came out to be in good agreement to those of the corresponding 4-pulse PELDOR experiment. However, comparison in the performance of the two dipolar pulse sequences was limited to the nitroxide–nitroxide PELDOR (using a nitroxide variant of peptide **3**). The photoexcited PELDOR experiment on peptide **3** was performed in X-band and it cannot be directly compared to the Q-band LaserIMD.

It is therefore important to apply exactly the same experimental conditions and use the same porphyrin–nitroxide spin labels in order to assess the performance of the two techniques in term of signal-to-noise ratio (see Experimental details). The corresponding X-band experiments on peptide **3** are reported in Figure 7, where they are shown after background removal. Since the two data sets differ considerably in their modulation depth  $\lambda$ , the time traces have also been scaled on the modulation depth. The same main modulation frequency is visible in both traces and the same distances are derived by the Tikhonov regularisation procedure, although in the LaserIMD experiment the low  $S/N$  precludes to see the details of the modulated trace. The main difference between the two form factors is the modulation depth:  $\lambda$ -LaserIMD is  $\simeq 6\%$  while  $\lambda$ -PELDOR is  $\simeq 40\%$  (see the normalised traces reported in the central panel of Figure 7). The noise level, calculated as the standard deviation of the experimental data to the Tikhonov regularised fit, is  $\simeq 0.006$  a.u. for LaserIMD and  $\simeq 0.014$  a.u. for PELDOR. A significant improvement of the  $S/N$ , determined as the ratio between the modulation depth and the noise level of the background corrected and normalised form factors according to [35], has been obtained. Altogether a  $S/N$  enhancement of 2.8 times has been quantified for PELDOR, which corresponds to a reduction in measuring time of more than 8 times. This is the reason why LaserIMD, which has a worse sensitivity in X-band compared to the Q-band, does not give satisfactory results, as already pointed out in [27], where, however, the spectra are not shown.

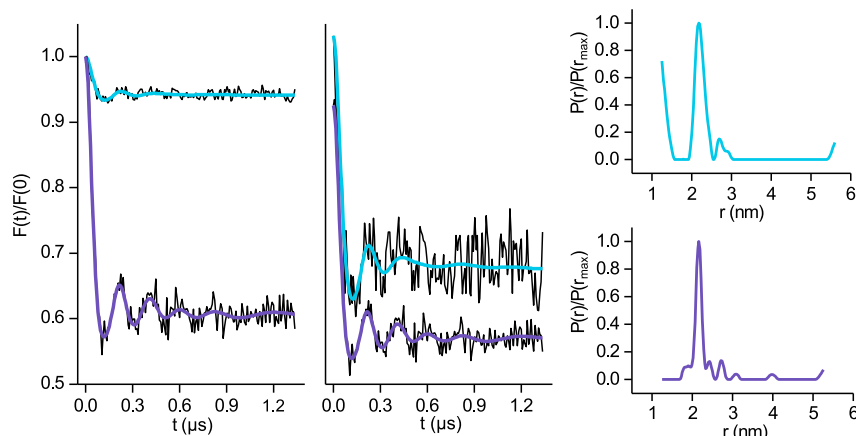


**Figure 7.** Left panel: X-band background-corrected experimental data  $F(t)/F(0)$  applying the LaserIMD sequence and the 4-pulse PELDOR sequence and best fits as calculated by DeerAnalysis2016. Central panel: modulation depth scaled experimental form factors and best fits as calculated by DeerAnalysis2016. Right panel: distance distributions  $P(r)/P(r_{\text{max}})$  obtained by Tikhonov regularisation. Light blue indicates the LaserIMD data and blue indicates the PELDOR data.

Both experiments exploit the triplet spin label but in a different way, taking advantage of different characteristics of this paramagnetic state. To understand the physics underneath the different performance of the two techniques, a detailed theoretical description of the pulse sequences is provided in the next section.

### 3.5. Theory

The analytical expression describing the echo modulation for the 4-pulse PELDOR and the LaserIMD experiment, considering a system composed by a photoexcited triplet state weakly interacting with a radical, was derived by using the density matrix formalism, described in detail by Mims [36]. The spin Hamiltonian for a generic system can be written as the sum of a time independent contribution  $\hat{H}_0$  and a time-dependent contribution  $\hat{H}_1(t)$  accounting for the interaction with the microwave pulses:

$$\hat{H}(t) = \hat{H}_0 + \hat{H}_1(t) \quad (1)$$

where  $\hat{H}_1(t)$  is present only during the application of the microwave pulses.

When the spin Hamiltonian is time-dependent the integration of the Liouville-von Neuman equation is not straightforward. Simplification in the description of the experiment is obtained carrying out the derivation in the rotating frame where the time dependence is moved from the Hamiltonians to the observables [37].

The details of the derivation are different for the PELDOR and LaserIMD sequences and are described in separate sections.

#### 3.5.1. PELDOR

A series of simplifying assumptions was necessary to derive the analytical expressions. First of all, the high-field approximation is applied: the spins are assumed to be both quantised along the static magnetic field direction and only the secular part of the ZFS and of the dipolar interactions are retained. No hyperfine interaction or g-anisotropy are considered. The Heisenberg exchange coupling between the triplet state and the radical has also been neglected. The case where the system is oriented with the  $z$  axis of ZFS tensor parallel to the static magnetic field is considered.

The static Hamiltonian in frequency units, expressed in the rotating frame, is:

$$H_0 = \Omega_t S_{zt} + \Omega_r S_{zr} + (S_{zt}^2 - S_t^2/3)D + \omega_{dd} S_{zt} S_{zr} \quad (2)$$

where the labels ‘t’ and ‘r’ indicate the triplet and the radical, respectively,  $\Omega_t$ ,  $\Omega_r$  are the resonance frequencies of the two species,  $D$  is the ZFS parameter and  $\omega_{dd}$  is the dipolar frequency between the triplet state and the radical. The corresponding eigenfunctions, which constitute the basis set used in the derivation, are the products of the radical and the triplet high-field eigenfunctions.

The free precession operators are expressed as:

$$R_{ev} = \exp\{-iH_0\tau\} \quad (3)$$

where  $\tau$  is the duration of the free evolution period during which no pulses are applied. In analogy to what is done in the experiment, the calculation has been carried out considering the photoexcited triplet state as the observer spin and the radical as the pump spin. We made the further assumption that the observer pulses affect

only the triplet state whereas the pump pulse acts only on the radical. Ideal nutation operators, in which the static Hamiltonian has been neglected, are used for both the observer and the pump spins.

The Hamiltonian describing the interaction of the radical with the microwave magnetic field in the rotating frame and the corresponding nutation operator are:

$$\begin{aligned} H_{1p} &= \omega_p S_{xr} \\ R_p &= \exp\{-iH_{1p}t_p\} \end{aligned} \quad (4)$$

where  $\omega_p$  is the Rabi frequency of the pump spin and  $t_p$  is the pump  $\pi$ -pulse length.

For the triplet observer spin, transition selective microwave pulses are considered since the spacing of the triplet-state sublevels, due to the ZFS, is generally such that the microwave frequency cannot simultaneously excite transitions that share a common sublevel. The orientational selectivity of the detection pulses on the triplet spin is taken into account introducing a single transition operator  $S_{-1t}$ . This is analogous to the  $S_{xt}$  matrix, but with zero elements in the levels not involved in the transition:

$$\begin{aligned} H_{1ob} &= \omega_{ob} S_{-1t} \\ R_{ob} &= \exp\{-iH_{1ob}t_{ob}\} \end{aligned} \quad (5)$$

where  $\omega_{ob}$  is the Rabi frequency of the observer spin and  $t_{ob}$  is the detection  $\pi/2$ -pulse.

The density matrix of the system is calculated as the Kronecker product of the density matrix of the radical and of the polarised triplet state in the corresponding high-field eigenbasis:

$$\rho_0 = \rho_r' \otimes \rho_t'' \quad (6)$$

In Equation (6),  $\rho_r'$  is the radical equilibrium density matrix,  $\rho_t''$  is the density matrix of the triplet after the laser flash containing, along the diagonal, the populations of the triplet sublevels multiplied by the triplet yield  $\Phi_t$ . The superscripts indicate that the two density matrices are expressed in the radical and the triplet high-field eigenbasis, respectively.

Considering the 4-pulse PELDOR sequence, the density matrix at the time of the echo appearance is obtained applying the proper sequence of nutation and free precession operators to the initial density matrix:

$$\begin{aligned} \rho_E &= R_{ev4} \cdot R_{ob}^2 \cdot R_{ev3} \cdot R_p \cdot R_{ev2} \cdot R_{ob}^2 \cdot R_{ev1} \cdot R_{ob} \cdot \rho_0 \\ & R_{ob}^\dagger \cdot R_{ev1}^\dagger \cdot R_{ob}^{2\dagger} \cdot R_{ev2}^\dagger \cdot R_p^\dagger \cdot R_{ev3}^\dagger \cdot R_{ob}^{2\dagger} \cdot R_{ev4}^\dagger \end{aligned} \quad (7)$$

The dipolar trace is then calculated as the expectation value of the operator  $S_y + iS_x$  on the final density matrix:

$$V(t) = \text{Tr}\{(S_y + iS_x) \cdot \rho_E\} \quad (8)$$

where  $S_{x,y} = S_{x,yt} + S_{x,yr}$ .

The modulation formula for the 4-pulse PELDOR experiment for a triplet state coupled to a radical is the following:

$$\begin{aligned} V(t) &= V_0(1 - \chi(1 - ((p_\alpha + p_\beta)(\Delta_1 + \Delta_3) \\ & + i(p_\alpha - p_\beta)(\Delta_2 + \Delta_4)) \cos[t\omega_{dd}] \\ & + (i(p_\alpha - p_\beta)(\Delta_1 + \Delta_3) - (p_\alpha + p_\beta) \\ & (\Delta_2 - \Delta_4)) \sin[t\omega_{dd}])) \end{aligned} \quad (9)$$

where  $V_0$  is the echo of the triplet state in the absence of the pump pulse,  $p_\alpha$  and  $p_\beta$  are the Boltzmann populations of the  $\alpha$  and the  $\beta$  radical sublevels,  $\chi$  is an empirical modulation depth, which does not take into account the partial excitation of the radical probe,  $\Delta_{1,2,3,4}$  are the coefficients which determine the relative weight of the in-phase and out-of phase components. The explicit expressions for  $V_0$ ,  $\chi$  and all the coefficients are reported in the [Appendix](#).

In the simplifying assumption that ideal  $\pi/2$  and  $\pi$  pulses have been applied, inserting in the expression the correct values of the pulse lengths and the microwave frequency for both the observer and the pump pulses, the formula becomes:

$$\begin{aligned} V(t) &= \frac{1}{\sqrt{2}} \Phi_t (p_{-1} - p_0) ((p_\alpha + p_\beta) \cos[(t - \tau_1)\omega_{dd}] \\ & + i(p_\alpha - p_\beta) \sin[(t - \tau_1)\omega_{dd}]) \end{aligned} \quad (10)$$

where  $p_1$ ,  $p_0$  and  $p_{-1}$  are the non-equilibrium populations of the triplet-state sublevels. In both cases, an out-of phase component of the echo is present but its contribution is negligible considering the ratio  $(p_\alpha + p_\beta)/(p_\alpha - p_\beta) \simeq 44$  at 20 K at Boltzmann equilibrium [38]. In the simplified case of  $\pi/2$  and  $\pi$  pulses, the empirical modulation depth parameter ( $\chi$ ) disappears in the formula. The  $\chi$  parameter, when the static Hamiltonian is neglected in the nutation operators, as in our case, is solely determined by pump pulses characteristics. It should resemble the typical modulation depth of a nitroxide-nitroxide PELDOR experiment that in the case of 100% labelling, in X-band, has an efficiency corresponding to 50% [39]. There is no effect of the triplet-state counterpart on the modulation depth: the spin polarisation increases the intensity of the observer echo and therefore influences only the value of  $V_0$ .

### 3.5.2. LaserIMD

In the LaserIMD sequence, analogously to what was done in [27], the generation of the photoexcited triplet is considered to take place after the first microwave pulse. Experimentally, the laser flash is moved also beforehand but this contributes only to the baseline and not to the dipolar modulation of the radical echo. Also in the case



of the LaserIMD, the high-field approximation has been applied and no hyperfine interaction or g-anisotropy are considered. The basis set used for the calculation before the generation of the triplet state is the radical high-field eigenbasis. All the operators expressed in this basis are indicated by a superscript (e.g.  $S'_{zr}$ ). The corresponding spin Hamiltonian is:

$$H'_{0r} = \Omega_r S'_{zr} \quad (11)$$

This is the only term contributing to the free precession operators in all the evolution periods. In the nutation operators, similarly to what was done in the PELDOR case, the static Hamiltonian  $H'_{0r}$  is neglected.

The initial density matrix is simply the equilibrium density matrix of the radical, while the density matrix right before the generation of the triplet is the following:

$$\rho'_1 = R'_{ev1} \cdot R'_{ob} \cdot \rho'_r \cdot (R'_{ob})^\dagger \cdot (R'_{ev1})^\dagger \quad (12)$$

The photoexcitation of the triplet state introduces a new species in the system, therefore, from this point in the sequence, the calculations are carried on in a new basis given by the product of the triplet and the radical high-field eigenfunctions. The density matrix becomes:

$$\rho_1 = \rho'_1 \otimes \rho''_t \quad (13)$$

where  $\rho''_t$  is the triplet-state density matrix which includes also the triplet yield and the second superscript indicates the triplet high-field eigenbasis.

After the generation of the triplet state, the dipolar coupling between the triplet and the radical has to be included in the static Hamiltonian:

$$H_0 = H_{0r} + \omega_{dd} S_{zr} S_{zt} \quad (14)$$

where the Zeeman and ZFS of the triplet state has been neglected because there are no pulses acting on the triplet state.

The density matrix at the time of the echo appearance is:

$$\rho_E = R_{ev3} \cdot R_{ob}^2 \cdot R_{ev2} \cdot \rho_1 \cdot R_{ev2}^\dagger \cdot R_{ob}^{2\dagger} \cdot R_{ev3}^\dagger \quad (15)$$

The modulation formula for the LaserIMD experiment for a triplet-state coupled to a radical is the following:

$$V(t) = V_0 (\Phi_t p_0 + 1 - \lambda (1 - \Phi_t (p_{+1} + p_{-1})) \times (\Delta_1 \cos[t\omega_{dd}] + i\Delta_2 \sin[t\omega_{dd}])) \quad (16)$$

where  $V_0$  is the echo of the nitroxide in the absence of the triplet state,  $\lambda$  is the modulation depth and  $\Delta_{1,2}$  are the coefficients which indicate direction of the magnetisation in the  $x, y$ -plane. The explicit expressions for  $V_0$ ,  $\lambda$  and the coefficients are shown in the [Appendix](#).

In the simplifying assumption that ideal  $\pi/2$  and  $\pi$  pulses have been applied, the formula becomes:

$$V(t) = \frac{1}{2} (p_\alpha - p_\beta) (\Phi_t p_0 + \Phi_t (p_{+1} + p_{-1}) \cos[t\omega_{dd}]) \quad (17)$$

This simplified expression allows to directly compare the PELDOR and LaserIMD analytical formulas and derive the relevant differences when comparing the two techniques. While in the PELDOR experiment an out-of phase component of the echo is present not only for pulses of generic length and microwave frequency but also when  $\pi/2$  and  $\pi$  pulses are applied (Equations 10 and 9), in the LaserIMD this component is lost in the presence of  $\pi/2$  and  $\pi$  pulses. Only when the high-field approximation is not valid an out-of phase component appears in the dipolar trace.

Equation 17 can be rearranged in terms of the modulation depth according to [27], in this case  $\lambda$  corresponds to  $\Phi_t (p_{+1} + p_{-1})$ . The modulation depth, as already pointed out in [27], is limited by the triplet yield and by the amount of triplet population which resides in the  $m_S = 0$  level. For tetraphenylporphyrin  $\Phi_t \simeq 0.8$  at room temperature [40]. In the high-field limit, integrating over all the molecular orientations with respect to the magnetic field,  $p_{+1} = p_0 = p_{-1} = 0.33$ . Considering the value of  $\Phi$  and the triplet sublevel populations, a modulation depth corresponding to ca. 46% should be expected. The effect of the ZFS interaction on the triplet populations does not produce a significant effect to explain the reduction of the modulation depth (details on the calculation are reported in the Experimental section).

Furthermore, exciting the Q absorption band instead of the Soret band, has not substantially affected the value of the modulation depth. This proves that the reason for the low modulation depth is not related to a variation of the triplet quantum yield compared to the value reported in the literature, as it was suggested in [27]. In the LaserIMD experiment the modulation depth is probably limited by the incomplete triplet excitation due to the characteristics of the experimental set-up (EPR tube instead of a cuvette, typical concentrations of EPR samples, small optical window). Sample excitation is a critical parameter which requires optimisation in the LaserIMD experiment. The same problem is not present in the PELDOR experiment because the triplet state works as the observer and is therefore not influencing the modulation depth. In this case, the incomplete excitation affects instead the intensity of the observer echo. When considering the overall effect of the pump and the observer pulses on the S/N, a significant improvement has been obtained for the PELDOR technique. There are, however, some

potential advantages of the LaserIMD experiment compared to PELDOR which derive from the virtually infinite optical excitation bandwidth characterising LaserIMD as it is underlined in [27]. An extended range of distances, which is an important requisite for pulsed dipolar spectroscopy, becomes accessible to this technique.

#### 4. Conclusions

We have reviewed the recent achievements in pulsed dipolar EPR using an orthogonal spin labelling approach in which a chromophore probe, in the photoexcited triplet state, is combined with the conventional nitroxide spin label. The novel methodology provides high-sensitive and accurate measurements of interspin distances and it is applicable to protein complexes where endogenous photo-probes are present.

In this work we compare the two dipolar spectroscopic methods introduced to measure radical-triplet interspin distances: photoinduced PELDOR and LaserIMD. Both an experimental and theoretical approach has been used for this comparative study. While PELDOR exploits the spin polarisation properties of the triplet state, LaserIMD does not take any advantage from this specific property of the triplet state and, in addition, it is characterised by a reduced modulation depth due to lack of contribution of the  $m_S = 0$  level to the dipolar interaction. An increase of S/N has been found for PELDOR when measuring in the same conditions. The use of LaserIMD provides other advantages, as underlined in [27] and in the present paper. For this reason, the two techniques complement each other and depending on the specific case they should be used in the most appropriate way to get the best results. Higher frequency experiments might give different results since the fraction of excited spins decreases with increasing field, as the ratio of excitation bandwidth to spectral width decreases. This affects PELDOR to the square (observer and pump), but LaserIMD only linearly. The balance between laser and microwave partial excitation might give different results. For this reason sensitivity comparison in Q-band considering various experimental conditions are underway.

In a general perspective, the triplet-based spin labelling methodology has the potential to introduce highly impactful applications in a wide range of different bio-molecular systems, starting from proteins where the prosthetic group can work as photo-active spin centre: photosynthetic proteins, heme proteins and flavoproteins. Appropriate spin labelling protocols can finally extend this novel strategy to any macromolecular system with a more general impact in structural biochemistry.

#### Acknowledgments

The authors thank all collaborators involved in the realisation of the work reviewed in this contribution and whose names are given in the corresponding references.

#### Disclosure statement

No potential conflict of interest was reported by the authors.

#### Funding

Financial support from the University of Padova [PRAT2014-CPDA145097/14] is gratefully acknowledged.

#### References

- [1] O. Schiemann, T.F. Prisner, and Q. Rev. Biophys. **40** (1), 1 (2007).
- [2] S.K. Misra and J.H. Freed, *Multifrequency Electron Paramagnetic Resonance: Theory and Applications*, 1st ed. (Wiley-VCH Verlag GmbH & Co, New York, 2011). p. 545.
- [3] Y.D. Tsvetkov and Y.A. Grishin, *Instrum. Exp. Tech.* **52** (5), 615 (2009).
- [4] G. Jeschke, *Annu. Rev. Phys. Chem.* **63**, 419 (2012).
- [5] R. Ward, A. Bowman, E. Sozudogru, H. El-Mkami, T. Owen-Hughes, and D.G. Norman, *J. Magn. Reson.* **207** (1), 164 (2010).
- [6] T. Schmidt, M.A. Wälti, J.L. Barber, E.J. Hustedt, and G.M. Clore, *Angew. Chemie Int. Ed.* **2** (2), 147 (2015).
- [7] S. Saxena and J.H. Freed, *J. Chem. Phys.* **107** (5), 1317 (1997).
- [8] S. Milikisyants, F. Scarpelli, M.G. Finiguerra, M. Ubbink, and M. Huber, *J. Magn. Reson.* **201** (1), 48 (2009).
- [9] J.E. Banham, C.M. Baker, S. Ceola, I.J. Day, G.H. Grant, E.J.J. Groenen, C.T. Rodgers, G. Jeschke, and C.R. Timmel, *J. Magn. Reson.* **191** (2), 202 (2008).
- [10] J.P. Klare and H.J. Steinhoff, *Photosynth. Res.* **102** (2–3), 377 (2009).
- [11] A.J. Fielding, M.G. Concilio, G. Heaven, and M.A. Hollas, *Molecules* **19** (10), 16998 (2014).
- [12] A.M. Raitisimring, C. Gunanathan, A. Potapov, I. Efremenko, J.M.L. Martin, D. Milstein, and D. Goldfarb, *J. Am. Chem. Soc.* **129** (46), 14138 (2007).
- [13] D. Goldfarb, *Phys. Chem. Chem. Phys.* **16** (21), 9685 (2014).
- [14] L. Garbuio, E. Bordignon, E.K. Brooks, W.L. Hubbell, G. Jeschke, and M. Yulikov, *J. Phys. Chem. B* **117** (11), 3145 (2013).
- [15] M. Di Valentin, M. Albertini, M.G. Dal Farra, E. Zurlo, L. Orian, A. Polimeno, M. Gobbo, and D. Carbonera, *Chem. A Eur. J.* **22** (48), 17204 (2016).
- [16] M. Di Valentin, M. Albertini, E. Zurlo, M. Gobbo, and D. Carbonera, *J. Am. Chem. Soc.* **136** (18), 6582 (2014).
- [17] W. Lubitz, F. Lendzian, and R. Bittl, *Acc. Chem. Res.* **35** (5), 313 (2002).
- [18] C.W. Kay, M. Di Valentin, and K. Möbius, *Sol. Energ. Mater. Sol. Cells* **38** (1–4), 111 (1995).
- [19] C.E. Tait, P. Neuhaus, H.L. Anderson, and C.R. Timmel, *J. Am. Chem. Soc.* **137** (20), 6670 (2015).
- [20] L. Bolzonello, M. Albertini, E. Collini, and M. Di Valentin, *Phys. Chem. Chem. Phys.* **19**, 27173 (2017).

- [21] M. Ji, S. Ruthstein, and S. Saxena, *Acc. Chem. Res.* **47** (2), 688 (2014).
- [22] C.W.M. Kay, H.E. Mkami, R. Cammack, and R.W. Evans, *J. Am. Chem. Soc.* **129** (16), 4868 (2007).
- [23] A.M. Bowen, M.W. Jones, J.E. Lovett, T.G. Gaule, M.J. McPherson, J.R. Dilworth, C.R. Timmel, and J.R. Harmer, *Phys. Chem. Chem. Phys.* **18**, 5981 (2016).
- [24] C. Elsässer, M. Brecht, and R. Bittl, *J. Am. Chem. Soc.* **124** (42), 12606 (2002).
- [25] M. Asada, H. Nagashima, F.H.M. Koua, J.R. Shen, A. Kawamori, and H. Mino, *Biochim. Biophys. Acta Bioenerg.* **1827** (3), 438 (2013).
- [26] M. Di Valentin, M.G. Dal Farra, L. Galazzo, M. Albertini, T. Schulte, E. Hofmann, and D. Carbonera, *Biochim. Biophys. Acta Bioenerg.* **1857** (12), 1909 (2016).
- [27] C. Hintze, D. Bücken, S. Domingo Köhler, G. Jeschke, and M. Drescher, *J. Phys. Chem. Lett.* **7** (12), 2204 (2016).
- [28] M. Gobbo, E. Merli, B. Biondi, S. Oancea, A. Toffoletti, F. Formaggio, and C. Toniolo, *J. Pept. Sci.* **18** (1), 37 (2012).
- [29] G. Jeschke, V. Chechik, P. Ionita, A. Godt, H. Zimmermann, J.E. Banham, C. Timmel, D. Hilger, and H. Jung, *Appl. Magn. Reson.* **498**, 473 (2006).
- [30] M. Di Valentin and D. Carbonera, *J. Phys. B At. Mol. Opt. Phys.* **50**, 162001 (2017).
- [31] D.J. Miller, J. Catmull, R. Puskeiler, H. Tweedale, F.P. Sharples, and R.G. Hiller, *Photosynth. Res.* **86** (1–2), 229 (2005).
- [32] T. Schulte, D.M. Niedzwiedzki, R.R. Birge, R.G. Hiller, T. Polivka, E. Hofmann, and H.A. Frank, *Proc. Natl. Acad. Sci. USA* **106** (49), 20764 (2009).
- [33] M. Di Valentin, S. Ceola, E. Salvadori, G. Agostini, and D. Carbonera, *Biochim. Biophys. Acta Bioenerg.* **1777** (2), 186 (2008).
- [34] M. Di Valentin, C.E. Tait, E. Salvadori, L. Orian, A. Polimeno, and D. Carbonera, *Biochim. Biophys. Acta Bioenerg.* **1837** (1), 85 (2014).
- [35] P. Lueders, G. Jeschke, and M. Yulikov, *J. Phys. Chem. Lett.* **2** (6), 604 (2011).
- [36] W.B. Mims, *Phys. Rev. B* **5**, 2409 (1969).
- [37] A. Schweiger and G. Jeschke, *Principles of pulse electron paramagnetic resonance* (Oxford University Press, Oxford, 2001), pp. 67–92.
- [38] A. Marko, V. Denysenkov, and T.F. Prisner, *Mol. Phys.* **111** (18–19), 2834 (2013).
- [39] G. Jeschke, *Chemphyschem* **3** (11), 927 (2002).
- [40] M. Montalti, A. Credi, L. Prodi, and M. Gandolfi, *Handbook of Photochemistry*, 3rd ed. (Taylor & Francis, New York, 2006).

## Appendix

### A.1. PELDOR

$$\chi = (-1 + \cos[t_p \omega_p]) \times \frac{(p_\alpha + p_\beta)(k_3 - k_1/2) + (p_\alpha - p_\beta)(k_4 - k_2/2)}{(p_\alpha + p_\beta)k_1 + (p_\alpha - p_\beta)k_2} \quad (\text{A1})$$

$$V_0 = 2\Phi_1(p_{-1} - p_0)((p_\alpha + p_\beta)k_1 + (p_\alpha - p_\beta)k_2) \quad (\text{A2})$$

$$k_1 = -\frac{1}{2\sqrt{2}} \left( -\sin \left[ \sqrt{2} t_{\text{ob}} \omega_{\text{d}} \right] \right.$$

$$\begin{aligned} & + \cos \left[ \sqrt{2} t_{\text{ob}} \omega_{\text{ob}} \right]^2 \left( 1 - 2e^{i\epsilon_2/2} \cos \left[ \frac{\tau_2 \omega_{\text{dd}}}{2} \right] \right. \\ & \left. - e^{i(\epsilon_1 + \epsilon_2)} \cos \left[ (\tau_1 + \tau_2) \omega_{\text{dd}} \right] - 2e^{(1/2)i(\epsilon_1 + 2\epsilon_2)} \right. \\ & \left. \times \cos \left[ \frac{1}{2} (\tau_1 + 2\tau_2) \omega_{\text{dd}} \right] \right) \sin \left[ \sqrt{2} t_{\text{ob}} \omega_{\text{ob}} \right] \\ & + \cos \left[ \sqrt{2} t_{\text{ob}} \omega_{\text{ob}} \right]^2 \left( 1 + e^{-i\epsilon_1} \cos \left[ \tau_1 \omega_{\text{dd}} \right] + e^{-(i\epsilon_1/2)} \right. \\ & \left. \times \left( 2 \cos \left[ \frac{\tau_1 \omega_{\text{dd}}}{2} \right] + 2e^{i\epsilon_2/2} \cos \left[ \frac{1}{2} (\tau_1 - \tau_2) \omega_{\text{dd}} \right] \right) \right. \\ & \left. + 4e^{i\epsilon_2/2} \cos \left[ \frac{\tau_2 \omega_{\text{dd}}}{2} \right] + e^{i\epsilon_2} (\cos \left[ \tau_2 \omega_{\text{dd}} \right] \right. \right. \\ & \left. \left. + e^{i\epsilon_1} \cos \left[ (\tau_1 + \tau_2) \omega_{\text{dd}} \right] \right) \right. \\ & \left. + e^{i\epsilon_1/2} \left( 2e^{i\epsilon_2/2} \cos \left[ \frac{1}{2} (\tau_1 + \tau_2) \omega_{\text{dd}} \right] \right. \right. \\ & \left. \left. + 2e^{i\epsilon_2} \cos \left[ \frac{1}{2} (\tau_1 + 2\tau_2) \omega_{\text{dd}} \right] \right) \right) \sin \left[ \sqrt{2} t_{\text{ob}} \omega_{\text{ob}} \right]^3 \Big) \\ k_2 = & -\frac{1}{2\sqrt{2}} \left( \cos \left[ \sqrt{2} t_{\text{ob}} \omega_{\text{ob}} \right]^2 \sin \left[ \sqrt{2} t_{\text{ob}} \omega_{\text{ob}} \right] \right. \\ & \left. \times \left( 2ie^{i\epsilon_2/2} \sin \left[ \frac{\tau_2 \omega_{\text{dd}}}{2} \right] + ie^{(1/2)i(\epsilon_1 + 2\epsilon_2)} \right. \right. \\ & \left. \left. \times \left( e^{i\epsilon_1/2} \sin \left[ (\tau_1 + \tau_2) \omega_{\text{dd}} \right] \right. \right. \right. \\ & \left. \left. \left. + 2 \sin \left[ \frac{1}{2} (\tau_1 + 2\tau_2) \omega_{\text{dd}} \right] \right) \right) \right) \\ & + \cos \left[ \sqrt{2} t_{\text{ob}} \omega_{\text{ob}} \right]^2 \sin \left[ \sqrt{2} t_{\text{ob}} \omega_{\text{ob}} \right]^3 \\ & \left. \times \left( 2ie^{-(i\epsilon_1/2)} \sin \left[ \frac{\tau_1 \omega_{\text{dd}}}{2} \right] + ie^{-i\epsilon_1} \sin \left[ \tau_1 \omega_{\text{dd}} \right] \right. \right. \\ & \left. \left. + e^{i\epsilon_2/2} \left( 2ie^{-(i\epsilon_1/2)} \sin \left[ \frac{1}{2} (\tau_1 - \tau_2) \omega_{\text{dd}} \right] \right. \right. \right. \\ & \left. \left. \left. - 4i \sin \left[ \frac{\tau_2 \omega_{\text{dd}}}{2} \right] - 2ie^{i\epsilon_1/2} \sin \left[ \frac{1}{2} (\tau_1 + \tau_2) \omega_{\text{dd}} \right] \right) \right) \right. \\ & \left. \left. + e^{i\epsilon_2} (-i \sin \left[ \tau_2 \omega_{\text{dd}} \right] - ie^{i\epsilon_1} \sin \left[ (\tau_2) \omega_{\text{dd}} \right]) \right) \right) \\ k_3 = & \frac{1}{2\sqrt{2}} \left( e^{i\epsilon_2/2} \cos \left[ \sqrt{2} t_{\text{ob}} \omega_{\text{ob}} \right]^2 \cos \left[ \frac{\tau_2 \omega_{\text{dd}}}{2} \right] \right. \\ & \left. \times \sin \left[ \sqrt{2} t_{\text{ob}} \omega_{\text{ob}} \right] - e^{-(1/2)i(\epsilon_1 - \epsilon_2)} \cos \left[ \sqrt{2} t_{\text{ob}} \omega_{\text{ob}} \right]^2 \right. \\ & \left. \times \left( e^{i\epsilon_1} \cos \left[ \frac{1}{2} (\tau_1 - \tau_2) \omega_{\text{dd}} \right] + 2e^{i\epsilon_1/2} \cos \left[ \frac{\tau_2 \omega_{\text{dd}}}{2} \right] \right. \right. \\ & \left. \left. + \cos \left[ \frac{1}{2} (\tau_1 + \tau_2) \omega_{\text{dd}} \right] \right) \sin \left[ \sqrt{2} t_{\text{ob}} \omega_{\text{ob}} \right]^3 \right) \\ k_4 = & \frac{1}{2\sqrt{2}} \left( ie^{i\epsilon_2/2} \cos \left[ \sqrt{2} t_{\text{ob}} \omega_{\text{ob}} \right]^2 \sin \left[ \sqrt{2} t_{\text{ob}} \omega_{\text{ob}} \right] \right. \\ & \left. \times \sin \left[ \frac{\tau_2 \omega_{\text{dd}}}{2} \right] + ie^{-(1/2)i(\epsilon_1 - \epsilon_2)} \cos \left[ \sqrt{2} t_{\text{ob}} \omega_{\text{ob}} \right]^2 \right. \\ & \left. \times \sin \left[ \sqrt{2} t_{\text{ob}} \omega_{\text{ob}} \right]^3 \left( e^{i\epsilon_1} \sin \left[ \frac{1}{2} (\tau_1 - \tau_2) \omega_{\text{dd}} \right] \right. \right. \\ & \left. \left. - 2e^{i\epsilon_1/2} \sin \left[ \frac{\tau_2 \omega_{\text{dd}}}{2} \right] - \sin \left[ \frac{1}{2} (\tau_1 + \tau_2) \omega_{\text{dd}} \right] \right) \right) \quad (\text{A3}) \end{aligned}$$

$$\begin{aligned}
\Delta_1 = & \left( -e^{i\epsilon_1} \cos [\tau_1 \omega_{dd}] \sin \left[ \sqrt{2} t_{ob} \omega_{ob} \right]^4 \right. \\
& + \left( 1 + 2e^{i\epsilon_1/2} \cos \left[ \frac{\tau_1 \omega_{dd}}{2} \right] \right) \cos \left[ \sqrt{2} t_{ob} \omega_{ob} \right]^2 \\
& \sin \left[ \sqrt{2} t_{ob} \omega_{ob} \right]^2 \left. / \left( (p_\alpha + p_\beta) (-e^{i\epsilon_1} \right. \right. \\
& + \left( e^{i\epsilon_1} - e^{i(2\epsilon_1+\epsilon_2)} \cos [(\tau_1 + \tau_2) \omega_{dd}] - 2e^{(1/2)i(3\epsilon_1+2\epsilon_2)} \right. \\
& \times \cos \left[ \frac{1}{2} (\tau_1 + 2\tau_2) \omega_{dd} \right] \right) \cos \left[ \sqrt{2} t_{ob} \omega_{ob} \right]^2 \\
& + \left( e^{i\epsilon_1} + 2e^{i\epsilon_1/2} \cos \left[ \frac{\tau_1 \omega_{dd}}{2} \right] + \cos [\tau_1 \omega_{dd}] \right. \\
& + 2e^{\frac{1}{2}i(\epsilon_1+\epsilon_2)} \cos \left[ \frac{1}{2} (\tau_1 - \tau_2) \omega_{dd} \right] - 2e^{(1/2)i(3\epsilon_1+\epsilon_2)} \\
& \times \cos \left[ \frac{1}{2} (\tau_1 - \tau_2) \omega_{dd} \right] + e^{i(\epsilon_1+\epsilon_2)} \cos [\tau_2 \omega_{dd}] \\
& - 2e^{(1/2)i(\epsilon_1+\epsilon_2)} \cos \left[ \frac{1}{2} (\tau_1 + \tau_2) \omega_{dd} \right] + 2e^{(1/2)i(3\epsilon_1+\epsilon_2)} \\
& \times \cos \left[ \frac{1}{2} (\tau_1 + \tau_2) \omega_{dd} \right] + e^{i(2\epsilon_1+\epsilon_2)} \cos [(\tau_1 + \tau_2) \omega_{dd}] \\
& + 2e^{(1/2)i(3\epsilon_1+2\epsilon_2)} \cos \left[ \frac{1}{2} (\tau_1 + 2\tau_2) \omega_{dd} \right] \left. \right) \\
& \times \cos \left[ \sqrt{2} t_{ob} \omega_{ob} \right]^2 \sin \left[ \sqrt{2} t_{ob} \omega_{ob} \right]^2 + i(p_\alpha - p_\beta) \\
& \times \left( \left( 4e^{(1/2)i(2\epsilon_1+\epsilon_2)} \sin \left[ \frac{\tau_2 \omega_{dd}}{2} \right] + e^{(1/2)i(3\epsilon_1+2\epsilon_2)} \right. \right. \\
& \times \left( e^{i\epsilon_1/2} \sin [(\tau_1 + \tau_2) \omega_{dd}] \right. \\
& + 2 \sin \left[ \frac{1}{2} (\tau_1 + 2\tau_2) \omega_{dd} \right] \left. \right) \left. \right) \cos \left[ \sqrt{2} t_{ob} \omega_{ob} \right]^2 \\
& - \left( -2e^{i\epsilon_1/2} \sin \left[ \frac{\tau_1 \omega_{dd}}{2} \right] - \sin [\tau_1 \omega_{dd}] + e^{(1/2)i(\epsilon_1+\epsilon_2)} \right. \\
& \times \left( -2 \sin \left[ \frac{1}{2} (\tau_1 - \tau_2) \omega_{dd} \right] - 2e^{i\epsilon_1} \right. \\
& \sin \left[ \frac{1}{2} (\tau_1 - \tau_2) \omega_{dd} \right] + 8e^{i\epsilon_1/2} \sin \left[ \frac{\tau_2 \omega_{dd}}{2} \right] \\
& + e^{(1/2)i(\epsilon_1+\epsilon_2)} \sin [\tau_2 \omega_{dd}] + 2 \sin \left[ \frac{1}{2} (\tau_1 + \tau_2) \omega_{dd} \right] \\
& + 2e^{i\epsilon_1} \sin \left[ \frac{1}{2} (\tau_1 + \tau_2) \omega_{dd} \right] + e^{(1/2)i(3\epsilon_1+\epsilon_2)} \\
& \times \sin [(\tau_1 + \tau_2) \omega_{dd}] + 2e^{(1/2)i(2\epsilon_1+\epsilon_2)} \\
& \times \sin \left[ \frac{1}{2} (\tau_1 + 2\tau_2) \omega_{dd} \right] \left. \right) \left. \right) \cos \left[ \sqrt{2} t_{ob} \omega_{ob} \right]^2 \\
& \sin \left[ \sqrt{2} t_{ob} \omega_{ob} \right]^2 \left. \right) \left. \right) \left. \right)
\end{aligned} \tag{A4}$$

$$\begin{aligned}
\Delta_2 = & \left( e^{i\epsilon_1} \sin \left[ \sqrt{2} t_{ob} \omega_{ob} \right]^2 \sin [\tau_1 \omega_{dd}] \right. \\
& + \cos \left[ \sqrt{2} t_{ob} \omega_{ob} \right]^2 \sin \left[ \sqrt{2} t_{ob} \omega_{ob} \right]^2 \\
& \times \left( -2e^{i\epsilon_1/2} \sin \left[ \frac{\tau_1 \omega_{dd}}{2} \right] - e^{i\epsilon_1} \sin [\tau_1 \omega_{dd}] \right) \left. \right) / \\
& \times \left( (p_\alpha + p_\beta) \left( -e^{i\epsilon_1} + e^{i\epsilon_1} \cos \left[ \sqrt{2} t_{ob} \omega_{ob} \right]^2 \right. \right.
\end{aligned}$$

$$\begin{aligned}
& + \left( 2e^{i\epsilon_1/2} \cos \left[ \frac{\tau_1 \omega_{dd}}{2} \right] + \cos [\tau_1 \omega_{dd}] + e^{i\epsilon_1} \right. \\
& + e^{i(\epsilon_1+\epsilon_2)} \cos [\tau_2 \omega_{dd}] + 4 \left( e^{(1/2)i(\epsilon_1+\epsilon_2)} \right. \\
& - e^{(1/2)i(3\epsilon_1+\epsilon_2)} \left. \right) \sin \left[ \frac{\tau_1 \omega_{dd}}{2} \right] \sin \left[ \frac{\tau_2 \omega_{dd}}{2} \right] \\
& \times \cos \left[ \sqrt{2} t_{ob} \omega_{ob} \right]^2 \sin \left[ \sqrt{2} t_{ob} \omega_{ob} \right]^2 \\
& - \left( e^{i(2\epsilon_1+\epsilon_2)} \cos [(\tau_1 + \tau_2) \omega_{dd}] + 2e^{(1/2)i(3\epsilon_1+2\epsilon_2)} \right. \\
& \times \cos \left[ \frac{1}{2} (\tau_1 + 2\tau_2) \omega_{dd} \right] \left. \right) \cos \left[ \sqrt{2} t_{ob} \omega_{ob} \right]^4 \left. \right) \\
& + i(p_\alpha - p_\beta) \left( 4e^{(1/2)i(2\epsilon_1+\epsilon_2)} \cos \left[ \sqrt{2} t_{ob} \omega_{ob} \right]^2 \right. \\
& \times \sin \left[ \frac{\tau_2 \omega_{dd}}{2} \right] - \left( -2e^{i\epsilon_1/2} \sin \left[ \frac{\tau_1 \omega_{dd}}{2} \right] - \sin [\tau_1 \omega_{dd}] \right. \\
& + 8 \left( e^{(1/2)i(2\epsilon_1+\epsilon_2)} + \left( \frac{1}{2} e^{(1/2)i(\epsilon_1+\epsilon_2)} + \frac{1}{2} e^{(1/2)i(3\epsilon_1+\epsilon_2)} \right) \right. \\
& \times \cos \left[ \frac{\tau_1 \omega_{dd}}{2} \right] \sin \left[ \frac{\tau_2 \omega_{dd}}{2} \right] e^{i(\epsilon_1+\epsilon_2)} \sin [\tau_2 \omega_{dd}] \left. \right) \\
& \times \cos \left[ \sqrt{2} t_{ob} \omega_{ob} \right]^2 \sin \left[ \sqrt{2} t_{ob} \omega_{ob} \right]^2 \\
& + \left( e^{i(2\epsilon_1+\epsilon_2)} \sin [(\tau_1 + \tau_2) \omega_{dd}] + 2e^{(1/2)i(3\epsilon_1+2\epsilon_2)} \right. \\
& \times \sin \left[ \frac{1}{2} (\tau_1 + 2\tau_2) \omega_{dd} \right] \left. \right) \cos \left[ \sqrt{2} t_{ob} \omega_{ob} \right]^4 \left. \right) \left. \right) \left. \right)
\end{aligned} \tag{A5}$$

$$\begin{aligned}
\Delta_3 = & \left( e^{i(\epsilon_1+\epsilon_2)} \cos \left[ \sqrt{2} t_{ob} \omega_{ob} \right]^2 \left( \cos \left[ \sqrt{2} t_{ob} \omega_{ob} \right]^2 \right. \right. \\
& \times \left( e^{i\epsilon_1} \cos [\tau_2 \omega_{dd}] + 2e^{i\epsilon_1/2} \cos \left[ \frac{1}{2} (\tau_1 + 2\tau_2) \omega_{dd} \right] \right) \\
& - \cos [(\tau_1 + \tau_2) \omega_{dd}] \sin \left[ \sqrt{2} t_{ob} \omega_{ob} \right]^2 \left. \right) \left. \right) / \\
& \times \left( (p_\alpha + p_\beta) \left( e^{i\epsilon_1} + e^{i\epsilon_1} (-1 + e^{i(\epsilon_1+\epsilon_2)}) \right. \right. \\
& \times \cos [(\tau_1 + \tau_2) \omega_{dd}] + 2e^{(1/2)i(\epsilon_1+2\epsilon_2)} \\
& \times \cos \left[ \frac{1}{2} (\tau_1 + 2\tau_2) \omega_{dd} \right] \left. \right) \cos \left[ \sqrt{2} t_{ob} \omega_{ob} \right]^2 \\
& - \left( e^{i\epsilon_1} + 2e^{i\epsilon_1/2} \cos \left[ \frac{\tau_1 \omega_{dd}}{2} \right] + \cos [\tau_1 \omega_{dd}] \right. \\
& + 2e^{(1/2)i(\epsilon_1+\epsilon_2)} \cos \left[ \frac{1}{2} (\tau_1 - \tau_2) \omega_{dd} \right] - 2e^{(1/2)i(3\epsilon_1+\epsilon_2)} \\
& \times \cos \left[ \frac{1}{2} (\tau_1 - \tau_2) \omega_{dd} \right] + e^{i(\epsilon_1+\epsilon_2)} \cos [\tau_2 \omega_{dd}] \\
& - 2e^{(1/2)i(\epsilon_1+\epsilon_2)} \cos \left[ \frac{1}{2} (\tau_1 + \tau_2) \omega_{dd} \right] + 2e^{(1/2)i(3\epsilon_1+\epsilon_2)} \\
& \times \cos \left[ \frac{1}{2} (\tau_1 + \tau_2) \omega_{dd} \right] + e^{i(2\epsilon_1+\epsilon_2)} \cos [(\tau_1 + \tau_2) \omega_{dd}] \\
& + 2e^{(3\epsilon_1/2)+i\epsilon_2} \cos \left[ \frac{1}{2} (\tau_1 + 2\tau_2) \omega_{dd} \right] \left. \right) \\
& \times \cos \left[ \sqrt{2} t_{ob} \omega_{ob} \right]^2 \sin \left[ \sqrt{2} t_{ob} \omega_{ob} \right]^2 + i(p_\alpha - p_\beta)
\end{aligned}$$

$$\begin{aligned}
& \times \left( - \left( \left( e^{i(2\epsilon_1+\epsilon_2)} \sin [(\tau_1 + \tau_2) \omega_{dd}] + 2e^{(1/2)i(3\epsilon_1+2\epsilon_2)} \right. \right. \right. \\
& \times \sin \left[ \frac{1}{2} (\tau_1 + 2\tau_2) \omega_{dd} \right] + 4e^{(1/2)i(2\epsilon_1+\epsilon_2)} \\
& \times \sin \left[ \frac{\tau_2 \omega_{dd}}{2} \right] \cos \left[ \sqrt{2} t_{ob} \omega_{ob} \right]^2 \\
& + \left( 2e^{i\epsilon_1/2} \sin \left[ \frac{\tau_1 \omega_{dd}}{2} \right] + \sin [\tau_1 \omega_{dd}] \right. \\
& + \left( 2e^{(1/2)i(\epsilon_1+\epsilon_2)} \sin \left[ \frac{1}{2} (\tau_1 - \tau_2) \omega_{dd} \right] \right. \\
& + 2e^{(1/2)i(3\epsilon_1+\epsilon_2)} \sin \left[ \frac{1}{2} (\tau_1 - \tau_2) \omega_{dd} \right] - 8 \\
& \times e^{(1/2)i(2\epsilon_1+\epsilon_2)} \sin \left[ \frac{\tau_2 \omega_{dd}}{2} \right] - e^{i(\epsilon_1+\epsilon_2)} \sin [\tau_2 \omega_{dd}] \\
& - 2e^{(1/2)i(\epsilon_1+\epsilon_2)} \sin \left[ \frac{1}{2} (\tau_1 + \tau_2) \omega_{dd} \right] - 2e^{(1/2)i(3\epsilon_1+\epsilon_2)} \\
& \times \sin \left[ \frac{1}{2} (\tau_1 + \tau_2) \omega_{dd} \right] - e^{i(2\epsilon_1+\epsilon_2)} \sin [(\tau_1 + \tau_2) \omega_{dd}] \\
& \left. \left. \left. - 2e^{(1/2)i(3\epsilon_1+2\epsilon_2)} \sin \left[ \frac{1}{2} (\tau_1 + 2\tau_2) \omega_{dd} \right] \right) \right) \right) \\
& \times \sin \left[ \sqrt{2} t_{ob} \omega_{ob} \right]^2 \cos \left[ \sqrt{2} t_{ob} \omega_{ob} \right]^2 \Big) \Big) \quad (A6)
\end{aligned}$$

$$\begin{aligned}
\Delta_4 = & \left( e^{i(\epsilon_1+\epsilon_2)} \cos \left[ \sqrt{2} t_{ob} \omega_{ob} \right]^2 \left( -e^{i\epsilon_1} \cos \left[ \sqrt{2} t_{ob} \omega_{ob} \right]^2 \right. \right. \\
& \times \sin [\tau_2 \omega_{dd}] - 2e^{i\epsilon_1/2} \sin \left[ \frac{1}{2} (\tau_1 + 2\tau_2) \omega_{dd} \right] \\
& + \sin \left[ \sqrt{2} t_{ob} \omega_{ob} \right]^2 \left( \sin [(\tau_1 + \tau_2) \omega_{dd}] + 2e^{i\epsilon_1/2} \right. \\
& \times \sin \left[ \frac{1}{2} (\tau_1 + 2\tau_2) \omega_{dd} \right] \Big) \Big) \Big) \Big) / \\
& \times \left( (p_\alpha + p_\beta) \left( -e^{i\epsilon_1} + \left( e^{i\epsilon_1} - e^{i(2\epsilon_1+\epsilon_2)} \right. \right. \right. \\
& \times \cos [(\tau_1 + \tau_2) \omega_{dd}] - 2e^{(3i\epsilon_1/2)+i\epsilon_2} \\
& \times \cos \left[ \frac{1}{2} (\tau_1 + 2\tau_2) \omega_{dd} \right] \Big) \cos \left[ \sqrt{2} t_{ob} \omega_{ob} \right]^2 \\
& + \left( e^{i\epsilon_1} + 2e^{i\epsilon_1/2} \cos \left[ \frac{\tau_1 \omega_{dd}}{2} \right] + \cos [\tau_1 \omega_{dd}] \right. \\
& + 2e^{(1/2)i(\epsilon_1+\epsilon_2)} \cos \left[ \frac{1}{2} (\tau_1 - \tau_2) \omega_{dd} \right] \\
& - 2e^{(1/2)i(3\epsilon_1+\epsilon_2)} \cos \left[ \frac{1}{2} (\tau_1 - \tau_2) \omega_{dd} \right] + e^{i(\epsilon_1+\epsilon_2)} \\
& \times \cos [\tau_2 \omega_{dd}] - 2e^{(1/2)i(\epsilon_1+\epsilon_2)} \cos \left[ \frac{1}{2} (\tau_1 + \tau_2) \omega_{dd} \right] \\
& + 2e^{(1/2)i(3\epsilon_1+\epsilon_2)} \cos \left[ \frac{1}{2} (\tau_1 + \tau_2) \omega_{dd} \right] \\
& \left. \left. \left. + e^{i(2\epsilon_1+\epsilon_2)} \cos [(\tau_1 + \tau_2) \omega_{dd}] + 2e^{(3i\epsilon_1/2)+i\epsilon_2} \right) \right) \right)
\end{aligned}$$

$$\begin{aligned}
& \times \cos \left[ \frac{1}{2} (\tau_1 + 2\tau_2) \omega_{dd} \right] \Big) \\
& \times \cos \left[ \sqrt{2} t_{ob} \omega_{ob} \right]^2 \sin \left[ \sqrt{2} t_{ob} \omega_{ob} \right]^2 + i(p_\alpha - p_\beta) \\
& \times \left( \left( 4e^{(1/2)i(2\epsilon_1+\epsilon_2)} \sin \left[ \frac{\tau_2 \omega_{dd}}{2} \right] + e^{i(2\epsilon_1+\epsilon_2)} \right. \right. \\
& \times \sin [(\tau_1 + \tau_2) \omega_{dd}] + e^{(1/2)i(3\epsilon_1+2\epsilon_2)} 2 \\
& \times \sin \left[ \frac{1}{2} (\tau_1 + 2\tau_2) \omega_{dd} \right] \Big) \cos \left[ \sqrt{2} t_{ob} \omega_{ob} \right]^2 \\
& - \left( -2e^{i\epsilon_1/2} \sin \left[ \frac{\tau_1 \omega_{dd}}{2} \right] - \sin [\tau_1 \omega_{dd}] \right. \\
& + e^{(1/2)i(\epsilon_1+\epsilon_2)} \left( -2 \sin \left[ \frac{1}{2} (\tau_1 - \tau_2) \omega_{dd} \right] \right. \\
& - 2e^{i\epsilon_1} \sin \left[ \frac{1}{2} (\tau_1 - \tau_2) \omega_{dd} \right] + 8e^{i\epsilon_1/2} \sin \left[ \frac{\tau_2 \omega_{dd}}{2} \right] \\
& + e^{(1/2)i(\epsilon_1+\epsilon_2)} \sin [\tau_2 \omega_{dd}] + 2 \sin \left[ \frac{1}{2} (\tau_1 + \tau_2) \omega_{dd} \right] \\
& + 2e^{i\epsilon_1} \sin \left[ \frac{1}{2} (\tau_1 + \tau_2) \omega_{dd} \right] + e^{(1/2)i(3\epsilon_1+\epsilon_2)} \\
& \times \sin [(\tau_1 + \tau_2) \omega_{dd}] + 2e^{(1/2)i(2\epsilon_1+\epsilon_2)} \\
& \times \sin \left[ \frac{1}{2} (\tau_1 + 2\tau_2) \omega_{dd} \right] \Big) \Big) \cos \left[ \sqrt{2} t_{ob} \omega_{ob} \right]^2 \\
& \times \sin \left[ \sqrt{2} t_{ob} \omega_{ob} \right]^2 \Big) \Big) \quad (A7)
\end{aligned}$$

$$\epsilon_1 = \tau_1 (2D - 2\Omega_D)$$

$$\epsilon_2 = \tau_2 (2D - 2\Omega_D) \quad (A8)$$

## A.2. LaserIMD

$$\begin{aligned}
V_0 = & \frac{1}{2} (p_\alpha - p_\beta) e^{-2i\tau\omega_r} \sin[t_{ob}\omega_{ob}] \left( - (1 + 2e^{i\tau\omega_r}) \right. \\
& \times \cos[t_{ob}\omega_{ob}]^2 + e^{2i\tau\omega_r} \sin[t_{ob}\omega_{ob}]^2 \Big) \quad (A9)
\end{aligned}$$

$$\begin{aligned}
\lambda = & \left( \cos[t_{ob}\omega_{ob}]^2 \left( -1 - 2e^{i\tau\omega_r} + 2e^{i\tau\omega_r} \Phi_t(p_{+1} + p_{-1}) \right. \right. \\
& \times \cos[\tau\omega_{dd}] + e^{2i\tau\omega_r} \sin[t_{ob}\omega_{ob}]^2 \Big) \\
& \times \left( - (1 + 2e^{i\tau\omega_r}) \cos[t_{ob}\omega_{ob}]^2 + e^{2i\tau\omega_r} \sin[t_{ob}\omega_{ob}]^2 \right) \Big) \quad (A10)
\end{aligned}$$

$$\begin{aligned}
\Delta_1 = & \left( -\cos[t_{ob}\omega_{ob}]^2 \cos[2\tau\omega_{dd}] + e^{2i\tau\omega_r} \sin[t_{ob}\omega_{ob}]^2 \right) \\
& \times \left( \cos[t_{ob}\omega_{ob}]^2 \left( -1 - 2e^{i\tau\omega_r} + 2e^{i\tau\omega_r} \Phi_t(p_{+1} + p_{-1}) \right. \right. \\
& \times \cos[\tau\omega_{dd}] + e^{2i\tau\omega_r} \sin[t_{ob}\omega_{ob}]^2 \Big) \Big) \quad (A11)
\end{aligned}$$

$$\begin{aligned}
\Delta_2 = & \left( i \cos[t_{ob}\omega_{ob}]^2 \sin[2\tau\omega_{dd}] \right) \left( \cos[t_{ob}\omega_{ob}]^2 \left( -1 - 2e^{i\tau\omega_r} \right. \right. \\
& + 2e^{i\tau\omega_r} \Phi_t(p_{+1} + p_{-1}) \cos[\tau\omega_{dd}] \\
& \left. \left. + e^{2i\tau\omega_r} \sin[t_{ob}\omega_{ob}]^2 \right) \right) \quad (A12)
\end{aligned}$$



**CHAPTER** | **7**

**Refocused-echo Laser Induced Modulation  
Dipole Spectroscopy.**





---

# Refocused-echo Laser Induced Modulation Dipole Spectroscopy for accurate distance determination and orientation analysis.

Maria Giulia Dal Farra<sup>‡</sup>, Alice M. Bowen<sup>\*†</sup>, Sabine Richert<sup>†§</sup>, Charles F. J. Larminie<sup>†</sup>, Marina Gobbo<sup>‡</sup>, Chirstiane R. Timmel<sup>†</sup>, Marilena Di Valentin<sup>\*‡</sup>

<sup>†</sup>Centre for Applied Electron Spin Resonance, Inorganic Chemistry Laboratory, Department of Chemistry, University of Oxford, South Parks Road, Oxford OX1 3QR, U.K.

<sup>‡</sup>Dipartimento di Scienze Chimiche, Università di Padova, via Marzolo 1, 35131 Padova, Italy

<sup>§</sup>Current affiliation: Institute for Physical Chemistry, University of Freiburg, Albertstraße 21, 79104 Freiburg, Germany

---

**ABSTRACT:** In this work, an alternative pulse scheme for Laser-Induced Dipolar Modulation Enhancement (LaserIMD), based on the refocused-echo detection sequence, is proposed for accurate zero-time determination and reliable distance analysis. We demonstrate that the real modulation depth in LaserIMD experiments is obtained only by using a refocused echo pulse scheme. When the classic Hahn echo sequence is employed, effects related to the dynamic of the triplet formation process, artificially increase the modulation depth. By performing field-dependent experiments with the new pulse scheme on a bis-labeled model peptide, we show that light-induced pulse dipolar spectroscopy can lead to orientational selectivity which needs to be taken into account in the analysis of the time traces. Making use of this orientation selection, the relative orientation of the photoexcited porphyrin chromophore and the nitroxide radical is obtained.

---

## 1 Introduction

Electron paramagnetic resonance (EPR) pulsed dipolar spectroscopy (PDS) is an invaluable biophysical technique for studying complex biological assemblies [1, 2, 3, 4]. The dipolar interaction between two moieties with nonzero electronic spin is measured and the analysis of the time-trace obtained from the experiment can reveal the relative distance (ca. 1.5 to 8 nm) and orientation distributions of the two moieties [5, 6, 7], providing information about the structure and conformational ensemble of the (bio)molecule(s)

to which these moieties are attached [8, 9]. Typical EPR PDS techniques, such as double electron electron resonance (DEER), also known as pulsed electron double resonance (PELDOR), allows to study systems containing stable centers with non-zero electronic spin, such as radicals or native metal centers and clusters [10, 11, 12]. Radicals are usually introduced in the form of spin-labels such as MTSSL ((1-Oxyl-2,2,5,5-tetramethylpyrroline-3-methyl) methanethiosulfonate) via site directed mutagenesis [13, 14, 15].

Site-directed spin labeling coupled to PDS has enormously increased the scope of nitroxide

probes in the structural investigation of proteins [16]. Despite the versatility of nitroxide labels, much effort has been invested to research alternative probes that could be exploited as endogenous paramagnetic centers in order to reduce the risk of structural changes due to the incorporation of a non-native group in the macromolecule. Additionally native groups are rigidly held within protein structures in contrast to spin-labels attached at surface accessible sites, leading to more compact distance and orientation distributions and enabling a more complete analysis of the molecular properties. In particular, orientation analysis of PDS traces can be used to orientate docked proteins with respect to one another [9].

While traditionally the research of native paramagnetic probes has been mainly focused on metal-based centers such as Fe(III), iron sulfur clusters and manganese clusters, recently, the photoexcited triplet state of organic chromophores has been proposed as a probe for PDS [17, 18]. Many biological molecules, such as photosynthetic proteins and heme proteins, contain moieties that can act as optically activated spin centers, such that they are closed shell in their ground state but form electron spin-active triplet states after laser photoexcitation [19]. Next to being switchable by light, these probes are formed in a spin-polarized state and thus their EPR signals are stronger compared to that of Boltzmann populated paramagnetic centers [20]. Light-induced DEER (LiDEER) [17] and laser-induced magnetic dipole (LaserIMD) spectroscopy [21] are different PDS that allow the dipolar coupling between a photo-induced triplet and a stable radical to be studied. Comparisons between the two techniques have already been carried out both at X-band and at Q-band [22, 23]. In LiDEER, laser photoexcitation is performed at

the beginning of the microwave sequence and the triplet state acts as the detection spin. For this reason, the electron spin polarization can be exploited to enhance the signal. In LaserIMD the dipolar modulation is induced optically switching the triplet state while the signal of the observer spin is detected using a primary echo sequence (Figure 1). In this way laser photoexcitation replaces the pump pulse at the second microwave frequency and the pump efficiency depends on the triplet quantum yield, the illumination conditions and not on the triplet polarization [21, 22]. Since the dipolar modulation is induced by the laser flash instead of the microwave pulse, LaserIMD is dead-time free. Nonetheless, the shape of the LaserIMD trace makes the determination of the zero time not straightforward because the symmetry of first modulation cannot be exploited to this scope.

In this work we analyze the effect of the uncertainty of the zero time determination in LaserIMD on the distance analysis and we propose a modification of the experiment based on the refocused echo sequence called 4PLaserIMD that allows circumventing this problem (Figure 1). We also investigate the possibility of performing an orientationally selective LaserIMD experiment in order to gain information on the relative orientation of the two spin centers.

The measurements have been done on the  $\alpha$ -helix peptide, already used in [17] labeled at the N-terminal end with a tetraphenylporphyrin moiety and with an unnatural amino acid TOAC (4-amino-1-oxyl-2,2,6,6-tetramethylpiperidine-4-carboxylic acid). The chemical structure of the model peptide is shown in Figure 1. The rigidity of this system makes it particularly adapt for investigating orientation selection effects in LaserIMD.

## 2 Materials and Methods

### Sample preparation

For the sample preparation procedure refer to [17]. The concentration of the EPR samples was 100  $\mu\text{M}$  in 98% d-methanol, 2%  $\text{D}_2\text{O}$ . EPR tubes were sealed after several freeze-thaw cycles.

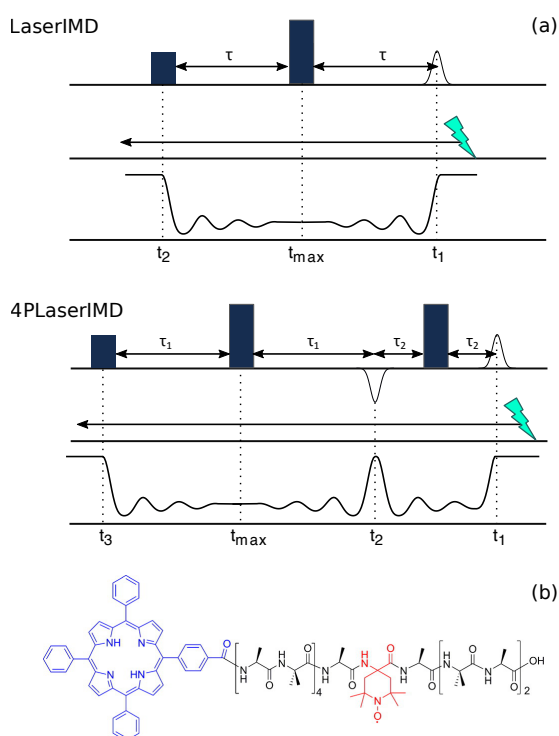


**Figure 1:** (a) pulse sequences and representation of the corresponding dipolar traces for LaserIMD (top) and 4P-LaserIMD (bottom); (b) chemical structure of the model peptide.

### EPR measurements

The pulsed and time-resolved EPR experiments were conducted on a Bruker ELEXSYS E580 spectrometer fitted with a Spinjet Arbitrary Waveform Generator (AWG) using a TII resonator at Q-band (34 GHz). The temperature was maintained at 20 K using liquid helium and a CF935 cryostat with an Oxford Instruments ITC103 temperature controller. Laser excitation of the samples was performed using an OPO pumped by the third harmonic of a

Nd:YAG laser (Opotek, Opolette355), operated at a repetition rate of 20 Hz (5 ns pulses). Laser pulse energies of 2 mJ were used at an excitation wavelength of 512 nm, and the delay after the laser flash (DAF) was set to 1600 ns.

For the electron spin-echo experiments a standard Hahn echo sequence (laser flash-DAF- $\pi/2$  -  $\tau$  -  $\pi$  -  $\tau$  - echo) was employed with a nominal length of 28 ns for all the pulses and a  $\tau$  value of 200 ns. The data were collected with 5 scans and 50 shots-per-point.

The LaserIMD experiments were performed with the pulse sequence proposed in [21] ( $\pi/2$  -  $\tau$  -  $\pi$  -  $t$  - laser flash -  $(\tau - t)$  - echo) with a  $\tau$  of 1500 ns and 28 ns pulse lengths. The ReLaserIMD experiments were performed with a pulse scheme:  $\pi/2$  -  $\tau_1$  -  $\pi$  -  $t$  - laser flash -  $(\tau_1 + \tau_2 - t)$  -  $\pi$  -  $\tau_2$  - echo with 28 ns pulse lengths, a  $\tau_1$  of 1500 ns and a  $\tau_2$  200 ns. In both cases a two-step phase cycle was applied to remove receiver offsets. Data were collected with 50 scans and 50 shots-per-point.

In all the dipolar experiments, the time increment of the dipolar traces was 8 ns.

### EPR data analysis

LaserIMD, ReLaserIMD time traces on the model peptide were analyzed using the Deer-Analysis2018 routine [24]. The study on the determination of the zero-time in the LaserIMD and the ReLaserIMD time traces, was carried out selecting different zero times, for both the datasets, and repeating the procedure of background fitting and Tikhonov regularization. For the LaserIMD, nine different the zero times, separated by 4 ns, were picked around the change of slope of the curve. For the ReLaserIMD, three different zero times, separated by 4 ns, were selected around the symmetry axis of the first modulation. The primary data from the experiments were background corrected by

fitting an exponential decay function to the data. In both cases, the portion of the trace, employed for the background fitting, was kept constant for all the trials. The regularization parameters were determined with the GCV criterion [25].

For the analysis of the orientationally selective ReLaserIMD data, the routine reported in [7], has been used.

### 3 Results and Discussion

In order to accurately analyze the dipolar oscillations and relate this to an inter-spin distance distribution, it is vital to accurately pinpoint the zero-time of the experiment. The zero time determines the start of the first oscillation, which is most pronounced and thus has a major impact on the calculated distance

distribution. The correct determination of the zero-time is particularly important for small inter-spin distances which give rise to high frequency dipolar oscillations. While in LaserIMD the first modulation starts as a baseline drop, in 4PLaserIMD, the symmetry of the first modulation, helps determining the correct zero time.

The data collected with the two techniques, on the porphyrin-based model peptide, are compared in Figure 2. For the LaserIMD data the left branch of the dipolar trace has been used. It can be clearly seen that, since the symmetry about the zero-time is lost in LaserIMD, the zero point has to be picked in the zone where the change of slope between the baseline and the drop of the first modulation occurs. However, this process is not free from bias and there is a wide range of points that could inadvertently be selected as zero-times.

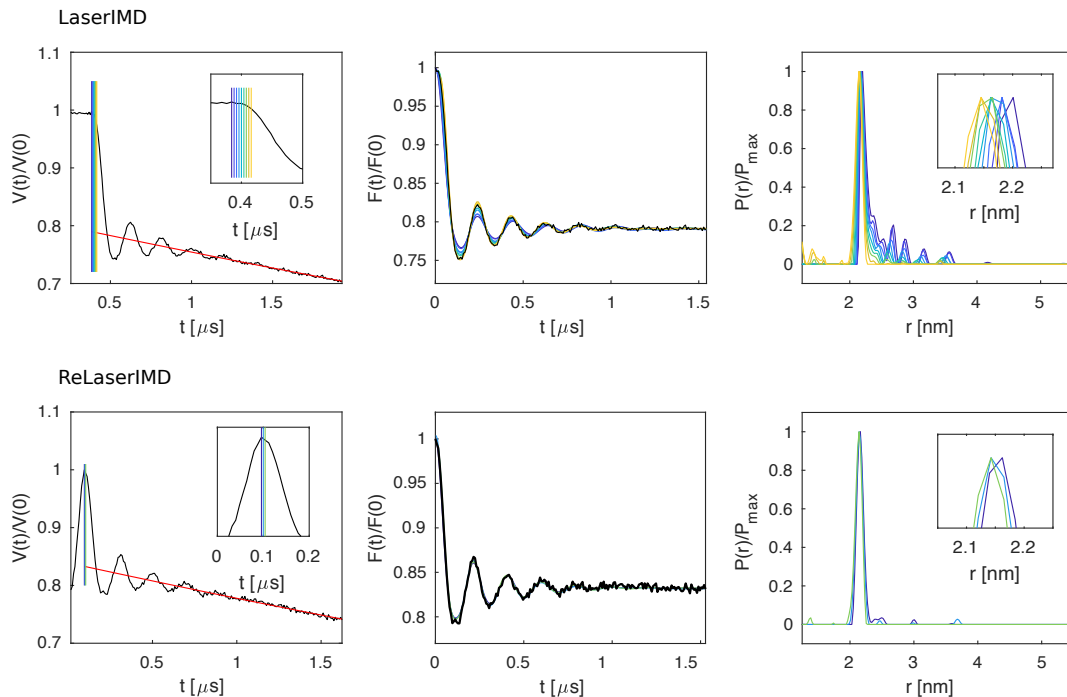


**Figure 2:** Raw dipolar time traces. The selected zero time positions, used in the distance analysis, are indicated in the inset if the right panel. The form factor together with the corresponding fittings and distance distributions are displayed in the central and the right panels respectively. The data in the top row have been collected using the LaserIMD sequence whereas those in the bottom row with the ReLaserIMD sequence.

In [21], a procedure based on symmetrization of the two branches of the LaserIMD trace about the point " $t_{\max}$ " and taking into account also the length of microwave pulses and the delays, has been described. However, the two branches are not always symmetric because the overlap of the tetraphenylporphyrin triplet signal with the nitroxide signal is such that when the laser flash occurs prior to the detection sequence (position (1) in Figure 1) the triplet signal contributes to the detected echo. The extent of the triplet contribution is both time and field dependent further complicating the previously proposed zero-time symmetrization protocol [21] (see Figure S1).

In order to demonstrate that the proposed 4PLaserIMD sequence allows an accurate determination of the zero-time, the distance analysis of both experimental traces, has been performed repeating the Tikhonov regularization procedure, implemented in DeerAnalysis, for a set of zero times selected for the two datasets. As it is possible to notice in the top left panel of Figure 2, for the Hahn echo-based trace there are several points that could be potentially picked as the zero time. Instead, in 4PLaserIMD the situation is less ambiguous and the zero times can be reasonably limited to three options.

Determination of the zero-time affects the form-factor fitting and consequently the distance distribution. The different distributions obtained from the LaserIMD trace have the maxima spread in a range of distances of 0.1 nm, whereas for the 4PLaserIMD this interval is limited to 0.01 nm. The goodness of the fit to the LaserIMD improves when the zero-time is selected toward the end of the considered range (yellow lines in Figure 2). At the same time, the spurious peaks at longer distances with respect to the main peak disappear in the

corresponding distance distributions. The best results are obtained selecting the zero time in a region where the drop of the first modulation has already initiated and therefore it may not represent the most obvious choice.

Beyond the differences already highlighted concerning the exact position of the zero-time, the traces collected with the two techniques differ also in terms of modulation depth. In Figure 3 a comparison between the Hahn echo and the refocused echo LaserIMD experiments is shown. As it can be seen, the modulation depth in the first case is higher. A decrease of modulation depth is observed also going from 3-pulse to 4-pulse DEER and this has been attributed to a dynamic phase shift induced by the pump pulse on the detection spins [26, 27, 28]. However, this does not apply to LaserIMD because the microwave pump pulse is replaced by the optical photoexcitation. One potential explanation is related to the fact that the formation of the triplet state is not instantaneous, for TPP at cryogenic temperatures it occurs on a time scale of 10 ns [29]. The resulting time dependent generation of a magnetic dipole in the TPP moiety as it undergoes inter-system crossing, generates a time dependent magnetic field that initiates a torque on the nitroxide magnetization.

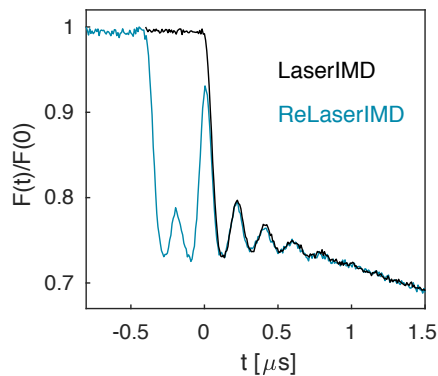


**Figure 3:** Comparison between the intensity of the first modulation in the LaserIMD (black) and in the ReLaserIMD (blue) experiment.

This alters the direction of the nitroxide spin vector modifying the signal observed at the symmetric zero time of the ReLaserIMD compared to that observed when the triplet is generated after the detection sequences. It has previously been proposed that the modulation depth of Hahn echo LaserIMD could be used as a method to determine the amount of triplet state formed [21]. However, if formation of the triplet state causes a change in the projection of the nitroxide magnetization reducing the size of the signal observed after the zero time, this will artificially inflate the modulation depth measured and casts doubt on the appropriateness of this methodology.

We have also analyzed the dependence of the modulation depth on the illumination conditions. In Figure 4 a comparison between the two LaserIMD sequences recorded at different laser powers, is shown. The dipolar traces have been normalized to the corresponding zero times. As expected, the modulation depth, changes with the laser power in both cases. For the same reason different illumination setups, either through the optical window or through the top of the sample holder using an optical fiber, are also affecting the modulation depth (see Figure S2). This proves that illumination is a critical parameter that has to be optimized when performing the LaserIMD experiment.

Not only the modulation depth but also the baseline position varies with the laser power. In both LaserIMD experiments, the baseline of the right branch, corresponding to position " $t_1$ " in Figure 1, changes due to two main reasons: one is related to the formation of the triplet state that, as explained above, induces a torque on the nitroxide echo, the other is that the triplet contributes to the detection echo when laser photoexcitation comes before the Hahn echo sequence (see Figure S1 and S3).

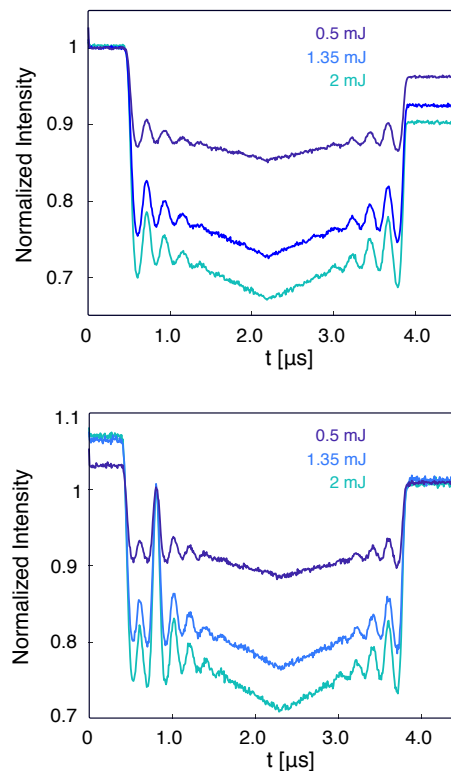


**Figure 4:** LaserIMD (top) and ReLaserIMD (bottom) data collected at different laser powers: 2 (violet), 1.35 (azure) and 0.5 (turquoise) mJ. The traces have been normalized to 1 at the corresponding zero-times.

However, the traces have been collected in a region in which the contribution of the triplet state to the detected echo is minimal. In the case of the ReLaserIMD, in fact, the baselines of the right branch match. This is a further evidence supporting the fact that the modulation depth in the Hahn echo based LaserIMD sequence cannot be completely ascribed to the triplet nitroxide dipolar interaction.

Field-dependent ReLaserIMD experiments also demonstrate significant orientation selection (see in Figure 5). This allows the relative orientation of the nitroxide and dipolar vector to be determined by fitting a library of orientation dependent simulated traces to the experimental data [7]. The results of these simulations agree well with the expected structures, in which TOAC adopts a conformation with the backbone carboxylate group axial to the ring

(pink and blue structures in Figure 5). They also indicate that a small amount of a 2nd chair conformation with the backbone carboxylate group equatorial to the ring (taupe structure Figure 5), may also be present in a lower proportion. The variation in dipolar frequency with field position indicates a strong correlation between the nitroxide frame and the dipolar tensor orientation, suggesting that the spin labeled peptide must be relatively rigid. Indeed the TOAC moiety keeps the nitroxide at a fixed position with respect to the peptide backbone and, in addition, the long axis of the peptide limits the orientational flexibility of the inter-

spin vector.

The presence of orientation selection in the ReLaserIMD experiments implies that analysis of a single trace using DeerAnalysis [24], that employs an orientation independent kernel function, may yield inaccurate distance distribution results. Instead an *ad hoc* routine, that takes into account for the orientational dependence of the modulated echo intensity, is required for the correct elaboration of the PDS data and the extraction of the structural information. As it has already been shown for other PDS techniques, such as DEER [4, 9], orientation selection constitutes a powerful tool in PDS.

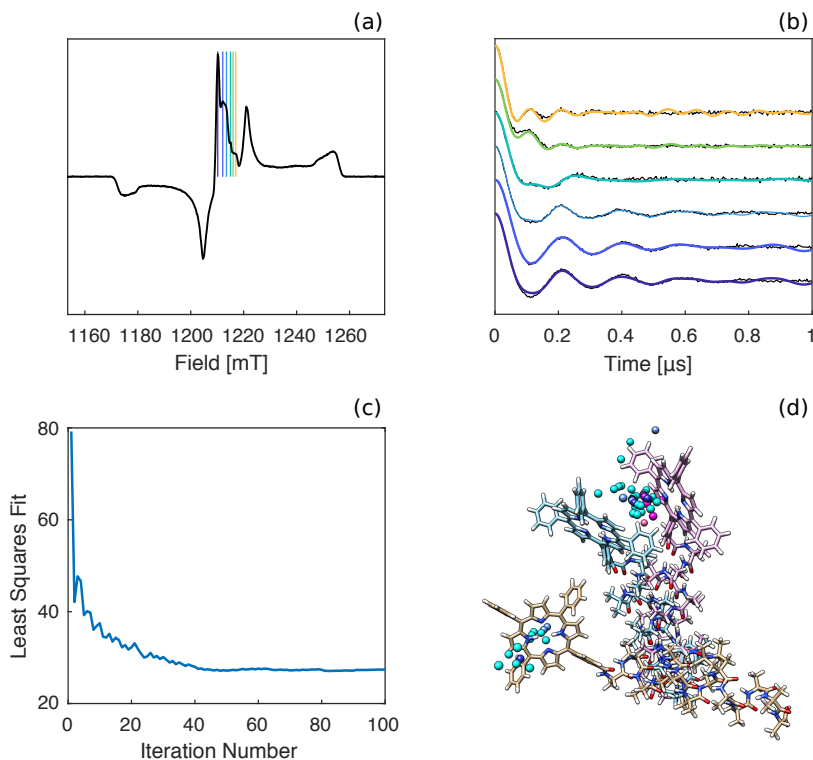


**Figure 5:** (a) Electron-spin echo field sweep in which, the field positions used in the ReLaserIMD experiment, are indicated. (b) ReLaserIMD traces (black) shown with the orientation dependent simulations. The modulation depth has been normalized to 1 for ease of analysis. 100 least squares fitting iterations were performed in which the trace providing the best improvement in fit to experimental data was added to the previous best fits. (c) The least square fit seen as a function of iteration number, by 100 iterations a self-consistent result has been achieved. (d) Orientations determined by the fitting procedure plotted as colored spheres relative to the peptide structures in the g-frame of the nitroxide, represented by the axis system. The color of the spheres relative to the peptide structures in the g-frame of the nitroxide, represented by the axis system. The color of the sphere represents the number of times an orientation contributes to the fit (cyan = 1 to pink = 6). The pink and the blue peptide structures show the range of movement expected for the peptide and are displayed keeping the TOAC group in the conformation determined by DFT calculation [18]. The taupe structure has the TOAC in a second chair conformation, as predicted by [30].

In fact it adds further constraints to the equation describing the dipolar time trace and it can be exploited for obtaining information not only on the interspin distance but also on the reciprocal orientation between the spin centers.

## 4 Conclusions

In the present work we have introduced a variation of the LaserIMD technique based on the refocused echo sequence that allows an accurate determination of the zero time making the distance analysis more reproducible and reliable. We have also shown that modulation depth obtained when using the ReLaserIMD sequence is not affected by the dynamics of triplet formation as it is the case in LaserIMD and can therefore be considered more reliable. Measurements of the dipolar traces at different field positions highlight a strong orientation selection deriving from the spectral selectivity of the detection pulses, that has been correlated to the relative orientation between the two spin centers. These effects enable orientationally selective PDS studies involving photoexcited triplet probes.

### AUTHOR INFORMATION

#### Corresponding Author

\*alice.bowen@chem.ox.ac.uk

\*marilena.divalentin@unipd.it

## Bibliography

- [1] Gunnar Jeschke. DEER Distance Measurements on Proteins. *Annu. Rev. Phys. Chem.*, 63(1):419–446, 2012.
- [2] Gunnar Jeschke. *Interpretation of Dipolar EPR Data in Terms of Protein Structure*, pages 83–120. Springer Berlin Heidelberg, Berlin, Heidelberg, 2011.
- [3] Gunnar Jeschke, M Pannier, and H W Spiess. *Double Electron-Electron Resonance*, pages 493–512. Springer US, Boston, MA, 2002.
- [4] Olav Schiemann and Thomas F Prisner. Long-range distance determinations in biomacromolecules by EPR spectroscopy. *Q. Rev. Biophys.*, 40(01):1, feb 2007.
- [5] Gunnar Jeschke. Distance measurements in the nanometer range by pulse EPR. *ChemPhysChem*, 3:927–932, 2002.
- [6] Bela E. Bode, Jörn Plackmeyer, Thomas F. Prisner, and Olav Schiemann. PELDOR measurements on a nitroxide-labeled Cu(II) porphyrin: Orientation selection, spin-density distribution, and conformational flexibility. *J. Phys. Chem. A*, 112(23):5064–5073, 2008.
- [7] Janet E. Lovett, Markus Hoffmann, Arjen Cnossen, Alexander T J Shutter, Hannah J. Hogben, John E. Warren, Sofia I. Pasqu, Christopher W M Kay, Christiane R. Timmel, and Harry L. Anderson. Probing flexibility in porphyrin-based molecular wires using double electron electron resonance. *J. Am. Chem. Soc.*, 131(38):13852–13859, 2009.
- [8] Alice M. Bowen, Claudia E. Tait, Christiane R. Timmel, and J. R. Harmer. Orientation-Selective DEER Using Rigid Spin Labels, Cofactors, Metals, and Clusters. In Christiane R Timmel and Jeffrey R Harmer, editors, *Struct. Inf. from Spin-Labels Intrinsic Paramagn. Centres Biosci.*, pages 283–327. Springer, Berlin, Heidelberg, 2013.
- [9] Alice M. Bowen, Eachan O. D. Johnson, Francesco Mercuri, Nicola J. Hoskins, Ruihong Qiao, James S. O. McCullagh, Janet E. Lovett, Stephen G. Bell, Weihong Zhou, Christiane R. Timmel, Luet Lok Wong, and Jeffrey R. Harmer. A Structural Model of a P450-Ferredoxin Complex from Orientation-Selective Double Electron–Electron Resonance



- Spectroscopy. *J. Am. Chem. Soc.*, 140(7):2514–2527, feb 2018.
- [10] Irene M C van Amsterdam, Marcellus Ubbink, Gerard W Canters, and Martina Huber. Measurement of a Cu-Cu Distance of 26Å by a Pulsed EPR Method. *Angew. Chemie Int. Ed.*, 42(1):62–64, jan 2003.
- [11] M. Ezhevskaya, Enrica Bordignon, Yevhen Polyhach, L. Moens, Sylvia Dewilde, Gunnar Jeschke, and S. Van Doorslaer. Distance determination between low-spin ferric haem and nitroxide spin label using DEER: the neuroglobin case. *Mol. Phys.*, 111(18-19):2855–2864, 2013.
- [12] Maxie M Roessler, Martin S King, Alan J Robinson, Fraser A Armstrong, Jeffrey Harmer, and Judy Hirst. Direct assignment of EPR spectra to structurally defined iron-sulfur clusters in complex I by double electron-electron resonance. *Proc. Natl. Acad. Sci. U. S. A.*, 107(5):1930–5, feb 2010.
- [13] Enrica Bordignon and Heinz-Jürgen Steinhoff. *Membrane Protein Structure and Dynamics Studied by Site-Directed Spin-Labeling ESR*, pages 129–164. Springer US, Boston, MA, 2007.
- [14] Johann P Klare and Heinz-Jürgen Steinhoff. Spin labeling EPR. *Photosynth. Res.*, 102(2-3):377–390, dec 2009.
- [15] Christoph Abé, Daniel Klose, Franziska Dietrich, Wolfgang H. Ziegler, Yevhen Polyhach, Gunnar Jeschke, and Heinz-Jürgen Steinhoff. Orientation selective DEER measurements on vinculin tail at X-band frequencies reveal spin label orientations. *J. Magn. Reson.*, 216:53–61, mar 2012.
- [16] Wayne L Hubbell, Adrian Gross, Ralf Langen, and Michael A Lietzow. Recent advances in site-directed spin labeling of proteins. *Curr. Opin. Struct. Biol.*, 8(5):649–656, oct 1998.
- [17] Marilena Di Valentin, Marco Albertini, Enrico Zurlo, Marina Gobbo, and Donatella Carbonera. Porphyrin triplet state as a potential Spin label for nanometer distance measurements by peldor spectroscopy. *J. Am. Chem. Soc.*, 136(18):6582–6585, 2014.
- [18] Marilena Di Valentin, Marco Albertini, Maria Giulia Dal Farra, Enrico Zurlo, Laura Orian, Antonino Polimeno, Marina Gobbo, and Donatella Carbonera. Light-Induced Porphyrin-Based Spectroscopic Ruler for Nanometer Distance Measurements. *Chem. - A Eur. J.*, 22(48):17204–17214, nov 2016.
- [19] Marilena Di Valentin, Maria Giulia Dal Farra, Laura Galazzo, Marco Albertini, Tim Schulte, Eckhard Hofmann, and Donatella Carbonera. Distance measurements in peridinin-chlorophyll a -protein by light-induced PELDOR spectroscopy. Analysis of triplet state localization. *Biochim. Biophys. Acta - Bioenerg.*, 1857(12):1909–1916, dec 2016.
- [20] S. P. McGlynn, T. Azumi, and M. Kinoshita. *Molecular Spectroscopy of the Triplet State*. Prentice-Hall, 1969.
- [21] Christian Hintze, Dennis Bückler, Silvia Domingo Köhler, Gunnar Jeschke, and Malte Drescher. Laser-Induced Magnetic Dipole Spectroscopy. *J. Phys. Chem. Lett.*, 7(12):2204–2209, 2016.
- [22] Maria Giulia Dal Farra, S. Ciuti, M. Gobbo, D. Carbonera, and Marilena Di Valentin. Triplet-state spin labels for highly sensitive pulsed dipolar spectroscopy. *Mol. Phys.*, 0(0):1–15, aug 2018.
- [23] Anna Bieber, Dennis Bückler, and Malte Drescher. Light-induced dipolar spectroscopy – A quantitative comparison between LiDEER and LaserIMD. *J. Magn. Reson.*, 296:29–35, nov 2018.
- [24] Gunnar Jeschke, V. Chechik, P. Ionita, A. Godt, H. Zimmermann, J. Banham, Christiane R. Timmel, D. Hilger, and H. Jung. DeerAnalysis2006—a comprehensive software package for analyzing pulsed ELDOR data. *Appl. Magn. Reson.*, 30(3-4):473–498, jun 2006.
- [25] Thomas H. Edwards and Stefan Stoll. Optimal Tikhonov regularization for DEER spectroscopy. *J. Magn. Reson.*, 288:58–68, 2018.

- [26] Michael K. Bowman and Alexander G. Maryasov. Dynamic phase shifts in nanoscale distance measurements by double electron electron resonance (DEER). *J. Magn. Reson.*, 185(2):270–282, 2007.
- [27] Alexander G. Maryasov and Yuri D. Tsvetkov. Formation of the pulsed electron-electron double resonance signal in the case of a finite amplitude of microwave fields. *Appl. Magn. Reson.*, 18(4):583–605, 2000.
- [28] A. D. Milov, Yuriy A. Grishin, S. A. Dzuba, and Yuri D. Tsvetkov. Effect of Pumping Pulse Duration on Echo Signal Amplitude in Four-Pulse PELDOR. *Appl. Magn. Reson.*, 41(1):59–67, 2011.
- [29] David Dolphin, editor. *The Porphyrins Volume III*. Academic Press, 1st edition, 1978.
- [30] Celine Elsässer, Bernhard Monien, Wolfgang Haehnel, and Robert Bittl. Orientation of spin labels in de novo peptides. *Magn. Reson. Chem.*, 43(S1):S26–S33, 2005.

## Supplementary Information

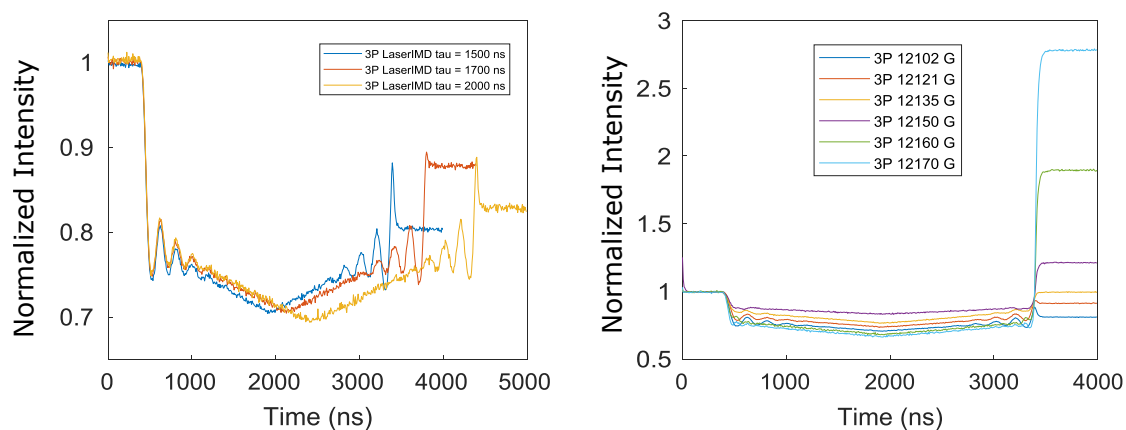


**Figure S1:** Inter-pulse delay (left) and field (right) dependence of the right branch of LaserIMD trace.

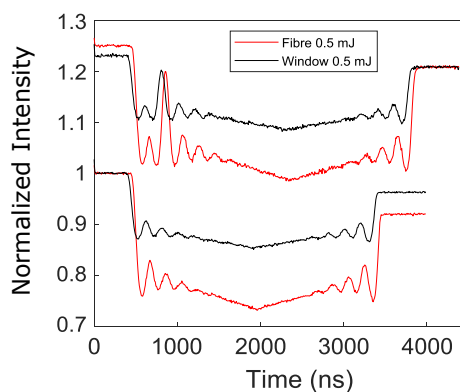


**Figure S2:** Dependence of the modulation depths of ReLaserIMD (top traces) and LaserIMD (bottom traces) on the illumination conditions: using the same laser power, illumination via fiber guarantees better performance compared to illumination through the optical window. The small delay in the traces is related to the different paths of the light before reaching the cavity.

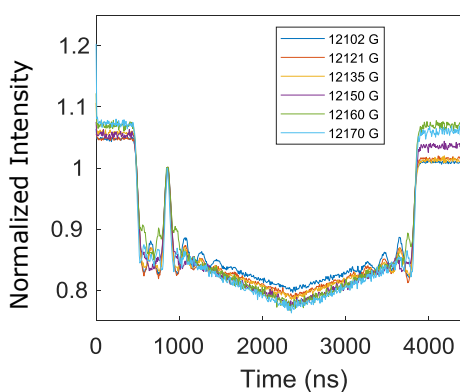


**Figure S3:** Field dependence of the right branch of the ReLaserIMD trace.



**CHAPTER** | **8**

**Light-Induced Pulsed Dipole Spectroscopy in a  
Paradigmatic Hemeprotein**



---

# Light-induced pulsed dipolar spectroscopy in a paradigmatic heme protein

Maria Giulia Dal Farra\*<sup>†‡</sup>, Alice M. Bowen<sup>‡</sup>, Caterina Martin<sup>†</sup>, Sabine Richert<sup>‡§</sup>, Elisabetta Bergantino<sup>†</sup>, Chirstiane R. Timmel<sup>‡</sup>, Marilena Di Valentin<sup>†</sup>

<sup>†</sup> *Dipartimento di Scienze Chimiche, Università di Padova, via Marzolo 1, 35131 Padova, Italy*

<sup>‡</sup> *Centre for Applied Electron Spin Resonance, Inorganic Chemistry Laboratory, Department of Chemistry, University of Oxford, South Parks Road, Oxford OX1 3QR, U.K.*

<sup>§</sup> *Current affiliation: Institute for Physical Chemistry, University of Freiburg, Albertstraße 21, 79104 Freiburg, Germany*

---

**ABSTRACT:** Light-induced pulsed dipolar spectroscopic methods allow to estimate nanometer distances between orthogonal spin labels, one of which is a chromophore triplet state. In this work, accurate distance measurements are reported in singly labeled human neuroglobin. It is shown that Zn-substitution of the heme, to populate the Zn(II) protoporphyrin IX triplet state, makes it possible to perform light-induced dipolar spectroscopy on heme proteins. Three different pulse dipolar techniques, exploiting different properties of the triplet state, have been employed and are compared in this work. In addition to double electron electron resonance (DEER) and to the four-pulse version of laser-induced magnetic dipolar spectroscopy (LaserIMD), relaxation-induced dipolar modulation enhancement (RIDME) is applied, for the first time, to the photoexcited triplet state.

---

During the past two decades, distance measurements in spin-labeled biological macromolecules have become an important application of dipolar spectroscopy. Pulsed Dipolar Spectroscopy (PDS) groups a series of pulse electron paramagnetic resonance (EPR) techniques that measure, via the dipolar electron–electron coupling between two paramagnetic species, distances and distance distributions in the range 1.5–8 nm with high precision and reliability [1, 2, 3, 4]. Among PSD techniques, double electron-electron resonance (DEER), also known as pulsed electron double resonance (PELDOR), plays the main role [5, 6]. EPR techniques

for measuring electron–electron couplings include the Double-Quantum Coherence (DQC) [7, 8] and relaxation-induced dipolar modulation enhancement (RIDME) [9, 10].

Conventionally, PDS measurements are performed between two nitroxide spin labels which have been attached to biological molecules either by site-directed spin labelling (SDSL) or by chemical modification [11]. For proteins, the most commonly used spin label is (1-oxyl-2,2,5,5-tetramethylpyrroline-3-methyl)-methanethiosulfonate (MTSSL), which specifically reacts with the thiol group of cysteine residues [12].

As a contribution to the development of alternative spin labels, which is one main issue in the application of PDS, we have demonstrated that the triplet state of the porphyrin chromophore can be exploited to determine the interspin distances when chemically incorporated into a peptide-based molecular ruler together with a nitroxide probe [13, 14]. Due to the sensitivity acquired from the spin polarization of the photoexcited triplet state in the intersystem crossing process, the method has been applied not only to model systems working as molecular rulers but also to a photosynthetic protein, containing an endogenous carotenoid triplet state probe [15]. The dipolar measurements were performed with light induced DEER (LiDEER), a variation of the conventional 4-pulse DEER sequence where a laser flash is used to generate the triplet state before the application of the microwave pulses. In the meantime, the new technique of laser-induced magnetic dipole (LaserIMD) spectroscopy, based on optical switching of the

dipole–dipole coupling, was proposed as an alternative for triplet-nitroxide dipolar spectroscopy on the same porphyrin-based model system [16].

Not only photosynthetic proteins, but also proteins belonging to other classes, like heme proteins and flavins, contain a photoactive cofactor, which, in principle, can be exploited as an endogenous paramagnetic center [17, 18]. Tentatively, the heme protein cytochrome C, spin labeled with MTSSL at the free cysteine position, was investigated in order to demonstrate that LaserIMD could provide distance measurements between the endogenous prosthetic group and a nitroxide label [16]. However, no triplet state was observed by EPR spectroscopy, as it should have been expected for a low-spin ferric heme. Zn-substitution of the heme is necessary in order to populate the Zn(II) protoporphyrin IX triplet state and perform the triplet–nitroxide dipolar spectroscopy on this class of proteins.

Recently, as a further step in the development of the light-induced PSD techniques, a LaserIMD sequence based on the refocusing echo instead of the Hahn echo detection has been proposed. The new sequence (ReLaserIMD) yields a symmetric zero-time which enables more accurate extraction of the dipolar frequencies [19].

In this work, human neuroglobin has been chosen as a benchmark heme protein to demonstrate the feasibility of the dipolar spectroscopy experiment between a triplet state, photo-generated on the endogenous porphyrin-derivative group, and a nitroxide probe attached to a one of the native cysteines of the protein via SDSL. Human neuroglobin is a good model system in this respect because there are both high resolution X-ray structure and DEER data available [17, 20, 21]. In the work by M. Ezhevskaya *et al.* [17], the DEER trace was measured exploiting the low-spin Fe(III) ion of the heme group as an endogenous probe. Here we have replaced the heme cofactor with the Zn(II) protoporphyrin IX [22] in order to photo-generate a triplet state spin label. Following the nomenclature by M. Ezhevskaya *et al.* [17] the mutant G19 of neuroglobin has been

prepared (see the Supplementary information for detail). The mutant after substitution of the heme cofactor and SDSL with the MTSSL probe is referred to as ZnG19 (Figure 1).

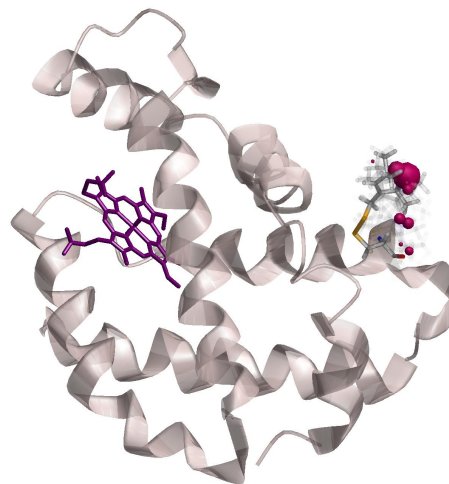


**Figure 1:** Representation of neuroglobin (PDB: 4MPM [21]) in which the rotamers of the MTSSL spin label is attached at the residue Cys120. The calculation of the rotamers has been done by using the software Multiscale Modeling of Macromolecules (MMM) [23].

Here we have employed LiDEER and ReLaserIMD to study the dipolar interaction between the triplet state of Zn protoporphyrin IX and the nitroxide radical in ZnG19 and prove the feasibility of the light-induced PSD experiment on heme proteins. For the first time, the light-induced RIDME (LiRIDME) sequence, in the five-pulse dead-time free version, is also applied to a triplet state in order to exploit the longitudinal relaxation properties of this high spin system.

All three pulse sequences are reported in Figure 2. The experimental traces and distance distributions extracted from the dipolar traces by means of the program DeerAnalysis are shown in Figure 2. The LiDEER experiment on this system gives a very poor result, with a high level of noise and a low modulation depth (6%). The signal to noise ratio S/N, calculated as the ratio of these two parameters, is  $\sim 3.7$ .



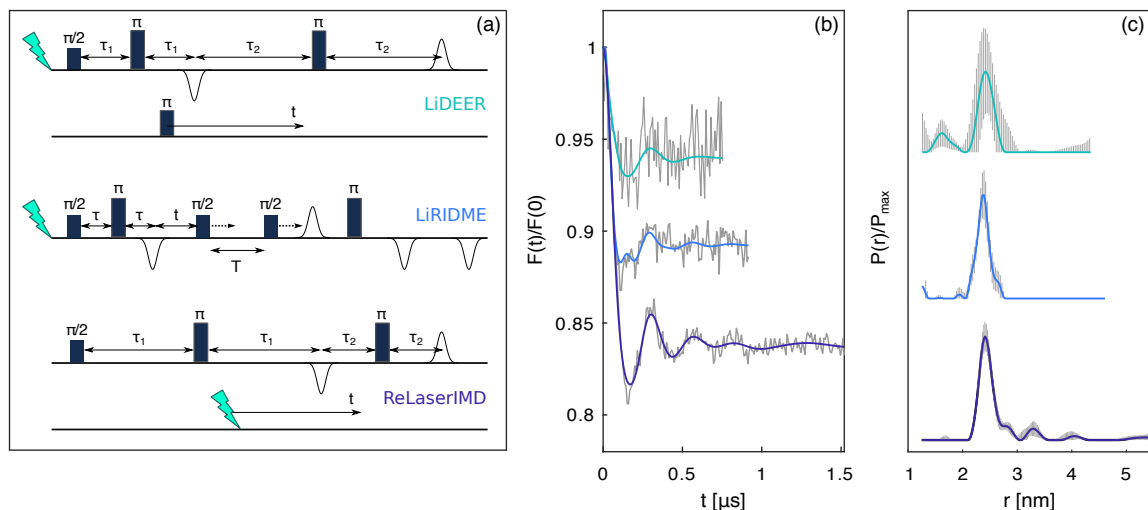


**Figure 2:** LiDEER, LiRIDME and ReLaserIMD pulse schemes (left panel), form factors (grey) and best fits of the LiDEER (turquoise), LiRIDME (azure) and ReLaserIMD (violet) data (central panel) and corresponding distances distributions (right panel). The distance analyses have been performed with DeerAnalysis [24], for LiDEER and ReLaserIMD, and with OvertoneAnalysis [25] for LiRIDME in order to remove spurious peaks related to relaxations with  $\Delta m_S \pm 2$ . The error bars have been obtained using the validation procedure, implemented in both softwares, varying the starting point for the background fitting between 300 and 500 ns and adding 50% of the original noise.

The LiRIDME experiments is instead characterized by a modulation depth of 11% and a S/N  $\simeq 18$ , while for ReLaserIMD the time trace features a modulation depth of 18% and a S/N  $\simeq 49$ . Note that each method has its own specific factors influencing the value of the modulation depth. In ReLaserIMD, the improvement in modulation depth and S/N, allows observing more than two well-resolved periods of the dipolar modulation.

The distance analysis has been performed and for all the three datasets and the same most-probable distance (2.4 nm) and similar distance distributions have been obtained. The excellent agreement with the distance predicted in the MMM analysis (see Figure 1) demonstrates that the triplet state, photo-generated on the endogenous probe after the Zn-substitution protocol, can be successfully exploited to determine the inter-spin distance in the heme-protein. Moreover the availability of diverse pulse schemes that can be applied in systems containing photoexcited triplet states allows one to select, case-by-case, the tech-

nique that warrants the best performance in term of S/N.

In order to get an estimate of the error in the distance distributions, the validation analysis implemented in DeerAnalysis and OvertoneAnalysis has also been performed by checking the influence of the starting point for the background fitting and the noise level on the form factor fitting [24, 25]. The parameters employed for the validation are specified in the caption of Figure 2. As it could be easily expected given the poor S/N of the DEER trace, the distance distribution in this case has a big error band that partially delete also the main distance peak. Instead, the validation analysis performed for both the LiRIDME and the ReLaserIMD time traces, modifies very little the two distance distributions, confirming the reliability of the structural information obtained from these two techniques.

The performance of the three different PSD sequences can be rationalized in terms of the relaxation behavior of the triplet state and the nitroxide probes. For this reason, the triplet state

kinetics, taken at the canonical triplet positions indicated in the echo-detected EPR spectrum, were measured recording the two-pulse Hahn echo intensity as a function of the delay after the laser flash (Figure 3). The kinetics depends

on both the triplet sublevels decay rates to the ground state and on the spin-lattice relaxation time.

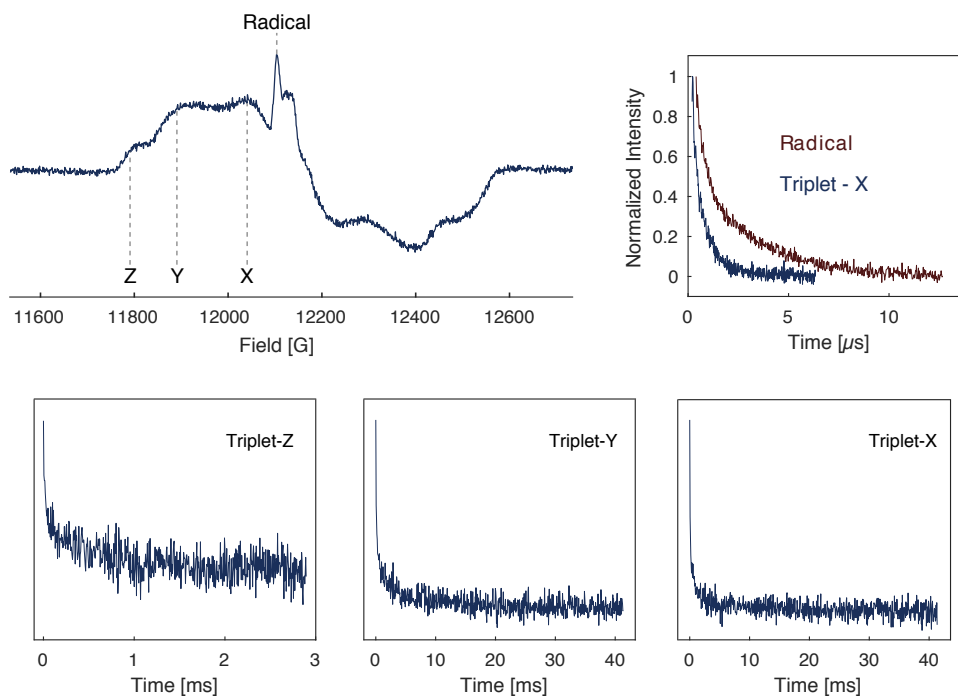


**Figure 3:** Top row: field-swept electron spin echo experiment of ZnG19 recorded with pulse parameters optimized for the triplet. The canonical positions of the triplet are indicated. 2-pulse electron spin echo decay data collected along the X canonical position of the triplet (blue) and at the maximum of the nitroxide (red). Bottom row: integrated Hahn-echo intensity, as a function of the delay after the laser flash, recorded along the canonical positions.

The phase memory time for both the radical and triplet species were measured with variable interpulse delay Hahn echo pulse sequence and are reported in the same figure. All these sets of experiments were performed at 20 K, as was the PDS. The fits of the traces and the corresponding parameters can be found in the Supplementary Information.

The relative phase memory times of the two species make either DEER or LaserIMD the more suited experiment in terms of S/N. While LiDEER depends on the relaxation times of the triplet observer spin, LaserIMD, based on a simple two pulse sequence applied to the nitroxide spin, is instead influenced by the ni-

troxide phase memory time. This is the reason why, in the specific case of neuroglobin, where the phase memory time of Zn protoporphyrin IX in the triplet state is of the order of only 500 ns, the use of the LiDEER is almost precluded, despite the favorable spin polarization of the triplet [26]. Comparison between the two techniques in X-band under equivalent conditions is showing that LiDEER is characterized by an increased S/N [27].

The RIDME performance is also satisfactory since the longitudinal relaxation time of the triplet state is suited for this technique, in a similar way as for metal centers. The only drawback is that the extraction of distance

distributions using a fast relaxing high spin paramagnetic center, as is the case for the triplet state, is affected by the presence of overtones of the dipolar frequencies. For this reason, modulations in the dipolar trace are not clearly distinguishable and distance analysis must take into account the overtone contributions.

In conclusion, in this work we prove accurate determination of distance distributions from LaserIMD and LiRIDME data, using as endogenous probe the triplet state of Zn protoporphyrin IX coupled to a nitroxide spin label in human neuroglobin. This is the first time that the feasibility of the dipolar experiment has been demonstrated for a paradigmatic protein belonging to the class of the hemeproteins. We have also demonstrated that LiRIDME can provide reliable information on the distance between nitroxides and triplet state chromophores similarly to LaserIMD. Both single-frequency techniques become advantageous compared to LiDEER when the chromophore in the triplet state is characterized by short relaxation times.

The availability of different light-induced PDS techniques is an important requisite to broaden the applicability of the triplet spin labels in biological macromolecules. These techniques complement each other and, depending on the nature of the triplet spin label, they can be used interchangeably to take advantage of specific properties of the triplet state.

## Bibliography

- [1] Gunnar Jeschke and Yevhen Polyhach. Distance measurements on spin-labelled biomacromolecules by pulsed electron paramagnetic resonance. *Phys. Chem. Chem. Phys.*, 9(16):1895, 2007.
- [2] Olav Schiemann and Thomas F. Prisner. Long-range distance determinations in biomacromolecules by EPR spectroscopy. *Q. Rev. Biophys.*, 40(01):1, feb 2007.
- [3] Gunnar Jeschke. DEER Distance Measurements on Proteins. *Annu. Rev. Phys. Chem.*, 63(1):419–446, 2012.
- [4] Peter P Borbat and Jack H Freed. *Pulse Dipolar Electron Spin Resonance: Distance Measurements*, pages 1–82. Springer Berlin Heidelberg, Berlin, Heidelberg, 2013.
- [5] A.D. Milov, A.B. Ponomarev, and Yu.D. Tsvetkov. Electron-electron double resonance in electron spin echo: Model biradical systems and the sensitized photolysis of decalin. *Chem. Phys. Lett.*, 110(1):67–72, sep 1984.
- [6] M. Pannier, S. Veit, A. Godt, Gunnar Jeschke, and H.W. Spiess. Dead-Time Free Measurement of Dipole–Dipole Interactions between Electron Spins. *J. Magn. Reson.*, 142(2):331–340, 2000.
- [7] Petr P. Borbat and Jack H. Freed. Multiple-quantum ESR and distance measurements. *Chem. Phys. Lett.*, 313(1-2):145–154, nov 1999.
- [8] Petr P. Borbat and Jack H. Freed. Double-Quantum ESR and Distance Measurements. In Lawrence J. Berliner, Sandra S. Eaton, and Gareth R. Eaton, editors, *Distance Meas. Biol. Syst. by EPR*, pages 383–459. Academic/Plenum, New York, 2000.
- [9] L.V. Kulik, S.A. Dzuba, I.A. Grigoryev, and Yu.D. Tsvetkov. Electron dipole–dipole interaction in ESEEM of nitroxide biradicals. *Chem. Phys. Lett.*, 343(3-4):315–324, aug 2001.
- [10] Sergey Milikisyants, Francesco Scarpelli, Michelina G. Finiguerra, Marcellus Ubbink, and Martina Huber. A pulsed EPR method to determine distances between paramagnetic centers with strong spectral anisotropy and radicals: The dead-time free RIDME sequence. *J. Magn. Reson.*, 201(1):48–56, nov 2009.

- [11] Johann P. Klare and Heinz-Jürgen Steinhoff. Spin labeling EPR. *Photosynth. Res.*, 102(2-3):377–390, dec 2009.
- [12] Lawrence J. Berliner, Jacob Grunwald, H. Olga Hankovszky, and Kalman Hideg. A novel reversible thiol-specific spin label: Papain active site labeling and inhibition. *Anal. Biochem.*, 119(2):450–455, jan 1982.
- [13] Marilena Di Valentin, Marco Albertini, Enrico Zurlo, Marina Gobbo, and Donatella Carbonera. Porphyrin triplet state as a potential Spin label for nanometer distance measurements by peldor spectroscopy. *J. Am. Chem. Soc.*, 136(18):6582–6585, 2014.
- [14] Marilena Di Valentin, Marco Albertini, Maria Giulia Dal Farra, Enrico Zurlo, Laura Orian, Antonino Polimeno, Marina Gobbo, and Donatella Carbonera. Light-Induced Porphyrin-Based Spectroscopic Ruler for Nanometer Distance Measurements. *Chem. - A Eur. J.*, 22(48):17204–17214, nov 2016.
- [15] Marilena Di Valentin, Maria Giulia Dal Farra, Laura Galazzo, Marco Albertini, Tim Schulte, Eckhard Hofmann, and Donatella Carbonera. Distance measurements in peridinin-chlorophyll a -protein by light-induced PEL-DOR spectroscopy. Analysis of triplet state localization. *Biochim. Biophys. Acta - Bioenerg.*, 1857(12):1909–1916, dec 2016.
- [16] Christian Hintze, Dennis Bückner, Silvia Domingo Köhler, Gunnar Jeschke, and Malte Drescher. Laser-Induced Magnetic Dipole Spectroscopy. *J. Phys. Chem. Lett.*, 7(12):2204–2209, 2016.
- [17] M. Ezhevskaya, Enrica Bordignon, Yevhen Polyhach, L. Moens, Sylvia Dewilde, Gunnar Jeschke, and S. Van Doorslaer. Distance determination between low-spin ferric haem and nitroxide spin label using DEER: the neuroglobin case. *Mol. Phys.*, 111(18-19):2855–2864, 2013.
- [18] Erik Schleicher, Radoslaw M. Kowalczyk, Christopher W M Kay, Peter Hegemann, Adelbert Bacher, Markus Fischer, Robert Bittl, Gerald Richter, and Stefan Weber. On the reaction mechanism of adduct formation in LOV domains of the plant blue-light receptor phototropin. *J. Am. Chem. Soc.*, 126(35):11067–11076, 2004.
- [19] Maria Giulia Dal Farra, Alice M. Bowen, Sabine Richert, Charles F. J. Larminie, Marina Gobbo, Christiane R. Timmel, and Marilena Di Valentin. 4-pulse echo LaserIMD for accurate distance determination and orientation analysis. *Under Prep.*, 2018.
- [20] Claire L. Motion, Janet E. Lovett, Stacey Bell, Scott L. Cassidy, Paul A. S. Cruickshank, David R. Bolton, Robert I. Hunter, Hassane El Mkami, Sabine Van Doorslaer, and Graham M. Smith. DEER Sensitivity between Iron Centers and Nitroxides in Heme-Containing Proteins Improves Dramatically Using Broadband, High-Field EPR. *J. Phys. Chem. Lett.*, 7(8):1411–1415, apr 2016.
- [21] Beatriz G. Guimarães, Djemel Hamdane, Christophe Lechauve, Michael C. Marden, and Béatrice Golinelli-Pimpaneau. The crystal structure of wild-type human brain neuroglobin reveals flexibility of the disulfide bond that regulates oxygen affinity. *Acta Crystallogr. Sect. D Biol. Crystallogr.*, 70(4):1005–1014, apr 2014.
- [22] Diane M. Scholler, Ming-Yu R. Wang, and Brian M. Hoffman. [51] Metal-substituted hemoglobin and other hemoproteins. *Methods Enzymol.*, 52:487–493, jan 1978.
- [23] Yevhen Polyhach, Enrica Bordignon, and Gunnar Jeschke. Rotamer libraries of spin labelled cysteines for protein studies. *Phys. Chem. Chem. Phys.*, 13(6):2356–2366, 2011.
- [24] Gunnar Jeschke, V. Chechik, P. Ionita, A. Godt, H. Zimmermann, J. Banham, Christiane R. Timmel, D. Hilger, and H. Jung. DeerAnalysis2006—a comprehensive software package for analyzing pulsed ELDOR data. *Appl. Magn. Reson.*, 30(3-4):473–498, jun 2006.
- [25] Katharina Keller, Valerie Mertens, Mian Qi, Anna I. Nalepa, Adelheid Godt, Anton Savitsky,

- 
- Gunnar Jeschke, and Maxim Yulikov. Computing distance distributions from dipolar evolution data with overtones: RIDME spectroscopy with Gd(III)-based spin labels. *Phys. Chem. Chem. Phys.*, 19(27):17856–17876, 2017.
- [26] M. Fahnenschmidt, R. Bittl, R. Bittl, E. Schloder, W. Haehnel, and W. Lubitz. Characterization of de novo synthesized four-helix bundle proteins with metalloporphyrin cofactors. *Phys. Chem. Chem. Phys.*, 3(18):4082–4090, 2001.
- [27] Maria Giulia Dal Farra, S. Ciuti, M. Gobbo, D. Carbonera, and Marilena Di Valentin. Triplet-state spin labels for highly sensitive pulsed dipolar spectroscopy. *Mol. Phys.*, 0(0):1–15, aug 2018.

## Supplementary Information

### Sample preparation

Human neuroglobin contains three cysteine residues: Cys55 in position 5 of the D helix, Cys120 in position 19 of the G helix and Cys46 in position 7 of the CD loop, and all of them can be exploited as potential target for SDLS. To avoid multiple labeling, a mutant of neuroglobin, containing a single cysteine residue, has been expressed. The choice of the cysteine to label has been made on the basis of the X-ray crystallographic structure (PDB: 4MPM<sup>1</sup>) and of the available DEER data<sup>2</sup>. Cys46 was discarded because it is located in a random coil which is a highly flexible region and this could broaden the distance distribution between the two probes making the measurement of the dipolar trace more difficult. Cys55 was also eliminated because it is located in a buried position and this could diminish the labeling efficiency. As a further confirmation of these considerations, the two DEER traces recorded by M. Ezhevskaya *et al.*<sup>2</sup> labeling Cys55 in one mutant and Cys46 the other gave unsatisfactory signal-to-noise ratios and very poor modulation depths. For this reason, we expressed a neuroglobin mutant in *Escherichia coli*, where only Cys120 was present while Cys55 and Cys46 had been replaced by serine residues. Following the nomenclature by M. Ezhevskaya *et al.*<sup>2</sup> the mutant is called G19. After the expression of G19, the heme group was substituted with the Zn(II) zinc protoporphyrin (ZnPP) following the denaturation-purification-reconstitution procedure described by Scholler *et al.*<sup>3</sup> Subsequently the Cys120 was labeled with the nitroxide probe (1-oxyl-2,2,5,5-tetramethylpyrroline-3-methyl) methanethiosulfonate (MTSSL).

### *Preparation of the Zn-substituted G19 mutant*

The expression and purification protocol was performed following the procedure previously implemented<sup>1,4</sup>. The human neuroglobin DNA coding sequence cloned in the vector pET3a was kindly donated by Professor T. Burmester (Department of Biology, University of Hamburg). The GENART® Site-Directed Mutagenesis System kit was used to make the G19 mutant: Cys46Ser/Cys55Ser. After the mutagenesis, the G19 coding sequence was cloned in pET28a, giving the plasmid pET28hNGB G19. The latter was finally used to transform the *Escherichia coli* strain BL21DE3 Codon Plus RP. The cells were grown at 25°C in TB medium containing 1.2% bactotryptone, 2.4% yeast extract, 0.4% glycerol, 72 mM potassium phosphate buffer, pH 7.5. 200 µg/ml ampicillin, 30 µg/ml chloramphenicol and 1 mM d-amino-levulinic acid were added to the medium. At OD<sub>600</sub> = 0.8 the culture was induced by the isopropyl-1-thio-D- galactopyranoside to a final 0.4 mM concentration and cells were let growing overnight. The cells were then harvested, resuspended in lysis buffer (50 mM Tris-HCl pH 8.0, 1 mM EDTA, 0.5 mM dithiotre-

---

<sup>1</sup>B. G. Guimarães, D. Hamdane, C. Lechauve, M. C. Marden, B. Golinelli-Pimpaneau. *Acta Crystallogr. Sect. D Biol. Crystallogr.*, 70(4):1005–1014, 2014.

<sup>2</sup>M. Ezhevskaya, E. Bordignon, Y. Polyhach, L. Moens, S. Dewilde, G. Jeschke, and S. Van Doorslaer. *Mol. Phys.*, 111(18-19):2855–2864, 2013.

<sup>3</sup>D. M. Scholler, M.-Y. R. Wang, B. M. Hoffman, *Methods Enzymol.* 52:487–493, 1978

<sup>4</sup>S. Dewilde, K. Mees, L. Kiger, C. Lechauve, M. C. Marden, A. Pesce, M. Bolognesi, L. Moens, *Methods Enzymol.* 436:341–357, 2008.

itol) and exposed to three freeze-thaw cycles. After that, sonication was done until the cells completely lysed. The extract was clarified by low (10 min at 10,000 g) and high (60 min at 105,000 g) speed centrifugation. The obtained supernatant was collected and fractionated by 60% ammonium sulphate precipitation. The pellets were dialyzed against 5 mM Tris-HCl pH 8.5 and loaded onto a DEAE Sepharose fast flow column for ion exchange chromatography. The recombinant neuroglobin G19 was eluted by 200 mM NaCl from the Sepharose column, concentrated by Amicon filtration (PM10) and passed through a Sephacryl S200 column for gel filtration. SDS-PAGE was done to test the protein purity and the Bradford reagent was used for measuring protein yield. The ZnPP-substitution was performed following the procedure described by Scholler *et al.*<sup>1</sup> ZnPP was purchased from Sigma Aldrich. All manipulations were performed in the dark because of the light sensitivity of ZnPP. In a first step, the original heme group was removed. In order to prepare the apo-G19, a cold acid acetone solution (50 mL of acetone + 40  $\mu$ L of HCl 6N) was added drop by drop to G19, constantly stirred at  $-20^{\circ}\text{C}$ . White apo-protein flakes were centrifuged for 1 min at 1200 g to separate them from the red heme solution. The supernatant was discarded. The apo-protein was washed with cold acid acetone and again centrifuged. The sediment was dissolved in a minimum amount of water and dialyzed 24 h in  $\text{NaHCO}_3$  1 mM, DTT 0.1 mM and overnight in buffer 5 mM Tris-HCl pH 8.5. The obtained apo-protein was used to prepare ZnPP-substituted neuroglobin. ZnPP was solubilized in 0.1 M NaOH and dissolved in buffer 5 mM Tris-HCl pH 8.5. This was added to the apo-neuroglobin solution, which was then incubated for 4 hours, dialyzed overnight against 5 mM Tris-HCl buffer at pH 8.5 and concentrated by Amicon filtration (PM10). The yield of ZnPP-substituted neuroglobin from apo-protein resulted to be 50% (measured by ZnPP absorbance using  $\epsilon_{424} = 122 \text{ mM}^{-1} \text{ cm}^{-1}$ ). The residual apo-protein, remaining denatured or mis-folded, was easily eliminated by centrifugation.

#### *Spin labeling*

Before starting the spin labeling procedure, the protein was incubated for 30 minutes in a 10 mM DTT solution in 5 mM Tris-HCl pH 8.5 buffer. The sample buffer was exchanged with 5 mM Tris-HCl pH 8.5 using a desalting column. Spin labeling was carried out by adding a 10-fold molar excess of MTSL to the single cysteine G19 mutant. The sample was incubated first for 2 hours at room temperature and then overnight at  $4^{\circ}\text{C}$ . It was then washed in a desalting column to remove the unbound spin label. The labeling yield, determined by CW-EPR, was 68%. The buffer for the EPR sample was prepared with deuterated water (Cambridge Isotopes) and oxygen was removed with the glucose/glucose oxidase/catalase enzymes. 66% v/v of deuterated glycerol (Sigma Aldrich), previously degassed via freeze-thaw cycles, was added to the solution to obtain a transparent matrix. The final sample concentration was 400  $\mu\text{M}$ .

#### **EPR measurements**

The pulsed and time-resolved EPR experiments were conducted on a Bruker ELEXSYS E580 spectrometer fitted with a Spinjet Arbitrary Waveform Generator (AWG) using a TII resonator at Q-

<sup>1</sup>D. M. Scholler, M.-Y. R. Wang, B. M. Hoffman, *Methods Enzymol.* 52:487–493, 1978

band (34 GHz). The temperature was maintained at 20 K using liquid helium and a CF935 cryostat with an Oxford Instruments ITC103 temperature controller. Laser excitation of the samples was performed using an OPO pumped by the third harmonic of a Nd:YAG laser (Opotek, Opolette355), operated at a repetition rate of 20 Hz (5 ns pulses). Laser pulse energies of 2 mJ were used at an excitation wavelength of 552 nm while the Delay After Flash (DAF) was set to 1600 ns. For the electron spin-echo experiments a standard Hahn echo sequence (laser flash-DAF- $\pi/2$  -  $\tau$  -  $\pi$  -  $\tau$  - echo) was employed with a nominal length of 28 ns for all the pulses and a  $\tau$  value of 200 ns. Data were collected with 5 scans and 50 shots-per-point.

For the LiDEER experiments a standard four-pulse sequence (laser flash - DAF -  $\pi/2$  -  $\tau_1$  -  $\pi$  -  $t$  -  $\pi_{\text{pump}}$  - ( $\tau_1 + \tau_2 - t$ ) -  $\pi$  -  $\tau_2$  - echo) was applied with 28 ns pulses a  $\tau_1$  of 200 ns and a  $\tau_2$  of 1300 ns. The difference between the pump (nitroxide maximum) and observer (protoporphyrin triplet state, at the Y zero-field splitting canonical transition) frequency was set to 440 MHz. A two-step phase cycle was applied to remove receiver offsets while deuterium nuclear modulations were suppressed using an 8 step  $\tau_1$  cycle with 16 ns increment steps.

The ReLaserIMD experiments were performed with a pulse scheme:  $\pi/2$  -  $\tau_1$  -  $\pi$  -  $t$  - laser flash - ( $\tau_1 + \tau_2 - t$ ) -  $\pi$  -  $\tau_2$  - echo with 28 ns pulse lengths, a  $\tau_1$  of 1500 ns and a  $\tau_2$  200 ns. In both cases a two-step phase cycle was applied to remove receiver offsets. Data were collected with 50 scans and 50 shots-per-point.

RIDME experiments were performed with the five-pulse sequence adding the laser photoexcitation as shown in Figure 2: laser flash - DAF -  $\pi/2$  -  $\tau$  -  $\pi$  -  $\tau$  -  $t$  -  $\pi/2$  -  $T$  -  $\pi/2$  - ( $\tau_2 - t$ ) -  $\pi$  -  $\tau_2$  - echo with 28 ns pulses and  $\tau_1 = 200$  ns,  $\tau_2 = 1300$  ns,  $T = 80$  ns. To eliminate the contribution of unwanted echoes, an eight-step phase cycle was applied.

In all the experiments, the time increment of the dipolar traces was 8 ns.

The relaxation and decay of the triplet state were measured at the field positions corresponding to the zero-field splitting canonical orientations, integrating the Hahn echo at increasing values of the DAF. The data were measured accumulating 50 scans with 1 shot-per-point. A time increment of 60  $\mu\text{s}$  was used along both the X and Y zero-field splitting canonical transitions, while an increment of 5  $\mu\text{s}$  was used for the Z transition.

### *EPR data analysis*

LiDEER, ReLaserIMD time traces were analyzed using the DeerAnalysis2018<sup>1</sup> routine, while LiRIDME data were analyzed in OvertoneAnalysis<sup>2</sup>. The traces were elaborated dividing, from raw data, the background contribution and processing the form factor by Tikhonov regularization to extract the distance distributions. For the ReLaserIMD data, a third degree polynomial function was employed to effectively remove the background contribution, while exponential functions, with dimensions  $d = 3$  and  $d = 6.8$ , were used for the LiDEER and the LiRIDME data, respectively. The distance analysis was performed, in the case of the ReLaserIMD and the LiDEER data, by Tikhonov regularization, using the GCV criterion for determining the optimum regulariza-

<sup>1</sup>G. Jeschke, V. Chechik, P. Ionita, A. Godt, H. Zimmermann, J. Banham, C. R. Timmel, D. Hilger, H. Jung. *Appl. Magn. Reson.*, 30(3-4):473–498, 2006.

<sup>2</sup>K. Keller, V. Mertens, Mian Qi, A. I. Nalepa, A. Godt, A. Savitsky, G. Jeschke, M. Yulikov. *Phys. Chem. Chem. Phys.*, 19(27):17856–17876, 2017.



tion parameter <sup>1</sup>. The Tikhonov regularization implemented in OvertoneAnalysis was employed to analyze the LiRIDME form factor. The value of the first and the second harmonic overtone coefficients was set to 0.5 while the regularization parameter was selected at the edge of the L-curve.

### Relaxation data

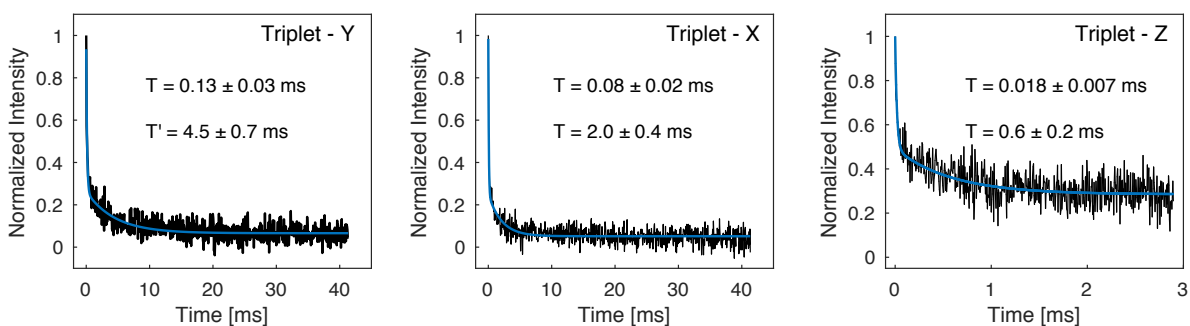


**Figure S1:** Delay-after flash data recorded along the triplet canonical positions and corresponding fits with a bi-exponential decay functions.

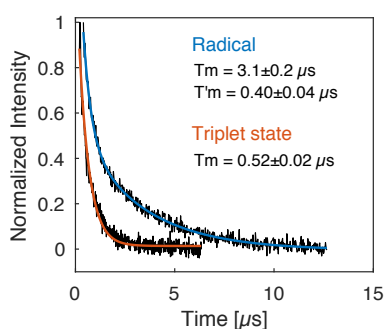


**Figure S2:** 2-pulse echo decay data and corresponding fittings recorded along the Y canonical positions of the triplet (orange) and at the maximum of the nitroxide spectrum (blue). A mono-exponential decay function was used to fit the triplet phase memory time, while a bi-exponential decay was used for the radical.

<sup>1</sup>T. H. Edwards, S. Stoll, *J. Magn. Reson.*, 288:58–68, 2018.



**CHAPTER** | **9**

**CIDEP in Human Neuroglobin**



---

# Electron spin polarization induced by triplet-radical interaction in the weakly coupled regime

Maria Giulia Dal Farra, Caterina Martin, Elisabetta Bergantino, Marilena Di Valentin

*Dipartimento di Scienze Chimiche, Università degli studi di Padova, Padova, Italy*

---

**Abstract:** We report the first in-protein observation of the polarized radical signal of a nitroxide probe induced by the weak interaction with the triplet state of a porphyrin-derivative group. The system investigated is a mutant of human neuroglobin (NGB) in which the iron of the heme group has been substituted with a Zn(II) ion and a nitroxide spin label has been attached via site-directed spin labeling on the Cys120 residue. The TREPR spectrum of the NGB sample presents an absorptive feature at  $g \simeq 2.010$  which has been attributed to the polarized nitroxide. This hypothesis is supported by the fact that this signal is missing in the spectra of two negative control samples in which either of the radical–triplet partners was missing. The presence of the nitroxide in NGB does not quench the triplet state and the observation of its signal is related to a combination of spin-selective depopulation and flip-flop relaxation mechanisms.

---

## 1 Introduction

Electron spin polarization is an extensively studied phenomenon in EPR spectroscopy. Spin polarization increases the sensitivity of EPR detection of paramagnetic centers. Particularly interesting in this sense are photoexcited triplet state populated by inter-system crossing (ISC) from an excited singlet state. Such a mechanism is anisotropic for the three spin sublevels and leads to a non-Boltzmann population of the triplet state. [1, 2]

Spin polarization provides detailed information about the spin chemistry of radicals, radical pair and triplet states occurring in photochemical reactions. Beyond ISC, induced by the photoexcitation, there are a number of other mechanisms that generate spin polarization in paramagnetic centers. The polarization of radical products, generated by ho-

molytic bond breaking or by photo-induced chemical reactions, was at first named CIDEP (chemically-induced dynamic electron polarization), in analogy to the chemically-induced dynamic nuclear polarization observed in NMR [3, 4]. The term CIDEP is now used to identify a wide range of mechanisms: not only the polarization of radicals generated by bond breaking or photo-chemical reactions but also that induced by the interaction with photoexcited triplet states [5, 6, 7, 8, 9]. To explain the polarization observed in triplet-doublet systems two mechanisms have been proposed: the radical–triplet pair mechanism (RTPM) and the electron spin polarization transfer (ESPT) [8, 10]. Quenching of the triplet state in the presence of free radicals is a well known phenomenon [9]. This process involves

the formation of a transient radical–triplet pair in which anisotropic decays to the ground state lead to the observation of a polarized radical signal. RTPM originates by the mixing of excited doublet and quartet states and, depending on the interaction that induces this mixing, it can lead to the observation of net or multiplet effect [11]. This mechanism can take place in liquid solution where the two partners are free to diffuse toward each other but also in samples in which the triplet and the radical are kept at a fixed distance because covalently linked or because they are in frozen/highly viscous solutions [12, 13, 14]. In ESPT the polarization of the photoexcited triplet state, generated by the anisotropic ISC, is transferred to a stable radical via energy transfer or spin exchange interaction. Both these mechanisms require a strong interaction between the two paramagnetic species.

While the case of the strongly interacting radical–triplet pair has been extensively investigated, to the best of our knowledge, only one study has been proposed for the weakly-coupled system [15, 16]. In [15, 16], they investigated a copper(II) porphyrin–free base porphyrin dimer in which they observed a radical contribution, with anti-phase polarization, generated by selective relaxations and depopulations of the spin sublevels. Even though a completely absorptive feature, falling at a  $g$  value compatible with that of a radical, was observed also in [15, 16], this was attributed to a conformational molecular of the system in which the copper(II) and the free base porphyrins were strongly interacting. Instead, a polarized radical signal, with a completely absorptive polarization induced by the weak interaction with a triplet, has never been reported.

In this paper we investigate the evolution of spin polarization in a protein system in which

the triplet and the radical partners are weakly interacting.

Among the numerous organic chromophores that, upon photoexcitation, populate the triplet state, porphyrin-derivatives have been widely investigated in EPR due to their high triplet yields, strong spin polarization and suitable relaxation times. Moreover their presence in several biological systems make such chromophores highly attractive for application as endogenous probes [17, 18].

Human neuroglobin (NGB), a protein belonging to the globin family, has been recently employed in a dipolar spectroscopy study, where the coupling between the triplet state, generated on the endogenous porphyrin-derivative group, and a nitroxide label, attached on a cysteine residue, has been measured [19]. In the wild-type NGB, the presence of the heme group, strongly complicates the photophysical path induced by laser photoexcitation, therefore in [19] the prosthetic group was replaced with a Zn(II) protoporphyrin IX that it is well known to populate the triplet state with good yield [20]. As radical counterpart, the (1-Oxyl-2,2,5,5-tetramethylpyrroline-3-methyl) methanethiosulfonate (MTSSL) was attached, via site-directed spin labeling, at the cysteine in position 120 of the sequence, at a distance of about 2.4 nm from the center of the porphyrin. Since the wild-type NGB contains three cysteine residues, in order to avoid multiple labeling, a mutant called G19, with only the cysteine at position 19 of helix G (Cys120), was expressed. The Zn-substituted G19 mutant, labeled with MTSSL, in this paper will be referred to as ZnG19L. Such a system, in which the protoporphyrin and the nitroxide kept at a relatively short distance, is ideal for investigating the eventual radical polarization in a regime of weak coupling with the triplet state. A repre-

sentation of the neuroglobin, in which the nitroxide probe has been attached at the Cys120 is shown in Figure 1.

Beside ZnG19L, other two protein variants, used as negative controls, have been investigated: (i) the Zn-substituted G19 mutant of NGB in which the Cys120 residue has not been labeled (ZnG19NL); (ii) the G19 mutant of NGB, with the native heme prosthetic group, labeled in position 120 with MTSSL (FeG19L).

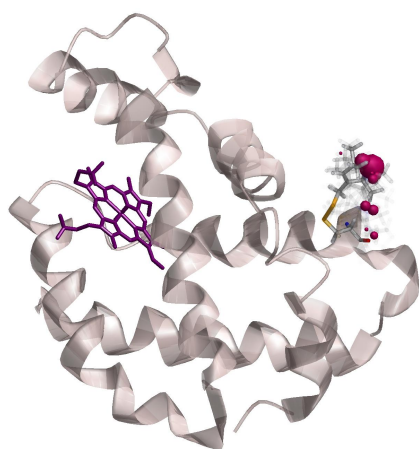


**Figure 1:** Representation of NGB (PDB: 4MPM [21]) in which the rotamers of the MTSSL spin label is attached at the residue Cys120 are depicted. The calculation of the rotamers has been done by the software MMM [22].

## 2 Materials and Methods

### *Sample preparation*

The details concerning the preparation of the ZnG19L sample are given in [19]. The negative controls samples have been prepared in a similar manner but skipping the spin labeling procedure in ZnG19NL and the Zn-substitution of the heme in FeG19L.

The concentration of the EPR samples is ca. 500  $\mu$ M.

### *EPR measurements*

TR-EPR spectra were recorded on a Bruker ELEXSYS E580 spectrometer equipped with a

dielectric resonator (ER4118X-MD5(W1)) and an Oxford CF900 cryostat. The temperature was controlled in a nitrogen-flow and all the spectra were recorded at 80 K. The signal coming from the detector (diode) was digitized by a LeCroy 9300 oscilloscope triggered by the laser flash. Time resolution has been estimated to be about 900 ns. No modulation of the magnetic field was applied. The triplet spectra were recorded with a resolution of 1 point every 4 Gauss or 1 point per Gauss. Nd:YAG pulsed lasers (Quantel Brilliant) equipped with both second and third harmonic modules and an optical parametric oscillators (OPOTECH) for tunable irradiation in the visible was used for samples photoexcitation. Typical parameters were  $\lambda = 544$  nm, pulse length = 5 ns, energy = ca. 3 mJ per shot, repetition rate = 10 Hz.

### *EPR data processing and simulations*

TREPR data were processed by subtracting: (i) the average baseline before the trigger event and (ii) a time profile taken at an off-resonance position. The spectra have been extracted from the 2D data set by numerically integrating over an appropriate time window. The simulations of the EPR spectra were performed using a program written in MATLAB with the aid of the EasySpin routine [23].

## 3 Experimental results

The TREPR spectrum, taken on the time window 1.20–1.28  $\mu$ s after the laser flash is shown in the top part of Figure 2.

The spectrum is that of a typical Zn-protoporphyrin(IX): the zero-field splitting (ZFS) parameters, and the triplet sublevels populations, obtained from the simulation, are in agreement with the values already reported in literature [18, 20]. This means that the pres-

ence of the nitroxide does not significantly affect the ISC process in the protoporphyrin moiety. In the central region of the spectrum a weak absorptive feature, with a maximum at  $g \approx 2.010$ , is present. At initial times, immediately after the laser flash, this is partially hidden by the intense triplet spectrum, but at longer times, when the triplet signal decays under the effect of relaxations, the feature becomes more visible.

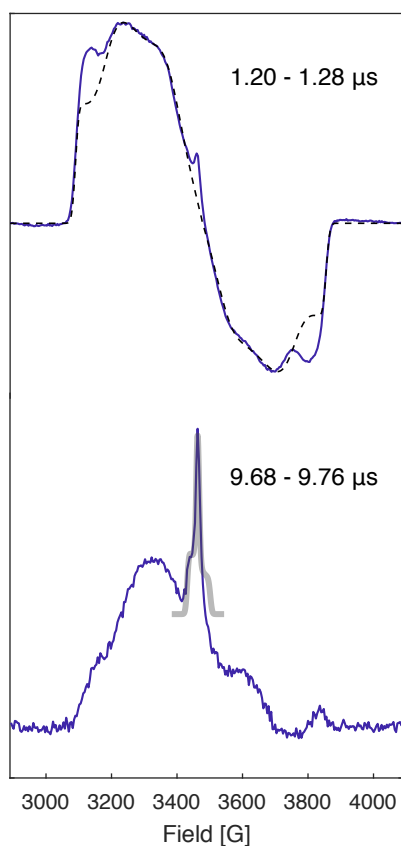


**Figure 2:** Top: TREPR spectrum of ZnG19L (solid line) integrated over a time window of 1.20 - 1.28 after the laser flash and simulation (dotted line) with parameters:  $[D,E] = [381 -64]$  G and  $[p_x;p_y;p_z] = [0.07;0.18;0.75]$ . Bottom: TREPR spectrum of ZnG19L integrated over a time window of 9.68 - 9.76  $\mu$ s after the laser flash overlapped to the calculated CW spectrum of a nitroxide radical (light gray) with  $[g_x;g_y;g_z] = [2.01;2.01;2.008]$  and  $A = [12;12;100]$  MHz.

In the bottom part of Figure 2 the TREPR spectrum, taken in a time window of 9.68–9.76  $\mu$ s after the laser flash, is shown together with the calculated spectrum of a typical nitroxide rad-

ical. The spectral width, and the relative intensities of the powder spectrum, are compatible with those of the nitroxide radical, but the signal must be due to a spin polarized radical since the detection of a Boltzmann populated species is precluded to TREPR. Therefore, we make the hypothesis that the signal is due to polarization of the nitroxide induced by the interaction with the photoexcited triplet state.

In order to verify this hypothesis we have compared the TREPR spectra of the negative controls, ZnG19NL and FeG19L, with that of ZnG19L (see Figure 3).

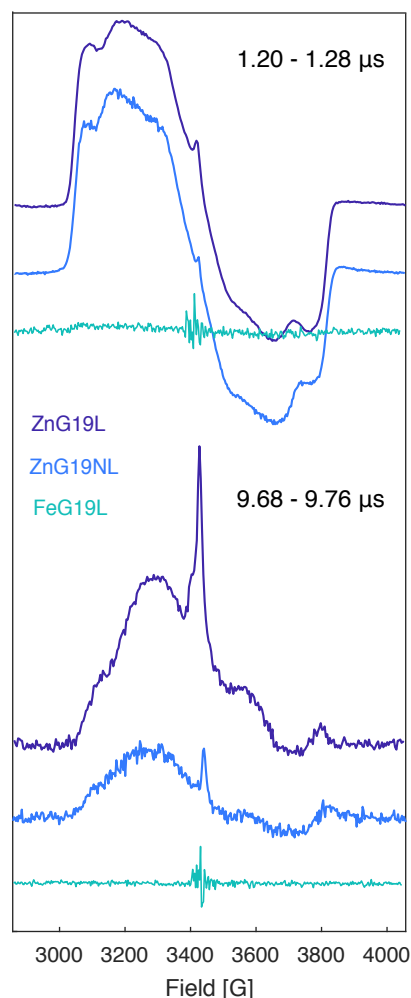


**Figure 3:** Top: TREPR spectra of ZnG19L (violet), ZnG19NL (azure) and FeG19L (turquoise) integrated over a time window of 1.20 - 1.28 (top) and 9.68 - 9.76  $\mu$ s after the laser flash.



In ZnG19NL, due to the absence of the nitroxide label, only the signal of the photoexcited triplet state is expected to be present in the spectrum. In FeG19L, instead, because of the presence of the paramagnetic iron center, the triplet state is not be populated and hence the nitroxide radical should have the Boltzmann equilibrium population and not be visible in the TREPR spectrum.

The TREPR spectra of the negative controls together with that of ZnG19L, have been extracted at two different time windows after the laser flash: 1.20–1.28 and 9.68–9.76  $\mu\text{s}$  (Figure 3). FeG19L does not show any triplet feature even though a small central signal, that might be due to the excited state contribution of the heme, is present at both times. ZnG19NL, at early times, has a strong contribution due to the Zn-protoporphyrin (IX) (ZnPP) triplet state, which is similar to that obtained in ZnG19L. Analogously to ZnG19L, also ZnG19NL has a central feature but with its maximum slightly shifted at  $g \approx 2.007$ . The relative intensities of the triplet and the radical contributions in the two spectra are different, with the central feature being much more intense in ZnG19L. This suggests that the two radicals may have different origins.

In order to better visualize the two radical contributions, the spectra collected in an interval of 160 G with a resolution of 1 point/G are shown in Figure 4 together with the calculated nitroxide spectrum.

Looking at the spectra of the two samples, extracted in a time window of 9.68 - 9.76  $\mu\text{s}$  after the laser flash, the radicals appear to be completely different one from the other. That radical in ZnG19NL is narrow and does not present any feature other than the central absorption. The radical detected after photoexcitation in ZnG19NL is broader and has two shoulders be-

side the central absorption: the first more intense at lower fields and a second one, which is partially hidden by the emissive feature of the triplet spectrum, at higher fields.

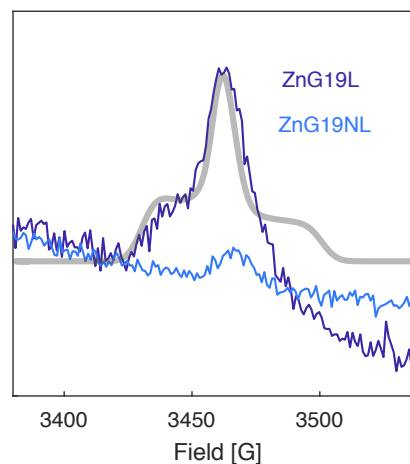


**Figure 4:** TREPR spectra collected with a resolution of 1 point/Gauss of ZnG19L (violet) and ZnG19NL (azure) integrated over a time window of 9.68 - 9.76  $\mu\text{s}$  after the laser flash. overlapped to the calculated CW spectrum of a nitroxide radical (light gray) with  $[g_x;g_y;g_z] = [2.01;2.01;2.008]$  and  $A = [12;12;100]$  MHz.

The differences between the two radicals are evident also in the time-domain evolution (Figure S9).

In Figure 5, the transient signal taken along the  $z$ -ZFS canonical orientation of the ZnPP triplet is shown together with that extracted at the maximum of the radical.

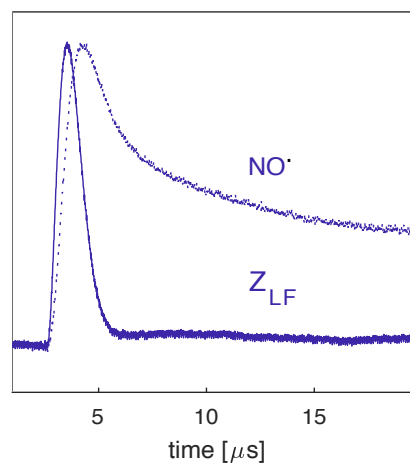


**Figure 5:** Transient signals of ZnG19L extracted along the  $z$ -ZFS canonical transition (solid line) and at the maximum of the radical  $g \approx 2.01$  (dotted line).

The rise time of the triplet signal is determined by the time-resolution of the TREPR setup, whereas, the rise of the radical signal, is much slower and its maximum falls about  $1.65 \mu\text{s}$  after the laser flash.

In Figure 6 are shown the transient signals taken along the canonical transitions of the ZnPP triplet in ZnG19L.

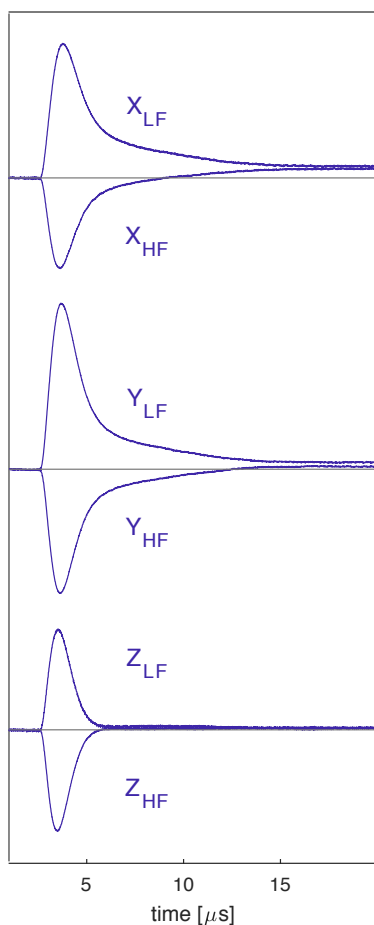


**Figure 6:** Transient signals of ZnG19L extracted along the  $x$ -ZFS (top),  $y$ -ZFS (center) and  $z$ -ZFS (bottom) canonical orientations. The low field (LF) transients, for the  $x$ -ZFS and  $y$ -ZFS orientations correspond to the  $T_{-1} \rightarrow T_0$  transitions while the high field (HF) transients are the  $T_0 \leftarrow T_{+1}$ . For  $z$ -ZFS the low field transition is the  $T_0 \rightarrow T_{+1}$  and the high field transient is the  $T_0 \rightarrow T_{-1}$ .

The transient signals along the  $z$ -ZFS direction ( $Z_{LF}$  and  $Z_{HF}$ ) decay much faster than those taken along the other canonical directions. The time evolution of the signal extracted along the  $x$ - and  $y$ -ZFS directions ( $X/Y_{LF}$  and  $X/Y_{HF}$ )

are characterized by a strong asymmetry of the high field transitions compared to the low field ones, and a change of sign is observed in both cases for the  $T_0 \leftarrow T_{+1}$  transition.

## 4 Theoretical mechanism

A net absorptive signal of a polarized radical weakly interacting with a triplet state has never been reported before. Here we propose a possible explanation of the mechanism that leads to the observed experimental data.

The behavior of any coupled system depends on the strength of the coupling between the two species. For a triplet state interacting with a radical there are always six eigenstates. In the strong coupling regime these are better described in terms of doublet and quartet eigenfunctions. In a weakly-coupled system instead, it is more convenient to use the doublet and the triplet eigenfunctions.

As it has been demonstrated in a previous work [19], in ZnG19L, the triplet state of ZnPP and the nitroxide radical are just weakly interacting. The two probes are kept at a mean distance of about 2.4 nm by the protein backbone, the dipolar coupling frequency is about 3.4 MHz while the exchange interaction can be considered negligible. In this regime, it is possible to make the assumption that the quantization axes of the radical and the triplet spins are not significantly affected by the dipolar coupling. Therefore, the system is better represented in terms of the uncoupled basis, which is simply the product of the triplet  $|T_{+1}\rangle$ ,  $|T_0\rangle$ ,  $|T_{-1}\rangle$  and the radical  $|\alpha\rangle$ ,  $|\beta\rangle$  eigenfunctions. Here, we call the six resulting states  $\psi_i$ , with  $i = 1, 2, 3, 4, 5, 6$ . Such a system can be described by a spin Hamiltonian that is the sum of the Zeeman interaction of the two spins, the ZFS interaction of the triplet state, the hyper-

fine coupling with the nitrogen nucleus of the nitroxide, the quadrupole interaction and the dipolar coupling between the triplet and the radical. For the sake of simplicity, we consider the case in which the static magnetic field lies along the  $z$ -ZFS direction and we assume that the radical is quantized along the field direction (i.e. the hyperfine and the quadrupole interactions are negligible compared to the Zeeman). The detailed expressions of the eigenfunctions and eigenvalues for such a system are given in Appendix.

In order to describe the TREPR spectrum of ZnG19L we now consider the radical and the triplet transitions in the weakly-coupled system. These are depicted in the left and the right diagrams of Figure 7 respectively. Immediately after the laser flash, the populations of  $\psi_5$  and  $\psi_2$  are close to that of the  $|T_0\rangle$  triplet level and, for this particular orientation, they correspond to the  $p_z$  zero-field population.  $\psi_6$ ,  $\psi_3$  and  $\psi_1$ ,  $\psi_4$  instead are similarly populated (as the  $|T_{-1}\rangle$  and  $|T_{+1}\rangle$  triplet sublevels respectively) but with the first two slightly less than the latter because of the asymmetry generated

by the ZFS interaction.

There are two pairs of triplet transitions:  $\psi_1 \leftrightarrow \psi_2$ ,  $\psi_4 \leftrightarrow \psi_5$  which fall at  $\sim \omega_t + D \pm \omega_{dd}$  and  $\psi_2 \leftrightarrow \psi_3$ ,  $\psi_5 \leftrightarrow \psi_6$  which fall at  $\sim \omega_t - D \pm \omega_{dd}$  ( $\omega_t$  is the triplet Larmor while  $\omega_{dd}$  is the triplet–radical dipolar coupling). The difference of population between the levels involved in such transitions is almost equal to that of a pure triplet. The spectrum therefore should be analogous to that of an isolated triplet state but with the features slightly broadened by the dipolar interaction. Similar considerations can be done for all the other orientations of the ZFS-frame with respect to the magnetic field. In ZnG19L the coupling between the protoporphyrin triplet and the nitroxide is 3.4 MHz, which corresponds roughly to 1.2 G. Such a broadening is too small visibly modify the TREPR spectrum. In this situation therefore, the triplet spectrum, immediately after the laser flash, does not present any specific feature due to the presence of the nitroxide, and corresponds instead to the spectrum of an isolated triplet state.

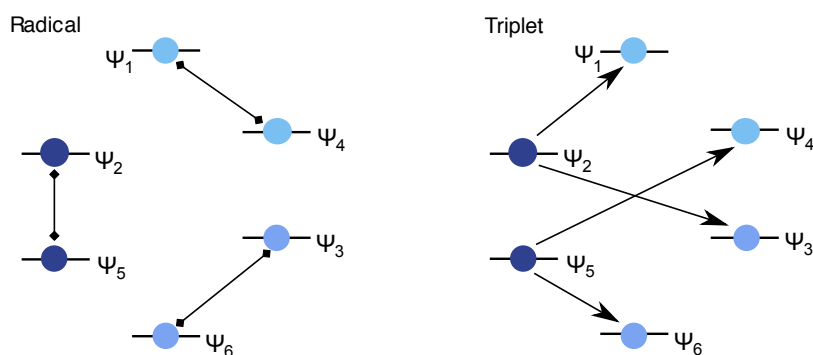


**Figure 7:** Diagram of the spin sublevels of the weakly coupled triplet-radical system. The system is assumed to be oriented with the magnetic field parallel to the  $z$ -ZFS axis of the triplet and the populations of the levels are represented, immediately after the laser flash, on a color scale, where the darkest is the blue the more populated it is the level. In the left diagram the levels involved in the allowed radical transitions are connected by black lines, but no arrows are present because the population difference between such levels is almost zero. In the right diagram, the triplet transitions are indicated by black arrows. The exact expressions of the spin eigenfunctions with the corresponding energies and populations are reported in Appendix.

This consideration is in agreement with the experimental result shown in the top part of Figure 2.

For the radical counterpart there are 5 possible transitions:  $\psi_1 \leftrightarrow \psi_4$ ,  $\psi_2 \leftrightarrow \psi_5$ ,  $\psi_3 \leftrightarrow \psi_6$ ,  $\psi_1 \leftrightarrow \psi_6$ ,  $\psi_3 \leftrightarrow \psi_4$  but two of them ( $\psi_1 \leftrightarrow \psi_6$ ,  $\psi_3 \leftrightarrow \psi_4$ ) are strongly forbidden, therefore we will focus only on three allowed ones. These fall at  $\sim \omega_r - \omega_{dd}$ ,  $\sim \omega_r$  and  $\sim \omega_r + \omega_{dd}$ . Immediately after the laser flash, the difference in population between the radical sublevels is almost zero (it is proportional to the Boltzmann population but is too low to be detected in TREPR). In this situation therefore only the triplet signal is expected to contribute to the TREPR spectrum. Indeed, the appearance of the radical signal comes later in time (see Figure 5) and is related to dynamic processes that take place after the laser flash in a time scale of few microseconds. The time evolution of the TREPR spectrum rely on several competitive processes:  $T_2$  relaxation that cause a loss of spin coherence in the  $xy$ -plane through flip-flop mechanisms,  $T_1$  relaxation that bring the populations to Boltzmann equilibrium and the decay of the different triplet sublevels to the ground state. The decay to the ground state is a spin selective process and, since the ground state is a doublet, the fastest rate of decay is expected for those levels having a stronger doublet character. In the weakly-coupled system, the levels that have this characteristic are  $\psi_2$ ,  $\psi_5$  and, to a minor extent, also  $\psi_3$  and  $\psi_4$ . At the same time flip-flop relaxations, which are mainly due to fluctuation of the dipole-dipole coupling, lead to equalization of the population between spin states with the same quantum number  $m_z$ . In our system, this involves the pair of levels  $\psi_2$ - $\psi_4$  and  $\psi_5$ - $\psi_6$ . This combination of spin selective processes introduces anisotropies in the time evolution of the differ-

ent sublevels and is probably the reason why we can observe the signal of the polarized nitroxide radical. A pictorial representation of these phenomena is presented in the top diagrams of Figure 8.

A purely qualitative analysis of the effects of such spin-selective mechanisms allows to assess that both the  $\psi_1 \leftarrow \psi_2$  and the  $\psi_5 \rightarrow \psi_6$  transitions are weakened because the two most populated levels ( $\psi_5$  and  $\psi_2$ ) are depleted by relaxations. Also  $\psi_2 \rightarrow \psi_3$  and  $\psi_4 \leftarrow \psi_5$  becomes weaker because both the levels involved in each transition are depopulated.

Analogous considerations can be made on the radical. Depopulation of  $\psi_4$  and  $\psi_3$  enhances the two transitions  $\psi_1 \rightarrow \psi_4$  and  $\psi_3 \leftarrow \psi_6$ . Even if these transitions are in antiphase, they probably do not perfectly compensate each other, but it is hard to say which one prevails without a quantitative calculation. At the same time also  $\psi_2$  and  $\psi_5$  are rapidly depopulated because of their doublet character, but the flip-flop mechanism tend to equalize their population to that of  $\psi_4$  and  $\psi_3$ . Since  $\psi_4$  is slightly less populated than  $\psi_3$  we can expect this condition to be true also for  $\psi_2$  and  $\psi_5$ , with the first being more populated than the latter. The situation just described creates one net  $\psi_2 \leftarrow \psi_5$  absorption for the radical which is indeed what we experimentally observe.

## 5 Discussion

According to the mechanisms just described the anisotropic population of the two spin sublevels associated to the  $|T_{+1}\rangle$  state of the triplet ( $\psi_1$  and  $\psi_4$  in our representation) compared to those related to the  $|T_{-1}\rangle$  state ( $\psi_6$  and  $\psi_3$  in our representation) is necessary for the observation of a net absorptive radical signal. This

anisotropy, is due to a deviation from the high field limit induced by the ZFS, which is the strongest interaction in the spin Hamiltonian after the Zeeman. However, this is not enough to cause a population difference between  $\psi_2$  and  $\psi_5$  levels because, immediately after the laser flash, they are both populated proportionally to the  $|T_0\rangle$  triplet level. Anisotropic depopulation and flip-flop relaxations play a crucial role in creating the disparity of population between these two levels. A diversity of the time evolution of the  $|T_{+1}\rangle$ - and the  $|T_{-1}\rangle$ - related levels can be seen also on the transient signals taken along the triplet canon-

ical transitions in Figure 6. The high field and the low field transients evolves in very different manners especially along the  $x$ - and the  $y$ -ZFS canonical orientations where a change of sign is observed at long delays after flash. Indeed, the ZnG19L spectrum observed in the time window 9.68–9.76  $\mu\text{s}$  after the laser flash has almost completely positive polarization.

Radical polarization in the weakly coupled regime triplet-doublet pairs has been investigated also in a model  $\alpha$ -helix peptide labeled at one end with a tetraphenyl-porphyrin and in position 7 of the helix, at a distance of about 1.71 nm, with a nitroxide probe.

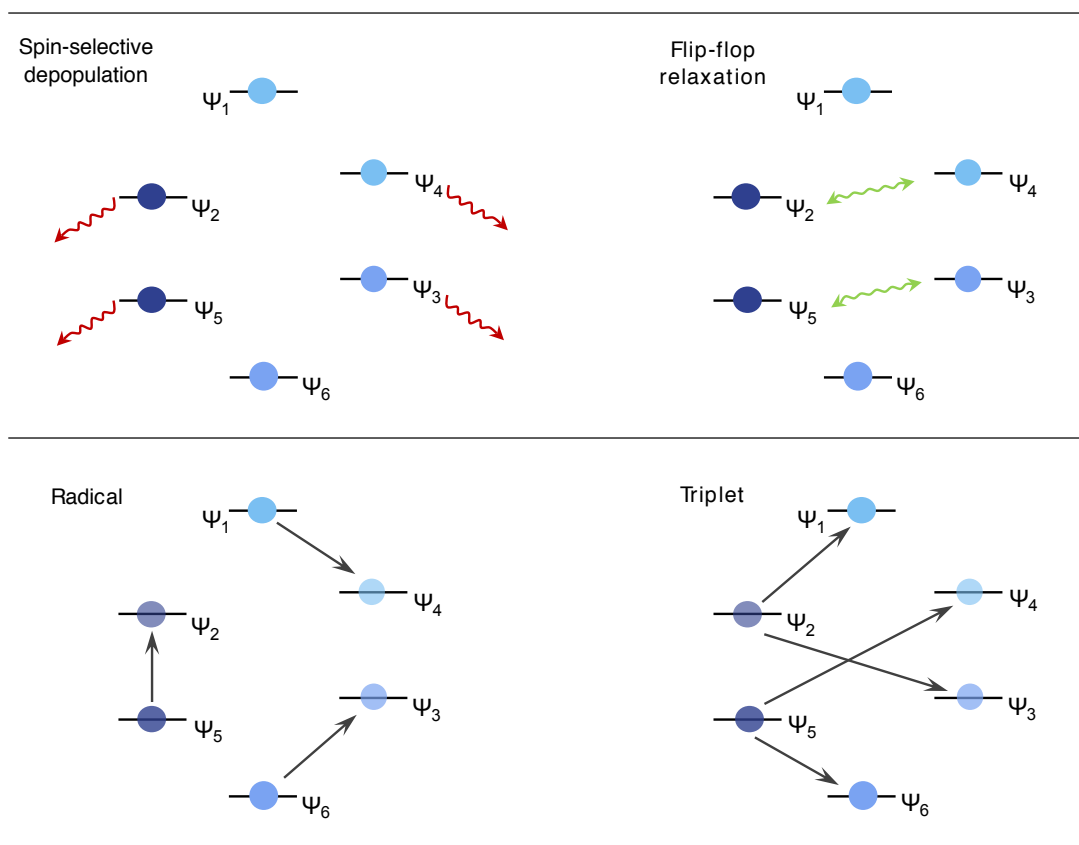


**Figure 8:** Top: representation of the spin-selective depopulation (left) and the flip-flop relaxation mechanism (right). Bottom: radical (left) and triplet (right) transitions after spin-selective depopulation and flip-flop relaxation acted.

The peptide is the first member of the spectroscopic ruler presented in [24]. Its TREPR spectrum is shown in Figure S10. In this case, even though the distance between the radical and the triplet is shorter than in ZnG19L none doublet signal is present. The reason is related to the highly isotropic relaxations of the system: the  $T_0 - T_{+1}$  and  $T_{-1} - T_0$  transitions decay with almost equal rate constants for all the molecular orientations and indeed a simple decrease of the intensity of the spectrum is observed in time. This is a further evidence that supports the presented mechanism.

## 6 Conclusions

In case of strongly interacting radical-triplet species, the formation of excited doublet and quartet states with subsequent decay to the ground state (RTPM) or the exchange interaction (ESPT) leads to the observation of polarized radical signals. When the two partners are too far to form a mixed state, anisotropic relaxations may still generate a disparity of population between the spin sublevels involved in the radical transitions causing a net absorptive or emissive doublet signal.

In this work we have reported the first observation of a polarized, absorptive radical signal in the weakly-coupled regime. In this situation no triplet quenching takes place therefore both the triplet and the radical signals are present in the TREPR spectrum. We have proposed a mechanisms to explain the observed signal based on anisotropic relaxations and depopulations of the spin sublevels. The presence of such anisotropies is experimentally visible in the transients signals which decay with different kinetic rates and in the spectrum taken at late delays after flash. The hypothesis that are anisotropic relaxations and not simply

spin–spin interaction that make possible the observation of the radical signal is supported also by the investigation done on the model peptide. In such system the inter-spin distance is shorter and is the dipolar coupling and exchange interaction are stronger, nonetheless no polarization is observed in the nitroxide.

## Appendix

The spin Hamiltonian for the weakly coupled triplet–radical system is the sum of the Zeeman interaction of the two spins, the ZFS interaction of the triplet, the hyperfine coupling with the nitrogen nucleus of the nitroxide, the quadrupole coupling and the dipolar interaction between the triplet and the radical. For a molecular orientation in which the static magnetic field is parallel to the  $z$ -axis of ZFS and considering the radical spin to be quantized along the field direction, neglecting hyperfine and the quadrupole interaction, the spin Hamiltonian can be written as:

$$H_0 = \omega_t S_{zt} + \omega_r S_{zr} + D \left( S_{zt}^2 - \frac{1}{3} S(S+1) \mathbb{1} \right) + E(S_{xt}^2 - S_{yt}^2) + \omega_{dd} S_{zt} S_{zr} \quad (9.1)$$

where  $\omega_t$  and  $\omega_r$  Larmor frequencies of the triplet and the radical respectively,  $D$  and  $E$  are the triplet ZFS parameters and  $\omega_{dd}$  is the dipolar frequency. The corresponding eigenfunctions are:

$$\begin{aligned} \psi_1 &= \cos(\phi_1) |T_{+1}\alpha\rangle + \sin(\phi_1) |T_{-1}\alpha\rangle \\ \psi_2 &= |T_0\alpha\rangle \\ \psi_3 &= -\sin(\phi_1) |T_{+1}\alpha\rangle + \cos(\phi_1) |T_{-1}\alpha\rangle \\ \psi_4 &= \cos(\phi_2) |T_{+1}\beta\rangle + \sin(\phi_2) |T_{-1}\beta\rangle \\ \psi_5 &= |T_0\beta\rangle \\ \psi_6 &= -\sin(\phi_2) |T_{+1}\beta\rangle + \cos(\phi_2) |T_{-1}\beta\rangle \end{aligned} \quad (9.2)$$

while the eigenvalues are:

$$\begin{aligned}
E_1 &= \frac{1}{6} \left( 2D + 3(2\omega_t + \omega_{dd}) \sqrt{1 + \tan[2\phi_1]^2} + 3\omega_r \right) \\
E_2 &= \frac{1}{6} \left( -4D + 3\omega_r \right) \\
E_3 &= \frac{1}{6} \left( 2D - 3(2\omega_t + \omega_{dd}) \sqrt{1 + \tan[2\phi_1]^2} + 3\omega_r \right) \\
E_4 &= \frac{1}{6} \left( 2D + 3(2\omega_t + \omega_{dd}) \sqrt{1 + \tan[2\phi_2]^2} - 3\omega_r \right) \\
E_5 &= \frac{1}{6} \left( -4D - 3\omega_r \right) \\
E_6 &= \frac{1}{6} \left( 2D - 3(2\omega_t + \omega_{dd}) \sqrt{1 + \tan[2\phi_2]^2} - 3\omega_r \right)
\end{aligned} \tag{9.3}$$

where  $2\phi_1 = \arctan\left[\frac{2E}{2\omega_t + \omega_{dd}}\right]$  and  $2\phi_2 = \arctan\left[\frac{2E}{2\omega_t - \omega_{dd}}\right]$ . The values of  $\phi_1$  and  $\phi_2$  define the amount of mixing of the  $|T_{+1}\rangle$  and the  $|T_{-1}\rangle$  triplet eigenfunctions. For this particular orientation in which the magnetic field  $B_0$  is parallel to the  $z$ -axis of ZFS,  $\phi_1$  and  $\phi_2$  are small, but their values increase moving from away this direction. The populations of weakly-coupled system are calculated transforming the product of the population matrices of the triplet and the radical, in the eigenstates of the Hamiltonian:

$$\begin{aligned}
P_1 &= \frac{1}{2} p_\alpha \left( p_x + p_y + \sin[2\phi_1](-p_x + p_y) \right) \\
P_2 &= p_\alpha p_z \\
P_3 &= \frac{1}{2} p_\alpha \left( p_x + p_y + \sin[2\phi_1](p_x - p_y) \right) \\
P_4 &= \frac{1}{2} p_\beta \left( p_x + p_y + \sin[2\phi_2](-p_x + p_y) \right) \\
P_5 &= p_\beta p_z \\
P_6 &= \frac{1}{2} p_\beta \left( p_x + p_y + \sin[2\phi_2](p_x - p_y) \right)
\end{aligned} \tag{9.4}$$

where  $p_\alpha$  and  $p_\beta$  are the populations of the radical sublevels, determined by the Boltzmann distribution, while the triplet population have been expressed in term of the zero-field populations  $p_x$ ,  $p_y$  and  $p_z$ . The intensities associated to the triplet transitions, im-

mediately after the laser flash, are determined by the transition dipole moment between the levels involved (the complete expressions are shown in Appendix). For small values of  $\omega_{dd}$ ,  $\phi_1 \simeq \phi_2 = \phi$  these are:

$$\begin{aligned}
I_{12} &= \frac{1}{4} p_\alpha \left( \cos[\phi] + \sin[\phi] \right)^2 \\
&\quad \left( p_x + p_y - 2p_z + \sin[2\phi]^2 (-p_x + p_y) \right) \\
I_{23} &= \frac{1}{4} p_\alpha \left( \cos[\phi] - \sin[\phi] \right)^2 \\
&\quad \left( p_x + p_y - 2p_z + \sin[2\phi]^2 (p_x - p_y) \right) \\
I_{45} &= \frac{1}{4} p_\beta \left( \cos[\phi] + \sin[\phi] \right)^2 \\
&\quad \left( p_x + p_y - 2p_z + \sin[2\phi]^2 (-p_x + p_y) \right) \\
I_{56} &= \frac{1}{4} p_\beta \left( \cos[\phi] - \sin[\phi] \right)^2 \\
&\quad \left( p_x + p_y - 2p_z + \sin[2\phi]^2 (p_x - p_y) \right)
\end{aligned} \tag{9.5}$$

Since  $p_\alpha$  and  $p_\beta$  are almost equal, the two transitions falling at  $\sim \omega_r + D$  have equal intensities ( $I_{12} \simeq I_{45}$ ) and in ZnG19L are both in absorption, whereas the transitions falling at  $\sim \omega_r - D$  are in emission again with nearly identical intensities ( $I_{23} \simeq I_{56}$ ). Immediately after the laser flash, for small values of  $\omega_{dd}$ ,  $\phi_1 \simeq \phi_2 = \phi$ , the intensities of such transitions are:

$$\begin{aligned}
I_{14} &= \frac{1}{8} (p_\alpha - p_\beta) \\
&\quad \left( (1 - \sin[2\phi]) p_x + (1 + \sin[2\phi]) p_y \right) \\
I_{25} &= \frac{1}{4} (p_\alpha - p_\beta) p_z \\
I_{36} &= \frac{1}{8} (p_\alpha - p_\beta) \\
&\quad \left( (1 + \sin[2\phi]) p_x + (1 - \sin[2\phi]) p_y \right)
\end{aligned} \tag{9.6}$$

Since  $p_\alpha \simeq p_\beta$ , the population difference between the levels involved in the radical transitions is almost zero.

## Bibliography

- [1] Alan Carrington and Andrew McLachlan. *Introduction to Magnetic Resonance*. Harper & Row and John Weatherhill, 1979.
- [2] S. P. McGlynn, T. Azumi, and M. Kinoshita. *Molecular Spectroscopy of the Triplet State*. Prentice-Hall, 1969.
- [3] K. M. Salikhov, Y. N. Molin, R. Z. Sagdeev, and A. L. Buchachenko. *Spin Polarization and Magnetic Effects in Radical Reactions*. Elsevier: Amsterdam, 1984.
- [4] L. T. Muus, P. W. Atkins, K. A. McLauchlan, and J. B. Pedersen. *Chemically Induced Magnetic Polarization*. Reidel: Dordrecht, The Netherlands, 1977.
- [5] Frank J. Adrian. Theory of anomalous electron spin resonance spectra of free radicals in solution. Role of diffusion-controlled separation and reencounter of radical pairs. *J. Chem. Phys.*, 54(9):3918–3923, 1971.
- [6] S. K. Wong, D. A. Hutchinson, and J. K. S. Wan. Chemically induced dynamic electron polarization. II. A general theory for radicals produced by photochemical reactions of excited triplet carbonyl compounds. *J. Chem. Phys.*, 58(3):985–989, 1973.
- [7] Takashi Imamura, Osamu Onitsuka, and Kinichi Obi. Memory of spin polarization in triplet-doublet systems. *J. Phys. Chem.*, 90(26):6741–6744, 1986.
- [8] C. Blättler, F. Jent, and H. Paul. A novel radical-triplet pair mechanism for chemically induced electron polarization (CIDEP) of free radicals in solution. *Chem. Phys. Lett.*, 166(4):375–380, 1990.
- [9] James A Green, Lawrence A Singer, and Joel H Parks. Fluorescence quenching by the stable free radical di-*t*-butylnitroxide. *J. Chem. Phys.*, 58(7):2690–2695, 1973.
- [10] Jun-ichi Fujisawa, Kazuyuki Ishii, Yasunori Ohba, Masamoto Iwaizumi, and Seigo Yamauchi. Electron Spin Polarization Transfer from Excited Triplet Porphyrins to a Nitroxide Radical via a Spin Exchange Mechanism. *J. Phys. Chem.*, 99(47):17082–17084, 1995.
- [11] Akio Kawai and Kinichi Obi. First Observation of a Radical-Triplet Pair Mechanism (RTPM) with Doublet Precursor. *J. Phys. Chem.*, 96(1):52–56, 1992.
- [12] Kazuyuki Ishii, Jun-ichi Fujisawa, Yasunori Ohba, and Seigo Yamauchi. A Time-Resolved Electron Paramagnetic Resonance Study on the Excited States of Tetraphenylporphinatozinc(II) Coordinated by *p*-Pyridyl Nitronyl Nitroxide. *J. Am. Chem. Soc.*, 118(51):13079–13080, 1996.
- [13] Carlo Corvaja, Michele Maggini, Maurizio Prato, Gianfranco Scorrano, and Maria Venzin. C60 Derivative Covalently Linked to a Nitroxide Radical: Time-Resolved EPR Evidence of Electron Spin Polarization by Intramolecular Radical-Triplet Pair Interaction. *J. Am. Chem. Soc.*, 117(34):8857–8858, aug 1995.
- [14] Carlo Corvaja, Elena Sartori, Antonio Toffoletti, Fernando Formaggio, Marco Crisma, and Claudio Toniolo. Interaction between TOAC free radical and photoexcited triplet chromophores linked to peptide templates. *Biopolym. - Pept. Sci. Sect.*, 55(6):486–495, 2000.
- [15] Motoko Asano-Someda, Art Van der Est, Uwe Krüger, Dietmar Stehlik, Youkoh Kaizu, and Haim Levanon. Intramolecular Energy Transfer in a Covalently Linked Copper(II) Porphyrin-Free Base Porphyrin Dimer: Novel Spin Polarization in the Energy Acceptor. *J. Phys. Chem. A*, 103(34):6704–6714, 1999.
- [16] Art Van der Est, Motoko Asano-Someda, Paul Ragnogna, and Youkoh Kaizu. Light-induced electron spin polarization of a weakly coupled triplet-doublet spin pair in a covalently linked porphyrin dimer. *J. Phys. Chem. A*, 106(37):8531–8542, 2002.
- [17] M. Ezhevskaya, Enrica Bordignon, Yevhen Polyhach, L. Moens, Sylvia Dewilde, Gunnar



- Jeschke, and S. Van Doorslaer. Distance determination between low-spin ferric haem and nitroxide spin label using DEER: the neuroglobin case. *Mol. Phys.*, 111(18-19):2855–2864, 2013.
- [18] M. Fahnenschmidt, R. Bittl, R. Bittl, E. Schloder, W. Haehnel, and W. Lubitz. Characterization of de novo synthesized four-helix bundle proteins with metalloporphyrin cofactors. *Phys. Chem. Chem. Phys.*, 3(18):4082–4090, 2001.
- [19] Maria Giulia Dal Farra, Alice M. Bowen, Caterina Martin, Sabine Richert, Elisabetta Bergantino, Chirstiane R. Timmel, and Marilena Di Valentin. Light-induced pulsed dipolar spectroscopy in a paradigmatic hemeprotein. *Under Prep.*, 2018.
- [20] Paul J. Angiolillo and J. M. Vanderkooi. Electron paramagnetic resonance of the excited triplet state of metal-free and metal-substituted cytochrome c. *Biophys. J.*, 68(6):2505–2518, 1995.
- [21] Beatriz G. Guimarães, Djemel Hamdane, Christophe Lechauve, Michael C. Marden, and Béatrice Golinelli-Pimpaneau. The crystal structure of wild-type human brain neuroglobin reveals flexibility of the disulfide bond that regulates oxygen affinity. *Acta Crystallogr. Sect. D Biol. Crystallogr.*, 70(4):1005–1014, apr 2014.
- [22] Yevhen Polyhach, Enrica Bordignon, and Gunnar Jeschke. Rotamer libraries of spin labelled cysteines for protein studies. *Phys. Chem. Chem. Phys.*, 13(6):2356–2366, 2011.
- [23] Stefan Stoll and Arthur Schweiger. EasySpin, a comprehensive software package for spectral simulation and analysis in EPR. *J. Magn. Reson.*, 178(1):42–55, 2006.
- [24] Marilena Di Valentin, Marco Albertini, Maria Giulia Dal Farra, Enrico Zurlo, Laura Orian, Antonino Polimeno, Marina Gobbo, and Donatella Carbonera. Light-Induced Porphyrin-Based Spectroscopic Ruler for Nanometer Distance Measurements. *Chem. - A Eur. J.*, 22(48):17204–17214, nov 2016.

## Supporting Information

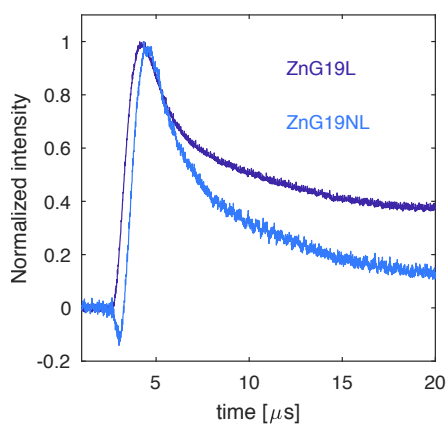


**Figure S9:** Transient signals of ZnG19L (violet) and ZnG19NL (azure) and at the maximum of the radical signal:  $g \approx 2.010$  and  $g \approx 2.007$  respectively.

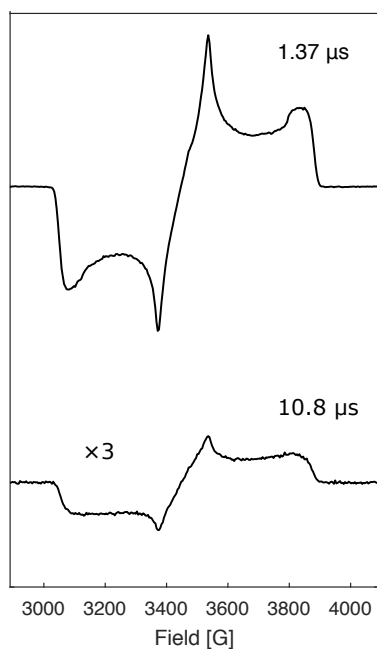


**Figure S10:** TREPR spectrum of the model peptide extracted at 1.37 (top) and 10.8 (bottom)  $\mu$ s after the laser flash. The bottom spectrum has been multiplied by a factor of 3.

**CHAPTER** | **10**

**Density matrix study of the photoexcited triplet  
state as spin probe in Double Electron-Electron  
Resonance spectroscopy**



# Density matrix study of the photoexcited triplet state as spin probe in Double Electron-Electron Resonance spectroscopy

Maria Giulia Dal Farra<sup>†</sup>, Claudia Tait<sup>‡§</sup>, Stefan Stoll<sup>\*‡</sup>, Marilena Di Valentin<sup>†</sup>

<sup>†</sup>*Dipartimento di Scienze Chimiche, Università degli studi di Padova, Padova, Italy*

<sup>‡</sup>*Department of Chemistry, University of Washington, Seattle, WA 98103, United States*

<sup>§</sup>*Current affiliation: Freie Universität Berlin, Berlin Joint EPR Lab, Institut für Experimentalphysik, Berlin, Germany*

---

**Abstract:** The photoexcited triplet state of organic chromophores has been recently added to the collection of spin labels for pulsed dipolar EPR spectroscopy. These probes have been demonstrated to dramatically increase the sensitivity of the dipolar technique thanks to the anisotropic population of the spin triplet sublevels. In this work, a computational study of photoexcited triplet probes, based on density matrix simulations, is presented. We characterize quantitatively the effects of triplet polarization and zero-field splitting (ZFS) on the dipolar traces. We have calculated the traces for different triplet polarizations highlighting how this affects the intensity of the dipolar oscillations and the damping of the traces. We have also computed the dipolar traces for a set of benchmark systems in which the ZFS interactions cover the range of values that are commonly encountered for triplet state chromophores used in EPR spectroscopy, demonstrating that, in this interval, the triplet state is a well behaving tool for distance determination via dipolar spectroscopy.

---

## 1 Introduction

The photoexcited triplet state is a well established spin probe for distance measurement in Double Electron–Electron Resonance (DEER) [1, 2]. The first demonstration of the feasibility a pulse dipolar spectroscopy experiment, on a photo-induced paramagnetic center was performed by Di Valentin *et al.* [1]. In [1] it was proposed a variation of the conventional DEER experiment, in which the laser photoexcitation was added at the beginning sequence in order to instantaneously populate the triplet state. In this proof of concept experiment the photo-generated species acted as the detection spin, while the pump spin was a nitroxide radical. This variation of the DEER technique is called light-induced DEER (LiDEER) (see Figure 1).

Compared to the conventional nitroxide labels, photoexcited probes exhibits some interesting features that make them particularly appealing for application in pulsed EPR dipolar spectroscopy. In their ground state, these chromophores are dia-

magnetic and thus EPR-silent, but, upon laser photoexcitation, the paramagnetic triplet state can be populated via inter-system crossing (ISC) from the lowest excited singlet state.

ISC makes the population of the triplet sublevels different from the Boltzmann distribution increasing therefore the intensity of its EPR signals that are in enhanced absorption and emission. This gain of signal observed for the photoexcited species, has been reported also dipolar spectroscopy, where, an improvement of about 10 times in signal-to-noise, was observed when detecting on a polarized triplet state compared to the Boltzmann populated radical [1].

The possibility of optically switching the triplet state, has been recently exploited to create a new *ad hoc* sequence called Laser-Induced Modulation Dipole spectroscopy (LaserIMD) based on the instantaneous photogeneration of the triplet state and, as a consequence, of the dipole–dipole coupling, at variable times during an Hahn echo sequence on the detection spin [3].

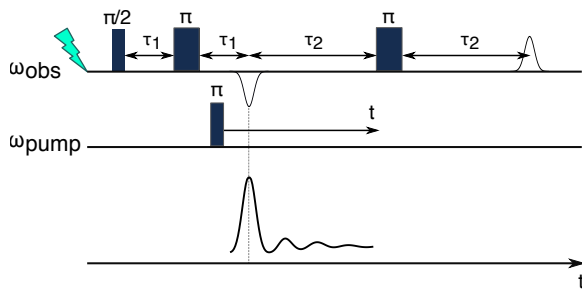


**Figure 1:** LiDEER pulse sequence and representation of the corresponding dipolar time-trace.

While a full spectroscopic characterization of triplet probes has already been carried out [1, 2], an exhaustive theoretical analysis is still lacking. In particular, it has not been systematically demonstrated yet, to which extend the characteristics of the photoexcited triplet state, i.e. the spin polarization and the strong spectral anisotropy, due to the Zero Field Splitting (ZFS) parameters, affect the DEER trace. Numerical studies on the influence of the magnitude of the ZFS interaction on the DEER trace are already available for gadolinium probes ( $S=7/2$ ) [4, 5, 6] thus, in the present work, the attention is focused on photoexcited triplet states ( $S=1$ ) of organic chromophores.

The analytical expression, that has been previously derived in [2, 7], describing the LiDEER echo modulation in a triplet–radical system, suffers from strong approximations that were introduced in the spin Hamiltonian and in the expression for the microwave pulses. Thus, the result gives only a qualitative insight of the problem, but it does not allow for a quantitative description of the experiment.

In order to overcome the limitations described above, a numerical study of the characteristics of the triplet state probes for LiDEER, based on the density matrix formalism, is here presented. The differences between the DEER traces of triplet–radical systems and radical–radical systems are investigated, focusing in particular on the effects of the spin multiplicity, the polarization and the ZFS parameters on the DEER trace. This is done calculating the dipolar traces for a series of different systems composed either by two radicals or by a triplet state interacting with a radical. In all the computed traces, a trityl radical has been used as the pump spin, while the observer spin has been

varied. A nitroxide label has been employed as detection spin in the radical–radical system whereas different triplet parameters have been used in the triplet–radical systems depending on the effect that had to be investigated.

The investigation on the influence of the polarization has been performed using the ZFS parameters of the tetraphenylporphyrin and adopting different sets of populations of the triplet sublevels.

The effects of the ZFS has been investigated using the triplet parameters of a series of benchmark chromophores: fullerene, porphyrin, flavin and eosin [8, 9, 10, 11]. These compounds have been selected because their ZFS parameters cover the whole range of values commonly encountered in the photoexcited chromophores that are encountered in EPR [8, 12, 13, 14]. Porphyrins and flavins are present in numerous biological systems and this enables to exploit such groups as switchable endogenous probes [15, 16].

## 2 Theory

The description of the DEER experiment is carried out by using the density matrix formalism based on the Liouville-von Neumann equation [17, 18, 19]:

$$\frac{d\hat{\rho}}{dt} = -i[\hat{H}(t), \hat{\rho}] = -i[\hat{H}(t)\hat{\rho} - \hat{\rho}\hat{H}(t)] \quad (1)$$

The effect of the pulse sequence can be divided in nutation periods, during which the microwave pulses are applied, and free-precession periods, during which the spin system evolves under the effect of the static Hamiltonian  $\hat{H}_0$ . The Hamiltonian  $\hat{H}_1$ , describing the interaction with the magnetic field of the microwave pulses, is:

$$\begin{aligned} \hat{H}_1(t) &= \frac{\mu_B}{\hbar} 2\mathbf{B}_1 \cdot \mathbf{g}\hat{\mathbf{S}} \cdot \cos(\omega_{mw}t) \\ &= \frac{\mu_B}{\hbar} \mathbf{B}_1 \cdot \mathbf{g} \cdot \hat{\mathbf{S}} (e^{i\omega_{mw}t} + e^{-i\omega_{mw}t}) \end{aligned} \quad (2)$$

where  $\mu_B$  is the Bohr magneton,  $\hbar$  is the reduced Planck constant,  $\mathbf{g}$  is the g-tensor and  $\omega_{mw}t$  is the frequency of the microwave pulse.

In free-precession periods, integration of Equation 1 yields:

$$\hat{\rho}(t) = \hat{U}\hat{\rho}(t_0)\hat{U}^\dagger \quad (3)$$

where the propagator  $\hat{U}$  is:

$$\hat{U} = \exp\{-i\hat{H}_0 t\} \quad (4)$$

During the pulses, the total Hamiltonian  $\hat{H} = \hat{H}_0 + \hat{H}_1(t)$  is time-dependent and the analytical integration of Equation 1 is no longer straightforward. The propagator then becomes:

$$\hat{U}(t) = \hat{T} \exp\{-i \int_0^y \hat{H}(t') dt'\} \quad (5)$$

$\hat{T}$  is the Dyson time-ordering operator which corresponds to the identity operator only when the Hamiltonians at different times commute ( $[\hat{H}(t_1), \hat{H}(t_2)] = 0$ ) [20].

The solution of the Liouville-von Neumann equation for time dependent Hamiltonians is in general very complicated, for this reason, at least when an analytical approach is required, the time dependence is usually moved from the Hamiltonian to the observables through a transformation to the interaction frame (see Appendix A). This however implies that some approximations are introduced in the equations. Alternatively, especially in numerical approaches, the calculation can be performed in the laboratory frame where the time dependence is kept in  $\hat{H}_1(t)$ , and Equation 5 is numerically integrated. In this case the computational costs grow because a signal, modulated at high frequency, has to be detected. However, the problem can be overcome detecting a down-converted signal. This is done dividing the sequence in two blocks: the mixing period, in which the pulses are applied, and the detection period, that starts after the last pulse and goes through the detection (see Figure 2).

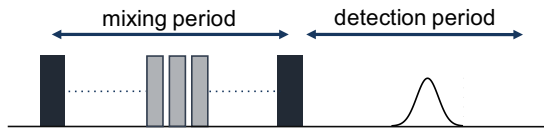


**Figure 2:** Scheme of the mixing period and the detection period.

The propagation of the density matrix is done in the laboratory frame but, during the detection, the signal is mixed with the reference microwave and the

high frequency component is filtered out (see Appendix B). At the end of the mixing period the signal is:

$$s(t) = \text{Tr}\{\hat{D}e^{-i\hat{H}_0 t} \hat{\rho}_{\text{mix}} e^{i\hat{H}_0 t}\} \quad (6)$$

Operating some basic algebraic transformations, it is possible to separate the modulated part of the signal from the intensity component. The modulated part is then mixed with the microwaves and only the high frequency component is filtered out:

$$\begin{aligned} s(t)^{\text{QP}} &= \text{Re}\left\{ \sum_{m=l} D_{mm} \rho_{mm} \right\} e^{i\omega_{\text{mw}} t} + \\ &\quad \sum_{m>l} [\text{Re}\{D_{ml} \rho_{lm}\} (e^{i\omega_{ml} t} + e^{-i\omega_{ml} t}) - \\ &\quad \text{iIm}\{D_{ml} \rho_{lm}\} (e^{-i\omega_{ml} t} - e^{i\omega_{ml} t})] e^{i\omega_{\text{mw}} t} \end{aligned} \quad (7)$$

$$\begin{aligned} &= \sum_{m>l} [\text{Re}\{D_{ml} \rho_{lm}\} e^{i(\omega_{\text{mw}} - \omega_{ml}) t} - \\ &\quad \text{iIm}\{D_{ml} \rho_{lm}\} e^{i(\omega_{\text{mw}} - i\omega_{ml}) t}] \\ &= \sum_{m>l} [\text{Re}\{D_{ml} \rho_{lm}\} - \\ &\quad \text{iIm}\{D_{ml} \rho_{lm}\} e^{i(\omega_{\text{mw}} - \omega_{ml}) t}] \end{aligned}$$

The signal in Equation 7 is modulated at a low frequency ( $\omega_{\text{mw}} - \omega_{ml}$ ) and a smaller number of points is required for correctly reconstruct the signal.

### 3 Method

The spin Hamiltonian (SH) of a system composed by two weakly interacting paramagnetic centers, in the presence of a static magnetic field  $\mathbf{B}_0$ , can be written as the sum of the SHs,  $\hat{H}_1$  and  $\hat{H}_2$ , of the two separate spins and the interaction term  $\hat{H}_{\text{EEI}}$ :

$$\hat{H}_0 = \hat{H}_{\text{obs}} + \hat{H}_{\text{pump}} + \hat{H}_{\text{EEI}} \quad (8)$$

We considered here a weakly coupled system in which the exchange interaction can be neglected and the spin-spin coupling is simply given by the dipolar interaction:

$$\begin{aligned} \hat{H}_{\text{EEI}} &= \hat{H}_{\text{dd}} \\ &= \frac{\mu_0 \mu_{\text{B}}^2 g_{\text{e}}^2}{4\pi \hbar r_{12}^3} [\hat{\mathbf{S}}_1 \cdot \hat{\mathbf{S}}_2 - 3(\hat{\mathbf{S}}_1 \cdot \mathbf{n}_{12})(\hat{\mathbf{S}}_2 \cdot \mathbf{n}_{12})] \end{aligned} \quad (9)$$

where  $\mu_0$  is the vacuum permeability,  $g_e$  is the g-factor of the free electron,  $r_{12}$  is the distance between the interacting spins and  $\mathbf{n}_{12}$  is the versor along the direction connecting them [21].

The SH,  $\hat{H}_{\text{pump}}$ , of the trityl is:

$$\hat{H}_{\text{pump}} = \frac{\mu_B}{\hbar} \mathbf{B}_0 \cdot \mathbf{g} \cdot \hat{\mathbf{S}} \quad (10)$$

In the case of the nitroxide observer spin the SH is:

$$\hat{H}_{\text{obs}} = \frac{\mu_B}{\hbar} \mathbf{B}_0 \cdot \mathbf{g} \cdot \hat{\mathbf{S}} + \hat{\mathbf{I}} \cdot \mathbf{A} \cdot \hat{\mathbf{S}} \quad (11)$$

while for the triplet is:

$$\hat{H}_{\text{obs}} = \frac{\mu_B}{\hbar} \mathbf{B}_0 \cdot \mathbf{g} \cdot \hat{\mathbf{S}} + \hat{\mathbf{S}} \cdot \mathbf{D} \cdot \hat{\mathbf{S}} \quad (12)$$

where  $\mathbf{D}$  and  $\mathbf{A}$  are the ZFS and the hyperfine tensors respectively.

The initial density matrix of the system is:

$$\hat{\rho}_0 = \hat{\rho}_{\text{obs}} \otimes \hat{\rho}_{\text{pump}} \quad (13)$$

where  $\hat{\rho}_{\text{obs}}$  and  $\hat{\rho}_{\text{pump}}$  are the initial density matrix of the detection and the pump spin respectively. The equilibrium density matrix is calculated according to the Boltzmann distribution:

$$\hat{\rho} = \frac{1}{\hat{Z}} \exp\{-\hat{H}_{\text{obs}} \hbar / k_B T\} \quad (14)$$

where  $\hat{Z} = \text{Tr}\{\exp\{-\hat{H}_{\text{obs}} \hbar / k_B T\}\}$ .

The density matrix of the photoexcited triplet state  $\hat{\rho}_T$ , instead is a function of the zero-field popula-

tions of the triplet sublevels  $[p_x, p_y, p_z]$  and no coherences are assumed to be present at the initial time [22].

The dipolar traces were calculated propagating the initial density matrix of the system, in the mixing period, under the effect of a series of operators describing the 4-pulse DEER sequence, and detecting the downconverted signal as shown in Eq.7.

The detection and the pump pulses are assumed to act exclusively on the detection and the pump spin respectively. The nutation operators, applied in the mixing period, are calculated dividing the pulse length in short time intervals and numerically integrating Equation 5.

The parameters of the model system used in the calculations are summarized in Table 1.

The DEER traces were calculated for a 4-pulse sequence:  $\pi/2 - \tau_1 - \pi - t - \pi_{\text{pump}} - (\tau_1 + \tau_2 - t) - \pi - \tau_2 - \text{echo}$  with detection pulse lengths of 8/16/16 ns and a pump pulse length of 8 ns. Given the small anisotropy of the Zeeman interaction of the trityl radical, the pump pulse can efficiently excite the whole spectrum. On the contrary, the observer spins are only partially excited by the detection pulses. In order to avoid orientation selection effects in the calculated traces, a set of conformers, with different orientations of the dipolar vector with respect to the detection frame, has been used [4].

The parameters of the model systems used in the calculations are summarized in Table 1.

**Table 1:** Spin systems parameters.

Spin multiplicity	g-observer $[g_x, g_y, g_z]$	g-pump $[g_x, g_y, g_z]$	$[T_x, T_y, T_z]$ (MHz)	$[A_x, A_y, A_z]$ (MHz)	$[D, E]$ (MHz)
S = 1/2 - S = 1/2	[2.0062 2.0091 2.0022]	[2.0034 2.0032 2.0023]	[5 5 -10]	[20 20 100]	—
S = 1 - S = 1/2	[2.0023 2.0023 2.0023]	[2.0034 2.0032 2.0023]	[5 5 -10]	—	[342 21] - [1175 239] - [1718 492] - [2039 570]

*\*Zero-field splitting parameters*



A representation of the geometric model is shown in Figure 3. The set of structures is generated regularly sampling the angles  $\chi$  and  $\xi$ , defining the position of the dipolar vector relative to the detection frame, in an interval between  $0^\circ$  and  $90^\circ$ .

The optimum number of conformers of the system that had to be adopted in order to avoid the orientation selection, has been found increasing the set of initial structures until the convergence of the calculated traces has been reached. We found that about 50 conformers are enough for avoiding artifacts in the traces.

Each DEER trace had been powder averaged over a sphere of orientations of the spin system with respect to the static magnetic field direction.

The average computational time for each trace was about one day using 16 Xeon E5-2698 cores.

## 4 Results and Discussion

In order to verify the influence of the spin multiplicity and the triplet polarization on DEER signal, the calculated traces for (i) a pair of interacting radicals, (ii) a Boltzmann populated triplet coupled to a radical and (iii) a photoexcited triplet state coupled to radical are compared in Figure 4.

The time traces of the three systems are shown both

before and after normalization. The normalized traces have all the same modulation frequency and similar amplitudes, with slightly more pronounced oscillations for the polarized triplet-radical system. The absolute signal obtained when the detection spin is the polarized triplet state, is about 30 times stronger than that of the radical, and about 200 times stronger than that of the Boltzmann populated triplet state. This result is in agreement with the experimental data presented by M. Di Valentin *et al.* [1] concerning the comparison of the DEER traces of two homologue peptides: one marked with a free base porphyrin and a nitroxide ( $S=1 - S=1/2$ ), in the other a copper (ii) ion was coordinated to the porphyrin ( $S=1/2 - S = 1/2$ ). In this work, it was demonstrated that the main dipolar modulation frequency is conserved in the two traces, while an increase of signal-to-noise of 10 times is observed detecting the photoexcited triplet state instead of the radical. This implies that, in order to experimentally achieve similar signal-to-noise for the two systems, 100 times more accumulations have to be done when detecting the radical. In order to investigate how the population of the triplet sublevels influences the amplitude of the modulations in the dipolar traces, the DEER signals for three different benchmark polarizations of the triplet state have been calculated.

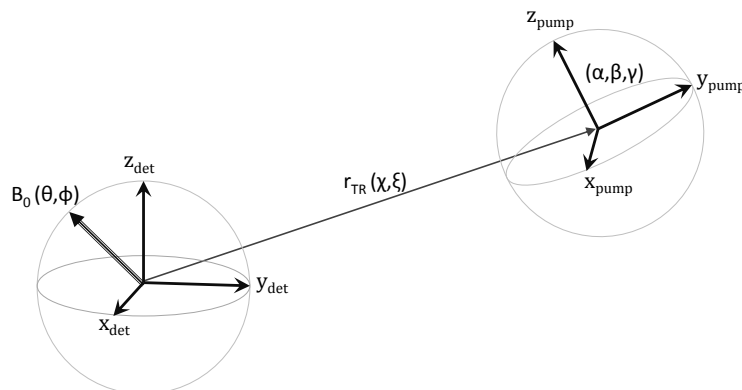


**Figure 3:** Reference frames of the detection spin and the pump spin and angles describing the relative orientations and the direction of the static magnetic field.

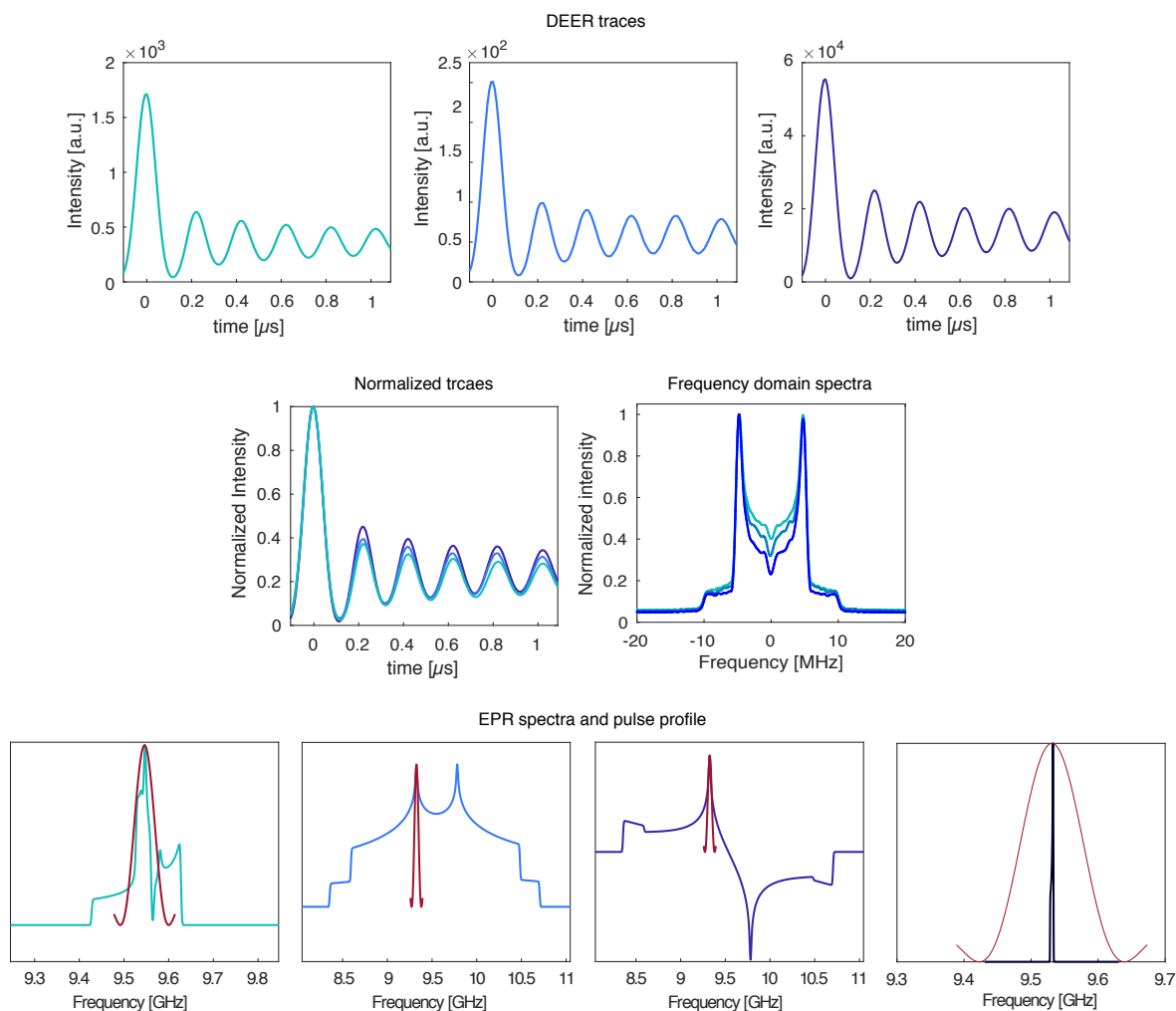


**Figure 4:** Top row: calculated DEER traces for radical-radical system (turquoise), a Boltzmann-populated triplet-state coupled to a radical (azure) and a polarized triplet-state coupled to a radical (violet). Central row: overlap of the normalized traces for the three different systems and relative Fourier transforms after apodization with a Hahn function. Bottom row: frequency-domain EPR spectra of the pump and the detection spin, with the same color code, calculated with the function *pepper* of EasySpin, and rectangular pulse profiles (red). The equilibrium populations for both the Boltzmann triplet-state and the radical were calculated at 175 K, whereas the populations of the polarized triplet state are:  $[p_x, p_y, p_z] = [0.58, 0.31, 0.11]$ .

In Figure 5, are shown both the normalized and the absolute dipolar signals, together with their Fourier transforms. The detection and pump spectra with the corresponding pulse profiles are represented in the bottom row of Figure 5. The polarization of the triplet spectrum influences not only the absolute intensity of the signal, but also the damping of the dipolar oscillations. The effect on the damping depends on the weights of the frequencies that contribute to the dipolar trace that are determined by the polarization of the triplet spectrum. In particular, if the detection pulse is placed in a position in which both positive and negative polarizations participate to the detection echo, the ratios between

the frequencies that take part to the spectrum may deviate from the typical Pake pattern distribution. The effect can be noticed in the Fourier transform of the trace corresponding to a  $[p_x, p_y, p_z] = [0, 0, 1]$  polarization of the detection spin (green). In this particular case, if the distance analysis is performed in DeerAnalysis [23] by Tikhonov regularization, without taking into account the effect of polarization, spurious peaks appear in the distance distribution. The correct interpretation of the data and extraction of a distance distribution require therefore an *ad hoc* analysis.

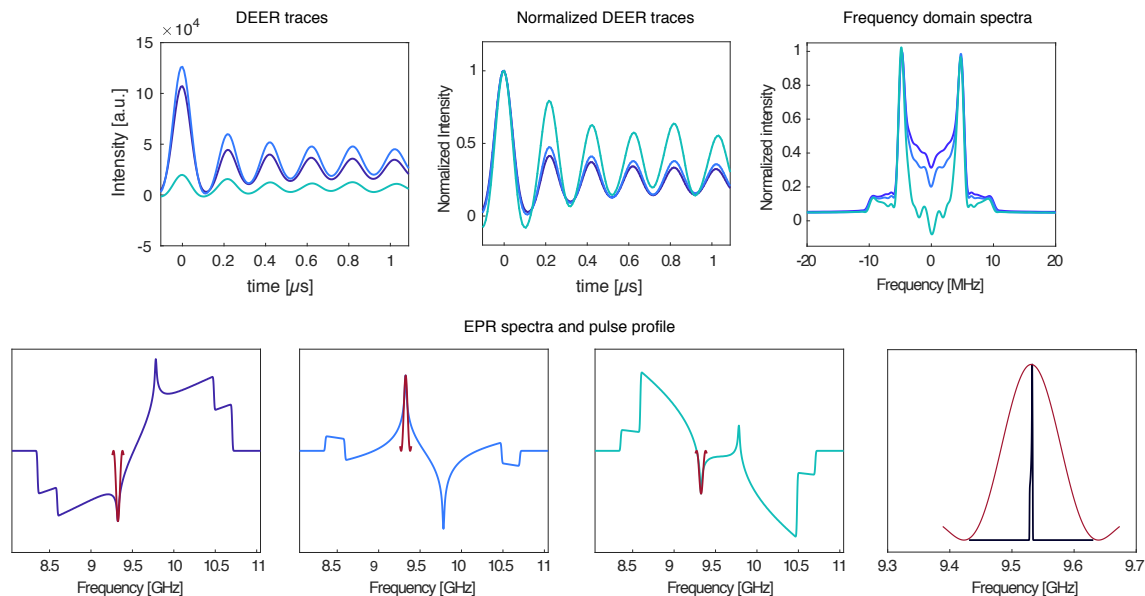


**Figure 5:** Top row: absolute DEER signals (left), normalized traces (center) and Fourier transforms of the traces after apodization with a Hann function (right), calculated for a polarized triplet state coupled to a radical, using different polarizations of the triplet state:  $[p_x, p_y, p_z] = [1, 0, 0]$  (violet),  $[p_x, p_y, p_z] = [0, 1, 0]$  (azure),  $[p_x, p_y, p_z] = [0, 0, 1]$  (turquoise). Bottom row: frequency-domain EPR spectra, with same color code, calculated with the function *pepper* of EasySpin and rectangular pulse profiles (red) for the pump and the detection spins.

In Figure 6 the DEER traces calculated for four different systems, in which ZFS parameters of the detection spins cover the range of values typically encountered in triplet state probes (Table 1), are presented. The traces have been calculated in order to investigate whether or not, artifacts, related to the drop of the high field condition, appear in the dipolar traces. Since pure effects of ZFS had to be studied, the signals have been computed for Boltzmann populated triplets in order to avoid the introduction of effects related to polarization. The EPR spectra and pump profiles of the different systems are shown in the bottom row of Figure 6. The dipolar traces of the four systems are all modulated at the same dipolar frequency, they do not show any apparent artifact and their Fourier transforms have a complete Pake pattern shape. Distance analysis performed in DeerAnalysis gave the same distance distribution for all the datasets allowing to assess that in the whole range of ZFS considered, there are no deviations due to the strong anisotropy of the spectrum and thus the triplet state is a reliable spin probe for application in pulse dipolar spectroscopy.

## 5 Conclusions

In this work, a numerical characterization of photoexcited triplet state spin probes, based on time-domain density matrix simulations, has been presented. The methodology that has been developed allowed to carry out laboratory frame calculations, employing soft pulses and using the complete spin Hamiltonian of the system, including also non secular terms. Calculating the DEER traces for a series of model systems we have explored the effects of triplet pin polarization and ZFS magnitude on the dipolar signals.

Comparison of the DEER traces calculated detecting the echo of a radical, a Boltzmann-populated triplet state and a polarized triplet state shows that the effect of spin polarization is to increase the signal of order of magnitudes while conserving the main modulation frequency.

Investigation on the effects of the spin polarization on the DEER traces demonstrates how different triplet probes, with diverse polarizations, could be exploited in order to enhance the intensity or the persistence of the dipolar oscillations.

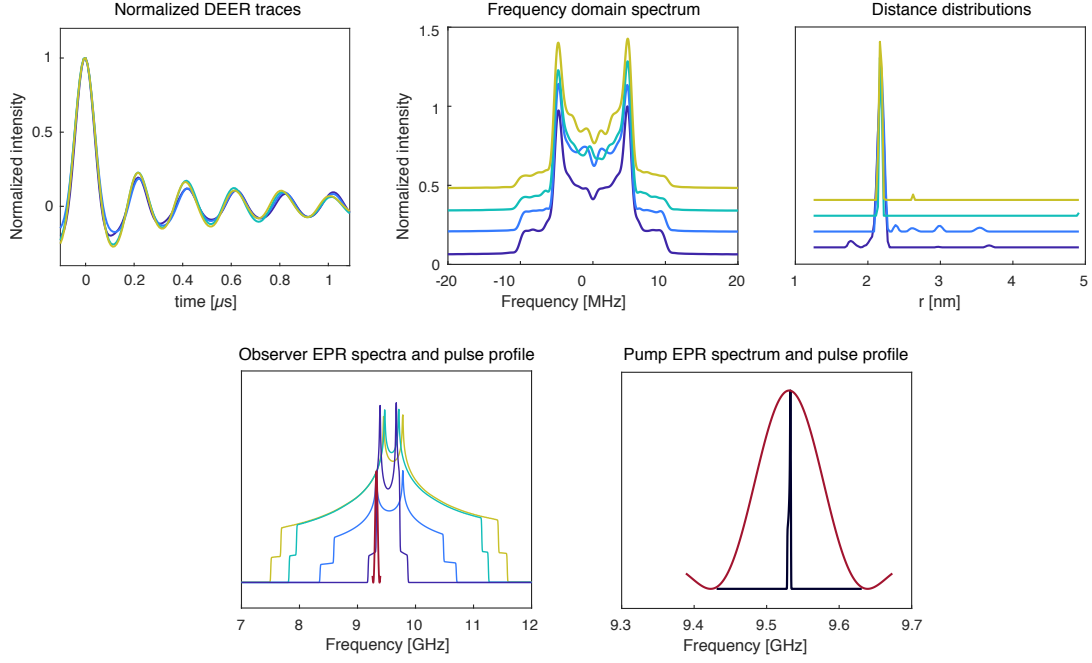


**Figure 6:** Top row: normalized DEER traces (left), Fourier transforms of the traces after apodization with a Hann function (center) and distance distributions extracted by Tikhonov regularization implemented in DeerAnalysis (right), calculated for different ZFS parameters:  $[D, E] = [342, 21]$  MHz (violet),  $[D, E] = [1175, 239]$  MHz (azure),  $[D, E] = [1718, 492]$  MHz (turquoise),  $[D, E] = [2039, 570]$  MHz (yellow). Bottom row: frequency-domain EPR spectra, with the same color code, calculated with the function *pepper* of EasySpin and rectangular pulse profiles for the pump and the detection spins (red). The EPR spectra have been normalized to 1 at the position of the detection pulse.

Placing the detection pulse in some particular positions of the spectrum, in which transitions with opposite polarizations contribute to the detection echo, causes distortions of the Pake distribution. In such cases the analysis of the data requires an *ad hoc* procedure to extract the correct distance distribution.

Comparison of the set of DEER traces calculated for triplet systems with ZFS parameters of fullerene, porphyrin, flavin and eosin chromophores proves that under no circumstances can be produces artifacts related to the drop the high field regime. Since these values cover the whole range of ZFS parameters commonly encountered in EPR, we can assess that photoexcited triplet states are reliable probes for application in light-induced pulsed EPR dipolar spectroscopy.

low the evolution of the density matrix under the effect of a specific Hamiltonian  $\hat{H}(t)$ :

$$\frac{d\hat{\rho}}{dt} = -i[\hat{H}(t), \hat{\rho}] = -i[\hat{H}(t)\hat{\rho} - \hat{\rho}\hat{H}(t)] \quad (\text{A1})$$

When the Hamiltonian  $\hat{H}(t)$  is time dependent the calculation of the dynamic of the density matrix is easier if a transformation to the interaction representation is operated:

$$\hat{\rho} = \hat{R}^\dagger \hat{\rho}_R \hat{R} \quad (\text{A2})$$

where  $\hat{R} = \exp\{i\hat{H}_{\text{core}} t\}$  and  $\hat{H}_{\text{core}}$  is a suitable operator whose form will be discussed in detail later in this Appendix. Substituting Eq.A2 into Eq.A1:

$$\frac{d(\hat{R}^\dagger \hat{\rho}_R \hat{R})}{dt} = -i[\hat{H}(t)\hat{R}^\dagger \hat{\rho}_R \hat{R} - \hat{R}^\dagger \hat{\rho}_R \hat{R}\hat{H}(t)] \quad (\text{A3})$$

## Appendix A

### The interaction frame

The Liouville-von Neuman equations allows to fol-

The derivative on the left side is:

$$\begin{aligned} \frac{d(\hat{R}^\dagger \hat{\rho}_R \hat{R})}{dt} &= \frac{d\hat{R}^\dagger}{dt} \hat{\rho}_R \hat{R} + \hat{R}^\dagger \frac{d\hat{\rho}_R}{dt} \hat{R} + \hat{R}^\dagger \hat{\rho}_R \frac{d\hat{R}}{dt} \\ &= -i\hat{H}_{\text{core}} \hat{R}^\dagger \hat{\rho}_R \hat{R} + \hat{R}^\dagger \frac{d\hat{\rho}_R}{dt} \hat{R} + i\hat{R}^\dagger \hat{\rho}_R \hat{H}_{\text{core}} \hat{R} \end{aligned} \quad (\text{A4})$$

Inserting Eq.A4 into Eq.A3 and multiplying both sides from the left and from the right by  $\hat{R}$  and  $\hat{R}^\dagger$  respectively, gives:

$$\begin{aligned} -i\hat{R}\hat{H}_{\text{core}}\hat{R}^\dagger\hat{\rho}_R\hat{R}\hat{R}^\dagger + \hat{R}\hat{R}^\dagger\frac{d\hat{\rho}_R}{dt}\hat{R}\hat{R}^\dagger + i\hat{R}\hat{R}^\dagger\hat{\rho}_R\hat{H}_{\text{core}}\hat{R}\hat{R}^\dagger \\ = -i(\hat{R}\hat{H}(t)\hat{R}^\dagger\hat{\rho}_R\hat{R}\hat{R}^\dagger - \hat{R}\hat{R}^\dagger\hat{\rho}_R\hat{H}(t)\hat{R}^\dagger) \end{aligned} \quad (\text{A5})$$

Considering that  $\hat{H}_0 = \hat{H}_0 + \hat{H}_1(t)$ , Eq.A5 can be rearranged in:

$$\begin{aligned} \frac{d\hat{\rho}_R}{dt} &= -i[\hat{R}(\hat{H}_0 + \hat{H}_1(t))\hat{R}^\dagger\hat{\rho}_R - \\ &\quad \hat{\rho}_R\hat{R}(\hat{H}_0 + \hat{H}_1(t))\hat{R}^\dagger - \hat{H}_{\text{core}}\hat{\rho}_R + \hat{\rho}_R\hat{H}_{\text{core}}] \\ &= -i[(\hat{R}\hat{H}_0\hat{R}^\dagger + \hat{R}\hat{H}_1(t)\hat{R}^\dagger)\hat{\rho}_R - \\ &\quad \hat{\rho}_R(\hat{R}\hat{H}_0\hat{R}^\dagger + \hat{R}\hat{H}_1(t)\hat{R}^\dagger) - \hat{H}_{\text{core}}\hat{\rho}_R + \hat{\rho}_R\hat{H}_{\text{core}}] \\ &= -i[(\hat{R}\hat{H}_0\hat{R}^\dagger - \hat{H}_{\text{core}})\hat{\rho}_R - \hat{\rho}_R(\hat{R}\hat{H}_0\hat{R}^\dagger - \hat{H}_{\text{core}}) + \\ &\quad \hat{R}\hat{H}_1(t)\hat{R}^\dagger\hat{\rho}_R - \hat{\rho}_R\hat{R}\hat{H}_1(t)\hat{R}^\dagger] \end{aligned} \quad (\text{A6})$$

The general expressions for the static Hamiltonian and the interaction Hamiltonian in the transformed frame becomes:

$$\begin{aligned} \hat{H}_{0,R} &= \hat{R}\hat{H}_0\hat{R}^\dagger - \hat{H}_{\text{core}} \\ \hat{H}_{1,R} &= \hat{R}\hat{H}_1(t)\hat{R}^\dagger \end{aligned} \quad (\text{A7})$$

and the nutation and the free-precession operators are respectively:

$$\begin{aligned} \hat{U}_{\text{nut}} &= \exp\{-i(\hat{H}_{1,R} + \hat{H}_{0,R})t_p\} \\ \hat{U}_{\text{ev}} &= \exp\{-i\hat{H}_{0,R}\tau\} \end{aligned} \quad (\text{A8})$$

When  $[\hat{H}_0, \hat{H}_{\text{core}}] = 0$ , then also  $[\hat{H}_0, \hat{R}] = 0$  and  $\hat{R}\hat{H}_0\hat{R}^\dagger = \hat{H}_0$ , leading to:

$$\hat{H}_{0,R} = \hat{H}_0 - \hat{H}_{\text{core}} \quad (\text{A9})$$

In this situation, the calculation of the dynamic of the density matrix is easier if the computation is

carried on in the eigenbasis of  $\hat{H}_0$  and  $\hat{H}_{\text{core}}$ :

$$(H_{0,R})_{mm} = \epsilon_m^0 - \epsilon_m^{\text{core}} \quad (\text{A10})$$

where  $\epsilon_m^0$  and  $\epsilon_{m(n)}^{\text{core}}$  are the  $m(n)$ -th elements of  $H_0$  and  $H_{\text{core}}$  respectively. Similarly,  $H_{1,R}$  is:

$$\begin{aligned} (H_{1,R})_{mn} &= \frac{\mu_B}{\hbar} (\vec{B}_1 \vec{g} \vec{S})_{mn} (\exp\{i(\epsilon_m^{\text{core}} - \epsilon_n^{\text{core}} + \omega_{\text{mw}})t\} \\ &\quad + \exp\{i(\epsilon_m^{\text{core}} - \epsilon_n^{\text{core}} - \omega_{\text{mw}})t\}) \end{aligned} \quad (\text{A11})$$

One of the two exponential terms in Eq.A11 is modulated at high frequency and it is usually neglected, whereas the other is a low frequency component. If the resonance condition  $\epsilon_m^{\text{core}} - \epsilon_n^{\text{core}} = \omega_{\text{mw}}$  is assumed then a time independent form of  $H_{1,R}$  is obtained.

$$(H_{1,R})_{mn} = \frac{\mu_B}{\hbar} (\mathbf{B}_1 \cdot \mathbf{g} \cdot \mathbf{S})_{mn} \quad (\text{A12})$$

The above derivation was carried out without explaining what exactly is  $\hat{H}_{\text{core}}$ . By definition, in a transformation to the interaction representation  $\hat{H}_{\text{core}}$  is coincident with the static Hamiltonian [24]. In this situation  $\hat{H}_{0,R}$  is null and only  $\hat{H}_{1,R}$  acts during the pulses.

In literature the most common case is the transformation to the standard rotating frame or sometimes to a partial interaction representation [25, 26, 27]. These transformations can be considered as a particular case of interaction representation in which  $\hat{H}_{\text{core}}$  includes only part of the static Hamiltonian or  $\hat{H}_{\text{core}}$  is equal to  $\omega_{\text{mw}}\hat{S}_z$  (as in the standard rotating frame). Depending on the form of  $\hat{H}_{\text{core}}$ , the use of Eq.A10 and Eq.A12, which are widely employed in spin dynamic calculations, introduces different extents of approximation in the equations because the condition  $[\hat{H}_0, \hat{H}_{\text{core}}] = 0$  may no longer be true. The transformation to the interaction frame requires that also the operator used for the detection of the signal is consistently transformed. Experimentally the signal is proportional to the electromotive force induced in the receiving coil by the os-

cillating transverse magnetic moment [28]:

$$\begin{aligned}
 s(t) &\propto \frac{d\langle \mathbf{x} \cdot \hat{\boldsymbol{\mu}} \rangle}{dt} = \frac{d}{dt} \text{Tr}\{\hat{\boldsymbol{\mu}}_x \hat{\rho}(t)\} = \text{Tr}\left\{\hat{\boldsymbol{\mu}}_x \frac{d\hat{\rho}(t)}{dt}\right\} \\
 &= \text{Tr}\{i\hat{\boldsymbol{\mu}}_x \hat{\rho}(t) \hat{H}_0 - i\hat{\boldsymbol{\mu}}_x \hat{H}_0 \hat{\rho}(t)\} \\
 &= \text{Tr}\{i\hat{H}_0 \hat{\boldsymbol{\mu}}_x \hat{\rho}(t) - i\hat{\boldsymbol{\mu}}_x \hat{H}_0 \hat{\rho}(t)\} \\
 &= \text{Tr}\{i[\hat{H}_0, \hat{\boldsymbol{\mu}}_x] \hat{\rho}(t)\}
 \end{aligned} \tag{A13}$$

where  $i[\hat{H}_0, \hat{\boldsymbol{\mu}}_x] = \hat{D}$  is the detection operator. In the  $\hat{H}_0$  eigenbasis:

$$\begin{aligned}
 (D_R)_{mn} &= (RDR^\dagger)_{mn} \\
 &= i(\mu_x)_{mn} (\epsilon_m^0 - \epsilon_n^0) \exp\{i(\epsilon_m^{\text{core}} - \epsilon_n^{\text{core}})t\} \\
 &= i(\mu_x)_{mn} (\epsilon_m^0 - \epsilon_n^0) (\cos\{(\epsilon_m^{\text{core}} - \epsilon_n^{\text{core}})t\} + \\
 &\quad i \sin\{(\epsilon_m^{\text{core}} - \epsilon_n^{\text{core}})t\})
 \end{aligned} \tag{A14}$$

Given the relations  $(\mu_x)_{mn} = (\mu_x)_{nm} = -i(\mu_y)_{mn} = i(\mu_y)_{nm}$ , it is possible to write:

$$\begin{aligned}
 (D_R) &= -(\epsilon_m^0 - \epsilon_n^0) \left( (\mu_y)_{mn} \cos\{(\epsilon_m^{\text{core}} - \epsilon_n^{\text{core}})t\} + \right. \\
 &\quad \left. (\mu_x)_{mn} \sin\{(\epsilon_m^{\text{core}} - \epsilon_n^{\text{core}})t\} \right)
 \end{aligned} \tag{A15}$$

The signal then is obtained calculating the expectation value of the transformed detection operator on the density matrix at the end of the pulse sequence. In most of the pulse experiments the quadrature detection is used, i.e. the signal is mixed with the microwave frequency and filtered to eliminate the fast components:

$$\begin{aligned}
 s_R(t) &\propto \text{Tr}\{D_R \rho_R\} e^{i\omega_{\text{mw}}t} \\
 &= \sum_n \sum_m -(\rho_R)_{nm} (\epsilon_m^0 - \epsilon_n^0) \\
 &\quad \left( (\mu_y)_{mn} (\exp\{i(\epsilon_m^{\text{core}} - \epsilon_n^{\text{core}})t\} + \right. \\
 &\quad \left. \exp\{-i(\epsilon_m^{\text{core}} - \epsilon_n^{\text{core}})t\}) - \right. \\
 &\quad \left. i(\mu_x)_{mn} (\exp\{i(\epsilon_m^{\text{core}} - \epsilon_n^{\text{core}})t\} - \right. \\
 &\quad \left. \exp\{-i(\epsilon_m^{\text{core}} - \epsilon_n^{\text{core}})t\}) \right) e^{i\omega_{\text{mw}}t}
 \end{aligned} \tag{A16}$$

Neglecting the fast oscillating component, the quadrature phase detection operator in the interac-

tion frame is:

$$\begin{aligned}
 (D_R^{\text{qp}})_{mn} &= (\epsilon_n^0 - \epsilon_m^0) \\
 &\quad \left( (\mu_y)_{mn} \exp\{i(\omega_{\text{mw}} - \epsilon_m^{\text{core}} + \epsilon_n^{\text{core}})t\} + \right. \\
 &\quad \left. i(\mu_x)_{mn} \exp\{i(\omega_{\text{mw}} - \epsilon_m^{\text{core}} + \epsilon_n^{\text{core}})t\} \right)
 \end{aligned} \tag{A17}$$

The time dependence is now in the observables and it is determined by the eigenvalues of  $\hat{H}_{\text{core}}$  which define the reference frame of the calculation. If the resonance condition  $\epsilon_m^{\text{core}} - \epsilon_n^{\text{core}} = \omega_{\text{mw}}$  is assumed, then a time independent form of detection operator is obtained:

$$(D_R^{\text{qp}})_{mn} = (\epsilon_n^0 - \epsilon_m^0) [(\mu_y)_{mn} + i(\mu_x)_{mn}] \tag{A18}$$

From the point of view of the computational cost, the use of both Eq.A12 and Eq.A18 allows for a considerable save of time because (i) the nutation operator does not include any time dependence and (ii) a low-frequency modulated signal is detected. However, this introduces some approximations in the equations due to the fact that the resonance condition and the commutation condition ( $[\hat{H}_0, \hat{H}_{\text{core}}] = 0$ ) are assumed at the same time. Moreover if the calculation is done in a total or a partial interaction representation, the contemporary use of Eq.A12 and Eq.A18 leads to a loss of information because the signal is "observed" from a reference frame always in resonance with the interactions included in  $\hat{H}_{\text{core}}$ . To avoid such a loss of information Eq.A17 has to be used but on the other hand there is no more saving of computational time.

In order to verify how the approximations, introduced in the equations by the transformation to the interaction frame, affect the quality of the spin dynamic computation, the Free-Induction (FID) decay signals were calculated, for a nitroxide spin, in the different frames. The static Hamiltonian used in the calculations is the sum of the Zeeman interaction and the hyperfine interaction:

$$\hat{H}_0 = \frac{\mu_B}{\hbar} \mathbf{B}_0 \cdot \mathbf{g} \cdot \hat{\mathbf{S}} + \hat{\mathbf{S}} \cdot \mathbf{A} \cdot \hat{\mathbf{I}} \tag{A19}$$

where  $\mathbf{g}$  and  $\mathbf{A}$  are the  $\mathbf{g}$  and the hyperfine-tensor respectively. The principal values of the two ten-

sors are  $[g_x, g_y, g_z] = [2.0062 \ 2.0091 \ 2.0022]$  and  $[A_x, A_y, A_z] = [12 \ 12 \ 100]$  MHz. In order to efficiently excite the whole nitroxide spectrum a  $0.1 \text{ ns } \pi/2$  pulse have been used.

In Figure 7 the Fourier transforms of the FID signals, computed in the different interaction frames, are shown together with the continuous wave spectrum calculated with the function *pepper* of EasySpin. The frames used in the density matrix computations are:

- Total Interaction Frame (TIF):  

$$\hat{H}_{\text{core}} = \frac{\mu_B}{\hbar} \mathbf{B}_0 \mathbf{g} \hat{\mathbf{S}} + \hat{\mathbf{S}} \mathbf{A} \hat{\mathbf{I}};$$
- Partial Interaction Frame (PIF):

$$\hat{H}_{\text{core}} = \frac{\mu_B}{\hbar} \mathbf{B}_0 \mathbf{g} \hat{\mathbf{S}}$$

- Standard Rotating Frame (SRF):

$$\hat{H}_{\text{core}} = \omega_{\text{mw}} \hat{S}_z.$$

Eq.A10 and Eq.A12 have been used for the static and the interaction Hamiltonians in the transformed frames. The spectra obtained with the time-dependent (Eq.A18) and the time-independent (Eq.A17) forms of detection operators are shown in the top and bottom panels of Figure 7 respectively. In the case of the TIF, the time independent form of detection operator is not shown because none time-signal is present in that case.

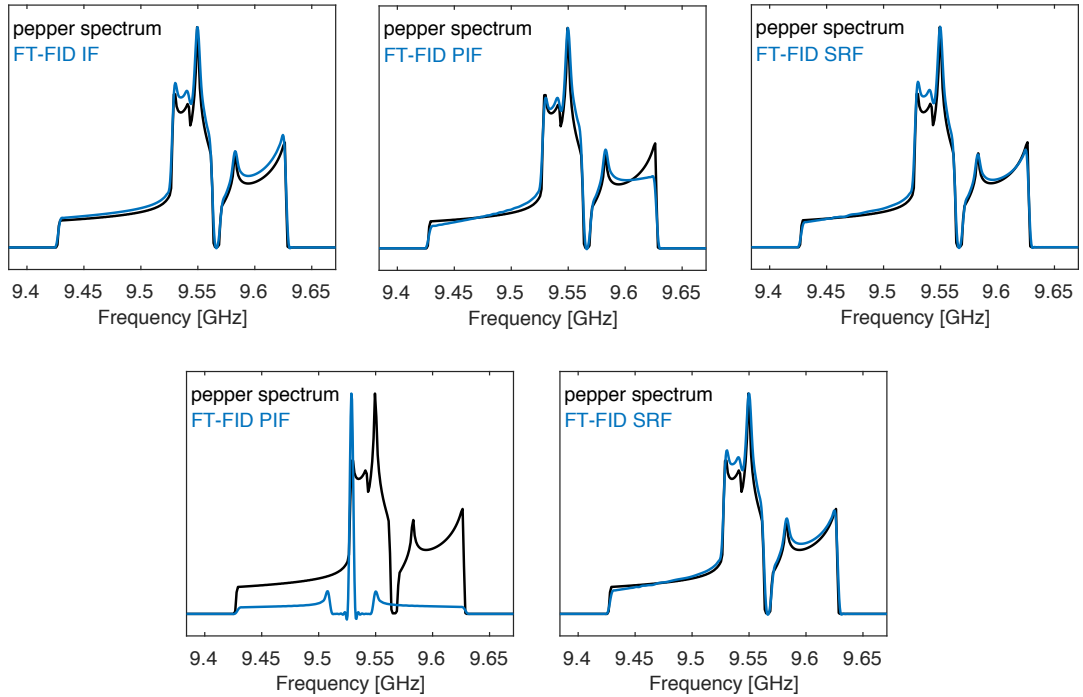


**Figure 7:** Top panels: overlap of the Fourier transforms of the FID signals, calculated in the TIF, PIF, SRF frames, and the frequency-domain EPR spectrum calculated with the function *pepper* of EasySpin. The signals in the top row have been detected by using Eq.A17, whereas in the bottom row the signals have been detected with Eq.A18

## Appendix B

### The signal in the laboratory frame

The calculation of a pulse EPR experiment in the laboratory frame is the most accurate spin dynamic description. This choice however, can be very demanding from the computational point of view because in principle it requires to record a signal modulated at high frequency. In order to reduce the computation time the evolution of the density matrix has to be divided into a mixing period, during which the pulses are applied, and a detection period, starting after the application of the last pulse and going through the detection. The signal then is:

$$s(t) = \text{Tr}\{\hat{D}e^{-i\hat{H}_0 t} \hat{\rho}_{\text{mix}} e^{i\hat{H}_0 t}\} \quad (\text{B1})$$

where  $\hat{\rho}_{\text{mix}}$  is the density matrix at the end of the mixing period obtained propagating the initial density matrix under the proper sequence of operators  $\hat{\rho}_{\text{mix}} = \hat{U} \dots \hat{\rho}(t_0) \dots \hat{U}^\dagger$ . Expressing Eq.B1 in the eigenbasis of  $\hat{H}_0$ :

$$s(t) = \sum_{m=l} D_{mm} \rho_{mm} + \sum_{m>l} D_{ml} \rho_{lm} e^{i(\epsilon_m - \epsilon_l)t} + \sum_{m<l} D_{lm} \rho_{ml} e^{i(\epsilon_l - \epsilon_m)t} \quad (\text{B2})$$

Knowing that  $D_{lm} \rho_{ml} = (D_{ml} \rho_{lm})^*$  and substituting  $\epsilon_m - \epsilon_l = \omega_{ml}$  and  $\epsilon_l - \epsilon_m = \omega_{lm} = -\omega_{ml}$ :

$$s(t) = \sum_{m=l} D_{mm} \rho_{mm} + \sum_{m>l} D_{ml} \rho_{lm} e^{i\omega_{ml} t} + \sum_{m<l} D_{ml}^* \rho_{lm}^* e^{-i\omega_{ml} t} \quad (\text{B3})$$

Taking only the real part of the signal:

$$\begin{aligned} s(t) &= \text{Re} \left\{ \sum_{m=l} D_{mm} \rho_{mm} + \right. \\ &\quad \left. 2 \sum_{m>l} D_{ml} \rho_{lm} e^{i\omega_{ml} t} \right\} \\ &= \text{Re} \left\{ \sum_{m=l} D_{mm} \rho_{mm} \right\} + \\ &\quad 2 \sum_{m>l} [\text{Re}\{D_{ml} \rho_{lm}\} \cos(\omega_{ml} t) - \\ &\quad \text{Im}\{D_{ml} \rho_{lm}\} \sin(\omega_{ml} t)] \end{aligned} \quad (\text{B4})$$

$$\begin{aligned} &= \text{Re} \left\{ \sum_{m=l} D_{mm} \rho_{mm} \right\} + \\ &\quad \sum_{m>l} [\text{Re}\{D_{ml} \rho_{lm}\} (e^{i\omega_{ml} t} + e^{-i\omega_{ml} t}) - \\ &\quad \text{Im}\{D_{ml} \rho_{lm}\} (e^{-i\omega_{ml} t} - e^{i\omega_{ml} t})] \end{aligned}$$

Analogously to what is done in the experiment, the signal is mixed with the microwave frequency and the fast oscillating components are filtered out:

$$\begin{aligned} s(t)^{\text{qp}} &= \text{Re} \left\{ \sum_{m=l} D_{mm} \rho_{mm} \right\} e^{i\omega_{\text{mw}} t} + \\ &\quad \sum_{m>l} [\text{Re}\{D_{ml} \rho_{lm}\} (e^{i\omega_{ml} t} + e^{-i\omega_{ml} t}) - \\ &\quad \text{Im}\{D_{ml} \rho_{lm}\} (e^{-i\omega_{ml} t} - e^{i\omega_{ml} t})] e^{i\omega_{\text{mw}} t} \\ &= \sum_{m>l} [\text{Re}\{D_{ml} \rho_{lm}\} e^{i(\omega_{\text{mw}} - \omega_{ml}) t} - \\ &\quad \text{Im}\{D_{ml} \rho_{lm}\} e^{i(\omega_{\text{mw}} + \omega_{ml}) t}] \\ &= \sum_{m>l} [\text{Re}\{D_{ml} \rho_{lm}\} - \\ &\quad \text{Im}\{D_{ml} \rho_{lm}\}] e^{i(\omega_{\text{mw}} - \omega_{ml}) t} \end{aligned} \quad (\text{B5})$$

where  $s_{\text{qp}}(t)$  is the quadrature phase signal.

The Free-Induction (FID) decay signal, for a nitroxide spin, computed in the laboratory frame by using Eq.B5 is shown in Figure B8. In the same figure, also the continuous wave spectrum calculated with the function *pepper* of EasySpin is shown as a comparison. The calculation was done by using the same parameters as in Appendix A. In this case the Fourier transform of the FID matches almost perfectly the calculated continuous wave spectrum.

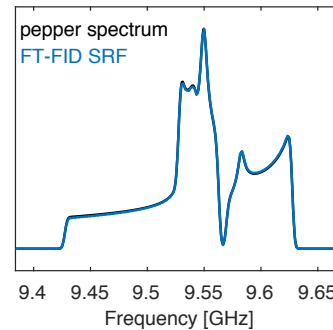


**Figure B8:** Overlap of the Fourier transform of the FID signal, calculated in the laboratory frame, and the frequency-domain EPR spectrum calculated with the function *pepper* of EasySpin.



## Bibliography

- [1] Marilena Di Valentin, Marco Albertini, Enrico Zurlo, Marina Gobbo, and Donatella Carbonera. Porphyrin triplet state as a potential Spin label for nanometer distance measurements by peldor spectroscopy. *J. Am. Chem. Soc.*, 136(18):6582–6585, 2014.
- [2] Marilena Di Valentin, Maria Giulia Dal Farra, Laura Galazzo, Marco Albertini, Tim Schulte, Eckhard Hofmann, and Donatella Carbonera. Distance measurements in peridinin-chlorophyll a -protein by light-induced PEL-DOR spectroscopy. Analysis of triplet state localization. *Biochim. Biophys. Acta - Bioenerg.*, 1857(12):1909–1916, dec 2016.
- [3] Christian Hintze, Dennis Bucker, Silvia Domingo Köhler, Gunnar Jeschke, and Malte Drescher. Laser-Induced Magnetic Dipole Spectroscopy. *J. Phys. Chem. Lett.*, 7(12):2204–2209, 2016.
- [4] Nurit Manukovsky, Akiva Feintuch, Ilya Kuprov, and Daniella Goldfarb. Time domain simulation of Gd <sup>3+</sup>–Gd <sup>3+</sup> distance measurements by EPR. *J. Chem. Phys.*, 147(4):044201, 2017.
- [5] Maxim Yulikov, Petra Lueders, Muhammad Farooq Warsi, Victor Chechik, and Gunnar Jeschke. Distance measurements in Au nanoparticles functionalized with nitroxide radicals and Gd<sup>3+</sup>–DTPA chelate complexes. *Phys. Chem. Chem. Phys.*, 14(30):10732, 2012.
- [6] Arina Dalaloyan, Mian Qi, Sharon Ruthstein, Shimon Vega, Adelheid Godt, Akiva Feintuch, and Daniella Goldfarb. Gd(III)–Gd(III) EPR distance measurements—the range of accessible distances and the impact of zero field splitting. *Phys. Chem. Chem. Phys.*, 17(28):18464–18476, 2015.
- [7] Maria Giulia Dal Farra, S. Ciuti, M. Gobbo, D. Carbonera, and Marilena Di Valentin. Triplet-state spin labels for highly sensitive pulsed dipolar spectroscopy. *Mol. Phys.*, 0(0):1–15, aug 2018.
- [8] Michael R. Wasielewski, Michael P. O’Neil, Keith R. Lykke, Michael J. Pellin, and Dieter M. Gruent. Triplet States of Fullerenes C60 and C70. Electron Paramagnetic Resonance Spectra, Photophysics, and Electronic Structures. *J. Am. Chem. Soc.*, 113(7):2774–2776, 1991.
- [9] H. Levanon and A. Wolberg. Electron spin polarization in the photoexcited triplet state of porphyrins. *Chem. Phys. Lett.*, 24(1):96–98, jan 1974.
- [10] J. M. Lhoste, A. Haug, and P. Hemmerich. Electron Paramagnetic Resonance Studies of the Triplet State of Flavin and Pteridine Derivatives. *Biochemistry*, 5(10):3290–3300, 1966.
- [11] D. H. Harryvan, W. H. Lubberhuizen, E. V. Faassen, Y. K. Levine, and G. Kothe. Characterization of the magneto-optical properties of eosin Y and erythrosin. *Chem. Phys. Lett.*, 257:190–196, 1996.
- [12] M. Montalti, A. Credi, L. Prodi, and M. Gandolfi. *Handbook of Photochemistry*. CRC Press, Boca Raton, 3rd editio edition, 2006.
- [13] P B Garland and C H Moore. Phosphorescence of protein-bound eosin and erythrosin. A possible probe for measurements of slow rotational mobility. *Biochem. J.*, 183(3):561 LP – 572, dec 1979.
- [14] T Shiga and L H Piette. TRIPLET STATE STUDIES OF FLAVINS BY ELECTRON PARAMAGNETIC RESONANCE—I. *Photochem. Photobiol.*, 3(3):213–222, 1964.
- [15] Erik Schleicher, Radoslaw M. Kowalczyk, Christopher W M Kay, Peter Hegemann, Adelbert Bacher, Markus Fischer, Robert Bittl, Gerald Richter, and Stefan Weber. On the reaction mechanism of adduct formation in LOV domains of the plant blue-light receptor phototropin. *J. Am. Chem. Soc.*, 126(35):11067–11076, 2004.
- [16] Haim Levanon and James R Norris. The Photoexcited Triplet State and Photosynthesis. *Chem. Rev.*, 227(5256):419–419, 1970.

- [17] W. B. Mims. Envelope Modulation in Spin Echo Experiments. Pdf. *Phys. Rev. B*, 5(7):2409–2419, 1972.
- [18] L. Rowan, E. Hahn, and W. B. Mims. Electron-Spin-Echo Envelope Modulation. *Phys. Rev.*, 137(1A):A61–A71, 1965.
- [19] Arthur Schweiger and Gunnar Jeschke. *Principles of pulse electron paramagnetic resonance*. Oxford University Press, New York, 2001.
- [20] F. J. Dyson. The radiation theories of Tomonaga, Schwinger, and Feynman. *Phys. Rev.*, 75(3):486–502, 1949.
- [21] Frank Neese. *Quantum Chemistry and EPR Parameters*, pages 1–22. American Cancer Society, 2017.
- [22] Marilena Di Valentin, Marco Albertini, Maria Giulia Dal Farra, Enrico Zurlo, Laura Orian, Antonino Polimeno, Marina Gobbo, and Donatella Carbonera. Light-Induced Porphyrin-Based Spectroscopic Ruler for Nanometer Distance Measurements. *Chem. - A Eur. J.*, 22(48):17204–17214, nov 2016.
- [23] Gunnar Jeschke, V. Chechik, P. Ionita, A. Godt, H. Zimmermann, J. Banham, Christiane R. Timmel, D. Hilger, and H. Jung. DeerAnalysis2006—a comprehensive software package for analyzing pulsed ELDOR data. *Appl. Magn. Reson.*, 30(3-4):473–498, jun 2006.
- [24] Jun John Sakurai. *Modern Quantum Mechanics*. Addison-Wesley Publishing Company, 1994.
- [25] Anderi V. Astashkin and Arnold M. Raitsimring. Electron spin echo envelope modulation theory for high electron spin systems in weak crystal field. *J. Chem. Phys.*, 117(2002):6121–6132, 2002.
- [26] R. Richard Ernst, Geoffrey Bodenhausen, and Alexander Wokaun. *Principles of Nuclear Magnetic Resonance in One and Two Dimensions*. Oxford University Press, 1987.
- [27] Alexander G. Maryasov and Michael K. Bowman. Spin dynamics of paramagnetic centers with anisotropic g tensor and spin of 1/2. *J. Magn. Reson.*, 221:69–75, 2012.
- [28] Stefan Stoll. *Spectral Simulations in Solid-State Electron Paramagnetic Resonance*. PhD thesis, ETH Zürich, 2003.